Exploring structure dependencies of gas-surface interactions with curved single crystals

Auras, S.V.

Exploring structure dependencies of gas-surface interactions with curved single crystals

Proefschrift

ter verkrijging van
de graad van Doctor aan de Universiteit Leiden,
op gezag van Rector Magnificus Prof. Dr. ir. H. Bijl,
volgens besluit van het College voor Promoties
te verdedigen op donderdag 11 maart 2021
klokke 11:15 uur

door

Sabine Veronika Auras

Geboren te Munchen, Duitsland in 1991

Promotiecommissie

Promotor:	Dr. L. B. F. Juurlink
	Prof. dr. M. T. M. Koper
Overige leden:	Prof. dr. S. J. van der Molen
	Prof. dr. M. A. Stöhr
	Prof. dr. A. W. Kleijn
	Prof. dr. E. J. Baerends
	Dr. I. M. N. Groot
	Prof. dr. H. S. Overkleeft

ISBN: 978-94-642-3153-3
Cover: Sabine Auras

An electronic version of this thesis can be found at
`https://openaccess.leidenuniv.nl/`.

Printed by ProefschriftMaken with financial support from Scienta Omicron

Meinen wundervollen Eltern gewidmet

CONTENTS

1

INTRODUCTION

1.1. CHEMICAL REACTIONS AND THE EFFECT OF CATALYSTS

CHEMISTRY studies the properties and transformations of matter. It is impossible to imagine a world without chemical reactions, which transform substances into new compounds, often with completely new properties. Schematically, we can write a chemical reaction as:

$$A + B \longrightarrow C \tag{1.1}$$

One essential example is the formation of water from hydrogen and oxygen:

$$2H_2 + O_2 \rightleftharpoons 2H_2O \tag{1.2}$$

Two core aspects determine whether we actually see a reaction occur. Firstly, the energy balance between reactants and products determines if it is thermodynamically favorable for the reaction to take place, or if the reverse reaction is preferred. This energy balance can change depending on the chemical environment, e.g. temperature, pressure, or concentration. Secondly, kinetics describe the reaction rate, i.e. how fast the reaction ensues. For example, graphite and diamond are two allotropes made of the element carbon. Thermodynamically, graphite is the more stable structure under the conditions at the earth's surface, however, we do not commonly see diamonds freely transform into graphite. That is because the rate of the process is so low that the transformation is imperceivably slow.

The reaction rate is described by the Arrhenius equation:[1–3]

$$k = \nu e^{-\frac{E_a}{RT}} \tag{1.3}$$

Here, k is the reaction constant, R is the universal gas constant, and T is the temperature. ν is the attempt frequency and E_a is the activation barrier. The last two terms are influenced by the conditions in which the reaction takes place. The activation energy is a barrier that needs to be overcome in order to go from the reactants to the products. Therefore, ν can be considered a descriptor of how frequently reactants attempt to overcome the barrier, and $e^{-\frac{E_a}{RT}}$ as the probability of successful attempts.

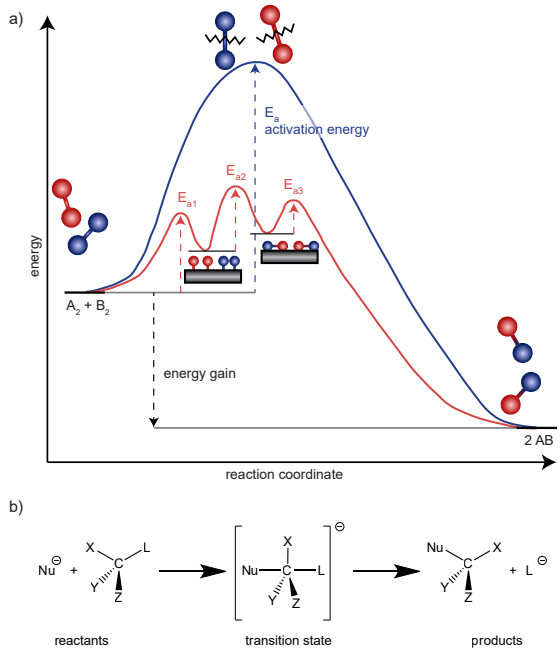

Figure 1.1: a) Schematic energy diagram of chemical reactions in the absence (blue) or presence (red) of a catalyst. The observed activation energy corresponds to the highest energy barrier that has to be overcome during the reaction path. b) Reaction mechanism of a S_N2 reaction, going through a transition state that is energetically less favorable than both reactants and products.

During the transformation of the reactants to products, they typically have to undergo a transition state that is less energetically favorable than both reactants and products. The blue line in figure 1.1a) illustrates this process. Figure 1.1b) shows an example where a nucleophilic substitution reaction undergoes a clearly unstable transition state. While the nucleophile (Nu^-) approaches the molecule and starts forming a bond and the leaving group (L) weakens its bond to the central carbon atom, a transition state is formed. As this transition state is energetically disfavored, the reactants need a certain amount of energy available to them, typically in the form of thermal energy, to reach this state. Once at the transition state, the reaction can then proceed towards the product while releasing energy.

Catalysts are substances that increase the rate of a reaction but are neither consumed

nor permanently changed by the reaction, or in the words of Friedrich Wilhelm Ostwald: "A catalyst is a substance which affects the rate of a chemical reaction without being part of its end products".[4, 5] The red line in figure 1.1a) shows a typical reaction path of a catalyzed reaction. The thermodynamic balance between reactants and products is not changed by catalysts, as the free energy of a reaction does not depend on the reaction path. For this reason, a catalyst cannot change the direction in which a reaction occurs. However, catalysts do lower the activation barrier of the reaction, e.g. by stabilizing intermediates and making transition states less unfavorable. The fraction $e^{-\frac{E_a}{RT}}$ in equation 1.3 therefore becomes larger, i.e. more "attempts" of the reactants are successful at overcoming the barrier, and as a result the reaction rate increases. In a laboratory setting, it can therefore appear as if a catalyst "makes the reaction happen", by increasing the reaction rate to a perceivable timescale.

Generally, two types of catalysis are distinguished: homogeneous catalysis, where catalyst and reactants are in the same (often liquid) phase, and heterogeneous catalysis, where reactants in the liquid or gas phase interact with a solid catalyst. Homogeneous catalysis finds application, e.g. in organic synthesis. There, catalysts can be mere protons in acid-catalyzed reactions, or complex structures of metal ions coordinated by organic ligands. A specific type of homogeneous catalysts are enzymes. All living organisms use catalyzed molecular modifications in their metabolic processes. Enzymes are large protein clusters that perform these highly targeted modifications on biological substrates under the mild conditions present in cells.

The work presented in this thesis relates to heterogeneous catalysis, and specifically catalytic reactions of small gas-molecules on solid surfaces.

1.2. HETEROGENEOUS CATALYSIS

The role of heterogeneous catalysis in today's world cannot be overstated. Finding a catalyst for the conversion of molecular nitrogen and hydrogen to ammonia, was crucial to the development of modern fertilizer. This conversion is now known as the Haber-Bosch process.[6, 7] Two Nobel prizes in chemistry were awarded for its development. Today, 50% of the global food production relies on synthetic nitrogen fertilizers.[8] In daily life, a heterogeneous catalyst in car exhausts reduces the amount of carbon monoxide and nitric oxide in the exhaust fumes. Fuel cells vehicles, which apply electrocatalysts, are nowadays commercially available.

Heterogeneous catalysis is crucial to today's economy due to the wide range of chemicals it has made available. Industrial processes in chemical manufacturing depend 80-90% on catalysis.[9] Catalysts can improve yields but also selectivity towards the

desired products by improving the reaction rate of certain reaction pathways more than others. Industrial catalysts often consist of metallic nanoparticles supported on oxide materials.

Schematically, reactions involving a heterogeneous catalyst can be described as reactants from the gas or liquid phase adsorbing at the surface, reacting (possibly in several steps) to form new compounds, and the products finally desorbing from the surface. The exact sequence of the reaction steps, i.e. the reaction mechanism, can vary. Different reaction mechanisms have been observed in gas-surface reactions. For example, CO oxidation on Pt can be described by the Langmuir-Hinshelwood mechanism:[10]

$$CO_{(g)} + * \rightleftharpoons CO_{ads} \tag{1.4}$$

$$O_{2(g)} + 2* \rightleftharpoons 2\,O_{ads} \tag{1.5}$$

$$CO_{ads} + O_{ads} \longrightarrow CO_{2(g)} + 2* \tag{1.6}$$

Here, CO adsorbs molecularly at an active surface site (*). Oxygen, on the other hand, undergoes dissociative adsorption, leading to two O atoms adsorbed at active sites. One adsorbed CO molecule can then recombine with an adsorbed O atom to form a CO_2 molecule, which desorbs from the surface. Adsorption on the surface stabilizes intermediate states during the reaction path, resulting in a lower activation energy compared to the uncatalyzed gas-phase reaction of CO and O_2.

During the Langmuir-Hinshelwood mechanism, the reacting species adsorb at separate sites, and subsequently react. The adsorption site may in some cases differ from the site of reaction. In this case, diffusion across the surface also has to be considered as part of the reaction. Other mechanisms have also been observed for surface reactions. For example, after one species pre-adsorbs, the second reactant may react directly from the gas phase (Eley-Rideal mechanism).[3] Alternatively an intial reaction with a reactive surface layer may occur, and a second species later replenishes the catalyst (Mars-van Krevelen mechanism). [11]

1.3. SURFACE SCIENCE APPROACH

The activity of heterogeneous catalysts is predominantly due to atomic layers at, or close to, the surface. The bulk material remains mostly unaffected. Understanding the reactivity of different types of surfaces in catalytic reactions is therefore of economic, as well as fundamental scientific interest. Surface chemistry, and specifically gas-surface dynamics, aim at unraveling how chemical reactions take place at surfaces, and how they are influenced by, e.g. catalyst material, surface structure, or the state of the reacting molecules. Reactants, reactions conditions, and the surface are controlled simultaneously for that reason. Theoretical and experimental studies

often go hand-in-hand in order to interpret observations and resolve details of the reaction mechanism.

Industrial heterogeneous catalysts are commonly composed of different materials and phases, with limited control over the exact surface structure. In contrast, surface science frequently makes use of single crystalline materials - a difference that is referred to as the material's gap.[12] The atomic arrangement in crystalline materials is defined by their lattice structure. Well-defined surfaces can be exposed, their structure depending on the orientation at which they are polished. Certain high symmetry planes result in atomically flat surface planes, while at a 'miscut' angle steps and kinks are introduced that separate high-symmetry terraces. Surfaces are generally described by their Miller indices (*hkl*), which indicate their orientation relative to the 3D lattice unit cell.[13] Figure 1.2 demonstrates the position of (111) and (001) planes within an *fcc* lattice.

Typically, flat single crystals exposing a defined plane are used to study surface reactions. Throughout this thesis, however, we make use of curved crystals cut from single crystalline materials. These type of samples are currently only employed by few research groups worldwide. Curved crystals provide a range of surface structures across their curvature, which is determined by the bulk lattice. We can therefore smoothly vary the composition of surface sites - terraces, steps and kinks - and determine their specific reactivity in gas-surface reactions. A thorough discussion of curved crystal surfaces is given in chapter 2.

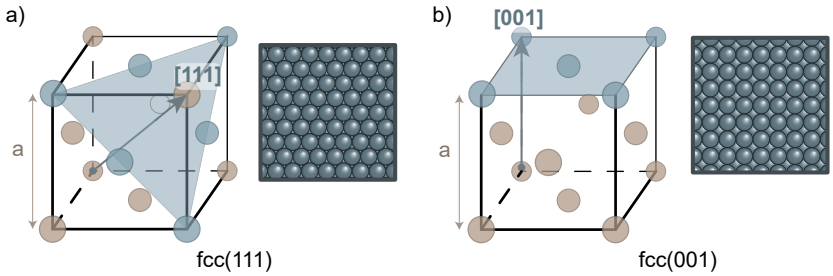

Figure 1.2: a) Unit cell of the *face-centered cubic* lattice with the atomically flat (111) plane indicated and atomic arrangement of a *fcc*-(111) surface. b) Unit cell of the *face-centered cubic* lattice with the atomically flat (001) plane indicated and atomic arrangement of a *fcc*-(001) surface.

Before experiments examining chemical reactions are carried out, single-crystalline surfaces are typically prepared by ion-bombardment (sputtering) to eliminate surface contamination and subsequent annealing at moderate temperatures to restore the surface structure. While this treatment may lead to almost perfect bulk-termination at the surface, in some cases surface reconstructions or faceting occur. Several methods are available to characterize the actual structure after surface preparation.

1

In this thesis low-energy electron diffraction (LEED), Scanning tunneling microscopy (STM), and Auger electron spectroscopy (AES) are used to characterize the surface across our curved crystals. LEED is a technique commonly applied to obtain information about the average structure probed by an electron beam. It makes use of the phenomenon that well-ordered surfaces can cause diffraction by elastically scattering electrons. Regularly stepped surfaces cause additional diffraction, resulting in split spots. STM, or other scanning probe techniques, can image the surface on a smaller scale, revealing local variations in surface structure. Electron spectroscopy techniques, e.g. AES, or x-ray photoelectron spectroscopy (XPS), are sensitive to the chemical nature of atoms at or near the surface, rather than the structure.[14] They can thus be used to examine the surface composition and reveal contamination.

At ambient pressure, gas molecules from the background would rapidly adsorb on the prepared surfaces. In order to maintain a clean surface, preparation and experiments must be carried out in ultra-high vacuum (UHV), i.e. at pressures $< 10^{-9}$ mbar. In this way, surface reactions of specific reactants can be observed almost exclusively. Gas-phase reactions are mostly avoided at such low pressures, as the large mean-free path of >60 km makes inter-molecular collisions unlikely. Additionally, signal detection for electron- or mass spectrometry-based techniques is much improved in vacuum. However, gas-surface reactions in UHV do not always reflect catalytic reactions in industrial applications; different reactions mechanisms or surface reconstructions may occur at higher pressures. This contrast is referred to as the pressure gap.

While the surface structure plays an important role in understanding gas-surface reaction mechanisms, a multitude of variables in the state of the reacting molecules also have to be considered.[15] Gas molecules are never completely still, they can move by translation, vibration, and rotation, and can be electronically excited. The exact state in which a molecule approaches the surface influences the subsequent reaction steps. Normally, the distribution of states is governed by temperature and pressure of the gas. Supersonic molecular beams, create a very narrow distribution of kinetic and rotational states, which can be modified among others by (anti-)seeding into other gasses, or heating the nozzle where the supersonic expansion takes place.[16] In this thesis (chapters 4 and 5), we use molecular beams to study dissociation and recombination of hydrogen on well-defined Pt surfaces. Similarly, the state in which a molecule desorbs from a surface can be influenced, e.g. by the way that it was adsorbed on the surface, surface coverage by other adsorbates, the reaction site and reaction kinetics. In the work presented in chapter 6, we use temperature-programmed desorption to explore differences of water nucleation on different Ag surfaces.

1.4. EXPERIMENTAL TECHNIQUES IN THIS THESIS

1.4.1. LOW-ENERGY ELECTRON DIFFRACTION

Low-energy electron diffraction (LEED) uses an electron beam with relatively low energy (20 – 200 eV), which is impinged on a surface. In this range, the wavelength of the electrons is on a similar length scale as the interatomic spacing of many crystalline materials. Well-ordered surfaces can thus cause diffraction of low-energy electrons. Experimentally, the diffraction pattern caused by elastically scattered electrons is visualized on a (hemispherical) fluorescent screen, while inelastically scattered electrons are filtered out by a series of hemispherical grids. The diffraction pattern displayed on the screen corresponds to the reciprocal lattice of the surface structure. For high-symmetry surface planes, the diffraction pattern is easily identified. Regularly stepped surfaces produce diffraction patterns with spot splitting, caused by the superlattice of steps.[17, 18] LEED can thus be employed to determine the average surface structure of the area probed by the electron beam.

1.4.2. SCANNING TUNNELING MICROSCOPY

Scanning tunneling microscopy can be used to investigate microscopic details of the local surface structure. An atomically sharp tip is placed close a conducting surface, and a potential is applied between them. Subsequently, the tip is further approached towards the surface, until the tunneling probability for electrons becomes large enough that a tunneling current can be measured. The tip is then scanned across an area of the surface. As the tunneling current decreases exponentially with sample-to-tip distance, even small variations in surface topography can be detected. With STM, atomic resolution of the surface structure can be achieved. However, STM images only probe a small fraction of the surface. In order to confirm the overall structure, several places across the surface need to be imaged.

1.4.3. AUGER ELECTRON SPECTROSCOPY

Auger electron spectroscopy (AES) is a technique used to characterize the chemical composition at (or near) the surface of a material. It makes used of the Auger effect, which is illustrated in figure 1.3. The surface is bombarded with high-energy electrons from an electron gun. This can cause the ejection of an core electron from surface atoms, creating an electron hole. The hole is subsequently filled with an electron from a higher energy level in the atom. The associated energy gain can lead to the emission of a third electron, the Auger electron. During AES, Auger electrons emitted from surface atoms are detected and their kinetic energy analyzed. The energies of Auger transitions are specific to the element and chemical environment of the surface atoms that the electron originated from. Auger spectra therefore give insight into the

chemical elements present at (or near) the surface.

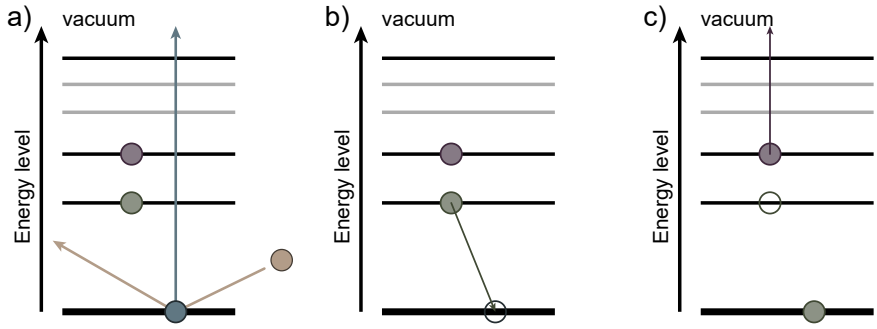

Figure 1.3: Auger emission process. a) An incident electron (beige), hitting a surface atom, causes the ejection of a core electron. b) A second electron (green) is de-excited from a higher energy to fill the electron hole. c) The transition energy is transferred to a third electron (purple), which is emitted into vacuum.

1.4.4. KING-AND-WELLS METHOD

The King-and-Wells method (KW) is used to determine sticking probabilities of gas molecules on surfaces.[19] In a source chamber, a (supersonic) molecular beam is created by the expansion of a high pressure gas mixture into vacuum. This expansion causes cooling, and a narrow distribution of kinetic and rotational states of molecules in the beam. The expanding gas plume is then shaped into a beam by skimmers. In this thesis, where curved crystal surfaces are employed, the last skimmer is a rectangular orifice that limits the footprint of the beam along the curvature to improve spatial resolution.

During a KW experiment, two flags initially block the molecular beam from entering the main chamber of a UHV system and hitting the sample surface. A quadrupole mass spectrometer (QMS) is used to determine the partial pressure of the gas species under investigation. Figure 1.4 shows a typical QMS signal during a KW experiment. Initially, the background signal in the main chamber is low. When the first flag is removed, the molecular beam enters into the main chamber. The partial pressure increases abruptly and then stabilizes. At this point the beam is still prevented from hitting the sample surface by the second flag. Once this second flag is removed, the molecular beam impinges on the sample, and a portion of the molecules in the beam stick to the surface. The initial sticking probability (S_0) is defined as the ratio between the pressure drop when flag 2 is opened (p_{drop}) and the pressure rise when flag 1 was initially opened (p_{rise}):

$$S_0 = \frac{p_{drop}}{p_{rise}} \tag{1.7}$$

S_0 can be used to describe the chemical reactivity of the surface towards adsorption of molecules. Different parameters, e.g. incident angle, kinetic energy (and energy distribution) of the beam, surface structure, and surface temperature. Varying these parameters and recording S_0 can therefore give insight into the underlying mechanism during adsorption.

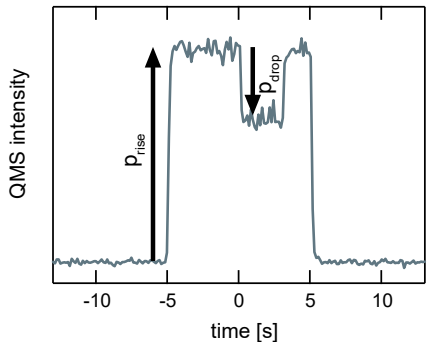

Figure 1.4: QMS trace of a gas species during a King-and-Wells experiment. Initially, the residual partial pressure is low. It increases rapidly, when the first flag is opened and the molecular beam enters the main chamber (p_{rise}). Once the second flag is removed and the beam hits the sample surface, the partial pressure decreases (p_{drop}). In this example, the subsequent closing of the two flags is also shown, the partial pressure then returns to the initial background.

1.4.5. TEMPERATURE-PROGRAMMED DESORPTION

For temperature-programmed desorption (TPD), a gas is first adsorbed on the surface, which is kept at a stable temperature. Subsequently, the sample is heated with a defined (programmed) temperature ramp. At the same time, the desorption of molecules from the surface is monitored with a QMS. TPD spectra contain information about desorption energy, rate, kinetics, as well as the surface coverage, making temperature-programmed desorption a useful technique in surface science. In order to correctly interpret results, thorough analysis is required. Different analysis methods are available to extract kinetic information.

A variation of TPD is temperature-programmed reaction (TPR), where reactant molecules are adsorbed at a temperature below the onset of reaction. During the temperature ramp, reaction eventually sets in and the desorbing product can be detected.

1

1.5. SCOPE OF THIS THESIS

In this thesis, we study reaction steps of small molecules on catalytic surfaces and unravel their structure dependencies by employing well-defined surfaces of curved crystals.

Chapter 2 lays out the design of curved crystals, which are used throughout this thesis. The macroscopic curvature of these types of single crystals grants microscopic control over the available surface sites. They can be oriented to precisely expose a desired range of tuneable surface structures. However, spatial resolution has to be considered when adapting standard surface science techniques to curved crystals. We discuss recent advances and applications of curved crystals in surface physics and chemistry, and particularly in research aimed at bridging the material's gap in heterogeneous catalysis.

Chapter 3 details the surface structure characterization of a curved Pt crystal, with fully-kinked steps that produce chiral surfaces. By low-energy electron diffraction, scanning-tunneling microscopy, and Auger electron spectroscopy, overall structures are confirmed, chiralities determined, and microscopic insight into the behavior of step arrays and atomic structure of step edges is obtained. This allows us to link chemical reactivities to specific surface sites in the following chapters.

In **chapter 4**, we use two different Pt crystals curved around the (111) plane to study hydrogen dissociation on vicinal surfaces featuring three types of steps. We use insights into the atomic composition of the kinked step edges to extract site-specific reactivities and define reactive cross-sections for all three types.

Chapter 5 revisits the surface structure of the curved crystal in chapter 3, focusing on areas near the apex without well-ordered arrays. We determine the range on the crystal where vacancy islands and freely meandering steps cause defect densities to deviate from those predetermined by the miscut angle. Extrapolating D_2 sticking probabilities to zero step density allows us to extract the dissociation probability on a perfect (111) surface. In addition to hydrogen dissociation, we measure H-D exchange on the crystal and discuss the relation between them.

In **chapter 6**, two curved Ag crystals are combined for H_2O desorption experiments from stepped surfaces. We explore differences in water nucleation on surfaces with three step- and two terrace types by quantifying changes in the desorption temperature of sub-monolayer coverages of H_2O. Linear relationships of desorption energy with step density are identified. The potential of combining curved crystals with different orientations is emphasized.

Chapter 7 discusses prospective applications of curved crystals in surface chemistry. We present preliminary results of studying CO_2 adsorption on Pt and characterize the

surface of a novel curved crystal of a bimetallic alloy.

REFERENCES

[1] S. Arrhenius. Über die Dissociationswärme und den Einfluss der Temperatur auf den Dissociationsgrad der Elektrolyte. *Zeitschrift für physikalische Chemie*, 4(1):96–116, 1889.

[2] S. Arrhenius. Über die Reaktionsgeschwindigkeit bei der Inversion von Rohrzucker durch Säuren. *Zeitschrift für physikalische Chemie*, 4(1):226–248, 1889.

[3] P. W. Atkins and J. De Paula. *Physikalische Chemie*. Wiley-VCH, Weinheim, 4 edition, 2006.

[4] W. Ostwald. Catalysis. *Phys. Z*, 3:313–322, 1901.

[5] W. Ostwald. Über Entwicklungs- und Wachstumsgesetze. *Pflüger's Archiv für die gesamte Physiologie des Menschen und der Tiere*, 133(1-3):1–6, 1910.

[6] F. Haber. *Thermodynamik technischer Gasreaktionen: Sieben Vorlesungen*. R. Oldenburg, 1905.

[7] C. Bosch. Process of producing ammonia., April 18 1911. US Patent 990,191.

[8] J. W. Erisman, M. A. Sutton, J. Galloway, Z. Klimont, and W. Winiwarter. How a century of ammonia synthesis changed the world. *Nature Geoscience*, 1(10):636–639, 2008.

[9] U. Hanefeld and L. Lefferts. *Catalysis: An Integrated Textbook for Students*. John Wiley & Sons, 2018.

[10] H.-J. Freund, G. Meijer, M. Scheffler, R. Schlögl, and M. Wolf. CO oxidation as a prototypical reaction for heterogeneous processes. *Angewandte Chemie International Edition*, 50(43):10064–10094, 2011.

[11] J. R. Ross. Chapter 7 - The Kinetics and Mechanisms of Catalytic Reactions. In J. R. Ross, editor, *Contemporary Catalysis*, pages 161 – 186. Elsevier, Amsterdam, 2019.

[12] L. Vattuone, L. Savio, and M. Rocca. Bridging the structure gap: Chemistry of nanostructured surfaces at well-defined defects. *Surface science reports*, 63(3):101–168, 2008.

[13] W. H. Miller. *A treatise on crystallography*. For J. & JJ Deighton, 1839.

[14] K. Oura, V. Lifshits, A. Saranin, A. Zotov, and M. Katayama. *Surface science: an introduction*. Springer-Verlag, 2003.

[15] C. T. Rettner, D. J. Auerbach, J. C. Tully, and A. W. Kleyn. Chemical Dynamics at the Gas-Surface Interface. *The Journal of Physical Chemistry*, 100(31):13021–13033, 1996.

[16] A. W. Kleyn. Molecular beams and chemical dynamics at surfaces. *Chemical Society Reviews*, 32(2):87–95, 2003.

[17] M. Henzler. LEED-investigation of step arrays on cleaved germanium (111) surfaces. *Surface Science*, 19(1):159–171, 1970.

[18] W. Ellis and R. Schwoebel. LEED from surface steps on UO_2 single crystals. *Surface Science*, 11(1):82–98, 1968.

[19] D. A. King and M. G. Wells. Molecular beam investigation of adsorption kinetics on bulk metal targets: Nitrogen on tungsten. *Surface Science*, 29(2):454–482, 1972.

2

RECENT ADVANCES IN THE USE OF CURVED SINGLE CRYSTAL SURFACES

In surface science, research traditionally employs macroscopically flat surfaces of single crystals. Curved surfaces have been applied more sporadically, but their history stretches back for many decades. Realization of the potential benefits and practical applications in surface physics and surface chemistry research progressed slowly in the 20th century. In more recent decades, research employing partial cylinders and dome-shaped crystals have found renewed interest. Modern surface sensitive techniques are being employed allowing the inherent large range of surface structures to reveal new insights. We briefly review the history, describe several types of surfaces and the range of structures they contain, suggest a notation for common types of curved surfaces, and discuss recent studies in more detail. We mainly focus on metal samples. We close with a short outlook.

This chapter is based on the following publication:
S. V. Auras and L. B. F. Juurlink. Recent advances in the use of curved single crystal surfaces. *Progress in Surface Science*, submitted.

2.1. INTRODUCTION

WHY USE SOMETHING OTHER than the well-defined, single surface structure offered by a near-perfectly flat polished single crystal? Flat samples are easily available in all kinds of shapes and sizes, and there is an enormous amount of experience built up over decades by the large surface science community in proper handling of these samples. There are well-defined cleaning procedures and one maximizes surface area with uniform structure at the atomic level. Surfaces with curvature may host a range of surface structures, but these may suffer from faceting and other forms of surface rearrangements that locally alter the ideal or expected bulk surface termination. Such non-continuous variations in surface structure needs to be dealt with and, at least, adequately studied. A large enough range of structure variations also requires larger samples and non-standard polishing techniques. Finding cleaning procedures that work properly for the entire range of surface structures present on a curved surface may also be nearly or entirely impossible, at least without inducing reconstructions of faceting somewhere along the surface. Larger samples also add experimental complexities as these are more difficult to heat and cool uniformly.

Regularly, researchers that attempted to reap the fruits of the single largest benefit of curved surfaces in modern scientific research - i.e. hosting a large range of surface structures in a single single crystal - speak of the technical difficulties. To investigate effects of terrace size, edges and kinks or corner atoms, one could revert to the use of nanocrystals. These may inherently contain various facets and 'defect' types and densities. Indeed, the use of nanoparticles grown on well-defined supports has shown to provide this option with high levels of control over crystal shape and size.[1] However, remaining heterogeneity and limited surface area may be reason to revert back to single crystals and consider using a curved surface instead of a flat surface to introduce controled variation of surface structure. The use of curved surfaces is now nearly 100 years old and still going strong, albeit well under the radar for many surface scientist raised with the idea that flat surfaces are the only norm. For those unfamiliar to the field, many types of continuously curved single crystal shapes have been made and used: spheres, solid and hollow full cylinders, partial cylinders, inverted cylinders, domes and cones. The history of surface science is long enough that pretty much every shape has been used, often for a particular reason. Figure 2.1 shows a small collection crystal shapes that have appeared in the 20^{th} century literature on metal curved surfaces.

This review starts with a brief historical overview of the use of curved surfaces of single crystals in surface science. It mostly pays homage to predecessors by illustrating studies prior to the widespread application of Scanning Tunneling Microscopy (STM). The following section has a pedagogical intention. It illustrates through examples which range of ideal truncations of bulk crystal structures may appear on commonly

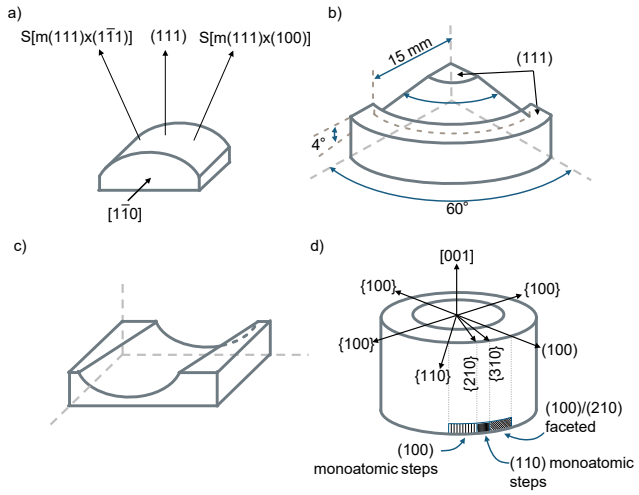

Figure 2.1: Examples of curved crystal shapes used in research in the 20th century. The solid sections of a Pt and Au cylinders included ~ 14°.[2] The conical [3] and extracted cylindrical [4] shapes were made from Cu single crystals. The full hollow Pt cylinder showed both monoatomic stepped and faceted regions.[5] Images are redrawn from original figures with minor alterations for clarity.

used shapes and sizes of curved single crystal surfaces. We propose a new notation that captures most commonly used crystal shapes for which one also easily extracts the available range of surface structures. We subsequently discuss recent studies and the advancements in the field in the last 20-25 years. We conclude with a short outlook.

2.2. BRIEF HISTORICAL OVERVIEW

At least as early as 1927 have properties of curved surfaces of clean metallic single crystals been studied. Ernest Linder at the State University of Iowa investigated the emission of electrons from a zinc single crystal rod under ultraviolet irradiation in vacuum.[6] The rod was cleaned by evaporating the outer layers of the moulded single crystal. To do so, Linder had to heat the entire glass vacuum apparatus, including the 4 cm long cylindrical Zn single crystal, to 400 °C with a Bunsen burner while ensuring that windows and other important parts did not get coated with Zn. He subsequently illuminated a 1 mm wide stripe along the cylinder's axis using light from a mercury arc lamp. The obtained photoelectric current varied a factor of 2 over a 90° rotation along the cylindrical axis of the sample. Linder suggested that it reflected the dependence of the work function on surface structure.

Around the same time, Hausser and Scholz at Siemens in Germany developed ways to grow macroscopic metallic single crystals in vacuum.[7] Sharing their Cu samples with Tammann and Sattorius at Göttingen University [8], they studied lattice struc-

tures and anisotropic behavior along the crystallographic axes using optical reflection and x-ray diffraction. Combining their observations with symmetry considerations, they arrived at conclusions regarding the dynamics of crystal growth and differences between ideal and real crystal structures.

Experimental techniques improved and at the end of the 1930's Martin at MIT's new George Eastman Laboratory imaged thermionic emission from a tungsten single crystal sphere of ~ 1 cm diameter in an apparatus originally designed by Shockley.[9] Photographs of patterns appearing on a bulb-shaped fluorescent screen illustrated the dependence of electron emission on crystallographic direction.

In subsequent years, chemists focused increasingly on dependencies of catalytic properties on surface structure. Improving crystal growth techniques and preparation of surfaces [10], Gwathmey and Benton showed that such dependencies occurred in reactions of O_2 and H_2 with copper spherical single crystals.[11, 12] They arrived at their conclusions based on experiments using no more than reflection of light from incandescent light bulbs and reporting color changes.[11, 13] Allen Gwathmey continued this work for many years to come, e.g. measuring relative rates for hydrogen oxidation on Cu(111) and Cu(100) planes.[14] Having noticed oxide formation, its dependence of crystallographic plane, and its effect on chemical reaction rates, he started combining research on spherical samples with flat single crystals. Both were produced by machining Cu rods grown under vacuum conditions. He also created larger flat areas on the surface of a Cu sphere, exposing surfaces, e.g. (100) and (111). Research on Cu oxidation and water formation went on [15] and expanded into the effect of impurities, e.g. Ag and Zn. These were added to the surface by electrodeposition, evaporation, or dipping the spheres in solutions containing the metal of interest.[16] An ellipsometer was constructed to measure surface structure dependent rates of oxidation [17] on flattened parts of Cu spherical crystals. X-Ray techniques were implemented to study the structure of Cu_2O grown by oxidation of spheres.[18] Gwathmey also studied catalytic reactions on Ni spheres [19, 20] and used spherical crystals to study friction and its dependence on surface structure.[21] The second PhD student that Allen Gwathmey worked with, Henry Leidheiser, also continued research on spherical crystals, e.g.. on the phase transition in Co [22] and catalytic reactions on its surface [23], and on the structure dependence of rate of development of silver chloride surfaces.[24]

More research groups picked up on the potential of curved surfaces in the last three decades of the 20^{th} century. The growing number of available experimental techniques and obtainable spatial resolution made the combination with curved surfaces of increasing interest to surface scientists. Wagner and coworkers in Jülich, Germany, used a 0.2 mm diameter electron beam from a LEED apparatus with partially curved W, Pt and Au samples and found a linear dependence of the work function with step density for these metals.[2] The dependence was attributed to the lowered dipole mo-

ment of steps in comparison to the low Miller index plane. At the Ecole Nationale Supérieure de Chimie in Paris, Domange and coworkers applied LEED and RHEED to study Cu vicinal surfaces.[3, 4, 25] They used crystals with multiple flattened parts at different relative angles and pioneered the use of smoothly curving conical samples. They also used a semiconducting GaAs crystal, predecessing extensive studies of such materials with curved shapes by Ranke.[26–28]. Bauer and coworkers in Clausthal, Germany, were the first to visualize how spot splitting in Low Electron Diffraction (LEED) patterns indicated a smoothly varying terrace width average over a 90° rotation, here for a W cylinder.[29] Spot splitting in LEED patterns of vicinal surfaces had only recently been explained by Ellis and Schwoebel as resulting from the interference between diffraction from the atomic low Miller index structure and step arrays.[30] For Bauer's W cylinder, it indicated stability of very rough surfaces with respect to faceting for the clean metal. In contrast, deposited Au overlayers diffused and formed faceted regions on parts where the W support showed high step densities. [31]

Beyond electron-based techniques, also H^+ ion scattering was applied to a study curved surfaces. Frenken and colleagues at AMOLF in Amsterdam used ion shadowing and blocking to study surface disordering (melting) and related it to the free energy difference between the solid and liquid states.[32] This difference varies with the local surface structure and explained (in part) their results for structure-dependent surface melting of a curved Pb sample.

Chemical properties and their importance to surface reactions were also explored in increasing detail in these decades. Probably being the first to employ a Pt curved sample, Comsa and coworkers in Jülich investigated O_2 and CO adsorption and reaction. [33] They reported that a LEED study of the clean crystal showed the expected variation in spot splitting, later published graphically for W by Bauer. Using Auger Electron Spectrscopy (AES) and a quadrupole mass spectrometer (QMS), subsequent experiments revealed a complex dependence of O_2 adsorption and CO oxidation reaction rates to surface structure. The two parallel mechanisms active in CO oxidation for Pt steps and (111) terraces were only very recently resolved by Wodtke and coworkers. [34]

Following Comsa's initial catalytic studies, Woodruff and coworkers at the University of Warwick in the UK used quantitative AES measurements and full cylindrical Cu and Ni samples. They studied surface structure dependencies in the absorbed and scattered electron currents and related them to variations in AES signal intensities. These were subsequently used to quantitatively relate dissociation kinetics of S_2, O_2 and N_2O to surface structure. [35–39].

Adding a rotatable Kelvin probe and photoemission electron microscopy (PEEM) to the list of employed techniques, Imbihl and Ertl used a full Pt cylinder to study struc-

ture dependencies in kinetic oscillations and spatiotemporal patterning in reactions of CO and NO under low vacuum conditions. [5, 40–43] With PEEM they obtained a spatial resolution of ~1 μm. They reported significant faceting along parts of the cylindrical surface, though, which may be related to their choice of the [001] direction of the Pt cylinder's rotational axis and the consequential combination of {100} and {110} planes making up the crystal's curved surface.[5]

One may expect that the invention of the STM in the early '80s was quickly applied in studies of curved surfaces. While LEED mostly provides averaged information on surface structure within the region probed by the relatively sizeable electron beam, STM yields structural information with much higher spatial resolution. Oddly, it took more than two decades before the first article appeared reporting a systematic STM study of surface structure variation along a curved surface. Results from the more recent decades by Bader, Fradin, and coworkers, by Ortega and coworkers, Gellman, Sykes and co-workers and our own will be discussed later. First, we consider the various surface structures and structural ranges obtainable using various crystal shapes for common unit cells of transition metals.

2.3. SURFACE STRUCTURES ON CURVED SURFACES OF SINGLE CRYSTALS

Macroscopically flat single crystals that are most commonly used in surface science studies are oriented, cut and polished to expose a single surface structure. Often an atomically flat, highly symmetric surface is chosen - a low Miller index plane. To consider surface structures exposed on a smooth curved surface, we find it most intuitive to start our consideration from such common low Miller index planes. They also often appear at the apex of partially curved samples.

For metals with a face-centered cubic (*fcc*) lattice, commonly used low-Miller index planes are the most densely packed hexagonal (111) and the more open square (001) surfaces. Figure 2.2a) and b) demonstrate their orientation within the *fcc* unit cell. Vectors drawn within the low Miller index plane indicate two azimuths pointing along different step structures. Alternatively, they may be considered two rotational axes for curved or cylindrical surfaces leading to ideal step structures as derived from the ordering of lattice points. The azimuths are 90° (30°) degrees apart for (111) and 45° degrees for (001). Figure 2.2c) and d) show two atomically flat planes in, respectively, *bcc* and *hcp* unit cells. While the first has a centered rectangular Bravais surface lattice, the second is hexagonal. Arrows again indicate two azimuths pointing along step directions or high-symmetry rotational axes. Note that, although *hcp*(0001) and *fcc*(111) are both hexagonaly close packed surfaces, stacking of subsequent atomic layers varies. While *hcp* has an A-B-A-stacking, *fcc* has A-B-C-A-stacking. This has consequences for the different types of steps appearing along a curved surface.

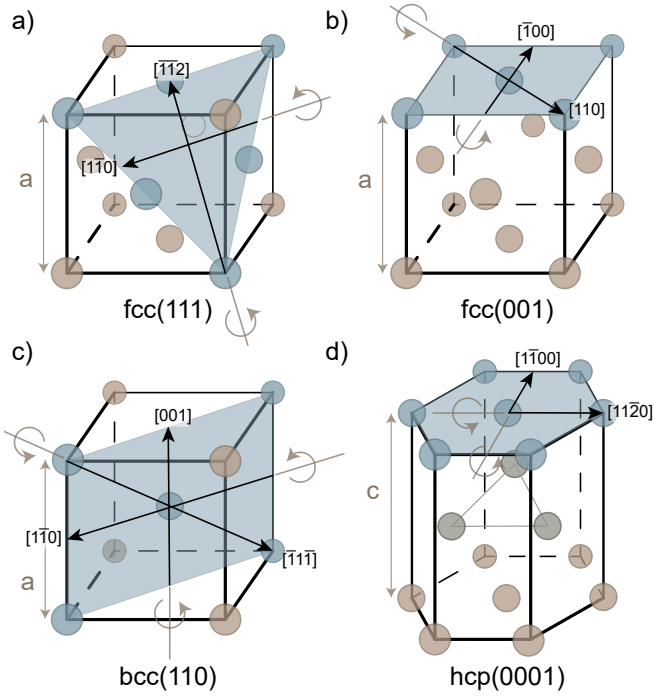

Figure 2.2: Unit cells of *fcc*, *bcc*, and *hcp* lattices and commonly used surface planes. The lattice constant a is indicated for the cubic unit cells. For *hcp* the second lattice constant c equals $\sqrt{\frac{8}{3}} \cdot a$. Blue arrows represent surface normals of the colored planes. Black arrows identify typical step directions and common rotational axes in curved and cylindrical samples. a) Hexagonal *fcc*(111) plane with close-packed A- and B-type step ([1$\bar{1}$0]) and fully-kinked step ([$\bar{1}\bar{1}$2]) directions. b) Square *fcc*(001) plane with close packed A'-type ([110]) and fully kinked step ([$\bar{1}$00]) directions. c) Centered rectangular *bcc*(110) plane with two achiral kinked step directions ([001] and [1$\bar{1}$0]). d) Hexagonal *hcp*(0001) plane with close-packed ([1$\bar{1}$00]) and kinked ([11$\bar{2}$0]) step directions.

For an ideally truncated surface, rotation from a low-Miller index plane introduces monoatomic steps. These steps separate terraces of the low-Miller index plane. With increasing angle, terraces are more frequently interrupted by steps, i.e. the step density increases and the average terrace width decreases. Rotation around different axes introduces different types of steps. They are characterized by the atomic arrangement in the step facet. In the case of single or double atomic steps, they are generally simply a microfacet of the first low-Miller index plane occurring on the arc between the surface normal and the azimuth. For example, in figure 2.2a), upward rotation of the (111) plane along $[1\bar{1}0]$ creates an arc connecting [111] to the $[\bar{1}\bar{1}2]$ azimuth. This arc passes through [001]. The atoms forming the microfacet are arranged in the same square manner as the (001) plane. This step type is often referred to as the A-type step. Downward rotation of the (111) plane along $[1\bar{1}0]$ passes through the (110) and, subsequently, $(11\bar{1})$ planes. The atomic ordering in the steps introduced into the (111) plane may thus be described as either a rectangular {110} or a hexagonal {111} microfacet. This type of step is generally referred to as the B-type step. In a similar fashion, different step facets connecting various types of planes may be derived from figure 2.2. Note that we here assume monoatomic steps. They are the shortest possible microfacet of a specific type. Step doubling is a term used to indicate that the microfacet stretches across two planes parallel to the surface. Stronger restructuring of a surface may expose large facets of (possibly) other planes than the microfacet of a monoatomic or double step. They are often the plane with the lowest free energy of the material. Although such faceting occurs, we focus here on monoatomic steps.

Figure 2.3 visualizes several different types of monoatomic steps by top view representations of domes with apices chosen identical to the planes indicated in figure 2.2. On (111) terraces of *fcc* metals, six directions of close-packed steps are possible. Figure 2.3a) shows the three equivalent directions exposing {001} microfacets (A-type steps) and three equivalent directions exposing {110} microfacets (B-type steps). Blue and red lines mark monoatomic steps. A closer look at the atomic arrangements of A- and B-type steps is given in figure 2.4. Color coding is maintained between these figures. In figure 2.4a), the step edge colored in red also illustrates how this B-type edge can be seen both as a {110} and {111} microfacet. For the latter, the lower (111) plane stretches one atomic row further into the edge than for the former.

Azimuthal directions in between two close-packed step types require kinks to be introduced in monoatomic steps. Taking the example of figure 2.3a) and figure 2.4a), {001} and {110} microfacets are connected alternately by outer and inner kinks. The highest repetition of kinks, i.e. the most corrugated edge, is formed with the shortest possible alternation of these type step sections. It is represented in purple in these figures. In between the most corrugated and the close-packed step types, the edges are in principle composed of longer stretches of one close-packed step type with less frequently occurring kinks and shorter stretches of the other close-packed step type.

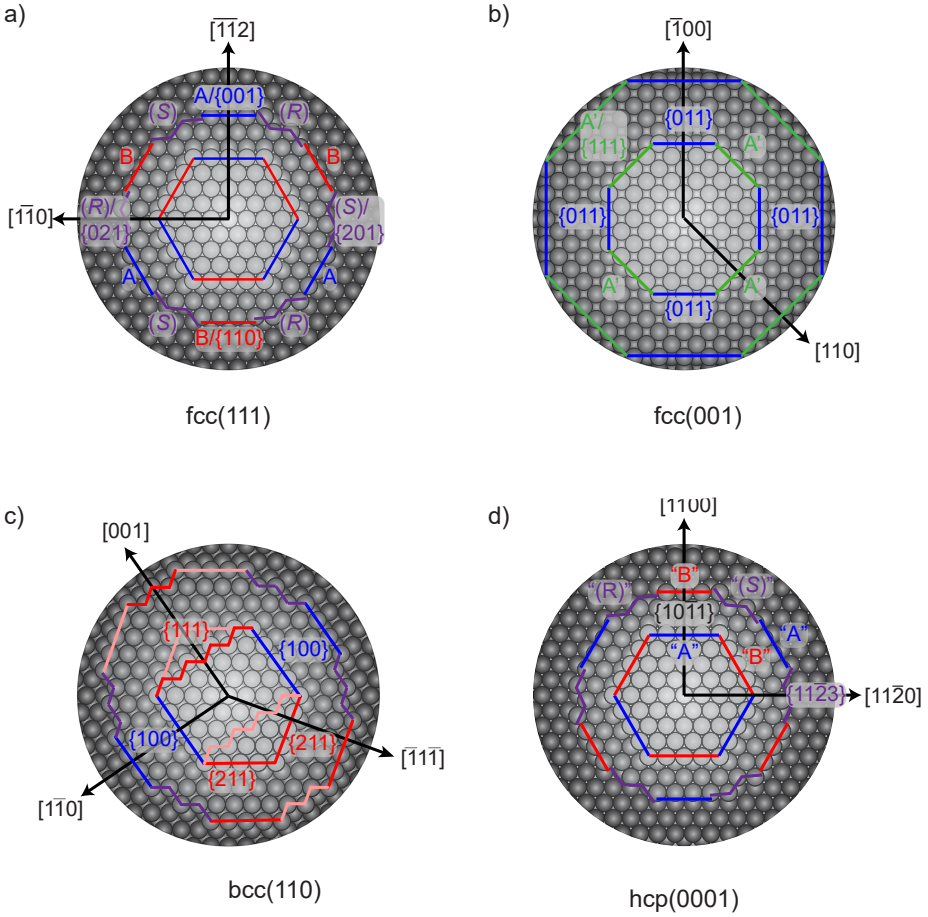

Figure 2.3: Top views of the atomically flat terraces of *fcc*, *bcc*, and *hcp* and possible step types. The displaed surface planes step down twice from the center towards the edges. a) Due to the hexagonal symmetry of *fcc*(111) terraces, three equivalent directions of {001}/A-type (blue) steps and {110}/B-type (red) steps are present. In between the close-packed step types, kinked steps can be found, consisting of A- and B-type segments separated by kinks. The resulting chirality (*(R)* or *(S)*) of stepped surfaces of this kind is indicated. Purple lines give directions of the fully kinked steps with equal lengths of A- and B-type steps. b) On *fcc*(001) terraces, four equivalent directions of close-packed {111}/A'-type steps can be found (green). Steps in between these orientations (blue) feature kinks separating short {111} segments, but do not inevitably cause chiral surfaces. c) On *bcc*(110) terraces, close-packed {211}-type steps (red) can be formed in four (not evenly spaced) directions. These types of close packed steps are inherently chiral. More open non-kinked steps are formed by {100} microfacets (blue) and are non-chiral. In between {211} and {100} directions, kinked steps form chiral surface. In between two adjacent {211} directions, a different type of kinked step (light red) is formed that does not automatically lead to chiral surfaces. d) On *hcp*(0001) terraces, six equivalent close packed step orientations are formed ({1011} microfacets). In subsequent steps of the same orientation, the step structure switches between arrangements like the *fcc* A-type and arrangements like the *fcc* B-type. In between close-packed step orientations kinked steps are formed, creating racemic surfaces.

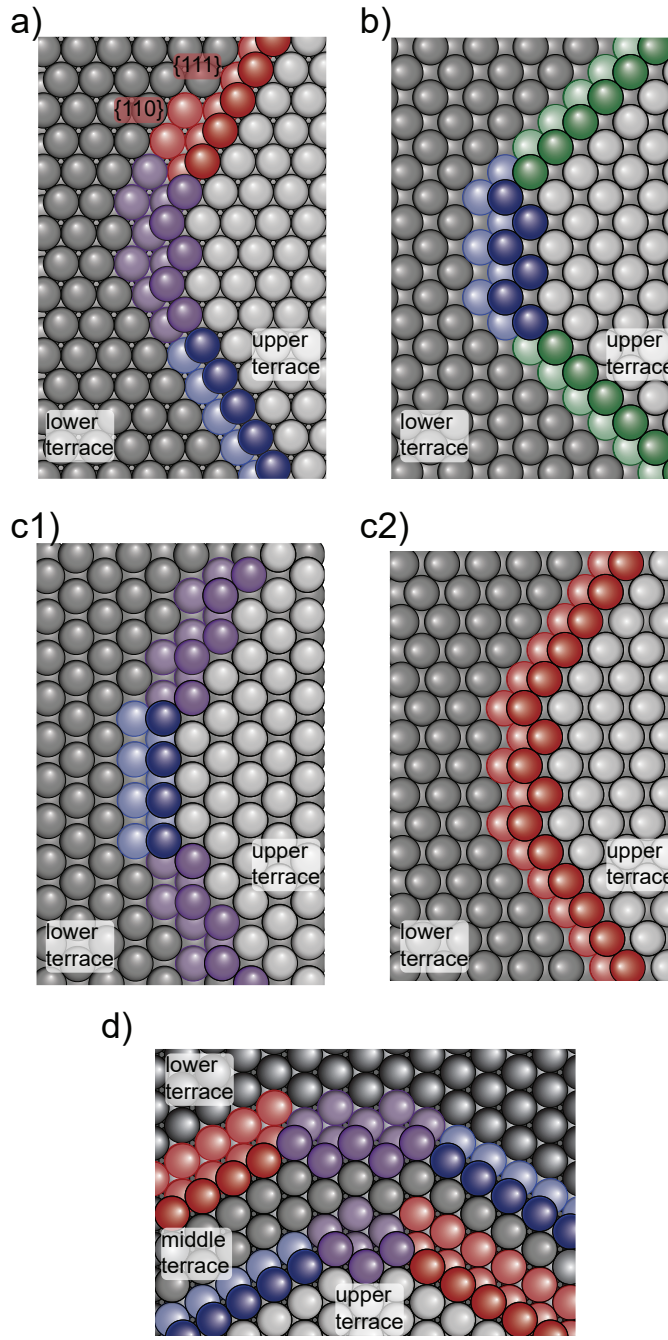

Figure 2.4: Atomic arrangement of different step types on a) *fcc*(111): A-type(blue), B-type(red), kinks(purple), b) *fcc*(001): A'-type (green), kinks (blue), c) *bcc*(110) c1): {100} steps (blue) and kinked steps consisting of {100} and {211} microfacets c2) Two {211} steps separated by a kinked achiral {111} step d) *hcp*(0001) close packed steps with A- and B-like structures on subsequent terraces, kinked step edges causing racemic surfaces.

The symmetry of kinked step edges is reduced compared to the close packed step edges. On stepped *fcc*(111) terraces this leads to chirality. While different nomenclatures have been proposed([44–46]), the established nomenclature uses the ordering of the Miller indices of the microfacets forming the inner kink. They are arranged by their atomic density (highest to lowest).[47] For terraces of *fcc*(111) with kinked steps, the three relevant microfacets are {111} for the lower terrace, and {001} and {110} for the edge segments forming the inner kink. Tracing the facets in the order of decreasing atomic density, i.e. {111} to {100} to {110}, gives a right-handed (*R*) or left-handed (*S*) rotation.[48] In figure 2.3a), the location of these *(R)* and *(S)* kinks are indicated. Figure 2.4a) shows the (R) version in between sections of A- and B- types steps. Kinked steps may partially reconstruct to reduce corrugation, but chirality is maintained.[49]

In contrast to (111) planes of the *fcc* unit cell, four equivalent directions yielding close-packed steps occur on (001) terraces, as displayed in figure 2.3b). They are {111} microfacets, or A'-type steps.[50] The inner corner of the step is identical to the A-type step, but the planes forming terrace and step are switched. In between the four equivalent azimuths, kinked steps are expected. Figure 2.4b) shows the atomic arrangement of A'-type steps, as well as fully-kinked steps in between the close-packed step orientations. Here, both sides of the inner kink are {111} microfacets. Chirality only occurs if unequal lengths of {111} facets separate the kinks. For a more detailed discussion on chirality of surfaces of different crystal lattices, we refer the reader to the roadmap laid out by Jenkins and Pratt.[46]

For the *bcc*(110) plane in figure 2.3c), we find the close packed steps forming {211} microfacets, as well as more open, but not kinked {100}-type steps, and different types of kinked steps. Kinked steps can be formed either from alternating segments of {211} microfacets and {100} microfacets, or by segments of {211} microfacets to both sides of a kink. The latter type of kinked step can be described as a {111}-type step. Figure 2.3 c) elucidates the orientation of different step types on a *bcc* (110) surface. It is noteworthy that stepped surfaces with {211}-type steps are chiral surfaces, despite the absence of kinks. This is due to the alignment of (110) planes, causing the atoms at the lower step edge to be slightly off-center relative to the upper step edge. Again, we refer to Jenkins and Pratt for detailed symmetry considerations.[46]

Lastly, step orientations on *hcp*(0001) resemble those of *fcc*(111) at first glance. Two close packed step types show the same arrangement as A- and B-type steps on *fcc*, we will therefore refer to them as such. However, subsequent steps in the same direction, show alternating A- and B-type steps, and as a result, curved crystals can never expose only one type of step. Consequently, the kinked steps at orientations away from the close-packed steps also alternate between *(R)* and *(S)* chirality, meaning that stepped surfaces involving kinks are always racemic surfaces.

2.4. CURRENTLY USED CRYSTAL SHAPES

In the absence of surface reconstructions, a macroscopic perfect sphere exhibits all possible terminations of the crystal lattice on its surface. Clearly, when performing research on the surface structure dependencies, this would be ideal. However, creating a perfectly polished single crystal sphere is rather complex. As discussed in section 2.2, single crystal spheres were used in experiments in the 20th century, but generally in an "as-created" spherical shape from a melt. Such spheres are often faceted away from low-Miller index planes and therefore do not exhibit a truly smooth and continuous range of step densities. In addition, spherical samples are also difficult to handle experimentally in modern surface science equipment, which are generally designed for studies of flat single crystal surfaces.

Instead of full spheres, dome-shaped samples, as schematically illustrated in figure 2.3, and (sections of) domes can be more easily implemented.[51] Figure 2.5 shows photos of dome-shaped crystals used by two separate groups in recent years. Domes maintain curvature in both directions, which allows studying a range of surface structures with large variations in both step and kink densities. With sizes comparable to standard flat single crystals, they are experimentally quite easily implemented. At the same time, curvature in two directions lowers surface area with a unique surface surface structure, thus requiring surface sensitive techniques with a small footprint. Scanning tunneling microscopy and electron- or ion based probes with a small beam focus are particularly suited to study dome-shaped crystals. Images from crystals as currently still in use by Sykes (Tufts University) and Gellman (Carnegie Mellon) are shown in figure 2.5b). Crystals as used by Qiu and Bader near the turn of the century are shown in figure 2.5c). Their samples are 10 mm in diameter with varying levels of curvature. The crystal from Qiu spans ~15°, whereas the Gellman crystals span 28°. The inherent (*R*) and (*S*) chirality of kinked steps is indicated in the image from Gellman.

Reducing the curvature to only one dimension, as done with a (part of a) cylinder, fixes the step type and surface structure along the cylindrical axis, but allows variations of step density along the curvature. Therefore, the same surface structure can be probed across the width of the sample and spatial resolution only has to be high in the direction of curvature. This still requires adaptions to most UHV surface science techniques, as they usually probe a circular area on a flat sample, but significantly improves signal-to-noise ratios for some surface sensitive techniques. For example, adsorption and desorption measurements relying on the use of a quadrupole mass spectrometer benefit from larger areas with uniform surface structure.

Cylindrical samples maintain the full 360° rotation of a complete sphere, but appear rather difficult to use in pre-exisiting ultra-high vacuum systems. Such crystals were used with a diameter on the order of 20 mm and a height of 10-20 mm in the 1980's

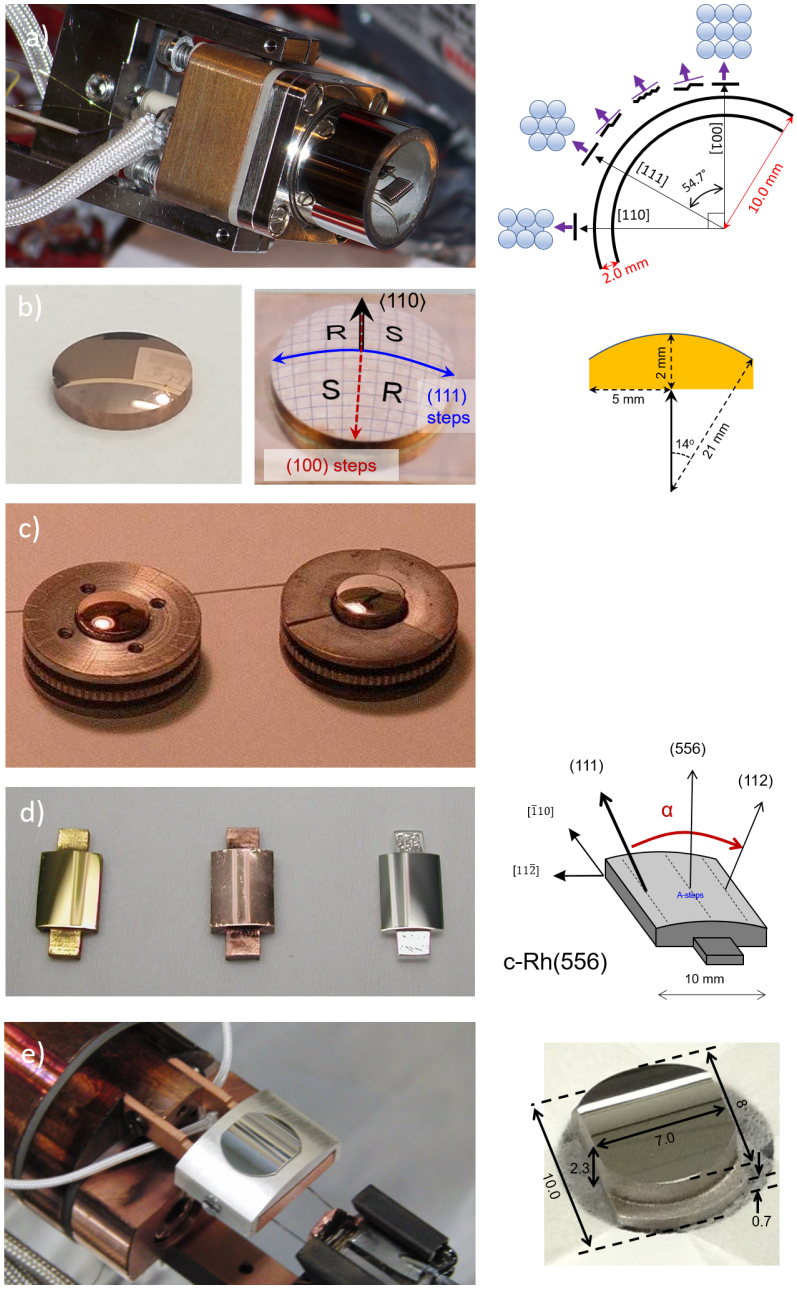

Figure 2.5: Photographs and schematics illustrating more recently used curved single crystals. a) A full Ni cylinder (own work). b) Dome-shaped Cu single crystal (courtesy of prof. dr. Andrew Gellman). c) Dome-shaped Cu and Ag crystals in sample holders (courtesy of prof. dr. Qiu). d) Partial cylinders of Au, Cu and Ag, and schematic drawing of a cylindrical section of a Rh single crystal (courtesy of prof. dr. Ortega). e) Partial Ag cylinder on a manipulator (left), and by itself (own work).

and 1990's. The only more recent example from studies of the Juurlink group is shown in figure 2.5a). Full cylindrical crystals are, as shown in a), bulky. This sample was 20.0 mm in diameter with a 2.0 mm wall thickness. The sample was 14 mm long and oriented along [1$\bar{1}$0]. The shape and externally polished surface make full (hollow) cylinders complicated to connect the sample tightly to a manipulator. The size and weight of full cylinders far exceeds that of typical flat single crystals, increasing demands on power supplies to heat the sample, sputter gun foci, and so on. One also needs to worry about temperature gradients in such large crystals, especially when the cylinder is connected on one side to a cryostat.

Along the cylindrical surface, each surface structure is repeated four times along the curved surface. It allows to check for reproducibility and offers identical surfaces from the same single crystal boule if a part of the polished area is damaged. We know of only the Ni cylindrical crystal to have been used in recent years in surface science studies. We have also produced a Pt sample with the same rotational axis direction, but only used the former in experiments to initiate the combination of curved surfaces with supersonic molecular beam techniques.

Minimizing differences with flat single crystal discs, the most commonly used crystal shape for curved crystals is a section of a cylindrical surface with a flat base. It presents a range of surface structures that depends on its size, the angle of curvature and the rotational axis. The sample size is generally comparable to that of the typical flat disk. Combining differently oriented curved crystals of the same material instead of a full cylinder or dome can be useful and offsets a part of the limitations in surface structure range.[49, 50, 52] Photographs of sections of cylinders are shown in figure 2.5d) and e). The first three crystals of coinage metals used by Ortega in figure 2.5d), curve over a 10 mm width and have extensions in the direction of curvature allowing for easy attachment of the crystal to a sample holder. Whereas these crystals had a low Miller index apex, the schematic illustration in figure 2.5d) shows how a recently used Rh sample has a high Miller index apex, yielding a large range of surface structures passing through the (111) plane. One of our own samples, i.e. a Ag partial cylinder with a (001) apex, is shown in figure 2.5e). Our samples are of similar size as those used by Ortega *et al.*, but have an extended base in the opposite direction. The left photograph shows how our crystals may be held by a cap made of the same material as the crystal and are gently pressed onto a base connecting the crystal to a cryostat.

2.5. NOTATION FOR CURVED CRYSTALS

Curved crystal surfaces were at first predominantly used in either spherical or dome shapes. A standard succinct notation that reflects shapes and surface structural ranges has not yet appeared in the literature. Hence, we suggest a standard notation

that inherently defines the range of surface structures for the most common crystal shapes used nowadays.

For dome shaped crystals it suffices to indicate the apex structure and the angle of curvature. Figure 2.3a-d) showed top views of surface structures near the apex of such domes. As an example of the proposed description, *d*-Cu(111)-90° indicates a dome (*d*) curving 90° in all directions from the apex, i.e. corresponding to a half sphere with (111) at the apex. As the (110) and (001) planes are 35.3° and 54.7° from (111), respectively, all ideal bulk truncated surface structures are well within the range of this surface. A dome with an angle of 55° from the apex would already suffice. Examples of dome shaped crystals with low and high Miller indices at the apex are *d*-Cu(111)-11° and *d*-Cu(432)-19° employed by Gellman and Sykes.[53]

Full cylinders were used by, e.g. Woodruff and coworkers [35–39], Imbihl and coworkers [5, 40–43], and more recently by Juurlink and coworkers [54, 55]. A notation including the rotational axis gives sufficient information to define the entire surface. For the Ni and Cu cylinders used by Woodruff we suggest notations of *cyl*-Cu[110] and *cyl*-Ni[110].

For partial cylinders, we have to specify the apex, direction of curvature, and the curvature's included angle. For example, *c*-Pt(111)[1$\bar{1}$0]-31° indicates a curved Pt crystal with the (111) plane at the apex, curving 31° around a rotational axis of [1$\bar{1}$0], i.e. 15.5° to either side of (111). The information included in this notation implies that A- and B-side steps will be found on the two sides of the crystal, with the (111) terrace widths decreasing from the apex to 4-5 atom rows at the sides.

For uncommon crystal shapes, a similar style could be used. For example for a conical crystal, *con*-M(*hkl*)X°could indicate (*hkl*) as the pointy apex of the cone and X the included angle.

2.6. CONSIDERATIONS REGARDING EXPERIMENTAL APPLICATIONS OF CURVED CRYSTALS

Curved samples may be created, e.g., by spark erosion, with subsequent hand-polishing. While various research groups still use this approach successfully, metal curved single crystal samples can, nowadays, also be purchased from, e.g., Surface Preparation Laboratories (Zaandam, the Netherlands). This company has developed an automated polishing technique with a high level of control over the pressure applied to the rotating crystal when slowly polishing it over a cloth that also rotates and translates.

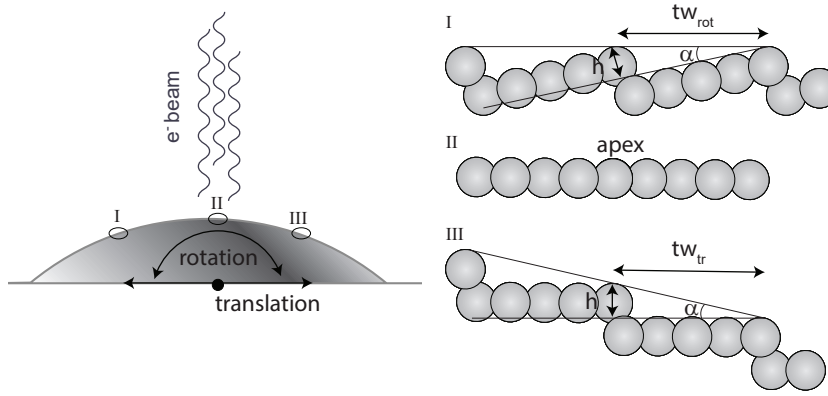

Figure 2.6: Illustration of the way in which stepped surfaces are exposed in the case of rotating or translating the curved crystal from the low-Miller index plane. If the apex of the crystal (II) is aligned normal to, e.g. an incoming electron beam, surface structures at the sides of the crystal can be exposed by either rotating the crystal along its axis, or translating away from the apex. In the case of rotation (I), stepped surfaces are exposed with their surface normal along the probing beam. In the case of translation (III), stepped surfaces are exposed with the low-Miller index terrace normal along the probing beam.

2.6.1. TERRACE WIDTHS AND STEP DENSITIES ON CURVED SURFACES

Some level of spatial resolution is required to make use of a curved crystal's potential and correlate physical properties or chemical reactivities to surface structure. A thorough understanding of where on the curved crystal which structures appear is thus essential. Surface structures along curved cylindrical crystals depend on the rotation axis and the miscut angle α from the low Miller index surface. Generally, either consecutive small fractions of the surface are probed and exposed to molecules, photons, or electrons in an experiment, or a signal coming from a small part of the surface is detected while the entire surface is treated (or exposed) in the same manner. In few experimental techniques, the entire surface is exposed and probed at once. For example, planar laser-induced fluorescence (PLIF) visualizes product formation above the entire surface while the crystal is uniformly exposed to reactant gases. Under most circumstances, however, moving the crystal's surface relative to some beam exposing or probing the surface is required. This may either be achieved by rotating or translating the crystal on an x, y, z, Θ-manipulator. Figure 2.6 provides illustrations to introduce some general considerations regarding experimental application of curved surfaces.

If the different parts of the curved crystal are probed by rotation, the probe is always directed to the surface along the surface normal. The observed terrace width from one step to the next in this case corresponds to:

$$tw_{rot} = \frac{h}{\sin\alpha} \tag{2.1}$$

where h is the step height or distance between low Miller index terraces.The parameters tw_{rot}, α, and h are illustrated in panel I of figure 2.6 for a monoatomic step. In the case of consistent step doubling, h is simply twice the layer-to-layer stacking height and the average tw becomes twice as large. For the low-Miller index surfaces displayed in figure 2.2, values for monoatomic step heights h as a function of the lattice unit cell height a (c for *hcp* lattices) are given in table 2.1. The step density, sd, for the case of sample rotation is

$$sd_{rot} = \frac{1}{tw_{rot}} \tag{2.2}$$

For accessing different parts of the curved crystal by translation instead of rotation, it is useful to convert the angle α to a translational distance, d.

$$d = \sin\alpha \cdot r \tag{2.3}$$

Here, r is the radius of the curved crystal. Surfaces are - in the case of a low Miller index apex, now always probed or exposed along the low Miller index terrace normal, i.e. not the macroscopic surface normal. The observed terrace width can be described by

$$tw_{tr} = \frac{h}{\tan\alpha} = \frac{h}{\tan\left(\sin^{-1}(d/r)\right)} \tag{2.4}$$

The step density (sd) is still given as

$$sd_{tr} = \frac{1}{tw_{tr}} \tag{2.5}$$

The parameters tw_{tr}, α, and h for translation are also shown in panel III of figure 2.6. Note that translating the crystal may lead to minor changes in signal intensity during experiments due to varying distance of the probed surface to the detector.

Figure 2.7 visualizes the consequences with respect to the probed terrace width and step density for the four atomically flat planes of *fcc*, *bcc* and *hcp* unit cells. The left and right axes present terrace widths and step densities normalized for the unit cell parameter, a (c for *hcp*), versus the angle from a low Miller index apex. The latter is also converted to a linear translation from the apex, normalized for the radius of curvature.
Normalized terrace widths and step densities versus angle from the low-Miller index apex (bottom axis) are given in solid lines. For cases where the curved surfaces is translated, dashed lines give normalized terrace widths and step densities as they vary with distance from the apex (top axis). Values on the top axis must be multiplied

terrace plane	monoatomic step height (h)	step type	step atom spacing (g)	spot splitting to row spacing (ss/rs)
fcc(111)	$\frac{1}{\sqrt{3}} \cdot a$	A / B	$\frac{1}{\sqrt{2}} \cdot a$	$\frac{\sqrt{3}}{\sqrt{2}} \cdot \sin\alpha$
		fully kinked	$\frac{\sqrt{3}}{\sqrt{2}} \cdot a$	$\frac{3}{\sqrt{2}} \cdot \sin\alpha$
fcc(001)	$\frac{1}{2} \cdot a$	A'	$\frac{1}{\sqrt{2}} \cdot a$	$\sqrt{2} \cdot \sin\alpha$
		fully kinked	a	$2 \cdot \sin\alpha$
bcc(110))	$\frac{1}{\sqrt{2}} \cdot a$	{211}	$\frac{\sqrt{3}}{2} \cdot a$	$\frac{\sqrt{3}}{\sqrt{2}} \cdot \sin\alpha$
		{111} / fully kinked	$\sqrt{2} \cdot a$	$2 \cdot \sin\alpha$
hcp(0001)	$\frac{1}{2} \cdot c$	A-B	$\frac{\sqrt{3}}{\sqrt{8}} \cdot c$	$\frac{3}{\sqrt{2}} \cdot \sin\alpha$
		fully kinked	$\frac{\sqrt{3}}{\sqrt{2}} \cdot c$	$\sqrt{6} \cdot \sin\alpha$

Table 2.1: Flat low-Miller index surfaces in the *fcc*, *bcc*, and *hcp* crystal lattices, and important parameters for vicinal surfaces. The step height (h) is defined as the stacking height between planes along the same orientation, and listed as a function of the crystal lattice parameter a (c for hcp) as indicated in figure 2.2. For all planes, close packed and fully kinked step types are given. The parameter g gives the separation of equivalent step atoms along the step edge of each type. Lastly, according to equation 2.6, the previous parameters can be used to determine the *spot splitting to row spacing* ratio observed in LEED patterns of vicinal surfaces, as a function of the angle α between the terrace normal and the surface normal.

by the radius of curvature of a sample, to obtain values with a unit, e.g. mm. Normalized terrace widths need to be multiplied by the lattice parameter a (c for *hcp*) to obtain values with a unit, e.g. nm, or Å. Normalized step densities need to be divided by the lattice parameter a (c for *hcp*) to obtain values with a unit, e.g. nm^{-1}, or $Å^{-1}$.

2.6.2. DIFFRACTION OF REGULARLY STEPPED SURFACES ALONG THE CURVATURE

The average step density at different position along the surface of a curved crystal can be examined by LEED. The well-known LEED patterns for low Miller index surfaces are easily identified along a curved crystal surface. When probing increasingly stepped surfaces, the 'superlattice' of steps arrays causes an additional diffraction criterion, resulting in spot splitting. [30, 56] For a low Miller apex, the specular spot in the LEED pattern overlaps with the (0,0) spot of the low Miller index plane and is - in most common equipment - hidden behind the electron gun. When subsequently translating the crystal, causing visible spots to split, the specular spot also moves and

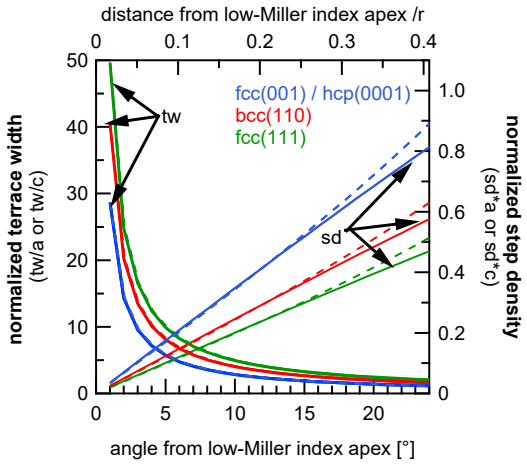

Figure 2.7: Change of normalized mean terrace width and normalized step density when rotating (bottom axis, solid lines) or translating (top axis, dashed lines) a curved crystal with a low-Miller index apex. Behavior is shown for fcc(111) (*green*), bcc(110) (*red*), and the identical fcc(001) and hcp(0001) (*blue*). The *tw* and *sd* are normalized for the unit cell parameter, *a* (*c*), of the respective material. The distance from apex (top axis) is normalized to the radius of curvature, *r*.

may becomes visible on the LEED screen. It is displaced by the miscut angle α, i.e. the angle between the overall surface normal and the low-Miller index terrace normal. When rotating the sample's surface at the focus of the LEED optics instead of translating, the entire observed diffraction pattern rotates while spot splitting varies. Here, the specular spot on the LEED screen also remains hidden behind the electron gun.

The splitting increases linearly with narrowing of the terraces. The ratio of the distance between split spots, *ss*, and the spacing between rows of split spots, *rs*, in LEED patterns of stepped surfaces is the inverse of the ratio between the average terrace width and spacing of equivalent atoms, *g*, along the step edge:

$$\frac{ss}{rs} = \frac{1}{tw_{rot}} \cdot \frac{g}{1} \tag{2.6}$$

Van Hove and Somorjai calculated these ratios for a limited number of stepped *fcc* surface structures.[57] Here, with the universal formula in equation 2.6, it becomes straightforward to predict spot splitting to row spacing ratios for any type of regularly stepped surface and for all lattice structures. Table 2.1 lists spot splitting to row spacing ratios for the types of stepped surfaces discussed before. They only dependent on the surface angle from the low-Miller index plane and the lattice constant *a* (or *c*) of the material.

2.7. RECENT ADVANCES

In the last two decades, advances in the polishing of curved crystals and adaptation of various surface science techniques to accommodate these samples have resulted in a new wave of curved crystal surface science studies. Of particular importance is the application of STM. The technique has proven extremely useful in studying the wide range of vicinals featured on curved crystals. It has, in many cases, revealed how subtle structural changes influence the physical properties or chemical reactivity. Research employing curved samples has primarily been carried forward by the groups of Ortega and coworkers at the DIPC in San Sebastian (Spain) and their recent collaboration with Lundgren and coworkers at Lund University (Sweden), a collaboration of the research groups of Sykes at Tufts University (USA) and Gellman at Carnegie Mellon (USA), and our own group at Leiden University (the Netherlands). Near the turn of the millennium, a series of papers were published by the groups of Bader (Argonne National Labs) at Qiu (UC Berkeley) on properties of overlayers deposited on curved single crystal samples. We take the order of first discussing what has been learned on the structure of clean transition metal curved surfaces in recent years prior to discussing adsorption and desorption of molecules, chemical reactions, as well as studies of overlayers grown on top of curved samples.

2.7.1. STRUCTURE AND ELECTRONIC STATES OF CLEAN METAL SURFACES

NOBLE METALS

The first thorough STM study of a clean and uncovered curved crystal surface was published in 2008 by the group of Ortega (San Sebastian, Spain).[58] There, a Au crystal was used to study faceting of (111) vicinals. A hill-and-valley structure was observed over a range of 6 °, i.e. 4 - 10 ° from the (111) apex. Outside this range, the surface showed atomically smooth terraces with single atom high steps. Faceting of the stepped surfaces into a hill-and-valley structure was observed. This structure comprised of two specific, experimentally determined terrace widths, d_w (wider terraces with herringbone reconstruction) and d_n (narrow terraces without herringbone reconstruction). The smoothly variable miscut angle made it possible to define the limits of faceting on the stepped Au surfaces. Furthermore, being able to compare the two sides of the crystal revealed differences in faceting behavior for the A- and B-type steps, i.e. a difference in the sequence of the d_w and d_n terraces.[59]

The combination of STM with angle-resolved photoemission spectroscopy (ARPES) yielded detailed and unprecedented insights into the origin of faceting. Synchrotron radiation for ARPES ensured a narrow energy profile as well as a small beam size on the curved surface (100 μm), minimizing convolution across different surface structures. The two terrace widths, caused by band splitting into a low and high energy

state, induce band folding and opening of energy gaps at the Fermi level. It was found that the two phases are favored on the vicinal surfaces because they lower the electronic surface energy (d_w) and improve faceting kinetics (d_n). The two phases differ in elastic interactions due to varying step stiffness, step dipole, and terrace stress. The different behavior on the two sides of the crystal were attributed to the respective step arrangement at A or B-type steps. These cause a preference for defined mixing of phases (A-type) or partial phase separation (B-type). For A-type steps, the regular arrangement of d_w and d_n phases gives a defined superlattice, resulting in coherent electronic coupling between the phases.

Realizing the possibilities of curved crystals in examining structural and electronic effects, a series of publications using curved noble metal crystals followed. Continuing their previous work on the interplay between electronic structure of noble metals and their surface structures, Ortega and coworkers utilized the step arrays on curved crystals as tuneable superlattices. They used the regularly stepped surfaces on the curved crystals to introduce periodic potential barriers to the free-electron-like surface bands of noble metals, causing the electrons to scatter off the steps. Comparing three partial cylindrical slices of noble metal surfaces, oriented around (111) and shown in figure 2.5d), namely *c*-Au(111)[1$\bar{1}$0]-30°, *c*-Ag(111)[1$\bar{1}$0]-30°, and *c*-Cu(111)[1$\bar{1}$0]-30° crystals,[60] the authors found terrace confinement effects of surface electrons in each case. The effect increases in strength from Ag to Cu to Au vicinals. The previously observed faceting for Au and structural instabilities around $\frac{1}{2}\lambda_F$ for Cu were detected, but no structural instability was observed for Ag. From ARPES data, the previously unknown effective barrier strengths of monoatomic steps on (111) terraces could be determined for all three metals. Later, they showed that such steps can act both as repulsive and transmissive barriers for surface electrons. The nature of the barrier does not depend on the spacing between steps, but on the order in step arrays which can cause coherence. [61] The (dis)order either leads to coherent 2D surface states or 1D quantum wells.

Beyond the regularity of close-packed step arrays and electronic effects, the (mostly) smoothly varying step density on curved crystal surfaces of noble metals makes them a prime tool to investigate step-step interactions. These interactions consist of elastic repulsion (dipole effects) and entropic repulsion (related to step stiffness). A bulk Ag curved crystal (*c*-Ag(645)[11$\bar{2}$]-24°), featuring (111) vicinals with fully-kinked step edges, was used to test the generalized Wigner-surmise.[62] The order parameter, ρ, which relates to the relative strengths of entropic and elastic step interactions, increases linearly with step density. This finding indicates a changing ratio of elastic-to-entropic interaction which had not previously been considered within the terrace-step-kink (TSK) model.

Studied in much less detail, the surfaces of two similar curved Ag samples were also used in our group. [50, 63] One is shown in figure 2.5e). Both crystal's surfaces were

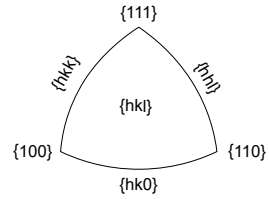

Figure 2.8: Schematic representation of the "stereographic triangle" of surfaces contained between the high-symmetry *fcc* planes, (001), (110), and (111).

initially studied using LEED only. Whereas a *c*-Ag(111)[1$\bar{1}$0]-31° crystal was easily cleaned and LEED results showed no indications of unexpected surface irregularities, *c*-Ag(001)[1$\bar{1}$0]-31° proved to be difficult to handle. Likely a single or few cleaning cycles involving sputtering at normal incidence damaged the surface consisting mostly of (001) terraces to an extent that it took more than 6 months to 'repair'. Several hundred cleaning cycles of mild Ar^+ sputtering at 45 ° incidence, interspersed with mild annealing, ultimately recovered the surface. Spot splitting-to-row spacing ratios in the square LEED patterns were found to be as expected along most of the curved surface.

STM studies of Cu surfaces with both atomically straight and kinked steps was also an integral part of the work on dome-shaped Cu crystals by Gellman et al. Six Cu crystals were polished in-house from disk-shaped samples to cover the entire *(S)*-chiral stereographic triangle of *fcc*, shown in figure 2.8.[51] One of these crystals is shown in figure 2.5b). These so called 'surface structure spread single crystals', *d*-Cu(111)-11°, *d*-Cu(100)-10°, *d*-Cu(110)-11°, *d*-Cu(432)-19°, *d*-Cu(821)-14°, and *d*-Cu(861)-10° allowed the characterisation of structures at all possible surface orientations. Surface structures were reported to predominantly follow the expected bulk-terminations with local fluctuations at specific orientations.

PT-GROUP METALS

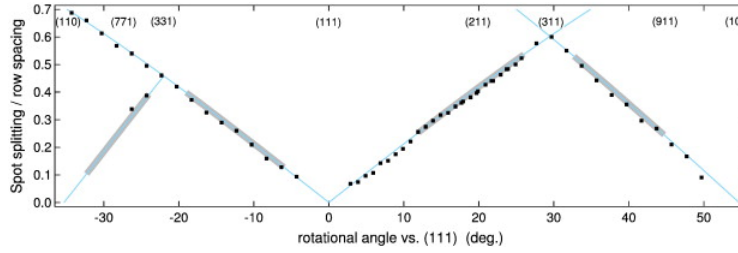

Figure 2.9: Spot splitting-to-row spacing analysis for a *cyl*-Ni[110] crystal. Data are shown as dots. The ideal expected values are shown as solid lines. Areas where streaking was observed are indicated by grey bars. Reprinted from [55], Copyright (2013), with permission from Elsevier.

A 12 mm diameter cylindrical nickel sample, *cyl*-Ni[110], has been used by Woodruff

and coworkers in the 1980's.[36] The study reported on cleanliness and oxidation of the surface, but the study lacked diffraction techniques to verify surface order. More recently, a 20 mm diameter cylindrical nickel crystal with the same orientation was used in our group.[54, 55] It is shown in figure 2.5a). The cleaned surface structure of this *cyl*-Ni[110] was studied by LEED.[55] Using a multichannel plate (MCP)-based LEED allowed for use of a very small electron beam (0.3 mm diameter), thus improving spatial resolution in comparison to the more common reverse view LEED with a hemispherical fluorescent screen. However, it complicated the interpretation of the diffraction patterns. They are distorted from the usual direct visualization of the Ewald sphere as a consequence of the MCP being flat instead of hemispherical. LEED patterns of surfaces with broad (111), (110) and (100) terraces appeared as expected as well as highly stepped surfaces. Where patterns appeared as expected, a step height analysis based on variation of the incident electron energy confirmed monoatomic high steps. LEED patterns showed significant streaking in between the more crisp patterns. The streaking was attributed to increased disorder and partial reconstruction of the surface. The spot splitting-to-row spacing analysis shown as a Bauer-plot is reproduced in figure 2.9. It visualizes that the cylindrical crystal over the probed 90° consists to some extent of expected monoatomic step arrays (B-type step in between the (331) and (111), A-type step in between (111) and (311), and A'-type step in between (311) and (100) surfaces), but likely also shows lower degrees of ordering and reconstruction over significant fractions of the circumference. Surface quality was suggested to relate to the exact cleaning procedures and a single cleaning procedure that does not induce faceting or other types of reconstruction on some parts of the included 90° curvature may not exist.

Several years later, a more detailed structural study was performed on a cylindrical section of a Ni single crystal, i.e. *c*-Ni(111)[1$\bar{1}$0]-27.5°.[64] Step-type dependent step-doubling was shown to result from strong elastic interactions between steps. A combination of STM and LEED (300 μm spot size of the electron beam) revealed the progressive transition from monoatomic steps to double steps (and consequently double terrace lengths) for A-type steps. Only monoatomic height steps occurred for B-type steps separating (111) terraces. The onset of the transition to doubling of A-type steps was found to be temperature dependent. The B side maintained consistently monoatomic steps over the probed temperature range, but saw a 10 % decrease of the spot splitting to row spacing at temperatures above 450 K as compared to room temperature. It was suggested to indicate an increase in entropic repulsion between steps. Varying the miscut angle on the curved crystals, as well as the surface temperature allowed the authors to construct an (α,T)-phase diagram for step doubling on Ni(111) vicinal surfaces.

Several studies have used curved Pt surfaces. These follow the earlier studies of a hand-polished *c*-Pt(111)[1$\bar{1}$0] sample used by Comsa and coworkers[33], who re-

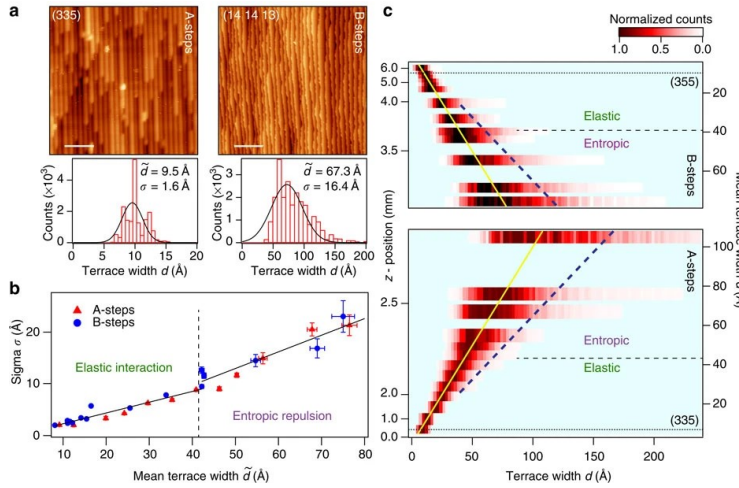

Figure 2.10: STM analysis of a *c*-Pt(111)[1$\bar{1}$0]-30° crystal, revealing changes in the interplay of elastic and entropic interactions in step arrays with varying terrace width. a) Two examples of STM images of surfaces with A- and B- type steps and the associated distributions of terrace widths including Gaussian lineshape fits and fit parameters (average terrace width, $\tilde{d}$, and standard deviation, σ) . b) Variation of standard deviation with mean average terrace width over a range of ~4 to 30 atom rows. c) Image plot of terrace width distributions spanning the curvature. Figure reprinted from reference[65], under Creactive Commons CC BY license. Copyright 2015, The authors.

ported that a LEED study showed the expected diffraction pattern with spot splitting smoothly increasing from the (111) apex up to the ~7 atom row wide terraces at the edges of the crystal, and a *cyl*-Pt[001] by Ertl and coworkers who reported faceting in between (100) and (110) planes as illustrated in figure 2.1.[5]

For a curved Pt(111) crystal with close-packed (A- and B-type) steps, i.e. *c*-Pt(111)[1$\bar{1}$0]-30°, a step density dependent transition from a regime dominated by elastic interactions to a regime with predominantly entropic repulsion was found by Ortega and coworkers.[65] Figure 2.10 illustrates results. Arrays of monoatomic steps were reported for both sides of the crystal with terrace width distribution from 4 to ~ 40 terrace atom rows that were fitted by Gaussian lines shapes. The plotted relation between the distribution's width and the average terrace width shows two linear regimes separated by a kink near 40 Å. It was argued to result from the predominant type of step-step interaction.

We very recently used a similar crystal, but with highly kinked steps, i.e. *c*-Pt(111)[11$\bar{2}$]-31°.[49] The structural analysis of this crystal is presented in chapter 3.

The surface of a *c*-Pd(111)[1$\bar{1}$0]-30° crystal has been studied as part of a broader study on the structure dependence in chemical activity toward CO oxidation.[66] The surface structure of the bare metal was beforehand investigated by STM, LEED, and XRD and showed no deviations from expected surface structures. The maxima in terrace

width distributions obtained from STM images consistently agreed with the value for mean terrace widths. In contrast to the study on *c*-Pt(111)[1$\bar{1}$0]-30°, no transition between regimes of dominant elastic and dominant entropic step-step interactions, was observed. This difference was attributed to stronger elastic repulsion between A- and B-type steps on Pd than on Pt(111) vicinals.

OTHER TRANSITION METALS

A *c*-Rh(111)[1$\bar{1}$0]-32°, employed in a CO oxidation study by Garcia-Martinez *et al.*, was investigated with regards to its surface structure by LEED.[67] Spot-splitting increases linearly with distance from (111), for both A- and B-type steps. No indications of deviations from the expected stepped surface structures were identified. Additionally, the XPS fingerprints of bulk, terrace and step species were identified. The XPS signal from the terraces decreases towards the sides of the crystal, which was attributed to tensile stress from the neighboring steps at narrow terraces.

A *c*-Co(0001)[1$\bar{1}$00]-31°crystal was briefly studied in our group by LEED only. The phase transition from *hcp* to *fcc* is a worry in cleaning Co single crystals. During surface preparation, temperatures remained well below the onset temperatures for the phase transition tabulated for this metal.[68] Regardless, LEED patterns showed a hexagonal pattern with some spot splitting that suggested massive surface reconstruction. However, the direction of spot splitting was inconsistent with the expected direction for kinked steps, leaning strongly toward the direction expected for close-packed steps. Spot splitting-to-row spacing ratios also did not vary as expected with distance from the apex. They even remained constant while translating the crystal relative to LEED electron beam. These results may suggest massive surface reconstructions, but are inconclusive and remain unpublished.

2.7.2. ADSORPTION AND DESORPTION FROM CURVED SURFACES

To study surface structure dependencies of (non-)dissociative adsorption and (recombinative) desorption of molecules from surfaces, several techniques have been applied in recent years. While some of these required adaptations to provide required spatial resolution, e.g. reflection-absorption infrared spectroscopy (RAIRS) and temperature programmed desorption (TPD), others, e.g. XPS and STM, may not.

TEMPERATURE PROGRAMMED DESORPTION

To use thermal desorption as a technique in studies of surface structure dependencies with curved crystals, one can deposit the species of interest onto a small (narrow) area of a curved crystal surface where structural variation is small or negligible, and subsequently monitor desorption. Here, imposing spatial resolution in the detection

is not required, but may help to improve the signal-to-noise ratio or other complications, e.g. slopes in background signals. It does require a dosing technique, e.g. a (supersonic) molecular beam that is appropriately skimmed prior to impact on a well-defined part of the crystal's curved surface. The other straightforward option is to monitor the desorption from a small area after exposing the entire surface, e.g. by a differentially pumped QMS with an orifice that strongly limits the acceptance of molecules desorbing from the curved surface. In Leiden, we have applied both options.

In a first proof-of-principle study using a *cyl*-Ni[110] crystal, a rectangularly skimmed supersonic molecular beam deposited deuterium atoms by dissociation of D_2 onto the surface.[54] The footprint of the beam was either 1.0 or 0.4 mm high and 5.2 mm wide along the [110] rotational axis. From the deposition position, the crystal was rotated by 180° along the axial [110] direction so that the exposed area faced the 1.0 mm high and 6.0 mm wide opening into a differentially pumped QMS housing. Successive experiments dosing and desorbing D_2 showed that the characteristic double-peaked feature of hydrogen desorption from Ni(111) could clearly be found along the surface, as well as the progressive changes in the TPD spectrum with changes in the probed surface structure. The incorporation of (100) steps separating (111) terraces led to a decrease in the intensity of the lower peak and an upward shift in the desorption temperature of the highest peak, suggesting that these A-type steps bind atomic deuterium stronger than (111) terraces. A peak shift of ~10 K was found for rotation of the crystal over 20°, i.e. from an area exposing very large (111) terraces to a surface with ~3 atom row wide (111) terraces.

Two more detailed studies using H_2O and two *c*-Ag single crystals were conducted without dosing from a supersonic molecular beam. Crystals were exposed to (deuterated) water from an effusive capillary array-based source. TPD spectra obtained using a rectangular orifice at 1 mm from the crystal surface showed that even smaller shifts could be accurately traced and interpreted. [50, 63] Results are presented in chapter 6 of this thesis.

REFLECTION ABSORPTION INFRARED SPECTROSCOPY

To study molecular adsorbates or fragments thereof, RAIRS is a powerful technique. It is most easily performed with fixed IR incident and reflected beam paths. A curved single crystal surface must then be applied so that the crystal can be rotated along its curved surface, with the IR beam, shaped to a narrow stripe, reflecting off the surface at the same angle regardless of the probed surface structure. While this may be the optimal approach for cylindrical samples, we have taken a different approach for partially curved crystals. Figure 2.11 illustrates in three views how we counter the varying deflection angle of the IR beam when translating a curved crystal's surface along the IR beam's focal point using an internally Au-coated curved mirror.[69] In

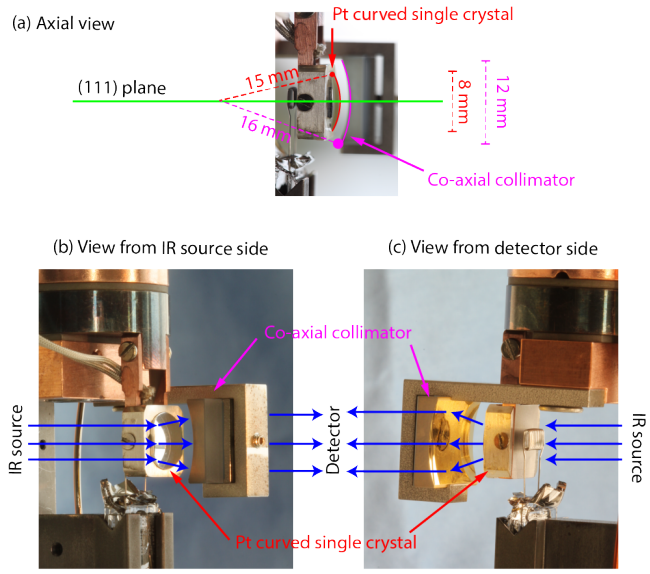

Figure 2.11: Views from different angles of the curved crystal and internally curved Au coated mirror. Both are individually attached to a cryostat. The internally coated Au mirror fixes the position of the exiting IR beam in RAIRS experiments and was used to probe CO adsorption to a c-Pt(111)[1$\bar{1}$0] curved crystal. A similar figure appears in reference [69].

this proof-of-principle study, we probed the adsorption and desorption of CO with c-Pt(111)[1$\bar{1}$0]-31° while translating the crystal up and down relative to the fixed IR focus in the UHV chamber. IR light reflected from the sample is deflected upward or downward depending on the crystal's vertical position. When the crystal is translated downward and the IR focus is above the apex, the reflected beam moves upward and vice versa. This deflection is countered by the sideways off-set Au-coated mirror. Besides correcting the deflection, it acts as a collimator to the diverging IR beam. While spatial resolution is limited and depends, *a.o.*, on the aperture size behind the IR source in the FTIR spectrometer, we showed that we could track the shifts and intensity variations for CO adsorbed at various coverages on the entire range of surface structures present on the curved samples. IR absorption by both on-top and bridge adsorption positions could be tracked quite accurately, illustrating how CO adsorbed to step sites act predominantly as defects to the exitons at intermediate step densities. As a consequence, the narrow line width that dominates the spectra at both high and low step densities, broadened at intermediate step densities. Bridge adsorption was, contrary to previous reports, not found on the A-type stepped surfaces, while it was clearly present on B-type stepped surfaces. As an XPS study on CO adsorption to a similar curved Pt sample confirmed the earlier assignments of different adsorption sites found by flat single crystals[65] (see below), a simple explanation may be that IR spectra of the curved surface in our study (ref. [69]) were accidentally reversed.

X-RAY PHOTOELECTRON SPECTROSCOPY

High spatial resolution on curved crystals can easily be be achieved when synchrotron radiation is employed. This approach was used by Ortega and coworkers, e.g. during experiments studying CO adsorption and oxidation at near-ambient pressures. On a *c*-Pt(111)[1$\bar{1}$0]-30° sample, XPS was used to demonstrate the preference for initial CO adsorption at steps.[65] Differences between step types were exposed by comparing the two sides of the crystal. CO adsorbs only at on-top positions at the upper edge of B-type steps and in both on-top and bridge positions at A-type steps. Terrace adsorption occurs after step edges are fully saturated with CO.

A similar study was also performed for *c*-Rh(111)[1$\bar{1}$0]-32°. CO adsorption occurred at the on-top sites of steps first, followed by terrace on-top sites. Only at higher coverages were bridge sites at steps and hollow sites on terraces occupied.[67]

As an alternative to synchrotron radiation, laboratory XPS equipment can be modified to improve spatial resolution. For example, a special XPS probe was used by Gellman and coworkers to achieve spatial resolution of less than 0.2° angular spread on dome-shaped sample to study, e.g. oxygen uptake during surface oxidation [53] and the activity of decomposition of aspartic and tartaric acid on Cu surfaces.[70, 71] The results will be discussed in section 2.7.3.

SCANNING TUNNELING MICROSCOPY

Clearly, STM can be applied to study adsorption of molecules on stepped surfaces. However, very few studies have appeared so far. STM studies of the surface oxidation of Cu and Ag surface are postponed to the following section, as well as studies of the adsorption and decomposition of chiral molecules on chiral Cu surfaces (discussed in section 2.7.3).

2.7.3. CHEMICAL REACTIONS AT CURVED SURFACES

SURFACE OXIDATION

A dome-shaped Cu(111) crystal was employed to study surface oxidation on Cu(111) and all vicinals by Gellman ad Sykes.[53] Oxidation in the topmost layer of (111) terraces, characterized as Cu_2O, was found to grow in triangular shapes given by the three possible directions of A-type steps. A subsequent oxidation layer, originating from Cu atoms expelled from the topmost layer, grew on top of the triangular oxide domains, but this second layer had itself no defined shape. At steps, boundaries between the step oxide phase and upper (111) terraces also followed the directions of A-type steps, leading to substantial faceting at B-type and kinked steps, but almost no reconstruction at A-type steps. Overall, the rate of oxidation was found to increase significantly with step density from (111) towards the edges of the crystal. However,

despite the structural differences of oxide phases, the rate depended not on step-type or kink density. XPS was used to determine rates and uptake of oxygen on parts of the dome-shaped crystal. Here, foregoing the use of synchrotron radiation, a special XPS probe was used to achieve spatial resolution of less than 0.2° angular spread on the sample. The potential of these types of crystals for the optimisation of possible structures and compositions of catalyst particles was quickly realised.[72]

The chiral metal surfaces on the *d*-Cu(111)-11° surfaces were recently used as a template for the growth of a chiral metal oxide surface.[73] There, depending on step chirality and predominant step-type, growth of homochiral domains of the "29" Cu oxide could be induced. This oxide features a chiral pore structure. A combined LEED and STM study of the dome-shaped crystal demonstrated direct transfer of chirality from a metal template to an oxide film for the first time. Figure 2.14 shows STM images of oxide structures on surfaces with varying step orientation, as published in the original publication.

A similar study using a curved *c*-Ag(111)[$1\bar{1}0$]-31°crystal has recently been conducted by Killelea and coworkers. Here, the oxidation requires a harsher oxidant as the dissociation probability of molecular O_2 is extremely low on silver. The curved surface was exposed to atomic oxygen created from a hot iridium filament kept in low pressure oxygen background. Progressive oxidation was followed by imaging the typical silver oxide overlayer at 35 K after various exposures at two different surface temperatures. Detailed results are forthcoming.[74]

Oxygen adsorption and dissociation was also studied on a curved platinum surface.[75] Here, the study intended to unravel how A- and B-type steps contribute to the increased sticking probability of O_2 on stepped (111) surfaces compared to the Pt(111).[76] At low incident energy, the sticking probability - as measured by molecular beam methods - was found to scale linearly with step density and did not vary with step type. At higher incident energies, the beneficial effect of step in trapping and dissociation O_2 vanished to a significant extent while a step type dependence appeared. A collaboration with dr. Kurahashi at the National Institute for Materials Science (Tsukuba, Japan) helped determine the origin by state-selecting and orienting impinging O_2 molecules. Here, the curved crystal was replaced by three flat single crystals that spanned the same range of surface structures as present on the curved Pt crystal. Results indicated that, at low incident energy, scattering of steps improves translation energy loss for molecules approaching along the [111] normal of the terraces, trapping the molecules initially into a physisorbed state. At higher kinetic energies, direct adsorption into molecular chemisorbed state becomes possible. The experiments confirmed that this molecular state is characterized by the O=O bond lying parallel to steps and the binding energy varying for the A- and B-type steps.

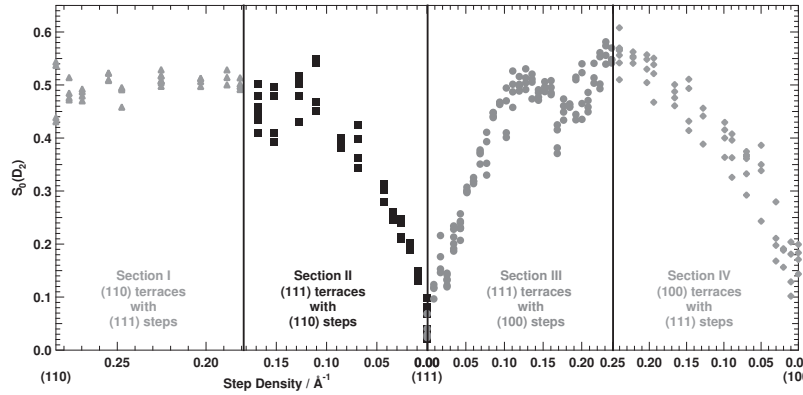

Figure 2.12: Initial dissociation probability, S_0, at 0.82 kJ/mol incident energy for D_2 as measured by the King and Wells technique on *cyl*-Ni[110] with incidence of the beam along the local surface normal.[77] S_0 is determined over a 90° angle, spanning all stepped surface structure from (110) via (111) to (100). Two additional vertical lines indicate the (331) and (311) positions.

HYDROGEN DISSOCIATION AND H-D EXCHANGE

The same supersonic molecular beam technique with a rectangularly skimmed footprint as described to study D_2 desorption from well-defined areas on a *cyl*-Ni[110] crystal (section 2.7.2) was also applied to study the structure and energy dependence of D_2 dissociation on Ni.[54] While the original publication showed various individual King and Wells traces for different surface structures and different incident energies, figure 2.12 shows the results for a low incident energy over the same 90° rotation as used in figure 2.9. The initial sticking probability, S_0, increases linearly over a large step density range vicinal to the (100) and (111) planes. It suggests that the dissociation probability at steps is much higher than at the respective terraces and that the measured reactivity represents a linear combination of both. Noteworthy were the step density independence in section I, i.e. in between the (110) and (331) planes, and the dip in the otherwise linearly increasing dissociation probability in section III, i.e. between (111) and (311). The first observation was taken to imply that slight stretching of the 111 facets making up the (110) plane does not alter the reactivity toward D_2 dissociation. For the second observation, the streaking observed in the same area in LEED patterns was taken to suggest faceting or some other local restructuring that would lower step densities close to (311). This idea was later confirmed by the structural study on the *c*-Ni(111)[1$\bar{1}$0]-27.5°crystal by the San Sebastian group who showed that the A-type step shows step doubling (i.e. region III), but not the B-type (i.e. region II). [64]

Dissociation of D_2 on steps of Pt was studied in a similar fashion, but with significantly improved spatial resolution and using a *c*-Pt(111)[1$\bar{1}$0]-31°crystal.[78] This first study focused on the mechanism of dissociation, which had been debated for ap-

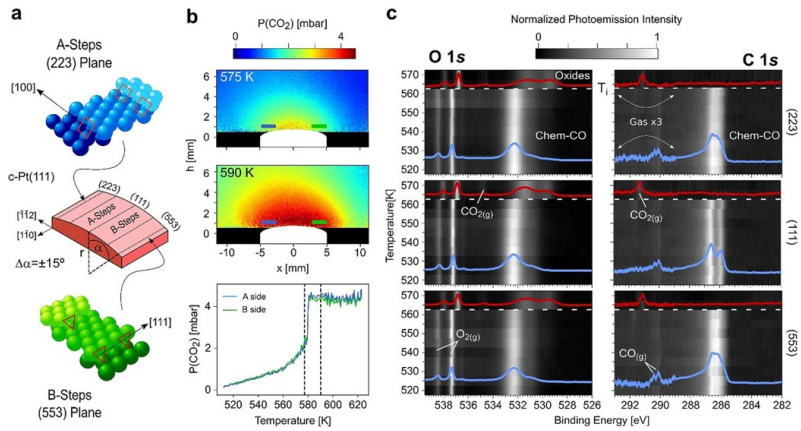

Figure 2.13: PLIF and XPS study of CO oxidation under near-ambient pressure on the surface of a *c*-Pt(111)[1$\bar{1}$0]-30° crystal. a) Representation of A- and B-type steps appearing on different sides of the curved crystal. b) Two images of planar laser-induced fluorescence of CO_2 created from CO oxidation above the curved surface at different surface temperatures and CO_2 partial pressure derived from integrated intensity of the PLIF signal versus surface temperature for both sides. c) Exemplary temperature dependence of O(1s) and C(1s) XP spectra measured at A- type, B-type, and apex. Figure reprinted with permission from reference[79].Copyright 2020, Wiley-VCH GmbH.

proximately 40 years. Two models in which steps play a crucial but different role had been suggested. One model was centered around the presence of an trapped molecular state for H_2 on (111) planes that would only lead to dissociation if the molecule would reach a step (defect) by ballistic diffusion. Only at the step would the molecule dissociate. The other model assumed two different (energy dependent) sticking probabilities for steps and terraces and did not invoke a long-lived molecular precursor and diffusion prior to dissociation. Measurement of the step density dependence of the dissociation probability at various incident energies for A- and B-type steps on *c*-Pt(111)[1$\bar{1}$0]-31° resolved that the latter model captures the dissociation characteristics. A linear dependence on step density over a very large step density range was found for the dissociation probability at low incident energy, being inconsistent with the former model. Also, the (mostly) surface temperature independence of the sticking probability and a step-type dependence (the B-type showing a higher reaction cross section than the A-type) for the dissociation probability disagreed with the first model.

CO OXIDATION

In recent years, the group of Ortega in collaboration with the Lundgren group (Lund, Sweden), has also undertaken research on chemical reactions on curved surfaces. Techniques such as near-ambient pressure XPS (NAP-XPS) and planar laser-induced fluorescence (PLIF) are there employed to study the effects of surface structure on surface chemistry away from UHV conditions. In this context, the correlation between surface changes on vicinal surfaces was explored in a series of publications on

CO chemisorption[65, 67] and oxidation[66, 79, 80] on curved crystals of transition metals.

The applicability of curved crystals at near-ambient pressure conditions was initially demonstrated for CO oxidation on a curved Pd sample (*c*-Pd(111)[1$\bar{1}$0]-30°) PLIF and XPS revealed step-type dependent differences in CO oxidation on Pd vicinals.[66, 80] The onset temperature for the transition from a low activity phase where CO poisons the surface to a high activity phase was found to be lower for B- than for A-type steps, and highest for (111) terraces. In contrast, the catalytic oxidation of CO at near ambient pressure on the curved Pt sample (*c*-Pt(111)[1$\bar{1}$0]-30°) showed no dependence on surface structure (or even reaction conditions).[79] There, NAP-XPS revealed that the uniform build-up of subsurface oxygen causes the simultaneous initiation of the reaction at all vicinal surfaces contained on the crystal. Figure 2.13, reprinted with permission from the original publication, shows the CO_2 PLIF signal before and after the onset of reaction, as well as XPS spectra of adsorbed species and reaction products.

CHIRAL REACTIONS

The potential of the naturally chiral surfaces on the dome shaped crystals as a purely structural form of enantioselectivity was further explored in a series of studies on the adsorption of chiral organic molecules. Using the dome as a high-throughput library of surface structures, the activity of decomposition of aspartic acid (Asp) was probed with spatially resolved XPS and adsorbate structures imaged by STM.[70] Surfaces with *(S)* chirality were found to be the least active towards decomposition of L-Asp, whereas in the case of D-Asp *(R)*-chiral surfaces were the least active, indicating that the adsorbed molecules were stabilised on these surfaces. By STM the adsorbed L-Asp was found to to adsorbed in rows rotated 20° from the close-packed directions on Cu(111). The adsorbate induced the facetting of steps into $\{320\}^S$ and $\{310\}^R$ microfacets, and the formation of Cu adatom islands with edges along the same directions. Surfaces on the dome that naturally exposed steps pre-aligned with the Asp rows were found to remain relatively straight while all other steps showed significant facetting. Both the reduced decomposition of adsorbed L-Asp and the facetting of steps on vicinal Cu into $\{320\}^S$ and $\{310\}^R$ microfacets thus indicated the energetic stabilisation of adsorbed L-Asp at these step facets. On the *d*-Cu(100)-10° crystal, the decomposition of both aspartic acid and tartaric acid (TA) in a surface explosion reaction was found to have highly enantiospecific kinetics.[71] A 2D map of the reaction rate of TA decomposition on a *d*-Cu(110)-11° dome was subsequently used to determine the maximum in enatioselectivity, Cu(14 17 2)$^{R\&S}$.[81]

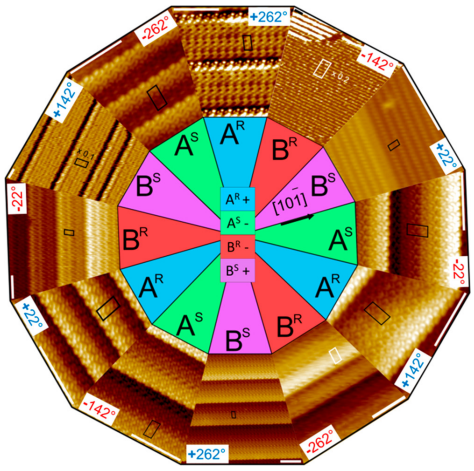

Figure 2.14: STM images of oxide formation on a dome-shaped *d*-Cu(111)-11° crystal. Angles indicate the rotational orientation of the oxide compared to (111), which corresponds to ± 22° with 120° increments. The predominant underlying Cu step type (A vs B) is indicated and the local chirality of kinks. Clearly, local orientation and surface chirality influence the chirality of the surface oxide. Figure reprinted with permission from reference [73]. Copyright 2020 American Chemical Society.

2.7.4. MAGNETIC, ELECTRONIC, AND CHEMICAL PROPERTIES OF FILMS GROWN ON CURVED CRYSTALS

In the late 1990's, the groups of Qiu and Bader (Berkeley, USA, and Argonne, USA) used crystals curved around the (001) plane of W, Ag, Cu, and Pd, as templates to grow stepped magnetic films (Fe or Co). As the steps on those films cause tuneable electron confinement on the nanometer scale, they were suited to systematically explore the quantum nature of short-range magnetic interactions, and the resulting magnetic properties, e.g. the magnetocrystalline anisotropy.

Initially, Kawakami *et al.* used two types of Ag crystalline samples to grow templated Fe films.[82] A 'fixed angle' (bifacial) crystal exposed the (001) surface on one half of a disk-shaped sample, the other half was polished to expose a stepped surface with a constant 6° vicinal angle. The second sample was a 'curved' crystal, where again half of a disk-shaped sample exposed (001), while the other half-disk was polished to smoothly curve to a 10° vicinal angle. Figure 2.15 shows the schematics of the bifacial curved crystals typically used by Qiu *et al.* The structure of Fe films grown on the Ag substrate were verified with LEED and RHEED. The surface magneto-optic Kerr effect (SMOKE) was used to examine the magnetic propertied. As SMOKE measurements were carried out using polarized light from a He-Ne laser, the beam spot size was inherently narrow (0.2 mm) enough to achieve sufficient spatial resolution on the 10 mm samples.

Measurements on 25 ML thick Fe films showed split loop hystereses on stepped surfaces when a magnetic field was applied perpendicular to the steps. These results

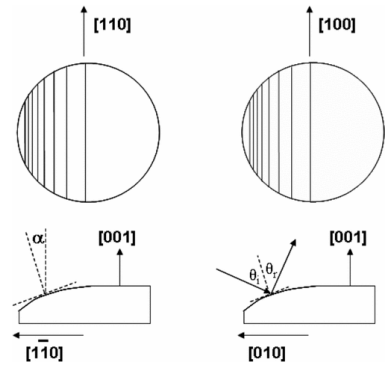

Figure 2.15: Schematic drawing of bifacial curved crystals, typically used in the work of Qiu *et al.*. Only part of the crystal's polished surfac is curved. Figure reprinted with permission from reference [83]. Copyright 2007 by the American Physical Society.

revealed, in addition to the Fe bulk anisotropy, the presence of a uniaxial in-plane magnetic anisotropy, caused by lattice symmetry breaking at the step edges. The easy axis was found to be parallel to the steps. The shift field H_s of the split loops was then used to determine the strength of the step-induced anisotropy at different points across the curvature of the sample. The anisotropy strength was found to depend quadratically on step density. This relation was explained by the Néel pair-bonding mechanism. In Néel's model, spin-orbit interactions influence the magnetic anisotropy through nearest neighbor electronic hybridization. Missing bonds at the step edges could thus locally change the hybridization and cause the anisotropy.

Additionally, a wedge of thinner Fe films was grown on the bifacial substrate. The critical thickness of the spin-reorientation transition from perpendicular magnetization to the in-plane magnetization found at thicker films was then determine for the two sides of the crystal. There, Fe on the 6° vicinal surface showed a higher critical thicknesses than on the (001) surface, indicating that steps stabilized perpendicular magnetization.

The sensitivity of the magnetocrystalline anisotropy on lattice symmetry was explored in a subsequent study by Choi et al.[84] Ultra-thin films (2 ML) of Fe were grown on a W(001) crystal, which similar to the previously described Ag sample, exposed (001) on half of the disk's surface, and on the other half curved around the [100] axis, from 0-9° vicinal angle. The spatial resolution of SMOKE experiments on the curved crystal was improved to 0.2° by placing a narrow slit in the beam path.

Both Fe and W crystallize in the *bcc* lattice, whereas Ag is a *fcc* metal, which has implications on the uniformity of the lattice mismatch between Fe films and the underlying substrate. Once again, the appearance of an in-plane uniaxial anisotropy was observed on stepped surfaces by SMOKE measurements, and increased quadratically with step density. In contrast to the first study on Ag, the easy-axis of the Fe

films on stepped W(001) was found perpendicular to the steps rather than parallel. The quadratic dependence on step density, while in line with the missing bond model (for bcc materials), could also be explained by biaxial strain of the *bcc* layer on the *fcc* substrate.

To further study the magnetic behavior, the effect of the anisotropy strength on film thickness was explored. Growing Fe wedges on the curved crystal made it possible to tune both vicinal angle and Fe layer thickness. However, the anisotropy strength was found to only depend weakly on the film thickness. A $1/d$ dependence, as expected for a surface-type anisotropy, could not be confirmed. While the authors discussed that a lattice mismatch may introduce a volume-type anisotropy an thus contribute to the anisotropy strength, no definite conclusions regarding the origin of the anisotropy could be made. In the Néel model, both biaxial strain, as well as the missing bonds could explain the quadratic dependence.

The role of biaxial strain could conclusively be dismissed in a study of magnetic Co layers on a curved Cu(001) crystal.[85] A Co layer (8 ML thickness) was dosed on a Cu(001) crystal, with half its surface curved up to 6° around the $[1\bar{1}0]$ axis. The step-induced magnetic anisotropy in the Co films was found to depend linearly on step density, as predicted for the effect of missing bonds in stepped *fcc* films by the Néel model. This linear dependence could not originate from biaxial strain. Furthermore, dosing partial coverages of Cu on the Co films caused suppression of the step-induced anisotropy, if the dosed Cu was able to diffuse to the Co step edges. Magnetic switching varied linearly with step density and occurred at doses where complete Cu rows could be formed at the step edges. The formation of horizontal Co-Cu bonds at the steps suppressing the step-induced anisotropy further confirmed the role of missing bonds as the origin of this anisotropy.

Remarkably, Fe films on a curved *fcc* Pd(001) template showed a linear dependence of the step-induced, in-plane anisotropy,[86] rather than the quadratic dependence that was observed for the Fe/Ag(001) and Fe/W(001) systems and predicted for *bcc* lattices. The additional effect for the Fe/Pd system is the strong spin-orbit interaction in Pd, which causes polarization at the interface and an induced magnetic moment in the topmost Pd layers. As a result, the observed step-induced anisotropy was 3 times larger than in the previously described systems. The anisotropy was thus dominated by the effect of the induced magnetic moment at the Pd step edges, rather than the magnetization of the Fe film, causing the *fcc*-like linear dependence of anisotropy strength on step density. Additionally, the induced magnetic moment caused an increase in the Curie temperature (T_C) of stepped Fe layers < 2 ML.

In a follow-up study in 2008, studying Fe films grown on a curved Pt(111) sample, a similar effect was observed.[87, 88] The strong induced ferromagnetic moment at the Fe/Pt interface resulted in a step-induced anisotropy that scaled with a power of 4

with step density. This strong anisotropy also enhanced the T_C of stepped Fe layers. While LEED had been applied to confirm the surface structure of the previously employed curved substrate crystals, this study provided a first STM image of the curved Pt crystal.

A large number of other systems were studied with an identical approach, e.g. Fe on curved Cr(001) [89–92], curved Ag(001) [93], and Pd(001) [94], Co on curved Cu(001) [95, 96], Ni on Cu(001) [97–99], NiO films on curved Ag(001) [100], and mixed FeMn/Co films on two types of curved Cu(001) [83].

In their first paper applying thin film growth on curved crystals, Ortega and coworkers recently exploited an additional benefit of these types of samples. Growing a wedge of Ag on a curved Au sample allowed variation of step density and film thickness on the same substrate.[101] The quantum-well states that are caused by confinement within the thin film of Ag were shown to scatter off steps at the Au/Ag interface. The Ag surface states on Au showed a more significant terrace-size confinement effect than in bulk Ag.

More recently, the San Sebastian group also started exploring other types of overlayers. Large-scale faceting occurred on a Ni crystal (*c*-Ni(111)[1$\bar{1}$0]-30°) when instead of terminating to vacuum, a hexagonal boronitride (hBN) layer was grown on the Ni surface.[102] However, step doubling, which occured on the bare Ni surface,[64] was not observed on the hBN-covered crystal. Growing variable sizes of semiconducting hBN films is particularly interesting in regards to applications in microelectronic applications and fuel cells. The growth of templated hBN films was shown to induce structural changes in the underlying substrate. Structural changes on the A-type step side were observed by STM. Two phases forming a hill-and-valley structure were found: (111) terraces and (115) facets of a few nm in size. On the B-type step side of the apex, (111) terraces and (110) facets with an incommensurate overlayer of hBN are found. Both forms of facetting were explained as face segregations minimizing the elastic free energy. The differences in facetting across the curved crystal would then be determined by the interface energy between hBN and different vicinal Ni surfaces.

The electronic structure and chemical environment of the hBN layer was further determined using near edge x-ray absorption spectroscopy (NEXAFS), x-ray photoelectron spectroscopy (XPS), and ARPES, all using synchrotron radiation. For both sides of the apex, the hBN layer was found to be less strongly bound and, thus, further away from the Ni surface than on the (111) terraces. This appeared of significance during subsequent molecular oxygen (O_2) treatment.[103] After dissociation on the metal-like surface of hBN overlayer on Ni, two possible outcomes for creation of atomic oxygen appeared possible: oxygen intercalation and hBN oxidation. While the lat-

ter was found to be uniformly distributed along the crystal's curvature, intercalation increased with miscut angle, resulting in even weaker hBN-Ni binding.

The potential of employing curved crystal substrates to gain unprecedented structural control in surface spintronics was demonstrated in a recent study.[52] On two curved Ag surfaces featuring either close-packed or fully-kinked steps, Bi was deposited to form a $BiAg_2$ alloy film, which replicated the superlattice of the Ag substrate. Step edges of the alloys formed zig-zag step edges on the Ag sample with A- or B-type steps, and atomically straight step edges of the alloy on the Ag substrate with fully-kinked steps. This behavior indicates Bi-termination of the alloy at edges. The latter alloy showed quatization of the terrace widths at vicinal surfaces. Subsequently only the $BiAg_2$ film forming straight step edges was used to investigate helical Rashba states, which were exhibited energy shifts and changes in the spin-orbit coupling with step density. The authors attributed this behavior to coherent scattering in spin-textured helical Rashba states.

2.8. CONCLUSION

We believe that the previous discussion of the recent advances illustrates that curved single crystal surfaces can be very useful to both fundamental studies focusing on physical and chemical properties of surfaces and to more applied studies aiming to develop (thin layer) materials with particular properties. For such aims, they may be by far the easiest approach, e.g. when step density dependencies are at the focus of the study. For other aims, they may really be the only option, e.g. when subtle differences may be masked by quality or purity variations between multiple 'flat' single crystals.

Clearly, a thorough study of the exposed surface structures is in all cases crucial. LEED gives insight, but the combination with scanning probe techniques is preferred. As the latter are being applied commonly by now, the uncertainties regarding surface structure that still prevailed in the studies of the 20^{th} century, are not a major issue anymore. It may, however, require for each new surface to be studied at first a significant effort to find cleaning procedures that yield the desired (continuous) range of surface structures. This effort should not be underestimated.

While by now a significant number of metals have been used in curved single crystal shape, in comparison to the number of interesting pure metals and alloys, there is still much unexplored. Most studies so far used the coinage and Pt group metals. Also other materials, e.g. oxides may also be of interest to study with a crystal shape that exposes a curved surface. Studies on, e.g. TiO_2 and oxygen vacancies therein[104] and ZnO [105], are indeed now starting to appear. Hence, with fundamental aspects, e.g. the importance and quantification of diffusion of intermediates in chemical reactions and the use of chirality of surfaces to heterogeneous catalysis largely unex-

plored, curved crystals not yet finding their way into electrochemical studies, and their potential to aid in growth of particular 2D and thin layer materials barely having started, we expect that many studies employing curved samples are still to come.

REFERENCES

[1] C. R. Henry. Morphology of supported nanoparticles. *Progress in surface science*, 80(3-4):92–116, 2005.

[2] K. Besocke, B. Krahl-Urban, and H. Wagner. Dipole moments associated with edge atoms; A comparative study on stepped Pt, Au and W surfaces. *Surface Science*, 68:39–46, 1977.

[3] J. Moison and J. Domange. Substrate steps/adsorbed layer interaction; selective effect on the possible epitaxial relationships: Case of the S/Cu(111) system. *Surface Science*, 69(1):336–348, 1977.

[4] J. Moison and J. Domange. LEED study of all copper vicinal surfaces 4° off (100) and (111) planes under S, O and Pb adsorption. *Surface Science*, 97(1):1–15, 1980.

[5] M. Sander, R. Imbihl, and G. Ertl. Kinetic oscillations in catalytic CO oxidation on a cylindrical Pt single crystal surface. *The Journal of chemical physics*, 97(7):5193–5204, 1992.

[6] E. G. Linder. Photo-electric effect and surface structure in zinc single crystals. *Physical Review*, 30(5):649, 1927.

[7] K. Hausser and Scholz. Metall-Einkristalle. *Wiss. Veröff. a. d. SIEMENS-Konzern*, V(3):144, 1927.

[8] G. Tammann and F. Sartorius. Ätzerscheinungen am Kupfereinkristall. *Zeitschrift für anorganische und allgemeine Chemie*, 175(1):97–120, 1928.

[9] S. T. Martin. On the thermionic and adsorptive properties of the surfaces of a tungsten single crystal. *Physical Review*, 56(9):947, 1939.

[10] A. T. Gwathmey and A. F. Benton. The Growth, Orientation, and Preparation of the Surface of Single Crystals of Copper. *The Journal of Physical Chemistry*, 44(1):35–42, 1940.

[11] A. T. Gwathmey and A. F. Benton. The directional oxidation of a single crystal of copper by heating in air at reduced pressure. *The Journal of Chemical Physics*, 8(5):431–432, 1940.

[12] A. T. Gwathmey and A. F. Benton. The directional catalytic activity of a single crystal of copper. *The Journal of Chemical Physics*, 8(7):569–570, 1940.

[13] A. T. Gwathmey and A. F. Benton. The Reaction of Gases on the Surface of a Single Crystal of Copper. I. Oxygen. *The Journal of Physical Chemistry*, 46(8):969–980, 1942.

[14] H. Leidheiser Jr and A. T. Gwathmey. The Catalytic Reaction of Hydrogen and Oxygen on Plane Faces of a Single Crystal of Copper[1]. *Journal of the American Chemical Society*, 70(3):1200–1206, 1948.

[15] J. B. Wagner Jr and A. T. Gwathmey. The Formation of Powder and its Dependence on Crystal Face during the Catalytic Reaction of Hydrogen and Oxygen on a Single Crystal of Copper1. *Journal of the American Chemical Society*, 76(2):390–391, 1954.

[16] R. E. Cunningham and A. T. Gwathmey. The Influence of Foreign Atoms on the Surface Rearrangement Produced by the Catalytic Reaction of Hydrogen and Oxygen on a Single Crystal of Copper[1]. *Journal of the American Chemical Society*, 76(2):391–393, 1954.

[17] F. W. Young Jr, J. V. Cathcart, and A. T. Gwathmey. The rates of oxidation of several faces of a single crystal of copper as determined with elliptically polarized light. *Acta Metallurgica*, 4(2):145–152, 1956.

[18] K. R. Lawless and A. T. Gwathmey. The structure of oxide films on different faces of a single crystal of copper. *Acta metallurgica*, 4(2):153–163, 1956.

[19] H. Leidheiser Jr and A. T. Gwathmey. The Selective Deposition of Carbon on the (111) Face of a Nickel Crystal in the Catalytic Decomposition of Carbon Monoxide[1]. *Journal of the American Chemical Society*, 70(3):1206–1206, 1948.

[20] R. E. Cunningham and A. T. Gwathmey. 5 The Reaction of Hydrogen and Ethylene on Several Faces of a Single Crystal of Nickel. In *Advances in Catalysis*, volume 9, pages 25–36. Elsevier, 1957.

[21] A. T. Gwathmey, H. Leidheiser, and G. Smith. Friction and cohesion between single crystals of copper. *Proceedings of the Royal Society of London. Series A. Mathematical and Physical Sciences*, 212(1111):464–467, 1952.

[22] V. J. Kehrer and H. Leidheiser Jr. The Phase Transformation of Cobalt as Observed on Single Crystals. *The Journal of Chemical Physics*, 21(3):570–570, 1953.

[23] V. J. Kehrer Jr and H. Leidheiser Jr. The catalytic decomposition of carbon monoxide on large metallic single crystals. *The Journal of Physical Chemistry*, 58(7):550–555, 1954.

[24] H. Leidheiser Jr and F. H. Cook. The Anistropic Rate of Photographic Development of Single Crystals of Silver Chloride[1,2]. *Journal of the American Chemical Society*, 76(2):617–617, 1954.

[25] F. Hottier, J. Theeten, A. Masson, and J. Domange. Comparative LEED and RHEED examination of stepped surfaces; Application to Cu(111) and GaAs(100) vicinal surfaces. *Surface Science*, 65(2):563–577, 1977.

[26] W. Ranke, Y. Xing, and G. Shen. Orientation dependence of oxygen adsorption on a cylindrical GaAs sample: I. Auger measurements. *Surface Science*, 120(1):67–89, 1982.

[27] W. Ranke. Oxygen Adsorption on a Cylindrical GaAs Single Crystal Prepared by Molecular Beam Epitaxy. *Physica Scripta*, 1983(T4):100, 1983.

[28] W. Ranke and D. Schmeisser. Adsorption of water on a cylindrical silicon crystal. *Surface science*, 149(2-3):485–499, 1985.

[29] T. Gardiner, H. Kramer, and E. Bauer. The surface structure of the <110> zone of tungsten: A LEED and work function study. *Surface Science*, 112(1-2):181–196, 1981.

[30] W. Ellis and R. Schwoebel. LEED from surface steps on UO_2 single crystals. *Surface Science*, 11(1):82–98, 1968.

[31] S. Mróz and E. Bauer. The interaction of gold with the surface of a cylindrical tungsten single crystal. *Surface science*, 169(2-3):394–404, 1986.

[32] B. Pluis, A. D. Van der Gon, J. Frenken, and J. van der Veen. Crystal-face dependence of surface melting. *Physical review letters*, 59(23):2678, 1987.

[33] H. Hopster, H. Ibach, and G. Comsa. Catalytic oxidation of carbon monoxide on stepped platinum (111) surfaces. *Journal of Catalysis*, 46(1):37–48, 1977.

[34] J. Neugebohren, D. Borodin, H. W. Hahn, J. Altschäffel, A. Kandratsenka, D. J. Auerbach, C. T. Campbell, D. Schwarzer, D. J. Harding, A. M. Wodtke, et al. Velocity-resolved kinetics of site-specific carbon monoxide oxidation on platinum surfaces. *Nature*, 558(7709):280–283, 2018.

[35] A. Armitage, D. Woodruff, and P. Johnson. Crystallographic incident beam effects in quantitative Auger electron spectroscopy. *Surface Science*, 100(3):L483–L490, 1980.

[36] H.-T. Liu, A. Armitage, and D. Woodruff. Anisotropy of initial oxidation kinetics of nickel single crystal surfaces. *Surface science*, 114(2-3):431–444, 1982.

[37] A. Armitage and D. Woodruff. Initial adsorption kinetics of oxygen and sulphur on copper cylindrical crystal surfaces. *Surface Science*, 114(2-3):414–430, 1982.

[38] J. Arlow and D. Woodruff. Structural specificity of dissociative chemisorption of oxygen from molecular oxygen and from nitrous oxide on copper surfaces. *Surface Science*, 157(2-3):327–338, 1985.

[39] J. Arlow and D. Woodruff. Structural specificity in CO and H_2 oxidation over single crystal copper surfaces. *Surface science*, 180(1):89–109, 1987.

[40] M. Sander, M. Bassett, R. Imbihl, and G. Ertl. Spatial coupling between kinetic oscillations on different regions of a cylindrical Pt single crystal. *Vacuum*, 41(1-3):272–274, 1990.

[41] M. Sander, G. Veser, and R. Imbihl. Spirals and propagating reaction fronts during catalytic CO oxidation on a cylindrical Pt single crystal. *Journal of Vacuum Science & Technology A: Vacuum, Surfaces, and Films*, 10(4):2495–2500, 1992.

[42] G. Veser and R. Imbihl. Spatial pattern formation in the oscillatory NO + CO reaction on a Pt (100) surface and its vicinal orientations. *The Journal of chemical physics*, 96(9):7155–7163, 1992.

[43] G. Veser, P. A. Thiel, and R. Imbihl. Homogeneous and heterogeneous front nucleation in a bistable surface reaction: the NO + CO reaction on a cylindrical Pt crystal. *The Journal of Physical Chemistry*, 98(8):2148–2151, 1994.

[44] C. F. McFadden, P. S. Cremer, and A. J. Gellman. Adsorption of Chiral Alcohols on "Chiral" Metal Surfaces. *Langmuir*, 12(10):2483–2487, 1996.

[45] A. Ahmadi, G. Attard, J. Feliu, and A. Rodes. Surface reactivity at 'chiral' platinum surfaces. *Langmuir*, 15(7):2420–2424, 1999.

[46] S. J. Jenkins and S. J. Pratt. Beyond the surface atlas: A roadmap and gazetteer for surface symmetry and structure. *Surface Science Reports*, 62(10):373 – 429, 2007.

[47] A. J. Gellman. *Enantioselectivity on Naturally Chiral Metal Surfaces*, pages 75–95. Springer New York, New York, NY, 2010.

[48] G. A. Attard, A. Ahmadi, J. Feliu, A. Rodes, E. Herrero, S. Blais, and G. Jerkiewicz. Temperature effects in the enantiomeric electro-oxidation of D- and L-glucose on Pt$\{643\}^S$. *Journal of Physical Chemistry B*, 103(9):1381–1385, 1999.

[49] S. V. Auras, R. van Lent, D. Bashlakov, J. M. Piñeiros Bastidas, T. Roorda, R. Spierenburg, and L. B. F. Juurlink. Scaling Pt-catalyzed hydrogen dissociation on corrugated surfaces. *Angewandte Chemie International Edition*, 2020.

[50] S. V. Auras, R. A. B. van Bree, D. L. Bashlakov, R. van Lent, and L. B. F. Juurlink. It's not just the defects - a curved crystal study of H_2O desorption from Ag. *Physical Chemistry Chemical Physics*, 21(28):15422–15430, JUL 28 2019.

[51] A. De Alwis, B. Holsclaw, V. Pushkarev, A. Reinicker, T. Lawton, M. Blecher, E. Sykes, and A. Gellman. Surface structure spread single crystals (S^4C): preparation and characterization. *Surface science*, 608:80–87, 2013.

[52] J. E. Ortega, G. Vasseur, I. Piquero-Zulaica, J. Raoult, M. A. Valbuena, S. Schirone, S. Matencio, A. Mugarza, and J. Lobo-Checa. Atomically precise step grids for the engineering of helical states. *arXiv preprint arXiv:1902.05777*, 2019.

[53] T. Lawton, V. Pushkarev, E. Broitman, A. Reinicker, E. Sykes, and A. Gellman. Initial oxidation of Cu(hkl) surfaces vicinal to Cu(111): A high-throughput study of structure sensitivity. *The Journal of Physical Chemistry C*, 116(30):16054–16062, 2012.

[54] C. Hahn, J. Shan, Y. Liu, O. Berg, A. W. Kleijn, and L. B. Juurlink. Employing a cylindrical single crystal in gas-surface dynamics. *The Journal of Chemical Physics*, 136(11):114201, 2012.

[55] R. V. Mom, C. Hahn, L. Jacobse, and L. B. Juurlink. LEED analysis of a nickel cylindrical single crystal. *Surface Science*, 613:15–20, 2013.

[56] M. Henzler. LEED-investigation of step arrays on cleaved germanium (111) surfaces. *Surface Science*, 19(1):159–171, 1970.

[57] M. Van Hove and G. Somorjai. A new microfacet notation for high-Miller-index surfaces of cubic materials with terrace, step and kink structures. *Surface Science*, 92(2-3):489–518, 1980.

[58] F. Schiller, M. Corso, J. Cordón, F. G. de Abajo, and J. Ortega. Interplay between electronic states and structure during Au faceting. *New Journal of Physics*, 10(11):113017, 2008.

[59] M. Corso, F. Schiller, L. Fernández, J. Cordón, and J. Ortega. Electronic states in faceted Au(111) studied with curved crystal surfaces. *Journal of Physics: Condensed Matter*, 21(35):353001, 2009.

[60] J. E. Ortega, M. Corso, Z. Abd-el Fattah, E. Goiri, and F. Schiller. Interplay between structure and electronic states in step arrays explored with curved surfaces. *Physical Review B*, 83(8):085411, 2011.

[61] J. E. Ortega, J. Lobo-Checa, G. Peschel, S. Schirone, Z. A. El-Fattah, M. Matena, F. Schiller, P. Borghetti, P. Gambardella, and A. Mugarza. Scattering of surface electrons by isolated steps versus periodic step arrays. *Physical Review B*, 87(11):115425, 2013.

[62] J. E. Ortega, G. Vasseur, I. Piquero-Zulaica, S. Matencio, M. A. Valbuena, J. E. Rault, F. Schiller, M. Corso, A. Mugarza, and J. Lobo-Checa. Structure and electronic states of vicinal Ag(111) surfaces with densely kinked steps. *New Journal of Physics*, 20(7):073010, 2018.

[63] J. Janlamool, D. Bashlakov, O. Berg, P. Praserthdam, B. Jongsomjit, and L. B. Juurlink. Desorption of water from distinct step types on a curved silver crystal. *Molecules*, 19(8):10845–10862, 2014.

[64] M. Ilyn, A. Magaña, A. L. Walter, J. Lobo-Checa, D. G. de Oteyza, F. Schiller, and J. E. Ortega. Step-doubling at vicinal Ni(111) surfaces investigated with a curved crystal. *The Journal of Physical Chemistry C*, 121(7):3880–3886, 2017.

[65] A. L. Walter, F. Schiller, M. Corso, L. R. Merte, F. Bertram, J. Lobo-Checa, M. Shipilin, J. Gustafson, E. Lundgren, A. X. Bríon-Ríos, et al. X-ray photoemission analysis of clean and carbon monoxide-chemisorbed platinum (111) stepped surfaces using a curved crystal. *Nature communications*, 6(1):1–7, 2015.

[66] S. Blomberg, J. Zetterberg, J. Zhou, L. R. Merte, J. Gustafson, M. Shipilin, A. Trinchero, L. A. Miccio, A. Magaña, M. Ilyn, et al. Strain dependent light-off temperature in catalysis revealed by planar laser-induced fluorescence. *ACS Catalysis*, 7(1):110–114, 2017.

[67] F. Garcia-Martinez, F. Schiller, S. Blomberg, M. Shipilin, L. R. Merte, J. Gustafson, E. Lundgren, and J. E. Ortega. CO Chemisorption on Vicinal Rh(111) Surfaces Studied with a Curved Crystal. *The Journal of Physical Chemistry C*, 124(17):9305–9313, 2020.

[68] T. Nishizawa and K. Ishida. The Co (cobalt) system. *Bulletin of Alloy phase diagrams*, 4(4):387–390, 1983.

[69] A. J. Walsh, R. van Lent, S. V. Auras, M. A. Gleeson, O. T. Berg, and L. B. Juurlink. Step-type and step-density influences on CO adsorption probed by reflection absorption infrared spectroscopy using a curved Pt(111) surface. *Journal of Vacuum Science & Technology A: Vacuum, Surfaces, and Films*, 35(3):03E102, 2017.

[70] A. Reinicker, A. Therrien, T. Lawton, R. Ali, E. Sykes, and A. Gellman. Influence of step faceting on the enantiospecific decomposition of aspartic acid on chiral Cu surfaces vicinal to Cu {111}. *Chemical Communications*, 52(75):11263–11266, 2016.

[71] P. Kondratyuk, B. Karagoz, Y. Yun, and A. J. Gellman. Initiation of Vacancy-Mediated, Surface Explosion Reactions: Tartaric and Aspartic Acid on Cu Surfaces. *The Journal of Physical Chemistry C*, 123(31):18978–18985, 2019.

[72] J. R. Kitchin and A. J. Gellman. High-throughput methods using composition and structure spread libraries. *AIChE Journal*, 62(11):3826–3835, 2016.

[73] A. C. Schilling, A. J. Therrien, R. T. Hannagan, M. D. Marcinkowski, P. L. Kress, D. A. Patel, T. A. Balema, A. M. Larson, F. R. Lucci, B. P. Coughlin, R. Zhang, T. Thuening, V. Çınar, J.-S. McEwen, A. J. Gellman, and E. C. H. Sykes. Templated Growth of a Homochiral Thin Film Oxide. *ACS Nano*, 14(4):4682–4688, 2020.

[74] M. E. Turano, L. B. F. Juurlink, M. Gillum, E. Jamka, and D. R. Killelea. Oxygen Adsorption on Different Step Geometries of curved Ag(111). *submitted*.

[75] K. Cao, R. van Lent, A. W. Kleyn, M. Kurahashi, and L. B. Juurlink. Steps on Pt stereodynamically filter sticking of O_2. *Proceedings of the National Academy of Sciences*, 116(28):13862–13866, 2019.

[76] L. Jacobse, A. den Dunnen, and L. B. Juurlink. The molecular dynamics of adsorption and dissociation of O_2 on Pt (553). *The Journal of chemical physics*, 143(1):014703, 2015.

[77] C. Hahn. *Steps away from flat land*. PhD thesis, Leiden University, Leiden, the Netherlands, 2015.

[78] R. van Lent, S. V. Auras, K. Cao, A. J. Walsh, M. A. Gleeson, and L. B. Juurlink. Site-specific reactivity of molecules with surface defects—The case of H_2 dissociation on Pt. *Science*, 363(6423):155–157, 2019.

[79] F. Garcia-Martinez, C. García-Fernández, J. P. Simonovis, A. Hunt, A. Walter, I. Waluyo, F. Bertram, L. R. Merte, M. Shipilin, S. Pfaff, S. Blomberg, J. Zetterberg, J. Gustafson, E. Lundgren, D. Sánchez-Portal, F. Schiller, and J. E. Ortega. Catalytic Oxidation of CO on a Curved Pt(111) Surface: Simultaneous Ignition at All Facets through a Transient CO-O Complex**. *Angewandte Chemie International Edition*, 59(45):20037–20043, 2020.

[80] F. Schiller, M. Ilyn, V. Pérez-Dieste, C. Escudero, C. Huck-Iriart, N. Ruiz del Arbol, B. Hagman, L. R. Merte, F. Bertram, M. Shipilin, S. Blomberg, J. Gustafson, E. Lundgren, and J. E. Ortega. Catalytic Oxidation of Carbon Monoxide on a Curved Pd Crystal: Spatial Variation of Active and Poisoning Phases in Stationary Conditions. *Journal of the American Chemical Society*, 140(47):16245–16252, 2018.

[81] B. Karagoz, M. Payne, A. Reinicker, P. Kondratyuk, and A. J. Gellman. A Most Enantioselective Chiral Surface: Tartaric Acid on All Surfaces Vicinal to Cu(110). *Langmuir*, 35(50):16438–16443, 2019. PMID: 31729881.

[82] R. Kawakami, E. J. Escorcia-Aparicio, and Z. Qiu. Symmetry-induced magnetic anisotropy in Fe films grown on stepped Ag(001). *Physical review letters*, 77(12):2570, 1996.

[83] J. Choi, J. Wu, Y. Wu, C. Won, A. Scholl, A. Doran, T. Owens, and Z. Qiu. Effect of atomic steps on the interfacial interaction of Fe Mn/ Co films grown on vicinal Cu(001). *Physical Review B*, 76(5):054407, 2007.

[84] H. J. Choi, Z. Qiu, J. Pearson, J. Jiang, D. Li, and S. Bader. Magnetic anisotropy of epitaxial Fe films grown n on curved W(001) with a graded step density. *PHYSICAL REVIEW-SERIES B-*, 57:R12–713, 1998.

[85] R. Kawakami, M. Bowen, H. J. Choi, E. J. Escorcia-Aparicio, and Z. Qiu. Effect of atomic steps on the magnetic anisotropy in vicinal Co/Cu(001). *Physical Review B*, 58(10):R5924, 1998.

[86] H. J. Choi, R. Kawakami, E. J. Escorcia-Aparicio, Z. Qiu, J. Pearson, J. Jiang, D. Li, and S. Bader. Curie temperature enhancement and induced Pd magnetic moments for ultrathin Fe films grown on stepped Pd(001). *Physical review letters*, 82(9):1947, 1999.

[87] R. Cheng, S. Bader, and F. Fradin. Magnetic properties of Fe on vicinal Pt(111). *Journal of Applied Physics*, 103(7):07B729, 2008.

[88] R. Cheng, S. Bader, and F. Fradin. Strong magnetic surface anisotropy of ultrathin Fe on curved Pt(111). *Physical Review B*, 77(2):024404, 2008.

[89] E. J. Escorcia-Aparicio, H. J. Choi, W. Ling, R. Kawakami, and Z. Qiu. The effect of interfacial steps on the ferromagnetic/antiferromagnetic interface of thin Fe films on Cr[001]. *IEEE transactions on magnetics*, 34(4):1219–1221, 1998.

[90] E. J. Escorcia-Aparicio, H. J. Choi, W. Ling, R. Kawakami, and Z. Qiu. 90° Magnetization Switching in Thin Fe Films Grown on Stepped Cr(001). *Physical review letters*, 81(10):2144, 1998.

[91] E. J. Escorcia-Aparicio, H. J. Choi, J. Wolfe, W. Ling, R. Kawakami, and Z. Qiu. Modification of the magnetic properties of Fe/Cr(001) by controlling the compensation of a vicinal Cr(001) surface. *Journal of applied physics*, 85(8):4961–4963, 1999.

[92] E. J. Escorcia-Aparicio, J. Wolfe, H. J. Choi, W. Ling, R. Kawakami, and Z. Qiu. Magnetic phases of thin Fe films grown on stepped Cr(001). *Physical Review B*, 59(18):11892, 1999.

[93] Y. Wu, C. Won, and Z. Qiu. Magnetic uniaxial anisotropy of Fe films grown on vicinal Ag(001). *Physical Review B*, 65(18):184419, 2002.

[94] H. J. Choi, R. Kawakami, E. J. Escorcia-Aparicio, Z. Qiu, J. Pearson, J. Jiang, D. Li, R. Osgood III, and S. Bader. Magnetic properties of ultrathin Fe films grown on stepped W(001) and Pd(001) substrates. *Journal of applied physics*, 85(8):4958–4960, 1999.

[95] R. Kawakami, M. Bowen, H. J. Choi, E. J. Escorcia-Aparicio, and Z. Qiu. Step-induced magnetic anisotropy in Co/stepped Cu(001) as a function of step density and Cu step decoration. *Journal of applied physics*, 85(8):4955–4957, 1999.

[96] Y. Wu, C. Won, H. Zhao, and Z. Qiu. Surface magneto-optic Kerr effect study of Co thin films grown on double curved Cu(001). *Physical Review B*, 67(9):094409, 2003.

[97] U. Bovensiepen, H. J. Choi, and Z. Qiu. Step-induced magnetic anisotropy in vicinal Ni/Cu(001) and its effect on the spin-reorientation transition. *Physical Review B*, 61(5):3235, 2000.

[98] H. Zhao, Y. Wu, C. Won, F. Toyoma, and Z. Qiu. Effect of the Cu capping layer on the magnetic anisotropy of Ni/Cu(100). *Physical Review B*, 66(10):104402, 2002.

[99] U. Bauer, J. Choi, J. Wu, H. Chen, and Z. Qiu. Effect of step decoration on the spin reorientation of Ni films grown on vicinal Cu(001). *Physical Review B*, 76(18):184415, 2007.

[100] Y. Wu, Z. Qiu, Y. Zhao, A. Young, E. Arenholz, and B. Sinkovic. Tailoring the spin direction of antiferromagnetic NiO thin films grown on vicinal Ag(001). *Physical Review B*, 74(21):212402, 2006.

[101] F. Schiller, Z. A. El-Fattah, S. Schirone, J. Lobo-Checa, M. Urdanpilleta, M. Ruiz-Osés, J. Cordón, M. Corso, D. Sánchez-Portal, A. Mugarza, et al. Metallic thin films on stepped surfaces: lateral scattering of quantum well states. *New Journal of Physics*, 16(12):123025, 2014.

[102] L. Fernandez, A. A. Makarova, C. Laubschat, D. V. Vyalikh, D. Y. Usachov, J. E. Ortega, and F. Schiller. Boron nitride monolayer growth on vicinal Ni(111) surfaces systematically studied with a curved crystal. *2D MATERIALS*, 6(2), APR 2019.

[103] A. A. Makarova, L. Fernandez, D. Y. Usachov, A. Fedorov, K. A. Bokai, D. A. Smirnov, C. Laubschat, D. V. Vyalikh, F. Schiller, and J. E. Ortega. Oxygen Intercalation and Oxidation of Atomically Thin h-BN Grown on a Curved Ni Crystal. *The Journal of Physical Chemistry C*, 123(1):593–602, 2019.

[104] L. A. Miccio, M. Setvin, M. Müller, M. Abadía, I. Piquero, J. Lobo-Checa, F. Schiller, C. Rogero, M. Schmid, D. Sánchez-Portal, U. Diebold, and J. E. Ortega. Interplay between Steps and Oxygen Vacancies on Curved TiO_2(110). *Nano Letters*, 16(3):2017–2022, 2016.

[105] E. Grånäs, B. Arndt, C. Seitz, M. Wagstaffe, and A. Stierle. Atomic scale step structure and orientation of a curved surface ZnO single crystal. *The Journal of Chemical Physics*, 152(7):074705, 2020.

3

SURFACE STRUCTURE CHARACTERIZATION OF A CURVED PT CRYSTAL WITH HIGHLY KINKED STEPS

Chemical reaction steps at surfaces e.g. in heterogeneous catalysis and astronomy, are often dominated by the presence of defects rather than high-symmetry planes. However, in surface science, these processes are frequently studied by atomically flat model surfaces. Stepped surfaces provide an approach to model line defects on particles. Curved single crystal surfaces provide a useful tool for studying the influence of these defects systematically. The influence of other types of defects, such as kinks or dislocations, has received less attention.

Here, we employ a curved Pt crystal oriented such that highly kinked step edges with {210} orientation are exposed. We characterize the continuous surface structure from (111) at the apex to (432) at the sides of the apex by Scanning Tunneling Microscopy and Low Energy Electron Diffraction. Observations are analyzed in regards to their microscopic and macroscopic structure and compared to the ideal crystallographic structure. Knowing the structure of the kinked surfaces on this crystal allows us to then determine site-specific reactivities in Chapters 4 and 5.

3.1. INTRODUCTION

THE SABATIER PRINCIPLE in heterogeneous catalysis states that a good catalyst should bind reactants and reaction intermediates neither too strongly nor too weakly, in order to promote the elementary reaction steps on a catalysts surface, e.g. adsorption, dissociation, diffusion, recombination, and desorption. This can be visualized in so-called 'volcano plots', where the catalytic activity of different materials is plotted against their adsorption energies towards specific reactants. The name-giving volcano form illustrates that peak catalytic performance is typically found at intermediate binding strengths. For a number of heterogeneously catalyzed reactions, Pt has been found to be an exceptionally well-suited catalyst, at or near the top of volcano plots. For example, the three-way catalyst built into car exhausts makes use of the catalytic performance of Pt towards CO oxidation, hydrocarbon oxidation, and NO_x reduction, all under the same reaction conditions. Moreover, CO oxidation on well-defined Pt(111) surfaces is one a standard system used to study all fundamental aspects of surface reactions. As the reaction follows the Langmuir-Hinshelwood mechanism, it is an example for a typical catalytic surface reaction involving several reactions steps, causing complex reaction dynamics.[1–4] The simplest reaction of the smallest molecule, hydrogen dissociation, also takes place readily on Pt(111) surfaces. Beyond its relevance industrial processes, this system is of central importance to the development of models in gas-surface dynamics and electrochemisty.[5, 6]

While reactions on high-symmetry faces are still most frequently studied in surface science, chemical reactivity on catalytic Pt surfaces is often improved by the presence of lower-coordinated sites, such as steps, kinks, and other surface defects.[7–12] Recently, even step-type and step density effects on chemical reactions have been observed.[13–16] In the case of nanoparticles, which are commonly deposited on an oxide support in industrial applications, lower-coordinated sites (edges, corners, as well as steps and kinks) may actually comprise a majority portion of the exposed surface.[17–19]

Line defects, i.e. steps on high-symmetry terraces, are among the more frequently studied defect sites, yet kink sites may increase chemical reactivity compared to close-packed steps.[20, 21] They can also cause different step-step interactions, thus influencing surface structure.[22–25] However, only few studies investigate the influence of kinks on catalytic reactions on Pt surfaces [14, 26, 27]

As kinked steps on (111) terraces of *fcc* metals are comprised of variable ratios of A- and B-type line segements ({001} and {110} microfacets), they are also inherently chiral and open possibilities to study enantioselective reactions.[28, 29] Chiral metal surfaces provide a way to introduce chirality to heterogeneous catalysis in a way that is stable at harsher environments used in industrial catalysis. Several examples of enan-

tioselective adsorption on chiral Cu surfaces have been identified,[30–34] as well as enantioselective decomposition reactions.[35, 36] Studies also point towards the potential of chiral chemistry on kinked Pt surfaces.[37–41]

In this context, curved crystals with varying surface structure offer the potential to study even small effects of surface defects. However, to unravel the influence of different surface sites, the changing surface structure must be characterized across the entire range of curvature of such samples. This is particularly important for the curved Pt crystal with kinked step edges we present here. It features surfaces of both chiralities, with varying compositions of (111) terraces, steps (from {001} and {110} microfacets), and kinks. This chapter aims to thoroughly characterize the surface structures found across the crystal, which is crucial to the interpretation of results reagrding chemical reactivity of achiral (chapters 4 and 5) molecules, as well as future adsorption experiments involving chiral organic molecules.

3.2. CRYSTALLOGRAPHIC ORIENTATION

Platinum crystallizes in the face-centered cubic (*fcc*) crystal structure. Its lattice can be described by three translational vectors. Surface terminations of the bulk lattice can be described by Miller indices (*hkl*) or the corresponding vector along the surface normal [*hkl*].

The curved crystal described here, shown in figure 3.1a), is cut from a Pt bulk single crystal. It can be seen as a slice of a cylinder with a rotational axis axis along the [11$\bar{2}$] vector, oriented such that at the apex (111) is exposed, as figure 3.1b) demonstrates. Due to the macroscopic curvature of the crystal, at the sides surfaces with an increasing 'miscut' angle are exposed. The entire crystal surface curves across 31°, causing surface structures to range from surfaces with (111) terraces that extend hundreds of nanometers to surfaces with terraces of less than a nanometer. Figure 3.1c) plots expected terrace widths and step densities along the curved surface. It therefore can be described as *c*-Pt(111)[11$\bar{2}$]-31°, according the nomenclature introduced in chapter 2. These surfaces exhibit {210}-oriented steps, i.e. steps with an orientation halfway in between {001}/A-type steps and {110}/B-type steps.[1] As a result, these {210} steps feature inner and outer kinks separating segments of A- and B-type steps. Surface atoms at a kink site are less coordinated by other surface atoms than they would be as part of a terrace or a straight step edge. They are thus often assumed to be more active towards adsorption and chemical reactions.

In figure 3.1d) we draw two surfaces with {210} steps. The atoms at the top edge illustrate how segments can be described as A- (blue) or B-type (red). There, segments are only one atom long, resulting in a maximum density of kinks along the

[1] We use Miller indices {hkl} to indicate the set of equivalent surfaces.

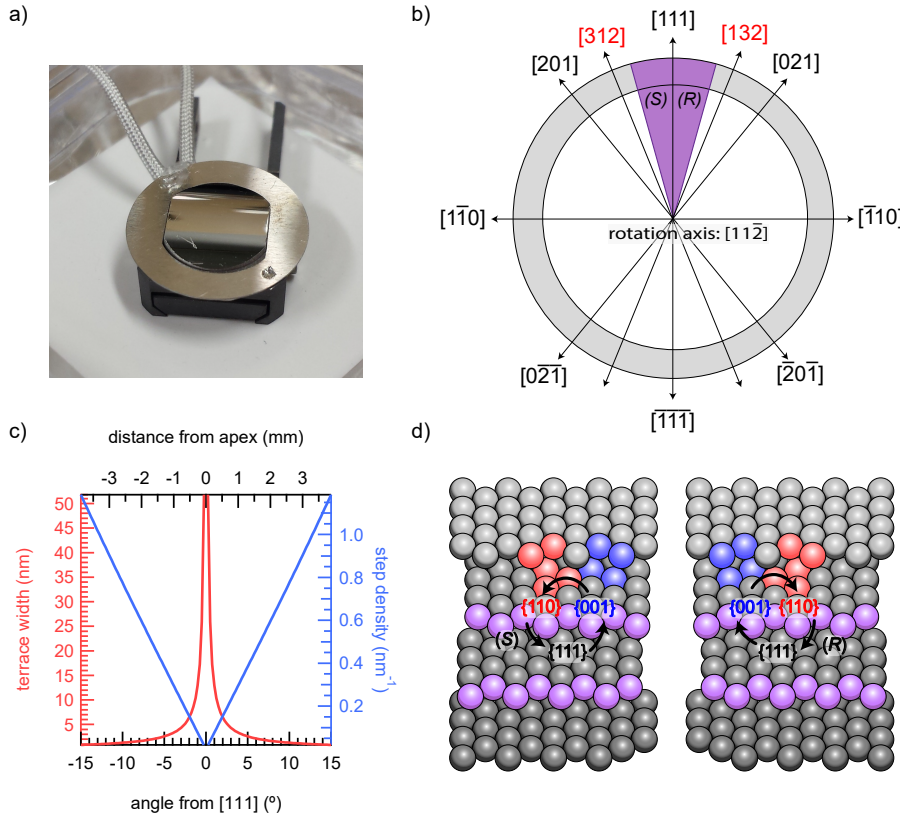

Figure 3.1: a) Photo of the curved Pt crystal. b) Depiction of crystallographic orientations along the surface of a cylinder with its rotational axis along [11$\bar{2}$] of a *fcc* crystal. The crystallographic range of the crystal sample displayed here is indicated in purple. As the surface curves away from the (111) apex, steps with [201] or [021] orientation are introduced on each side to accommodate the macroscopic curvature. The hollow sites at the step edge have *(S)* or *(R)* chirality respectively. c) Expected terrace widths (red) and step densities (blue) along the curved Pt single-crystalline surface with (111) at the apex. d) (423)$^{(S)}$ and (243)$^{(R)}$ surfaces that can be found to either side of the crystal. At the top step edge is illustrated how the kinked {210}-oriented step edges can be seen as consisting of small segments of {001}/A- and {110}/B-type steps. The middle step edge illustrates how the chirality is determined at the hollow site of the step edge. The (423) surface on the left has step edges with *(S)* chirality, the (243) surface on the right has step edges with *(R)* chirality.

step edge. However, the same crystallographic orientation/ Miller indices can also be maintained if the step edge forms longer facets and thereby reduces the amount of kinks, as long as the overall lengths of A- and B-type facets remain equal. Causes can be thermal roughening or reconstruction. Simulations of a kinked Pt(643) surface show a reduced kink density at elevated temperature.[38, 39] Characterizing the structure of these kinds of surfaces in regards to their kink density is thus crucial in order to interpret the results of subsequent experiments. Furthermore, it has to be determined if the kink density changes across the crystal from low to high step density.

Compared to straight steps, the kinked steps on this curved Pt crystal reduce surface symmetry due to the introduction of two separate microfacets. As a result, surfaces found at the two sides of the crystal are chiral to each other at the same angles from the apex. Figure 3.1d) depicts two {432} surfaces with opposite chirality, the (423) and (243) surfaces respectively. With the middle step edge we illustrate how the chirality of the surface is determined.[31, 41] Looking from above onto the hollow site of the step edge, three microfacets surround the inner corner: {110} and {001} facets along the step and a (111) terrace. Going from {001} to {110} to (111) will then result in a right-handed or left-handed turn. The surfaces are described as *(R)* (Latin *"rectus"*) or *(S)* (Latin *"sinister"*) chiral surfaces respectively.

For reactions involving only achiral reactants and products, no difference should be observed between *(R)*- and *(S)*-kinked surfaces. However, there may be steric advantages of one chirality when chiral molecules are part of a surface reaction. Indeed, the chirality of kinks on Pt surfaces has been shown to influence reactivity for chiral molecules, e.g. in the case of glucose oxidation. [41, 42]

3.3. SURFACE CLEANLINESS AND AVERAGE TERRACE WIDTH

The cleaning procedures employed for this Pt crystal and their implications on surface structure are detailed in chapter 5. After repeated cleaning cycles, Auger Electron Spectroscopy (AES) is employed to confirm the absence of contamination on the Pt surface. Exemplary spectra are plotted in figure 3.2 and show no significant peaks from elements other than Pt.

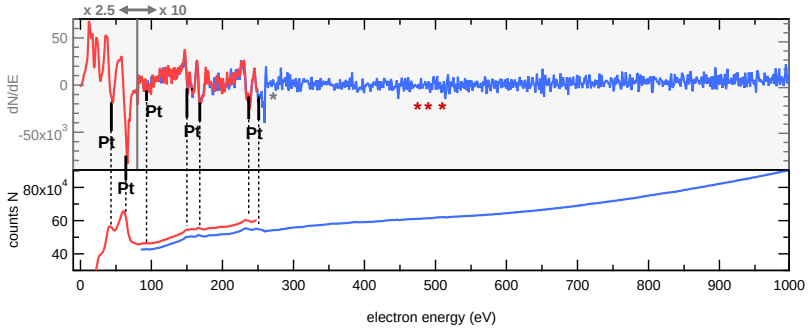

Figure 3.2: Typical Auger electron spectra of the Pt surface after cleaning. Black lines represent literature values of the most prominent dN/dE features for Pt.[43] Asterisks (*) mark most prominent features one would find in the presence of C (grey) or O (red). Spectra were recorded in several locations on the Pt surface, spanning the height and width of our sample, to ensure complete cleaning.

Subsequently, LEED is used to examine the regular ordering of the surface and check for possible surface reconstructions, step doubling, or faceting. The more ordered a surface is, the sharper the observed diffraction spots will appear. While a hexag-

onal diffraction pattern should be observed for the flat (111) surface, the diffraction spots will appear split at regularly stepped surfaces. The direction and extent of the spot splitting gives information about the average terrace width and step directions, see chapter 2. Streaking in the spot splitting would indicate wide variations in terrace widths. Figure 3.3 shows LEED patterns at the (111) apex as well as the sides of the crystal. At the center of the crystal (figure 3.3, middle of top row), we observe the reciprocal spots of a *fcc* (111) surface where the center spot is hidden behind the electron beam. Along the curvature of the crystal, we observe spot splitting which increases proportionally with the angle of curvature.

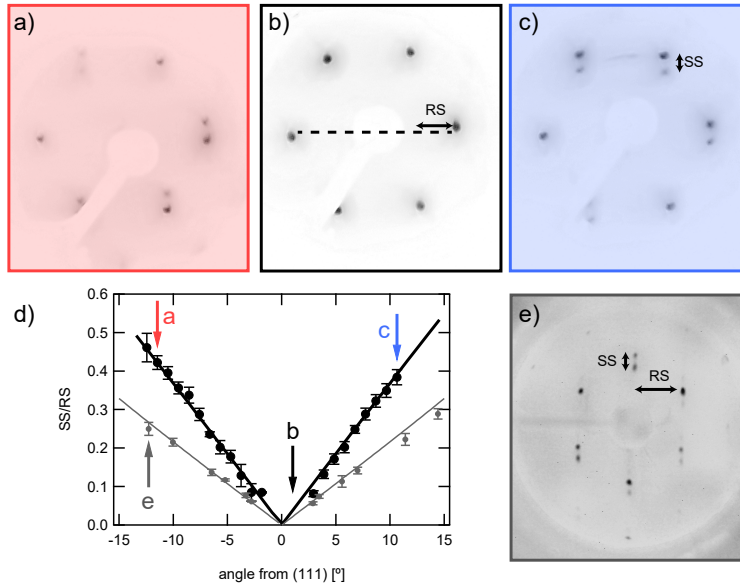

Figure 3.3: LEED patterns from different parts of the curved Pt crystal. a) - c) While around the apex a hexagonal diffraction pattern with well-defined spots is observed (b), to the sides the regular step arrays cause spot splitting (a&c). d) Spot splitting over row spacing ratios (SS/RS) along the crystal curvature. The black lines indicate expected ss/rs ratios, according to the terrace widths caused by the miscut angle from (111), see equation2. e) Demonstrates spot splitting on a similar curved crystal with close-packed steps. Both types of crystals are employed in chapter 4. Spot splitting to row spacing across the entire surface of this second crystal are added to the graph in d) in grey.

Figures 3.3a) and c) show spot splitting oriented perpendicular to the flat side of the hexagonal pattern, indicating steps along the $[11\bar{2}]$ vector, i.e. kinked {210}-oriented steps. In the case of straight A- or B-type steps, spot splitting would appear 30 ° rotated relative to the hexagon, as depicted in figure 3.3e). Figure 3.3 also plots spot splitting (SS) over row spacing (RS) ratios across the crystal. They match well with the expected ratios for monoatomically stepped surfaces at the corresponding angles away from (111), as obtained from table 2.1, confirming the expected average terrace width and the absence of reconstructions or faceting.

3.4. TERRACE WIDTH DISTRIBUTIONS

3.4.1. STEP-STEP INTERACTIONS AND THEIR IMPACT ON TERRACE WIDTH DISTRIBUTIONS

While the average terrace width can be determined by LEED at various positions of the curved surface, the microscopic structure may exhibit local variations, e.g. variations in terrace width, or deviations from the ideal step direction. These effects can be much more directly investigated by STM.

In general, step-step interactions on vicinal metal surfaces can be described via two universal effects. At short length scales, elastic repulsion between the dipoles at step edges forces steps into regular arrays to lower the free energy. This is a low entropy state.[44] Meandering of steps increases entropy in a stepped surface, and this effect dominates at larger step-step distances (d), as dipole interactions decrease with $1/d^2$.[44] Meandering, however, is limited by the fact that two steps can never cross one another.

In addition to the dipole and entropic interactions, a third effect can emerge due to the electronic band structure at the surface, at short step-step distances. This can be described by quantum confinement of electrons between the steps. Steps act as potential barriers, imposing boundary conditions to the wavefunction of the surface electrons, similar to the quantum mechanical description of a particle in a box. As a consequence, step-step distances where the electronic wavefunction forms a standing wave (eigenstates) can become favorable. For a metal, these distances correspond to multiple integers of half the Fermi wavelength ($\lambda_F/2$). This phenomenon, however, is only relevant if surface electrons can be decoupled from the band structure of the bulk, and form an independent surface states where they can behave as nearly free electrons. This condition, also called Shockley or Tamm state, is fulfilled for surfaces of Cu, Ag, and Au and is also what causes the so-called Friedel oscillations, which are spatial oscillations of the charge density. Friedel oscillations are observable when a wavefunction is reflected from a defect. Line defects, i.e. steps, can lead to similar charge density modulations. The question is whether electronic surface states can in turn shape the distribution of surface atoms. In the particle in a box analogy, this would be equivalent to the particle shrinking/expanding the boundaries of the box. Aligning the steps to match integers of the half wavelength of the surface electrons allows their wavefunction to form a standing wave, i.e. a lower state. While one might expect this to be a small energetic effect compared to the mentioned dipole and entropic interactions, a preference for 'magic' step-step distances has actually been observed on Ag surfaces with small terrace widths. With increasing terrace width, a clear transition in terrace width distributions was found.[22]

For Pt, no such clear *sp*-type surface state exists. However, surface resonances do. These do not fall into the energy gap of the bulk band structure. Specifically, a *sp* de-

rived surface resonance near the Fermi level has been shown to influence physisorption on Pt(111).[45] Quantum size effects to the conductance were found during the growth of thin layers of Pt, indicating an interaction between electronic and structural properties.[46]

For a stepped Pt surfaces with straight A- and B-type step edges a transition from the 'elastic regime' governing narrow terraces to the 'entropic repulsion' dominant at wider terraces was found to occur around 4 nm, marked by the terrace width distributions becoming wider and more asymmetric.[47] However, no quantum wells were indicated in the terrace width distributions.

Here we investigate the effects of step-step-interactions on the curved Pt crystal with kinked step edges. We investigate whether a similar transition between predominantly elastic interactions to entropic meandering can be observed for arrays with highly kinked step edges, and whether an influence of quantum size effects can be observed.

3.4.2. RESULTS OF TERRACE WIDTH ANALYSIS

We use the IGOR PRO software to analyze our STM images from various places on the crystal. The procedure can be found in Appendix D. In short, we take line profiles of the image perpendicular to the step direction given by the crystal's curvature. Finding minima along the line profile gives us the locations of the lower step edges. Terrace widths (w) are then determined pixel by pixel as distances between lower step edges. We find our terrace width distributions by sorting terrace width data in histograms. The bin width is 1/2 of the atom-atom distance (0.277 nm). The choice of our bins is due to the fact that in the case of the {210} steps, terrace width can take both full and half-integers of the interatomic distance, as figure 3.4 shows. We can determine width distributions by terrace as well as the overall distribution of all terraces in the array shown in the image.

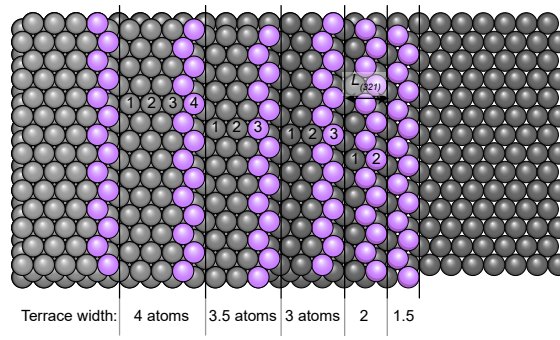

Figure 3.4: Possible terrace widths on the kinked surfaces in full and half-integer atom rows. Stepping down from the topmost step edge on the left, terraces with lengths of 4, 3.5, 3, 2, and 1.5 atom follow.

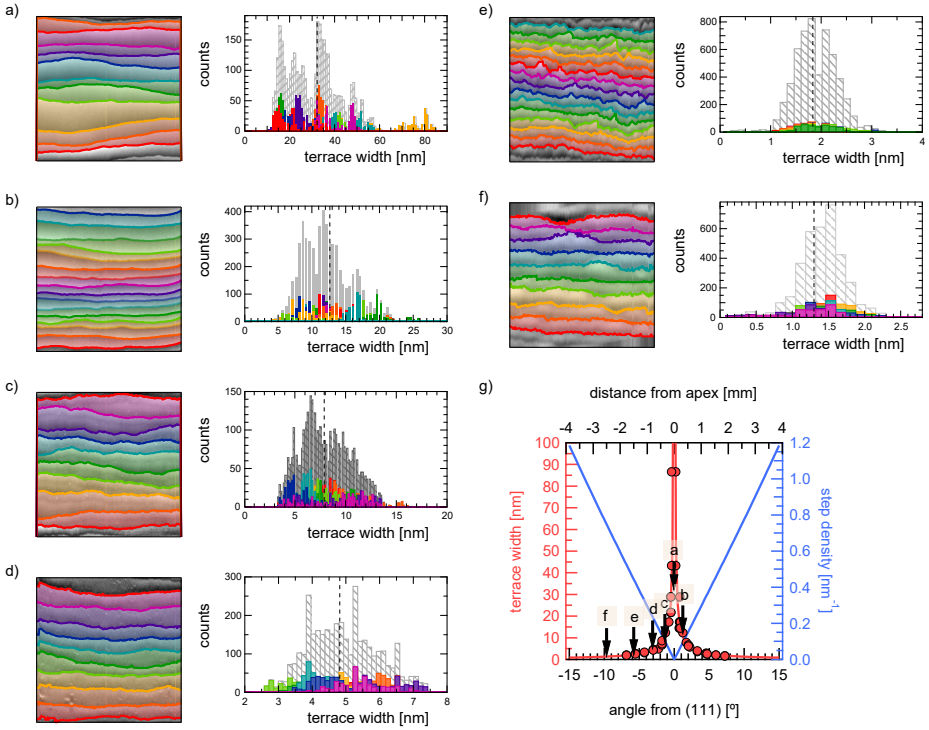

Figure 3.5: Typical STM images from various position along the crystal's curvature, and terrace width distributions for each image. Step edges determined by the analysis procedure and corresponding terraces, are overlaid in colors. The graphs on the right show terrace widths per terrace, as well as summed up (grey bars). Width of each bar in the histograms is 0.1385 nm, i.e. half integer atomic terrace widths. a) Image size: 375×375 nm; mean terrace width ($\tilde{w}$): 32.4 nm. (-0.00785 mm from apex) b) Image size: 300×300 nm; $\tilde{w}$: 12.3 nm. (+0.328 mm from apex) c) Image size: 80×80 nm; $\tilde{w}$: 7.92 nm. (-0.3446 mm from apex) d) Image size: 50×50 nm; $\tilde{w}$: 4.8 nm. (-0.8 mm from apex) e) Image size: 30×30 nm; $\tilde{w}$: 1.8 nm. (-1.5 mm from apex) f) Image size: 15×15 nm; $\tilde{w}$: 1.3 nm. (-2.5 mm from apex) g) Expected mean terrace widths and step densities versus position on the crystal. Black arrows indicate position where a) – f) were obtained.

Generally, surfaces close to the apex feature wide terraces, separated by strongly meandering step edges that may substantially deviate from the direction dictated by our curved crystal's orientation. They sometimes show local fluctuations of step densities that deviate from the expected average step density. For our analysis we can therefore only use data obtained some distance away from the apex, showing terraces in step arrays oriented in the right direction. Figure 3.5 shows typical STM images from different locations across the curved crystal, where regular step arrays were found. Figure 3.5a) shows an STM image of a step array with wide terraces. The mean terrace width ($\tilde{w}$) is 32.4 nm. The step edges as found by the Igor Pro procedure are outlined in different colors. To the right, we plot terrace width histograms per terrace (corresponding color), and the overall distribution (grey bars). The terrace width distribution is very irregular and shows several maxima and shoulders, as well as apparent gaps in the distribution. b) – f) show STM images with increasingly narrow

step arrays and the consequent distributions. They demonstrate how the distributions become first smoother (more continuous) and then more symmetric for higher step densities. Figure 3.5e) also is a good illustration of the kinked nature of the step edges.

While the analysis of individual STM images gives some qualitative insight into the behavior of little and highly stepped surfaces, individual images may not represent the average structure at this miscut angle appropriately. We therefore sum distributions obtained from several STM images with the same average terrace width to obtain histograms with 4600 – 11600 terrace widths included in the data. We normalize counts to a normalized probability. We also increase the bin size to 2 atomic sizes.

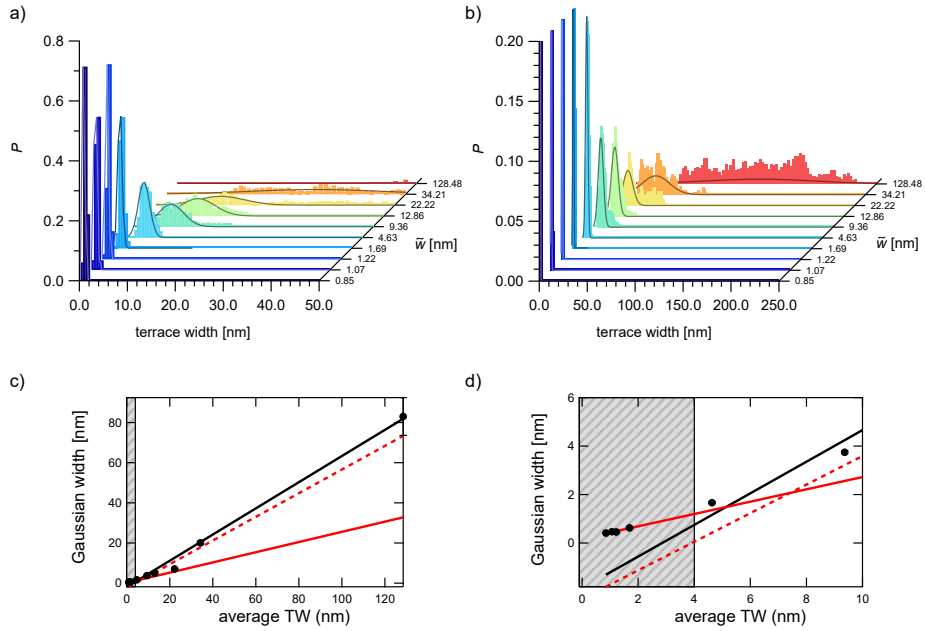

Figure 3.6: a) Normalized terrace width distributions for very narrow and increasingly wide step arrays on the curved Pt crystal with kinked step edges. The mean terrace widths $\tilde{w}$ of the distributions are noted on the right axis. For the 128.5 nm only the onset of the distribution is shown due to the x-axis being limited to 50 nm. Gaussian fits are included and give a good fit for the narrow arrays and deviate from the less symmetric distributions at higher terrace widths. b) Same as a) but showing the x-axis range is extended to 250 nm and y-axis reduced to 0.2, in order to show distributions at higher terrace widths. c) Round markers: $\tilde{w}$ parameter obtained from the Gaussian fits according to equation 3.1 versus mean terrace width of the distributions. Black line: Linear fit to all points. Red solid line: linear fit to the first 4 data points (TW < 4 nm). Red dashed line: Linear fit to the remaining 5 data points (TW > 4 nm). d) Zoom-in of Graph in c), to show data in fits in the range 0 – 10 nm.

We then obtain the distributions in figure 3.6 for statistical analysis. Figures 3.6a) and b) show the terrace width distributions used for analysis. For distributions with $\tilde{w} < 2$ nm, the distributions have a very narrow and symmetric shape. For distributions with $\tilde{w} > 4$ nm, instead of a symmetric shape, the distributions feature a steep onset before reaching their maximum and develop extensive tails. Similar tails were

observed for stepped Pt surfaces with straight steps by Walter *et al.*[47] However, for the very broad distributions, tails here seem to develop rather into a second peak, as the data from $\tilde{w} > 20$ nm demonstrates. This behavior, as discussed in regards to the individual distributions in figure 3.5, does not average out in the summed and normalised distributions here (figure 3.6b)). This indicates a inherent preference for introducing wider terraces into the regular arrays. Both LEED and STM confirm that these wider terraces are not caused by step doubling. For the widest set, it cannot be clearly distinguished what the main peak is. The distributions were fitted with a Gaussian distribution with y_0 fixed at 0:

$$f(x) = y_0 + A \cdot e^{-(\frac{x-x_0}{width})^2} \tag{3.1}$$

The resulting Gaussian fits match the distributions at small $\tilde{w}$ well. The distributions at wider terrace widths are not well described by Gaussian functions. It should be noted, that even though the wider distributions can be fitted with functions containing two or more Gaussian distributions, that the center positions of these Gaussians are unique to each distribution. In other words, no common fitting function can be defined using a set of Gaussians with fixed centers. The development of shoulders and second peaks in these distributions therefore do not indicate shared 'magic' terrace width sizes, as were found for vicinal Ag surfaces with the same kinked step-type.[22] As discussed before, Pt has no clear *sp*-surface state, making such clear quantum confinement effects unlikely.

We further analyze the Gaussian fits by plotting the *width* parameters for the fits in figures 3.6c) and d). In c), the entire range of terrace width over which we have analyzed distributions is shown, from a mean terrace width of 0.85 nm to a mean of 128.5 nm. The width parameter of the Gaussian fit increases with terrace width. A linear fit to the entire set of data (black line) agrees reasonably well and yields a slope of ~ 0.65. However, careful examination of the data in figure 3.6d) shows that the fit does not fit data below 10 nm well.

In an earlier study investigating step-step interactions on Pt surfaces with straight (A- or B-type) steps, the authors compared gaussian width to mean terrace width in a similar way as figure 3.6d).[47] There, a steeper increase of Gaussian width with terrace width was found at surfaces with a mean > 4.2 nm. This change was attributed as a transition from a regime governed by elastic interaction to a regime governed by entropic repulsion. While in the elastic regime the steps' dipoles interact with a constant strength, in the wider arrays steps behave as one-dimensional, non-interacting fermions.

The poor fit in figure 3.6d) suggests a similar behavior here. Fitting data from distributions with $\tilde{w}$<4 nm gives a trend line (solid red line) with a much smaller slope (~0.25) than the previous fit over the entire range, in line with the well-ordered step arrays and narrow terrace width distributions in this regime. This slope lies in be-

tween the ones found in the previous study for vicinal surfaces with close-packed steps in the elastic (~0.21) and entropic regime (~0.32).[47] A fit including data of 4 nm<$\tilde{w}$>40 nm (dashed red line), yield a much steeper slope (~0.59). Even though the data $\tilde{w}$>100 nm was excluded, this fit agrees well with the previous fit over the entire range (black line).

The drastic differences found here may be caused by a transition from elastic to entropic interactions dominating the step-step interactions. However, future work including more data around the terrace width of ~5 nm is required to elucidate the transition.

3.4.3. SUMMARY

In summary, while the average step density, as confirmed by LEED and STM behaves as expected across the *c*-Pt(111)[11$\bar{2}$]-31° crystal, we observe clear local fluctuations in the terrace width distributions. This fact may have to be taken into account when observing chemical reactions involving diffusion on the different surfaces. A more detailed STM study, including additional images at terrace widths around 2-10 nm and analysis of their terrace width fluctuations, may reveal insights into the underlying step-step interactions in the future.

3.5. DETERMINING THE STEP CHIRALITY[2]

While the orientation of step edges on the curved sample as confirmed by LEED generates chiral step edges as outlined in 3.2, it is not determined which side of the surface features which chirality. We use the morphology of vacancy islands on the cleaned surface to identify the chirality of the step edges.

The cleaning procedure for the curved Pt crystal as described in chapters 4 and 5 involves a sputtering step, followed by annealing in oxygen and subsequently in vacuum. The last cycle of our cleaning procedure before our STM study however consists of a modified sputter-anneal cycle to avoid high-temperature induced facetting. For the STM study, the final cleaning cycle consists of sputtering at 570 K, and annealing in vacuum at 770 K. See chapter 5 for a thorough discussion of the procedure. During STM imaging we observe that this final cleaning cycle can lead to the presence of vacancy islands that are a single atom layer deep if the annealing time was too short to completely restore the pristine surface after sputtering. These islands, as shown in figure 3.7, feature six flat edges joined by sharp inner corners. The edges follow the direction of straight A- or B-type steps on the (111) terraces. However, the six edges are not of equal lengths and instead alternate between shorter and longer segments.

[2]Parts of this section are included in: T. Roorda, S. V. Auras, and L.B.F. Juurlink. Chiral Surface Characterisation and Reactivity Toward H–D Exchange of a Curved Platinum Crystal. *Topics in Catalysis*, **59**, 1558-1568 (2020).

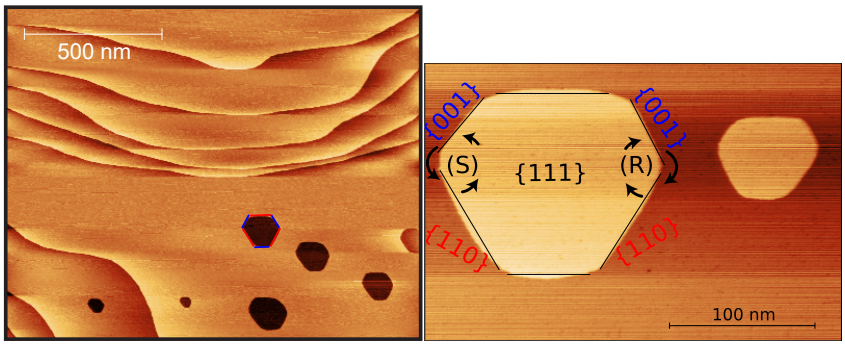

(a) (b)

Figure 3.7: STM images of the surface close to the (111), 80 μm from the approximated apex. After sputtering a short annealing step at 900 K leaves vacancy islands on the surface. Their shape is determined by the line free energies of the two straight step types on the (111) terraces. Segments corresponding to {110}(red) and {001}(blue) microfacets are marked on the vacancy in the center of the STM image.

Figure 3.7 exemplifies the vacancy islands found on the surface close to the apex. In all STM images we only find vacancy islands that are a single atomic layer deep, indicating that during our last sputter step at elevated temperature, the surface is strictly in a layer-by-layer removal regime. The subsequent, final annealing step at 773 K, is carried out at a temperature where vacancy islands on Pt(111) can assume their thermally equilibrated shape.[48] Clearly, the annealing time was not sufficient for all vacancies to be removed. The equilibrium shape can be determined as the Wulff construction of {001} and {110} facets. The length ratio between short and long edges (at equilibrium) then correlates to the line free energy of A- and B-type steps, as shown by Michely *et al.*[48] We have analysed 20 different vacancy islands at 10 locations close to the crystal's apex. The average ratio of long-to-short edge was determined as 0.65 ± 0.06. This agrees very well with the value obtained by Michely et. al at a similar annealing temperature. Since {110}/B-type steps are energetically favored,[49] we can identify the longer step edges as B-type steps and shorter edges as A-type steps.

All of the many vacancy islands appearing in our STM images have the same relative orientation. In combination with the identification of step types forming these islands, we can determine the chirality of stepped surfaces on either side of the crystal. First, we identify the chirality of the corners inside the vacancy islands. We then realize that the left side of a vacancy island reflects the steps on the right side of the curved crystal and vice versa. In figure 3.7, the short edges are marked, in blue, with {001} and the long edge with {110}, in red. We notice that the right corner of the vacancy island, which steps down towards the left, has a clockwise rotational chirality, denoted (*R*). Vice versa, in the left corner we observe a counter-clockwise chirality denoted by (*S*), stepping down towards the right of the crystal. The inherent vacancy defects near the (111) apex of our crystal thus enables us to determine the chirality of the crystal's sides, opening the possibility for controlled chiral adsorption

and reactivity experiments.

3.6. STRUCTURE OF THE KINKED STEP EDGES

3.6.1. MICROSCOPIC RECONSTRUCTIONS ALONG THE KINKED STEP

Figure 3.4 shows the kinked step edges in their fully-kinked form as obtained by the ideal bulk determination. However, the step edge may reconstruct into longer segments with a lower kink density while maintaining its overall orientation, as illustrated in figure 3.8. All possible configurations along this directions are described as energetically equivalent in the Ising model, which describes surfaces in terms of nearest-neighbor interactions.[44] Moreover, the process of reconstruction within a step edge may be influenced by the prevailing step-step interactions between steps, as well as the line free-energies of the microfacets that form the segments in between kinks.

In the limit of complete reconstruction, the entire step could facet into A- and B-type steps separated by a very low density of kink sites. In the two extreme cases, fully-kinked and fully-reconstructed step edges, very different physical and chemical properties may be expected. It is therefore necessary to analyze the structure of the kinked vicinal surfaces along the crystal's curvature before drawing conclusions about the experimentally observed results.

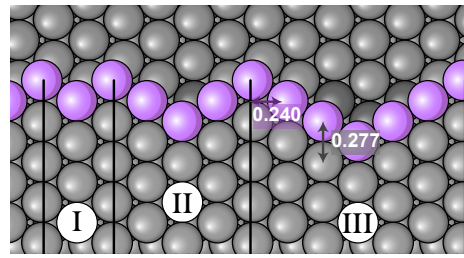

Figure 3.8: The fully-kinked step edge can reconstruct into longer facets while maintaining its overall orientation. I, II, and III show segments with one, two, and three atom wide {001} and {110} microfacets. The distance between atom rows, i.e the atomic spacing along the step edge, is indicated with the purple arrow and is 0.240 nm for Pt. The distance between atoms within a row, indicated by the grey arrow, is the nearest neighbour spacing, 0.277 nm for Pt.

3.6.2. STATISTICAL ANALYSIS OF THE KINKED STEP STRUCTURE

For a suitable set of STM images, where 1 px <1 atom=0.24 nm along the step, we analyse the size of microfacet segments along the step edge. We find the outline of the step with the same procedure as described above. Figure 3.9a) illustrates this. We then determine individual segments by following the step edge (in figure a) along the

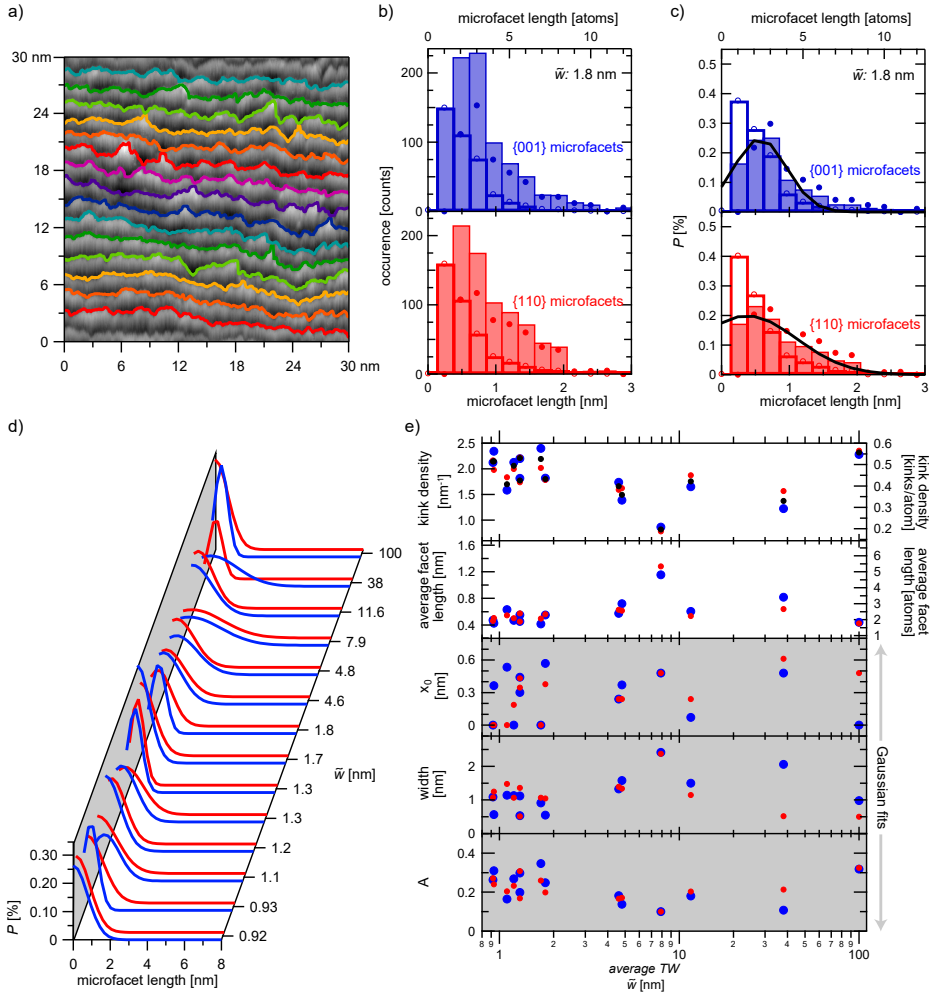

Figure 3.9: a) Example of an STM image (10×10 nm) used for the analysis of corrugation along the kinked step edges. Step edges as found by the Igor Pro procedure are marked in colour. As expected, a high density of kinks separates short segments with varying lengths. b) Distribution of segment lengths along all step edges marked in a), separated for {001} (blue) and {110} (red) facets. Each bin represents an additional atom along the segment length. Bars with thick outlines represent the absolute *number of segments* with a specific length. Filled bars represent the absolute *number of atoms* found in segments of a specific length. Empty circles indicate the cumulative number of (inner and outer) kinks found in segments of each length, filled circles indicate the number of atoms that are not directly at a kink site. c) Normalized distributions of segments, atoms, kink sites, and non-kink atoms in the image. d) Gaussian fits of the normalized distributions of atoms (filled bars in c) in segments of different lengths, for several images along the curvature of the crystal, with average terrace widths $\bar{w}$ ranging from <1 nm to >100 nm. Separate fits were carried out for distributions of {001} (blue) and {110} (red) microfacets. The complete set of distributions included in the analysis can be found in Appendix A. Details of the fitting protocol are explained in the main text. e) Top: kink densities and average facet lengths of the kinked step edges as derived directly from the distribution. (Blue and red markers represent kink densities/ facet lengths in {001} and {110} distributions respectively, black in the entire step.) Bottom: Variable fit parameters of Gaussian fits. While some variation of the parameters is obvious, no clear variation with terrace width or microfacet type is found.

horizontal direction) until its vertical direction (going "up" or "down") reverses for l>0.24 nm. As we have previously determined the step chirality at the two sides of the crystal, we can allocate which segments are {001} and {110} microfacets. We subsequently obtain distributions of microfacet lengths for each type per image in bins of 1 atom row spacing, see figure 3.9b). There, the first bin represents segments with one atom width, i.e. only inner and outer kinks, the second bin contains two atom wide segments, i.e. inner and outer kink atoms separated by one additional atom, etc. Therefore, we can also determine the total number of atoms that can be found in segments of each type, per image. In figure 3.9b), the empty bars with a thick outline show the number of segments of each type. Filled bars with a thin outline give the total number of atoms in segments of each type. Similarly, we can plot the total number of (inner and outer) kink atoms found in segments of each type (empty circles in the figure), and the total number of atoms that are not directly at the kink site (filled circles). For all analyzed images (see also Appendix A) we find the largest number of atoms within the first three bins, i.e. short segments are preferred. This can be explained by simple statistics, where larger deviations from the fully-kinked case have decreasing statistical weight.[44] The distributions in b) make it possible to obtain kink densities and average segment lengths for both types of microfacets. We find these values for kinked step edges in arrays ranging from average terrace widths $\tilde{w}$<1 nm to $\tilde{w}$>100 nm. While there is some variation in the kink densities found in different images, no clear trend is observed. Kink density values, displayed in figure 3.9e) lie consistently in between 1.5 and 2.5 nm^{-1}, corresponding to on average 1.7 - 2.8 atom wide segments along the kinked step edge. For a vicinal Ag surface with $\tilde{w}$ = 1.13 nm, an average length of kinked segments of 2 - 3 atoms has recently observed.[22]

It may be argued that kink densities at step arrays with $\tilde{w}$<2 nm are slightly elevated compared to arrays of larger terrace widths. However, this may also be a consequence of image sizes and consequent resolution at broader terraces; typically images at lower step densities need to be larger to show arrays of multiple steps. An exception to this is the data at $\tilde{w}$>100 nm. There, the mean terrace width was determined from large image that included multiple steps, whereas the kink density distributions were determined from a zoom-in on a single step to achieve the required resolution. The step-step interactions in the arrays of varying step densities thus do not appear to significantly influence the faceting of the kinked step edges.

The overall orientation of the kinked step dictates equal average kink densities for the {001} and {110}-type segments. This is confirmed in figure 3.9e), where kink densities of {001} (blue) and {110} (red) segments are similar for all images. Neither segment type has consistently lower kink densities than the other.

The difference in line free energies, however, may cause different distributions of the

two types. As the number of steps and atoms per image will depend on its size and local step density on the curved crystal, we normalize the distributions (of segments, atoms, kink atoms, non-kink atoms) individually, as demonstrated in figure 3.9c). We then fit the distributions of atoms (filled bars in figures b) and c)) with a Gaussian (see equation 3.1), where $y_0 = 0$ and x_0 is fixed to the x-value of the maximum of the distribution. Distributions for {001} and {110} segments are fitted separately for each analyzed image. All resulting Gaussian fits are displayed in figure 3.9d). Again, some fluctuations are observed, but no clear trend in the width of the Gaussian fits for different microfacet types, nor consistent changes with terrace width $\tilde{w}$. The fitting parameters as plotted in figure 3.9e), reflect this. We attribute variations in the fits to the limited amount of data available to the distributions (about 90 - 600 per distribution), resulting from the image size and steps in each image. We expect these distributions to become even more uniform if more images at the same $\tilde{w}$ would be analyzed.

The line-free energy of longer segments, which varies for A- and B-type steps does not appear to significantly influence the structure of the kinked step edges. This suggests a larger influence of the kink energy, as well as entropy.

3.6.3. SUMMARY

Detailed analysis of the {210} step edges allows us to atomically resolve the roughening of the step edge into segments of variable length. Only a fraction of the atoms along the kinked step edges are in fully-kinked, one atom wide, segments. However, reconstructions into very large segments that may behave as A-or B-type steps are statistically not favored. Furthermore, the different atomic arrangements of {001} or {110}-oriented segments do not lead to different distributions. Across the *c*-Pt(111)[11$\bar{2}$]-31° crystal, no consistent changes of kink densities or distributions of segment length with average terrace width are observed. We thus conclude that the atomic structure of the kinked step edges is similar for all surface structures contained on the crystal.

REFERENCES

[1] J. Wintterlin, S. Völkening, T. V. Janssens, T. Zambelli, and G. Ertl. Atomic and macroscopic reaction rates of a surface-catalyzed reaction. *Science*, 278(5345):1931–1934, 1997.

[2] H. Ueta and M. Kurahashi. Steric effect in CO oxidation on Pt(111). *Journal of Chemical Physics*, 147(19), 2017.

[3] H. J. Freund, G. Meijer, M. Scheffler, R. Schlögl, and M. Wolf. CO oxidation as a

prototypical reaction for heterogeneous processes. *Angewandte Chemie - International Edition*, 50(43):10064–10094, 2011.

[4] D. L. Bashlakov, L. B. Juurlink, M. T. Koper, and A. I. Yanson. Subsurface oxygen on Pt(111) and its reactivity for CO oxidation. *Catalysis Letters*, 142(1):1–6, 2012.

[5] G. J. Kroes and C. Díaz. Quantum and classical dynamics of reactive scattering of H_2 from metal surfaces. *Chemical Society Reviews*, 45(13):3658–3700, 2016.

[6] M. K. Sabbe, M. F. Reyniers, and K. Reuter. First-principles kinetic modeling in heterogeneous catalysis: An industrial perspective on best-practice, gaps and needs. *Catalysis Science and Technology*, 2(10):2010–2024, 2012.

[7] J. Neugebohren, D. Borodin, H. W. Hahn, J. Altschäffel, A. Kandratsenka, D. J. Auerbach, C. T. Campbell, D. Schwarzer, D. J. Harding, A. M. Wodtke, and T. N. Kitsopoulos. Velocity-resolved kinetics of site-specific carbon monoxide oxidation on platinum surfaces. *Nature*, 558(7709):280–283, 2018.

[8] L. Zhou, A. Kandratsenka, C. T. Campbell, A. M. Wodtke, and H. Guo. Origin of Thermal and Hyperthermal CO_2 from CO Oxidation on Pt Surfaces: The Role of Post-Transition-State Dynamics, Active Sites, and Chemisorbed CO2 . *Angewandte Chemie*, 131(21):6990–6994, 2019.

[9] A. Gutiérrez-González, M. E. Torio, H. F. Busnengo, and R. D. Beck. Site Selective Detection of Methane Dissociation on Stepped Pt Surfaces. *Topics in Catalysis*, 62(12-16):859–873, 2019.

[10] H. Chadwick, A. Gutiérrez-González, D. Migliorini, R. D. Beck, and G. J. Kroes. Incident Angle Dependence of CHD_3 Dissociation on the Stepped Pt(211) Surface. *Journal of Physical Chemistry C*, 122(34):19652–19660, 2018.

[11] H. Chadwick, A. Gutiérrez-González, R. D. Beck, and G. J. Kroes. Transferability of the SRP32-vdW specific reaction parameter functional to CHD_3 dissociation on Pt(110)-(2 × 1). *Journal of Chemical Physics*, 150(12), 2019.

[12] F. Garcia-Martinez, C. García-Fernández, J. P. Simonovis, A. Hunt, A. Walter, I. Waluyo, F. Bertram, L. R. Merte, M. Shipilin, S. Pfaff, S. Blomberg, J. Zetterberg, J. Gustafson, E. Lundgren, D. Sánchez-Portal, F. Schiller, and J. E. Ortega. Catalytic Oxidation of CO on a Curved Pt(111) Surface: Simultaneous Ignition at All Facets through a Transient CO-O Complex. *Angewandte Chemie - International Edition*, 2020.

[13] R. Van Lent, S. V. Auras, K. Cao, A. J. Walsh, M. A. Gleeson, and L. B. Juurlink. Site-specific reactivity of molecules with surface defects—the case of H_2 dissociation on Pt. *Science*, 363(6423):155–157, 2019.

[14] S. V. Auras, R. van Lent, D. Bashlakov, J. M. Piñeiros Bastidas, T. Roorda, R. Spierenburg, and L. B. Juurlink. Scaling Platinum-Catalyzed Hydrogen Dissociation on Corrugated Surfaces. *Angewandte Chemie - International Edition*, 2020.

[15] C. J. Bondue, F. Calle-Vallejo, M. C. Figueiredo, and M. T. Koper. Structural principles to steer the selectivity of the electrocatalytic reduction of aliphatic ketones on platinum. *Nature Catalysis*, 2(3):243–250, 2019.

[16] I. T. McCrum, X. Chen, K. A. Schwarz, M. J. Janik, and M. T. Koper. Effect of Step Density and Orientation on the Apparent pH Dependence of Hydrogen and Hydroxide Adsorption on Stepped Platinum Surfaces. *Journal of Physical Chemistry C*, 122(29):16756–16764, 2018.

[17] K. Honkala, A. Hellman, I. N. Remediakis, A. Logadottir, A. Carlsson, S. Dahl, C. H. Christensen, and J. K. Nørskov. Ammonia Synthesis from First-Principles Calculations. *Science*, 307(5709):555–558, 2005.

[18] G. Sun and P. Sautet. Metastable Structures in Cluster Catalysis from First-Principles: Structural Ensemble in Reaction Conditions and Metastability Triggered Reactivity. *Journal of the American Chemical Society*, 140(8):2812–2820, 2018.

[19] G. Sun, A. N. Alexandrova, and P. Sautet. Pt8 cluster on alumina under a pressure of hydrogen: Support-dependent reconstruction from first-principles global optimization. *Journal of Chemical Physics*, 151(19), 2019.

[20] H. Chadwick, A. Gutiérrez-González, R. D. Beck, and G. J. Kroes. CHD3 Dissociation on the Kinked Pt(210) Surface: A Comparison of Experiment and Theory. *Journal of Physical Chemistry C*, 123(23):14530–14539, 2019.

[21] S. M. Davis and G. A. Somorjai. The effect of surface oxygen on hydrocarbon reactions catalyzed by platinum crystal surfaces with variable kink concentrations. *Surface Science*, 91(1):73–91, 1980.

[22] J. E. Ortega, G. Vasseur, I. Piquero-Zulaica, S. Matencio, M. A. Valbuena, J. E. Rault, F. Schiller, M. Corso, A. Mugarza, and J. Lobo-Checa. Structure and electronic states of vicinal Ag(111) surfaces with densely kinked steps. *New Journal of Physics*, 20(7), 2018.

[23] M. Giesen and S. Dieluweit. Step dynamics and step-step interactions on the chiral Cu(5 8 90) surface. *Journal of Molecular Catalysis A: Chemical*, 216(2):263–272, 2004.

[24] J. Frohn, M. Giesen, M. Poensgen, J. F. Wolf, and H. Ibach. Attractive interaction between steps. *Physical Review Letters*, 67(25):3543–3546, 1991.

[25] N. C. Bartelt, T. L. Einstein, and E. D. Williams. The influence of step-step interactions on step wandering. *Surface Science*, 240:L591–L598, 1990.

[26] J. L. Gland, M. R. McClellan, and F. R. McFeely. Carbon monoxide oxidation on the kinked Pt(321) surface. *The Journal of Chemical Physics*, 79(12):6349–6356, 1983.

[27] A. D. Smeltz, W. N. Delgass, and F. H. Ribeiro. Oxidation of NO with O_2 on Pt(111) and Pt(321) large single crystals. *Langmuir*, 26(21):16578–16588, 2010.

[28] A. J. Gellman, J. D. Horvath, and M. T. Buelow. Chiral single crystal surface chemistry. *Journal of Molecular Catalysis A: Chemical*, 167(1-2):3–11, 2001.

[29] A. J. Gellman, Y. Huang, A. J. Koritnik, and J. D. Horvath. Structure-sensitive enantiospecific adsorption on naturally chiral Cu(hkl)$^{R\&S}$ surfaces. *Journal of Physics Condensed Matter*, 29(3), 2017.

[30] J. D. Horvath and A. J. Gellman. Enantiospecific desorption of chiral compounds from chiral Cu(643) and achiral Cu(111) surfaces. *Journal of the American Chemical Society*, 124(10):2384–2392, 2002.

[31] J. D. Horvath, A. Koritnik, P. Kamakoti, D. S. Sholl, and A. J. Gellman. Enantioselective separation on a naturally chiral surface. *Journal of the American Chemical Society*, 126(45):14988–14994, 2004.

[32] Y. Yun and A. J. Gellman. Enantioselective separation on naturally chiral metal surfaces: D,L-aspartic acid on Cu(3,1,17)$^{R\&S}$ surfaces. *Angewandte Chemie - International Edition*, 52(12):3394–3397, 2013.

[33] D. S. Wei, B. S. Mhatre, A. J. Gellman, and D. S. Sholl. Contributions of dispersion forces to R-3-methylcyclohexanone physisorption on low and high Miller index Cu surfaces. *Surface Science*, 629:35–40, 2014.

[34] Y. Yun and A. J. Gellman. Enantiospecific Adsorption of Amino Acids on Naturally Chiral Cu{3,1,17}$^{R\&S}$ Surfaces. *Langmuir*, 31(22):6055–6063, 2015.

[35] A. D. Reinicker, A. J. Therrien, T. J. Lawton, R. Ali, E. C. Sykes, and A. J. Gellman. Influence of step faceting on the enantiospecific decomposition of aspartic acid on chiral Cu surfaces vicinal to Cu{111}. *Chemical Communications*, 52(75):11263–11266, 2016.

[36] D. M. Rampulla, A. J. Francis, K. S. Knight, and A. J. Gellman. Enantioselective surface chemistry of R-2-bromobutane on Cu(643)$^{R\&S}$ and Cu(531)$^{R\&S}$. *Journal of Physical Chemistry B*, 110(21):10411–10420, 2006.

[37] D. S. Sholl. Adsorption of chiral hydrocarbons on chiral platinum surfaces. *Langmuir*, 14(4):862–867, 1998.

[38] T. D. Power, A. Asthagiri, and D. S. Sholl. Atomically detailed models of the effect of thermal roughening on the enantiospecificity of naturally chiral platinum surfaces. *Langmuir*, 18(9):3737–3748, 2002.

[39] D. S. Sholl, A. Asthagiri, and T. D. Power. Naturally chiral metal surfaces as enantiospecific adsorbents. *Journal of Physical Chemistry B*, 105(21):4771–4782, 2002.

[40] G. A. Attard. Electrochemical studies of enantioselectivity at chiral metal surfaces. *Journal of Physical Chemistry B*, 105(16):3158–3167, 2001.

[41] A. Ahmadi, G. Attard, J. Feliu, and A. Rodes. Surface reactivity at 'chiral' platinum surfaces. *Langmuir*, 15(7):2420–2424, 1999.

[42] G. A. Attard, A. Ahmadi, J. Feliu, A. Rodes, E. Herrero, S. Blais, and G. Jerkiewicz. Temperature effects in the enantiomeric electro-oxidation of D- and L-glucose on Pt{643}^{S}. *Journal of Physical Chemistry B*, 103(9):1381–1385, 1999.

[43] P. W. Palmberg, G. Riach, R. Weber, and N. MacDonald. *Handbook of Auger Electron Spectroscopy*. Physical Electronics Industries Inc., Edina, 1 edition, 1972.

[44] H. Ibach. *Physics of surfaces and interfaces*. 2006.

[45] P. Roos, E. Bertel, and K. D. Rendulic. Observation of an sp-derived surface resonance on Pt(111) indicating the crucial role of surface states in physisorption. *Chemical Physics Letters*, 232(5-6):537–541, 1995.

[46] G. Fischer and H. Hoffman. Oscillations of the electrical conductivity with film thickness in very thin platinum films. *Solid State Communications*, 35(10):793–796, 1980.

[47] A. L. Walter, F. Schiller, M. Corso, L. R. Merte, F. Bertram, J. Lobo-Checa, M. Shipilin, J. Gustafson, E. Lundgren, A. X. Brión-Ríos, P. Cabrera-Sanfelix, D. Sánchez-Portal, and J. E. Ortega. X-ray photoemission analysis of clean and carbon monoxide-chemisorbed platinum(111) stepped surfaces using a curved crystal. *Nature Communications*, 6:1–7, 2015.

[48] T. Michely and G. Comsa. Temperature dependence of the sputtering morphology of Pt(111). *Surface Science*, 256(3):217–226, 1991.

[49] A. M. Lahee, J. R. Manson, J. P. Toennies, and C. Wöll. Observation of Interference Oscillations in Helium Scattering from Single Surface Defects. *Physical Review Letters*, 57(18):2331–2331, 1986.

4

SCALING PT-CATALYZED HYDROGEN DISSOCIATION ON CORRUGATED SURFACES

Dissociative adsorption of hydrogen is central to the development of approaches that predict gas-surface reactions. Here, we determine absolute reactivities for dissociation at low coordinated Pt sites. Two curved Pt(111) single crystal surfaces allow us to probe either straight or highly kinked step edges with molecules impinging at a low impact energy. A simple model extracts the average reactivity of inner and outer kink atoms, which is compared to the reactivity of straight A- and B-type steps. We show that local surface coordination numbers do not adequately capture reactivity trends for H_2 dissociation. Instead, we utilize the increase of reactivity with step density to determine the area on the surface over which a step causes increased dissociation. This step-type specific reactive area extends beyond the step edge onto the (111) terrace. It defines the reaction cross-section for H_2 dissociation at the step, bypassing assumptions about the contributions of individual types of surface atoms. Our results stress the non-local nature of the interaction of molecular hydrogen with a surface and provide insight into reactivity differences for nearly identical step sites.

This chapter is based on the following publication:
S. V. Auras, R. van Lent, D. Bashlakov, J. M. Piñeiros Bastidas, T. Roorda, R. Spierenburg, and L. B. F. Juurlink. Scaling platinum-catalyzed hydrogen dissociation on corrugated surfaces. *Angewandte Chemie International Edition*, **59** 20973–20979 (2020).

4.1. INTRODUCTION

FOR GAS-PHASE REACTIONS INVOLVING THE SMALLEST OF MOLECULES, H_2, accurate theoretical descriptions are nowadays available and match experimental results.[1] However, the same remains challenging for gas-surface reactions.[2] The involvement of many atoms in the surface complicates the description of, a.o., energy dissipation mechanisms. The chemically accurate prediction of reactivity for the highly activated H_2 dissociation on Cu(111), using quantum dynamics calculations and density functional theory (DFT)-based potentials, is exceptional.[3] In other cases, simplifications in the description of the system are needed to lower the computational effort, and show continuing advancements. A relevant example is the successful application of quasi-classical trajectory calculations for the more reactive H_2 dissociation on Pt(111).[4]

Reactions on high-Miller index surfaces, such as regularly stepped surfaces, have often been claimed to be more relevant to real-world chemistry, e.g. heterogeneous catalysis. Such vicinal surfaces contain lower coordinated surface atoms, e.g. forming steps in terraces and kinks in steps, which resemble edges and corners on actual catalyst particles. Accurate calculations based on periodic potentials then require larger unit cells, hence much higher computational effort. The chemically accurate description of H_2 dissociation on Cu(211) is the state of the art.[5] The dissociation of a larger molecule, methane, can be described with chemical accuracy by *ab initio* molecular dynamics on select Pt surfaces, but the same approach does not describe reaction on a kinked surface to the same accuracy.[6–8]

The computational effort required to accurately describe the simplest dissociative event on well-defined surface structures highlights the challenges to constructing an accurate kinetic description for heterogeneous catalysis. Different methods are necessary in order to consider all surface sites available on a catalyst particle simultaneously. A recent addition to various approaches (see ref [9] for a thorough discussion) is the idea that one may generalize the reactivity dependence of surface sites on their coordination number.[10–12] Coordination numbers are commonly used in organic and inorganic chemistry. Consequently, it can seem intuitively logical to apply it to gas-surface interactions. To capture different surface geometries of nearly identical surface sites, a 'generalized coordination number', $\overline{CN}$, was introduced. It includes the coordination shell of all atoms neighboring the surface atom involved in the dissociation event. This concept was successfully applied in a study of bond energies of H- and O-containing adsorbates on Pt particles. The authors suggested it to be a predictive descriptor linking geometric arrangement of a surface to adsorption properties. As $\overline{CN}$ can simply be calculated by hand, it does not require electronic structure calculations.

Surface coordination approaches shift the focus in our chemical thinking about bond

breaking from the impinging molecule probing a surface potential, towards the local properties of the site of reaction. While for many systems, this may be acceptable and appropriate, we wonder whether it applies to the dissociative adsorption of H_2. First, the two types of straight step edges occurring on (111) facets of *fcc* metals, e.g. Pt or Ni, provide the same coordination numbers at the upper step edge, but are found to be chemically unique in desorption of H_2 (see e.g. refs [13, 14]). Second, the quantum dynamical nature of the molecule may allow it to probe the surrounding potential energy surface (PES) bypassing the highly localized nature of the collision as imposed by a coordination number approach. Dynamical calculations for H_2 interaction with Pt(211) by Baerends and coworkers suggested this: At low collisional energy, dissociation predominantly occurs via a dynamical chemisorbed molecular state that dissociates barrier-free at the upper edge of a step even though its center of mass impinged at the inner cusp.[15, 16]

Recent advances in the use of curved surfaces of single crystal samples allow us to critically evaluate the relation between dissociative reaction dynamics and the structure of the surface.[17, 18] Here, we use two Pt curved single crystals exposing surface atoms with various coordination numbers and local surface geometries to determine whether the dissociation of molecular hydrogen on platinum follows trends predicted by coordination number approaches. We experimentally determine the dissociation probability for molecular hydrogen along the curvatures and relate the absolute reactivity to the local structure of steps and kinks.

4.2. EXPERIMENTAL

Our apparatus and curved single crystals have been described before.[17] We impinge hydrogen from a supersonic molecular beam onto the curved surfaces of our Pt crystals. We use D_2 in the beam, as dissociation shows no isotope effect[19] and we obtain better signal-to-noise than using H_2. The King-and-Wells method is used to determine the initial sticking probability, S_0.[20] The kinetic energy of our Ar anti-seeded beam is determined to be 9.3 meV by time-of-flight (TOF) techniques. The corresponds to a de Broglie-wavelength of λ_{dB} = 0.148 nm. The final orifice defining our double-differentially pumped supersonic beam is rectangular. It produces a footprint for the beam of 0.126 mm x 6.0 mm on our curved crystals, minimizing convolution of step density variations along the curved surfaces. We move the curved crystal relative to the rectangular molecular beam to determine S_0 on different parts, characterized by different step densities, of the curved surface.

The crystals are cleaned by repeated cycles of sputtering (Ar^+, 1 keV, 1.3 μA, 5 min), annealing in O_2 ($3{\cdot}10^{-8}$ mbar, 900 K, 3 min) and annealing in vacuum (1200 K, 3 min). To avoid faceting, the last cycle before experiments consists of sputtering at elevated temperature (900 K) followed by annealing in vacuum (900 K).

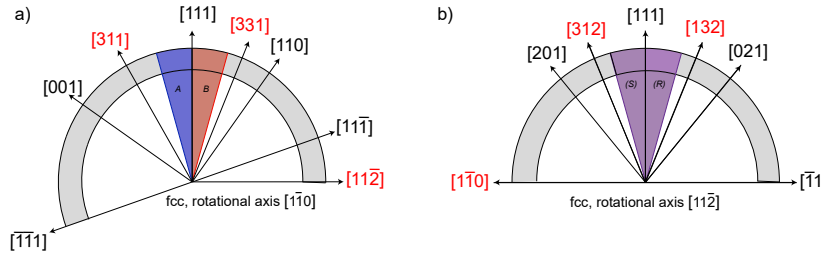

Figure 4.1: The two curved Pt crystals used in this chapter can be seen as slices from two cylinders with perpendicular rotational axes, [1$\bar{1}$0] and [11$\bar{2}$]. Both curved crystals expose the (111) surface at the apex. a) The *c*-Pt(111)[1$\bar{1}$0]-31° crystal curved towards the (001) and (110) planes. Steps therefore form {001} (A-type) or {110} (B-type) microfacets. b) The *c*-Pt(111)[1$\bar{1}$0]-31° crystal curves towards the (201) and (021) planes and exposes {210} microfacets as steps. Vicinal surfaces on the two sides of the crystal are chiral to each other.

4

4.3. RESULTS AND DISCUSSION

We impinge D_2 from a molecular beam onto the curved surfaces of two Pt crystals to determine the initial sticking probability (S_0). As D_2 chemisorbs dissociatively at the applied surface temperature of 155 K, sticking probabilities correspond to dissociation probabilities. The schematics of the curved samples and the relative size of the beam impinging on the surface with a rectangular profile are shown in figure 4.2a). Both Pt crystals contain the (111) surface at their apex and curve 15.5° degrees to either side. Figure 4.1 represents the two sample as cylindrical slices to illustrate their crystallographic orientation. The macroscopic curvature of the Pt crystals results from the introduction of a single step type with smoothly increasing density when moving toward the crystal's edges. The supersonic beam always impinges normal to the (111) terraces.

The two curved surfaces contain three different step structures. On the crystal with a [1$\bar{1}$0] rotational axis, (001)-oriented (or "A-type") steps and (110)-oriented (or "B-type") steps occur separately on the two sides of the apex. The second crystal has its rotational axis oriented along [11$\bar{2}$], exhibiting facets of the (201) and (021) planes, forming kinked steps. As their direction lies halfway in between A- and B-type steps, the kinked steps consist of short, alternating sections of A- and B-steps connected by inner and outer kinks. The kinked steps give rise to chiral stepped surfaces with opposite handedness on the two sides of the crystal. The chirality is not expected to impact reactivity for the achiral H_2. We therefore refer to the kinked steps on either side of the crystal as {210}-oriented steps.[1] Figure 4.2b) sketches A, B and kinked step structures in their ideal form. Note that we show the fully kinked step facets for the {210} case.

Figure 4.2c) plots S_0 of D_2 as a function of step density for an average kinetic energy of

[1] We use Miller indices {hkl} to indicate the set of equivalent surfaces.

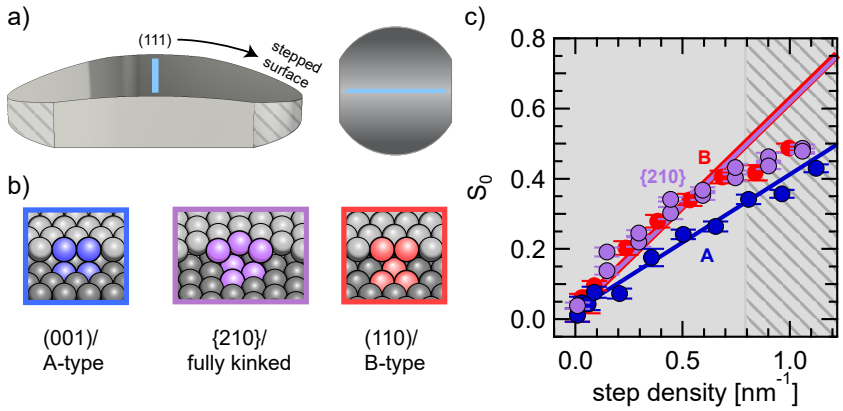

Figure 4.2: a) Schematic side and top view of the curved crystals and the hydrogen beam impinging onto a 0.126 nm wide section of the surface (light blue line). At the sides, the width of the crystal narrows as indicated by the hashed areas. b) Structures of the three step types found on the two curved crystals. For the kinked step edges, we display the fully-kinked form. c) Sticking probabilities S_0 of D_2 as a function of step density for the two different Pt surfaces at E_{kin} = 9.3 meV and $T_{surface}$ = 155 K. Colored markers indicate sticking on (111) surfaces with A-type (blue), B-type (red), and highly kinked steps (purple). The hashed part of the plot indicates the area where the crystals are narrower than the impinging molecular beam. Blue, red and purple lines are linear fits to the data. See text for details.

9.3 meV. The hatched area indicates where the crystal surface becomes more narrow than the beam due to the shape of our samples. The data are averages of multiple measurements on the same location of a curved surface. Error bars reflect one standard deviation of the average value. For the crystal with kinked steps, data from both sides of the crystal are included, but do not vary appreciably. At the (111) apices of the two crystals we measure an $S_0{}^{(111)}$ of 0.011±0.018 and 0.032±0.013 respectively, in good agreement with previous studies on flat Pt(111) surfaces for similar collision energies.[19, 21, 22] To the sides of the crystals, S_0 increases linearly with step density for all step types over the range where the molecular beam fits onto the crystal's surface. Scalability of the reactivity of stepped surfaces was previously suggested for A-type steps.[15]. Here S_0 can be described for all stepped surfaces as

$$S_0(SD) = S_0^{(111)} + \Sigma_0 \cdot SD \tag{4.1}$$

where SD is the step density and Σ_0 the rate of increasing S_0 with step density (i.e. the slope). Σ_0 quantifies the reactivity of the step type at the incident energy used here.[2] We apply linear fits to the data with appropriate weighting to compare Σ_0 for these step types. Here, we exclude data from the hatched area and fix $S_0^{(111)}$ at the average of the two values determined for (111) on the two separate single crystals, i.e. 0.025. For the crystal with kinked steps, we use data of both sides in a single fit. The resulting linear fits are displayed with colors matching the data. The extracted values for Σ_0 are listed in table 4.1. While Σ_0 for B-type and {210} steps are almost equal, i.e. ~ 0.6 nm,

[2] See Supplementary Information for a detailed discussion on the relation of Σ_0 and the sticking probabilities at steps S_0^{step}.

step type	coordination (upper edge)		Σ_0 / nm	a / nm	σ_0 / nm^2
	CN	$\overline{CN}$			
A / (001)	7	5.50	0.387	0.277	0.107
B / (110)	7	5.50	0.597	0.277	0.165
real kinked / {210}			0.593	0.48	0.285
fully kinked (max)	8^* / 6^+	6.17^* / 4.83^+	0.726	0.48	0.348

Table 4.1: Step types and their coordination (*CN*) and generalized coordination numbers ($\overline{CN}$) at the upper step edge. For the kinked step coordination numbers for the inner (*) and outer (+) kinks are listed. Rates of increasing sticking with step density (Σ_0) are determined by linear fits of the S_0 data in figure 4.2 for the first three rows. The value of Σ_0 in the bottom row is derived from equation 4.4. Multiplying Σ_0 with unit cells widths of the stepped surfaces (*a*) gives the resulting reaction cross sections (σ_0) of the three types of steps. Note that the unit cell width is considerably larger for the kinked step.

the A-type steps show a significantly smaller increase in reactivity with step density, i.e. ~ 0.4 nm.

While it is sometimes assumed that kinks would be more reactive than straight step edges, which in turn would be more reactive than flat terraces, our data at first glance does not represent this trend. However, the Σ_0 value we obtain for the {210} steps here does not necessarily reflect dissociation at ideal fully-kinked step. The kinked steps present on the surface may differ from the representation provided in figure 4.2a). The surface can maintain its overall crystallographic orientation while breaking the fully kinked step into larger segments (or microfacets) of A- and B-type steps, as observed for kinked Ag steps.[23] Figure 4.3a) illustrates two slightly longer segments. The number of kink sites is reduced from the fully kinked edge (section a) by introducing either 1 atom (section b) or 2 atoms (section c) in between kinks. Increasing the segment lengths decreases the kink density. In order to better understand the observed reactivity trend, we hereinafter determine the structural composition of the {210} steps using STM and apply a model that deconvolutes the contribution of inner and outer kinks.

Typical STM images with step arrays ranging from a step density of 0.086 nm^{-1} to 0.909 nm^{-1} are shown in figure 4.3b) – e). We determine the outline of the step (shown as colored lines) by taking line profiles and determining the local height gradient. We then determined the length of all segments separated by inner and outer kinks along the step edge. This process is repeated for multiple steps in the image. Histograms on the right side of figure 4.3 are normalized to represent the average percentage of segments with a length of one, two, three, etc. atoms. They are shown separately for both A- (blue) and B-type (red) microfacets. Each consecutive bin in the histograms represents a microfacet of one additional atom length. The lettering of the bins corresponds to the sections indicated in figure 4.3a).

The histograms in figure 4.3 show that approximately half of the segments forming

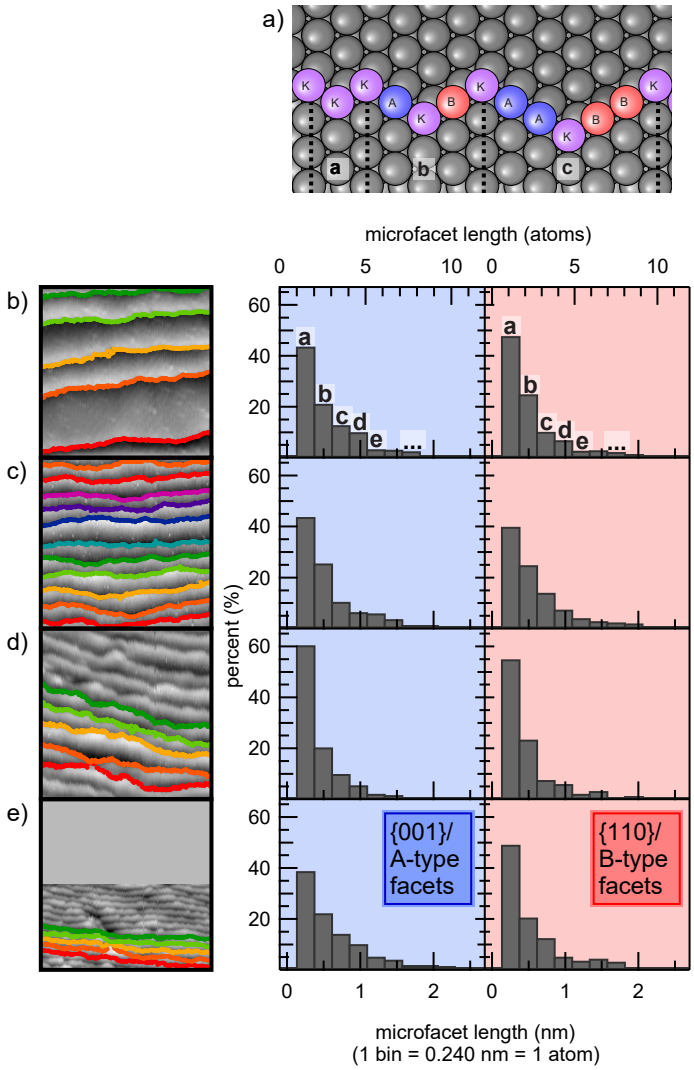

Figure 4.3: a) Kinked step edge with different widths of its {001}- and {110}-oriented segments. In a, segments are only one atom wide. Each atom is either at an inner or an outer kink site (purple). In b, two atom wide segments are formed. Half of the atoms are still kink sites, but in each orientation one atom is not directly a kink atom. These could be considered part of a short A-type (blue) or B-type (red) step segment. In c, three atom wide segments are formed. Only one third of all atoms in the step edge are direct kink atoms.
b)-e) Left: STM images from various positions on the curved crystal. Colored lines indicate step edge contours as found by our analysis procedure. b) image size: 53×53 nm; mean terrace width: 11.6 nm / 43.0 atoms. c) image size: 50×50 nm; mean terrace width: 4.6 nm / 17.0 atoms. d) image size: 17×17 nm; mean terrace width: 1.7 nm / 6.3 atoms. e) image size: 15×30 nm; mean terrace width: 1.1 nm / 4.1 atoms. b)-e) Right: Corresponding histograms of facet lengths along the step edge. Blue panel: facets oriented in {001}-direction. Red panel: facets oriented in {110} direction. The first column of each histogram contains 1 atom wide microfacets, the second column 2 atom wide microfacets, etc.

{210} steps on Pt are "ideal", i.e. they are fully-kinked. Roughly 40 to 60 % of the sections are in bin a. The remaining sections are longer, but very rarely do we observe segments of more than 5 atoms. All histograms show a similar smooth decrease in observed frequency with microfacet length from bin b onward. The distributions are independent of the average terrace width over the probed range of 43.0 atom rows in figure 4.3b) to 4.1 atom rows in figure 4.3e). This confirms that the linear increase in S_0 observed in figure 4.2 does not result from changes in the structure of {210} steps, but is exclusively caused by increasing step density. Furthermore, the distributions of A- and B-type facets are similar and suggest no preference for longer or shorter segments of one microfacet type despite varying line free energies of A- and B-type steps.[24]

From the distributions in figure 4.3 and the atomic compositions for microfacets with varying lengths (see table B.2 in the Supporting Information), we calculate the average number of kink (N_K), A-type (N_A) and B-type (N_B) atoms in an edge consisting of 100 segments in {001} orientation and 100 segments in {110} orientation. The total number of atoms in these 200 segments is:

$$N = N_A + N_B + N_K \tag{4.2}$$

The fractional occurrence of kinks along a step is given by N_K/N. It consistently lies between 0.4 and 0.5 in all STM images (see Appendix B). Assuming that additional atoms in microfacets exhibit the reactivity of the A- (blue) or B-type steps (red), we now define the reactivity of {210} steps ($\Sigma_0^{\{210\}}$) as a weighted average of reactivities of kink atoms, A-type atoms (Σ_0^A), and B-type atoms (Σ_0^B) in all segments and set it equal to the experimentally determined value from table 4.1:

$$\Sigma_0^{\{210\}} = \frac{N_K\Sigma_0^K + N_A\Sigma_0^A + N_B\Sigma_0^B}{N} = 0.593 \text{ nm} \tag{4.3}$$

We solve for Σ_0^K using the data from individual STM images and the already known values for Σ_0^A and Σ_0^B. Table B.3 in the Supporting Information lists the results. The average value of Σ_0^K is 0.726 nm. As our model enforces lower reactivities for all A- and B-type atoms in longer segments of kinked steps, it is the upper limit for the average reactivity of inner and outer kinks:

$$\Sigma_0^K = (\Sigma_0^{K_{in}} + \Sigma_0^{K_{out}})/2 = 0.726 \text{ nm} \tag{4.4}$$

This maximum reactivity for the "ideal" or fully-kinked step edge is shown in table 4.1 and used to define the upper limit of average kink reactivity in figure 4.4 (light purple line). This graph also shows a lower limit. It is derived from assuming that the facets along the kinked step edge act as type A and B steps with no additional reactivity

of kinks. This situation is identical to a {210} step edge that is fully reconstructed, containing large stretches of both the A-type and B-type steps (with a kink density comparable to that typically occurring in A- or B-type steps) . Its slope is given by

$$\frac{1}{2} \cdot (\Sigma_0^A + \Sigma_0^B) \cdot 1.16 = 0.570 \text{ nm} \tag{4.5}$$

The factor 1.16 accounts for the increased length of the step compared to a straight line connecting the first and last atom of a {210} step. The range of Σ_0^K as defined by these two extremes is indicated as the purple shaded area (in between the "no kinks" and "only kinks" lines) in figure 4.4b).

The reactivity of the kink sites may hence indeed exceed that of straight step edges, as expected by the reduced number of nearest numbers at the outer kinks. The lower reactivity of the A-type step, however, remains unexpected from a coordination number viewpoint. As listed in table 4.1, the number of nearest neighbors (coordination number *CN*) is identical for atoms forming the A- and B-type steps, i.e. $CN = 7$. On fully kinked steps, *CN* varies for the inner and outer kinks, being 8 and 6 respectively. Depending on their relative contribution to reactivity, their weighted average may coincide or deviate from straight steps. Based on *CN* alone, however, it cannot coincide with the B-type and deviate from the A-type. In fact, the difference in reactivity for the A and B-types already disagrees with *CN*. The inconsistency is also not resolved when considering coordination of atoms in the lower plane of the step, as discussed in Appendix B.

As *CN* fails to predict the reactivity trend, we verify whether the generalized coordination number, $\overline{CN}$, captures it. $\overline{CN}$ averages over all *CN* values belonging to an atom's nearest neighbors, hence capturing more of the surroundings of the surface atom involved in the chemical event.[10] Table 4.1 presents values for $\overline{CN}$. Again, reactivity is not represented properly. On the basis of upper edge atoms alone, the three edge types would be identical in reactivity if the average of inner and outer kinks is used. If one considers only the outer kinks, then kinked edges should have been considerably more reactive than both A- and B-type edges and the latter should have been identical in reactivity. Although our analysis suggests that fully kinked steps are likely more reactive than B-type steps, approaches considering reactivity of each atom site individually continue to fail representing the clear variations in reactivity of all three step types.

Abandoning atomistic approaches, where we consider the local reactivity of each surface atom, we swing our viewpoint back to a non-local nature of the interaction of D_2 with the stepped surface as suggested by earlier dynamical calculations. Earlier experimental and theoretical dynamics studies using vicinal Pt surfaces suggest that three dissociation mechanisms occur in parallel.[15, 25–27] First, dissociation at the upper edge is direct and non-activated. Second, molecules impinging into the bot-

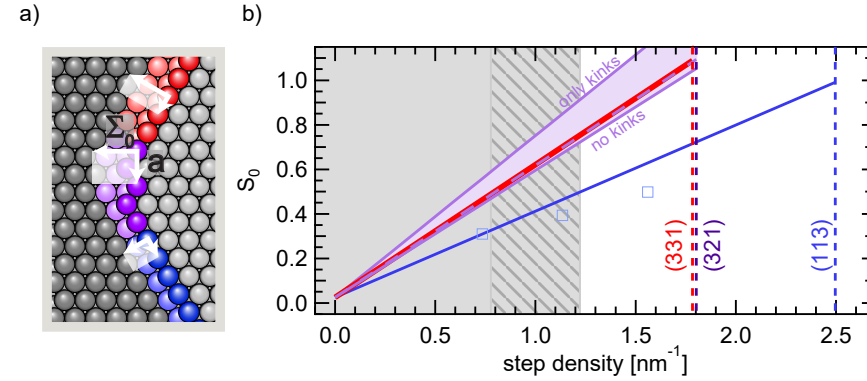

Figure 4.4: a) Relative positions of A-type, B-type and kinked steps on a (111) terrace. The absolute reaction cross-section of each type as listed in table 4.1 is indicated by white rectangles. Top to bottom: B-type, {210} (real), A-type.
b) Extended fits (blue, red, dashed purple lines) of the S_0 data from figure 4.2. The shaded purple area indicated the expected sticking behavior of the kinked step in the limits of only kinks and large faceting with minimal kinks. Blue squares: data from ref [25] for stepped surfaces, (extrapolated to E_{kin} = 9.3 meV, S_0 measured under an incident angle along surface normal). Dashed vertical lines: Step densities of (331) (red), (321) (purple), and (113) (blue).

tom cusp of the step may be dynamically trapped and react by following shallow potential wells leading toward the upper edge. Third, molecules impinging on (111) terrace sites encounter modest activation barriers. While the value of $S_0{}^{(111)}$ was shown to be small at low collision energies, a linear combination of three contributions explains the observed dependence on step density shown in figures 4.2 and 4.4. The slope (Σ_0) then gives the average length (measured normal to the edge) over which the step contributes to reactivity. It represents the cross section for the dissociation mechanisms related to steps, but reduced to a single spatial dimension.

Consequently, multiplying this length by the unit cell width (a) yields the initial reaction cross section (σ_0).

$$\sigma_0 = \Sigma_0 \times a \tag{4.6}$$

The values we obtain for σ_0 per step type are included in table 4.1. They are also illustrated as white areas at the different edge types in figure 4.4a). They may be compared to the area of molecular wells and the holes leading to non-activated dissociation in a PES. For the A-type, we have shown previously that it corresponds well to the reactive area of the PES calculated for H_2/Pt(211).[17] Our data suggests sizes of these areas for the B-type step and the corrugated {210}-type step. Both extend further onto the lower terrace than for the A-type step. Note that the larger σ_0 value for the {210} steps in table 4.1 is partially caused by a larger unit cell width *a*.

The step-type dependence of σ_0 for D_2 colliding at less than than 10 meV in kinetic

energy indicates that the distance over which steps may induce dynamical trapping and/or barrier-free dissociation critically depends on the local atomic arrangement in the step. For the A-type step, dissociation on the upper edge was found to be entirely barrier-free[15]. It is likely that the upper edges for the B-type and kinked edges also have these 'holes' in the potential. The difference we find for the various edges must then result from the capability to trap molecular hydrogen in the cusp of the step. For A-type steps, the molecular adsorption wells that cause trapping with subsequent dissociation are then the smallest. B-type steps trap and dissociate molecular hydrogen over a longer distance. This may be caused by the relative shifts of the upper and second layers of Pt atoms at these steps. For the B-type step, the lateral shift is 2/3 of the distance between atom rows parallel to the edge, whereas it is only 1/3 for the A-type. Kinks appear to cause an even larger disturbance to the local potential with deeper and/or wider wells.

Finally, in figure 4.4b), we extrapolate the fits with slope Σ_0 to predict reactivity beyond the range offered by our curved crystals to the highest possible step density for each step type, as indicated by the dashed lines. Our predictions for A-type steps agree reasonably well with the only published data obtained for surfaces with very short terraces, added as blue squares in figure 4.4b).[25]

Surfaces featuring short terraces of only a few atom rows, such as those that we approach with the extrapolation in figure 4.4b) are particularly interesting to heterogeneous catalysis, as they are featured on the surface of real nanoparticles.[28] Only the equilibrium shape of very small metal particles of <1 nm size one would expect to find sharp edges that do not feature a cusp to the adjacent terrace. There, the reactivities may vary from the ones derived here, due to the absence of dynamical trapping at the cusp. An impinging H_2 wavepacket would thus experience a smaller cross-section with such an edge than the ones derived here. For larger Pt nanoparticles, as well as regularly stepped Pt surfaces, we expect the 'chemical step size' Σ_0 to be a reliable descriptor of reactivity towards D_2 dissociation.

4.4. CONCLUSION

Our examination of Pt-catalyzed hydrogen dissociation on surfaces with close-packed and highly-kinked steps yields reactivities for different surface structural features. STM analysis of kinked steps allows us to extract an average reactivity for inner and outer kinks. Results show that kinks likely aid dissociation more than atoms in straight steps. However, the measured reactivity difference for the two close-packed step types is not adequately captured by models that rely on counting (nearest) neighbors of various types of surface atoms. We believe that the origin of the discrepancy is the dynamical nature of the interaction. For a light-weight molecule interacting at low collision energy with a surface that is characterized by (at most) modest barriers

to dissociation, molecular wells close to the dissociation site increase the dissociation probability. We therefore consider the interaction in terms of a cross section, σ_0. It reflects the physical area near the step where impingement leads to trapping and dissociation as found in earlier theoretical dynamics studies. The average length of this area, Σ_0, measured normal to the step, is derived directly from the experimentally determined dependence of reactivity on step density. We believe that the reactivities determined here, including the rule of thumb resulting from extrapolating experimental data to the smallest unit cells, provide a useful tool for modeling dissociation on vicinal surfaces with potentially large unit cells. Furthermore, they allow careful prediction of reactivities on industrially relevant catalyst sites by bridging the whole range of stepped Pt surfaces.

REFERENCES

[1] H. C. Schewe, Q. Ma, N. Vanhaecke, X. Wang, J. Kłos, M. H. Alexander, S. Y. Van De Meerakker, G. Meijer, A. Van Der Avoird, and P. J. Dagdigian. Rotationally inelastic scattering of OH by molecular hydrogen: Theory and experiment. *Journal of Chemical Physics*, 142(20):204310, 2015.

[2] G. J. Kroes and C. Díaz. Quantum and classical dynamics of reactive scattering of H_2 from metal surfaces. *Chemical Society Reviews*, 45(13):3658–3700, 2016.

[3] C. Díaz, E. Pijper, R. A. Olsen, H. F. Busnengo, D. J. Auerbach, and G. J. Kroes. Chemically accurate simulation of a prototypical surface reaction: H_2 dissociation on Cu(111). *Science*, 326(5954):832–834, 2009.

[4] E. Nour Ghassemi, M. Wijzenbroek, M. F. Somers, and G. J. Kroes. Chemically accurate simulation of dissociative chemisorption of D_2 on Pt(1 1 1). *Chemical Physics Letters*, 683:329–335, 2017.

[5] E. W. Smeets, G. Füchsel, and G. J. Kroes. Quantum Dynamics of Dissociative Chemisorption of H_2 on the Stepped Cu(211) Surface. *Journal of Physical Chemistry C*, 123(37):23049–23063, 2019.

[6] H. Chadwick, A. Gutiérrez-González, D. Migliorini, R. D. Beck, and G. J. Kroes. Incident Angle Dependence of CHD_3 Dissociation on the Stepped Pt(211) Surface. *Journal of Physical Chemistry C*, 122(34):19652–19660, 2018.

[7] H. Chadwick, A. Gutiérrez-González, R. D. Beck, and G. J. Kroes. Transferability of the SRP32-vdW specific reaction parameter functional to CHD 3 dissociation on Pt(110)-(2 × 1). *Journal of Chemical Physics*, 150(12):124702, 2019.

[8] H. Chadwick, A. Gutiérrez-González, R. D. Beck, and G. J. Kroes. CHD_3 Dissociation on the Kinked Pt(210) Surface: A Comparison of Experiment and Theory. *Journal of Physical Chemistry C*, 123(23):14530–14539, 2019.

[9] M. K. Sabbe, M. F. Reyniers, and K. Reuter. First-principles kinetic modeling in heterogeneous catalysis: An industrial perspective on best-practice, gaps and needs. *Catalysis Science and Technology*, 2(10):2010–2024, 2012.

[10] F. Calle-Vallejo, J. I. Martínez, J. M. García-Lastra, P. Sautet, and D. Loffreda. Fast prediction of adsorption properties for platinum nanocatalysts with generalized coordination numbers. *Angewandte Chemie - International Edition*, 53(32):8316–8319, 2014.

[11] F. Calle-Vallejo, D. Loffreda, M. T. Koper, and P. Sautet. Introducing structural sensitivity into adsorption-energy scaling relations by means of coordination numbers. *Nature Chemistry*, 7(5):403–410, 2015.

[12] F. Calle-Vallejo, J. Tymoczko, V. Colic, Q. H. Vu, M. D. Pohl, K. Morgenstern, D. Loffreda, P. Sautet, W. Schuhmann, and A. S. Bandarenka. Finding optimal surface sites on heterogeneous catalysts by counting nearest neighbors. *Science*, 350(6257):185–189, 2015.

[13] M. J. Van Der Niet, A. Den Dunnen, M. T. Koper, and L. B. Juurlink. Tuning hydrophobicity of platinum by small changes in surface morphology. *Physical Review Letters*, 107(14):1–4, 2011.

[14] M. J. Kolb, A. L. Garden, C. Badan, J. A. Garrido Torres, E. Skúlason, L. B. Juurlink, H. Jónsson, and M. T. Koper. Elucidation of temperature-programmed desorption of high-coverage hydrogen on Pt(211), Pt(221), Pt(533) and Pt(553) based on density functional theory calculations. *Physical Chemistry Chemical Physics*, 21(31):17142–17151, 2019.

[15] D. A. McCormack, R. A. Olsen, and E. J. Baerends. Mechanisms of H_2 dissociative adsorption on the Pt(211) stepped surface. *Journal of Chemical Physics*, 122(19):194708, 2005.

[16] R. A. Olsen, D. A. McCormack, M. Luppi, and E. J. Baerends. Six-dimensional quantum dynamics of H_2 dissociative adsorption on the Pt(211) stepped surface. *Journal of Chemical Physics*, 128(19):194715, 2008.

[17] R. Van Lent, S. V. Auras, K. Cao, A. J. Walsh, M. A. Gleeson, and L. B. Juurlink. Site-specific reactivity of molecules with surface defects—the case of H_2 dissociation on Pt. *Science*, 363(6423):155–157, 2019.

[18] K. Cao, R. van Lent, A. W. Kleyn, M. Kurahashi, and L. B. Juurlink. Steps on Pt stereodynamically filter sticking of O_2. *Proceedings of the National Academy of Sciences of the United States of America*, 116(28):13862–13866, 2019.

[19] A. C. Luntz, J. K. Brown, and M. D. Williams. Molecular beam studies of H_2 and D_2 dissociative chemisorption on Pt(111). *The Journal of Chemical Physics*, 93(7):5240–5246, 1990.

[20] D. A. King and M. G. Wells. Molecular beam investigation of adsorption kinetics on bulk metal targets: Nitrogen on tungsten. *Surface Science*, 29(2):454–482, 1972.

[21] B. Poelsema, K. Lenz, and G. Comsa. The dissociative adsorption of hydrogen on defect-'free' Pt(111). *Journal of Physics Condensed Matter*, 22(30):304006, 2010.

[22] K. Cao, R. van Lent, A. W. Kleyn, and L. B. Juurlink. A molecular beam study of D_2 on Pt(111): Testing SRP-DFT calculations. *Chemical Physics Letters*, 706:680–683, 2018.

[23] J. E. Ortega, G. Vasseur, I. Piquero-Zulaica, S. Matencio, M. A. Valbuena, J. E. Rault, F. Schiller, M. Corso, A. Mugarza, and J. Lobo-Checa. Structure and electronic states of vicinal Ag(111) surfaces with densely kinked steps. *New Journal of Physics*, 20(7):073010, 2018.

[24] T. Michely and G. Comsa. Temperature dependence of the sputtering morphology of Pt(111). *Surface Science*, 256(3):217–226, 1991.

[25] I. M. N. Groot, A. W. Kleyn, and L. B. F. Juurlink. Separating catalytic activity at edges and terraces on platinum: Hydrogen dissociation. *Journal of Physical Chemistry C*, 117(18):9266–9274, 2013.

[26] I. M. N. Groot, A. W. Kleyn, and L. B. F. Juurlink. The energy dependence of the ratio of step and terrace reactivity for H_2 dissociation on stepped platinum. *Angewandte Chemie - International Edition*, 50(22):5174–5177, 2011.

[27] A. T. Gee, B. E. Hayden, C. Mormiche, and T. S. Nunney. The role of steps in the dynamics of hydrogen dissociation on Pt(533). *Journal of Chemical Physics*, 112(17):7660–7668, 2000.

[28] K. Honkala, A. Hellman, I. N. Remediakis, A. Logadottir, A. Carlsson, S. Dahl, C. H. Christensen, and J. K. Nørskov. Ammonia synthesis from first-principles calculations. *Science*, 307(5709):555–558, 2005.

5

CHIRAL SURFACE CHARACTERISATION AND REACTIVITY TOWARD H-D EXCHANGE OF A CURVED PLATINUM CRYSTAL

Understanding heterogeneous catalysis at the atomic level requires detailed knowledge of the reactivity of different surface sites toward specific bond breaking and bond making events. We illustrate a new method in such investigations. We use a macroscopically curved Pt single crystal containing a large variation in density of highly kinked steps of two different chiralities. Scanning tunneling microscopy maps the entire range of surface structures present on the 31° section surrounding the Pt(111) apex. Whereas most of the surface shows the expected characteristic arrays of parallel steps, hexagonally-shaped, single-atom deep pits remain after cleaning procedures near the apex. Their orientation is indicative of the different chiralities present on the two sides of the crystal's apex. These unintended defects locally raise the surface defect concentration, but are of little consequence to subsequent reactivity measurements for D_2 dissociation and H-D exchange as probed by supersonic molecular beam techniques. We quantify absolute elementary dissociation and relative isotopic exchange rates across the surface with high spatial resolution. At low incident energies, elementary dissociation of the homonuclear isotoplogues is dominated by the kinked steps. H-D exchange kinetics depend also mostly linearly on step density. The changing ratio of D_2 dissociation to H-D formation, however, suggests that anisotropic diffusion of H(D) atoms is of influence to the measured HD production rate.

This chapter is based on the following publication:

T. Roorda*, **S. V. Auras***, and L. B. F. Juurlink. Chiral surface characterisation and reactivity toward H–D exchange of a curved platinum crystal. *Topics in Catalysis*, **59**, 1558-1568 (2020).

5.1. INTRODUCTION

MANY STUDIES IN CATALYTIC SURFACE SCIENCE make use of high symmetry, low Miller index planes of metal single crystals.[1] While they are the simplest types of surfaces to describe theoretically, experimentally a perfect, defect-free flat surface as described by theory, cannot be produced. Furthermore, real life chemical reactions at surfaces, such as they occur in heterogeneous catalysis or environmental chemistry, occur on surfaces featuring a multitude of sites.[2–5] Under-coordinated sites on surfaces, such as steps, kinks, edges and corners, are often found to be more reactive towards dissociation of reactant molecules and may be responsible for the dominant part of a catalyst's activity.

One way of studying more realistic surfaces involves the use of nanocrystals. Norbert Kruse and others explored this field already in the 1980's making use of techniques such as Field Ion Microscopy (FIM) in combination with pulsed field desorption mass spectrometry. [6, 7] The atom-probe technique is extremely powerful, visualizing multiple crystal planes that may contribute to the catalytic process at once. Kruse and colleagues showed, for example, that surface chemical reactions, oscillations in reactivity, and restructuring of facets can be studied under a rather wide range of experimental conditions. For example, nanocrystalline Pt field emitter tips were used to elucidate different catalytic rates and processes for NO and NO_2 reduction on Pt facets. [8–15] There, tips were specifically shaped to expose facets of interest. Kruse continues to study different catalytic processes and different metallic and alloy catalysts.

Another approach to studying the influence of surface heterogeneity to surface chemistry and catalysis employs flat single crystals of planes vicinal to low-Miller index directions. This is particularly useful in studies that require a macroscopic flat area of a single surface structure, e.g. one with a fixed number density of particular types of steps and/or kinks. Molecular beams, often used to study the dynamics of (activated) adsorption and overall reactions with control over the kinetic energy of the reactant(s), require such larger flat areas characterized by a single surface unit cell.[16] The lower symmetry of these unit cells make them more challenging to study with accurate theoretical methods. Nonetheless, the dynamics of molecule-surface collisions with vicinal surfaces have been subject of several theoretical and experimental studies, some even including rovibrational state-selection of the incident molecule.[17–23]

The approach using vicinal surfaces requires that the same reaction is studied on several different surface structures to extract site-specific reactivities.[24–28] Comparing reactivities of single crystals with varying number densities of particular types of terraces, steps, or kinks may yield direct and quantifiable evidence for the influence of each particular type of site on the reaction. Experimentally, this is tedious, though.

Subtle differences may be difficult to identify or hidden between variations in, e.g., contamination levels or sensitivity to surface restructuring of the various crystal surfaces. Deliberately introducing various levels of sputter defects to a nearly perfect single crystal surface presents a shortcut to the approach.[29, 30] It unfortunately grants poor control over the types of defects that are introduced.

Curved surfaces of single crystals have recently been re-invented as a powerful tool to elucidate the role of specific surface sites in catalytic reactions.[31–33] While in the past many different types of curved surfaces have been used, in the last decade the predominantly used shapes are a small section of a cylinder and a dome. Most commonly, the crystallographic orientation is chosen to exhibit a low-Miller index surface at the apex. The macroscopic curvature of the crystal results predominantly from monoatomic steps occurring with increasing frequency when moving away from the apex. Depending on the azimuthal angle, these steps may be atomically straight or kinked. This curved crystal approach to studying the influence of surface structure in catalysis strongly resembles the nanocrystal approach employed by Kruse - both use a single sample that contains a range of surface structures. The macroscopic size of these new curved crystals, however, allows for much smoother variation of surface structure. They often exhibit vicinal surfaces with a well-defined, continuous range of step densities. Although they do not reflect the shape of actual catalytic particles, the gradual variation in surface densities of various types of active sites make them ideal to unravelling individual contributions from such sites to overall reactivity.

We have recently determined site-specific reaction parameters of D_2 dissociation on stepped and kinked Pt(111) surfaces.[32, 34]. We have used two different curved Pt single crystals with (111) at the apex. One crystal provided close packed steps of {001} and {110} orientation (A- and B-type steps respectively) on either side of the apex. The second crystal had kinked steps consisting of short segments of A- and B-type interspersed by inner and outer kinks.Due to their orientation, the latter should nominally be fully kinked, however, we observed a partial reconstruction of the kinked step edges into slightly longer A- and B-type segments with a reduced kink density. Specific Pt surfaces are very sensitive to the cleaning treatment and may be prone to reconstructions and faceting.[35, 36] On a similar cylindrical Pt single crystal with a [001] axial direction, Imbihl *et al.* observed reconstructions and step doubling on parts of the curved surface.[37]

Considering the possible instabilities on vicinal Pt surfaces, it is important to fully and in detail characterise the surface of a curved crystal. This is especially important when trying to unravel the influence of specific surface sites, such as kinked steps, that increase the surface free energy. Here, we present an investigation of the surface structures along the curvature of a *c*-Pt(111)[11$\bar{2}$]-31° crystal, i.e. a 31° curved section of a cylinder with (111) at the apex and the rotational axis pointing in the [11$\bar{2}$] direction. Determining the densities of intentional and non-intentional (residual) defects

allows us to critically consider what areas of the curved surface can be used in evaluating absolute reactivities of specific surface sites. Notably, for this particular crystal, residual hexagonally shaped defects also indicate the handedness of the kinked step causing the macroscopic curvature. We subsequently show that we may extrapolate the previously reported reactivity of D_2 dissociation towards an otherwise unattainable perfect, defect-free Pt(111) surface. We finally show that the H-D exchange rate between H_2 and D_2, which Norbert Kruse developed as a technique to determine the surface area of metal catalysts,[38] mostly tracks the elementary dissociation of the reactants.

5.2. EXPERIMENTAL

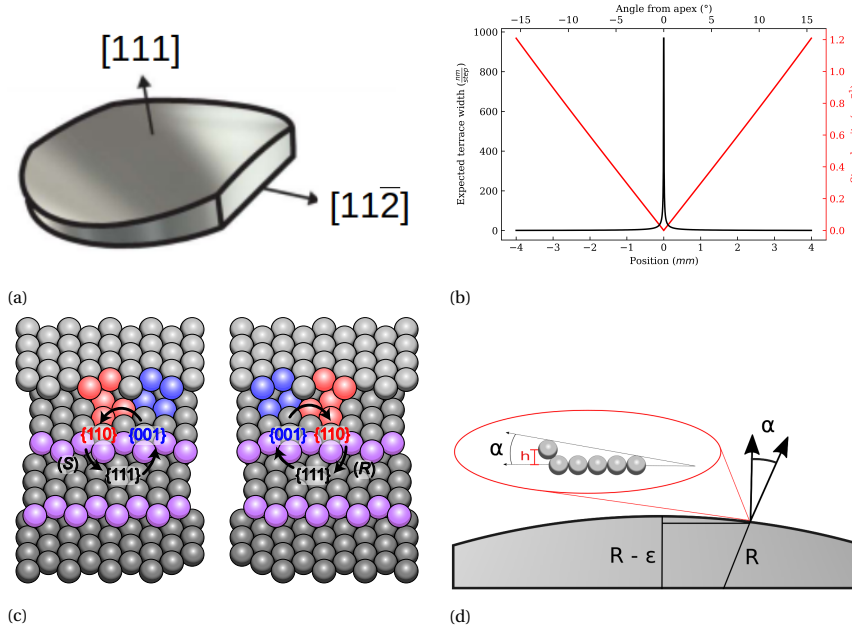

Figure 5.1: (a) Schematic drawing of our platinum crystal curving perpendicular to the (11$\bar{2}$) plane. Adapted from van Lent *et al.*[32] (b) Expected terrace widths and step densities along the curvature of the crystal, calculated for monoatomic height steps, represented in distance from the apex and angle. The matching results from STM imaging are shown in the supplementary information. (c) Crystal structure of *fcc* {432} planes showing the kinked step consisting of short segments of A-type (blue) and B-type (red) steps. The chirality in the left and right images, identified as (*S*) and (*R*) chirality respectively, represent the surfaces on opposing sides of the curvature. (d) Depiction of a side view of the crystal with a zoom-in of a single terrace with adjacent step atom to indicate how the terrace width is calculated. The terrace width, TW, is determined by the height of a step, $h = 0.226$ nm, and the angle α which represents the angle between the (111) terrace normal and the stepped surface normal, as well as the angle between the apex and the position along the curvature with position x and radius R in the equivalent triangle.

The 8 × 7 mm Pt curved single crystal was prepared by spark erosion and sanding at Surface Preparation Laboratories (Zaandam, The Netherlands). The crystal shape is depicted in figure 5.1a). It curves 15.5° to both sides from the (111) plane at the apex, with a 15 mm radius of curvature around the [11$\bar{2}$] axis. Towards the sides of

the crystals, the (111) terraces become shorter as the step density increases linearly towards the edge (figure 5.1b)). Concomitantly, the terrace width decreases with 1/x, where x is the distance from the apex. Due to the direction of curvature, the steps causing macroscopic curvature are in principle the most highly kinked steps. They are illustrated by purple spheres in figure 5.1c). The kinked steps consist of alternating {001}-oriented and {110}-oriented microfacets, denoted as A-type (blue spheres) and B-type (red spheres) respectively. Due to the reduced symmetry of the kinked steps, surfaces with opposite chirality are formed on the two sides of the crystal. The notation of chirality for kinked steps on *fcc*(111) terraces, as described by McFadden *et al.*,[39] is obtained by ordering the microfacets around an inner kink by their atomic density. Going from the {111} terrace to the {100} segment to the {110} segment, we observe a counterclockwise rotation, denoted by *(S)* in the left depiction of figure 5.1c), and vice versa for *(R)* chirality.

With increasing distance from the apex (x), the angle of curvature α increases as defined by the radius of curvature R. At the same time, α determines the angle between the (111) normal and the vicinal surface normal. Therefore, on a microscopic level, α links the average terrace width (TW) of the stepped surfaces, to the height between atomic layers, h=0.226 nm. Figure 5.1d) demonstrates the relationships between macroscopic (x, R) and microscopic (TW, h) parameters and α. We obtain the following relation to determine TW along the curved crystal:

$$TW = \frac{h}{tan(\alpha)} = \frac{h}{tan(sin^{-1}(x/R))} = \frac{h \cdot (R - \epsilon)}{x} \tag{5.1}$$

The size and shape of this crystal thus, in principle, encompasses (111) terrace widths ranging from very large at the apex to approximately 3 atoms wide at the edges of the crystal. However, the polished section of the curved surface tapers toward the outer edges and we can not use the full width of 7 mm along the entire surface. As discussed below, we mostly use the available area ranging to approximately 5 atom wide terraces to unravel site-specific reactivities.

The surface of our curved crystal is cleaned and analyzed initially using a commercial UHV system with a variable temperature scanning tunneling microscope (VT-STM, Omicron). It has been altered in-house and contains, a.o., optics for Auger Electron Spectroscopy (AES) and Low Energy Electron Diffraction (LEED). We clean the crystal's surface by repeated cycles of argon ion sputtering, oxygen or hydrogen annealing and vacuum annealing. The sample can be heated radiatively up to ~ 575 K by a homemade W filament, higher temperatures are reached by electron bombardment when a positive potential is applied to the sample. A typical cleaning cycle consists of Ar^+ sputtering at room temperature, 0.52 keV and 7 μA for a duration of 10 minutes at 1.3×10^{-5} mbar followed by oxygen annealing at 3×10^{-8} mbar and ~

900 K and finished with vacuum annealing at ~ 1200 K. Due to potential sensitivity of the vicinal surfaces to restructuring and faceting at 1200 K,[35, 36] the final cleaning cycle consists only of sputtering and annealing *in vacuo* at a reduced temperature. To reduce the formation of deep pits during sputtering, the surface temperature is raised during the last sputtering step, to facilitate adequate subsequent annealing. In the STM apparatus, the last cleaning cycle consisted of Ar^+ sputtering at an elevated temperature of 573 K (no electron bombardment) followed by vacuum annealing at 773 K, each for 5 minutes. Annealing temperatures >700 K ensure increased interlayer Pt atom mobility on the surface due to evaporation from the step edges.[40] We use the AES and LEED optics to verify the chemical purity and surface structure of the crystal surface. Results of the LEED study are shown in the supplementary information. For our analysis of intentional and non-intentional (residual) defects on the surface, the surface is imaged by STM along the curvature in a single line. Although our system in principle allows for cooling of the sample temperature, all of our STM imaging was performed with the crystal near room temperature. We have taken ~ 1000 images (2 direction scans per position). Of these, ~150 suitable images were selected for quantitative analysis. The apex can be easily located by where the surface steps change in direction. Distance travelled along the surface is regulated by counting clicks with a stepping motor.

To determine structure-dependent chemical reactivities, the crystal is mounted in the UHV chamber of a second apparatus, i.e. a home-built system that also contains multiple chambers for creating a supersonic molecular beam.[32, 34] Here, a slightly modified cleaning procedure is applied, consisiting of repeated cycles of sputtering (Ar^+, 1 keV, 1.3 μA, 5 min), annealing in O_2 (3×10^{-8} mbar, 900 K, 3 min) and annealing in vacuum (1200 K, 3 min). The technical setup in the second apparatus made it possible to use electron bombardment during sputtering by applying a negative potential to the filament used for heating, allowing us to sputter at an elevated temperature of 900 K, followed by annealing in vacuum (900 K). As a consequence, there are likely even less non-intentional defects during molecular beam experiments than during the STM study. We then impinge molecules from a supersonic molecular beam onto well-defined parts of the sample. The molecular beam is formed by supersonic expansion of gas mixtures with subsequent skimming of the gas plume and two stages of differential pumping prior to the beam entering the UHV chamber that holds the curved Pt sample. The beam's final skimmer is rectangular. It projects a 0.126 mm high and 6.0 mm wide beam along the (111) normal onto different parts of the curved crystal. The height of the beam limits convolution with the varying step density along the curved surface.

Initial dissociation probabilities for D_2, $S_0(D_2)$, are determined using the King-and-Wells method.[41] A D_2 beam anti-seeded with Ar is used. D_2 molecules impinge with

an average kinetic energy of 9.3 meV as determined by time-of-flight measurements using a quadrupole mass spectrometer (QMS) mounted on-axis in the UHV chamber of the system (UTI100c) with the crystal retracted from the beam, and the beam being chopped at high frequency into short pulses in the first differential pumping stage. For the dissociation probability measurements, the surface is kept at T_s = 155 K. At this temperature, molecular hydrogen sticks via dissociative adsorption. Recombinative desorption is avoided by keeping the surface temperature far below the onset of desorption from Pt(111) and comparable vicinal surfaces.[42–46]

For determining relative HD formation rates, a mixed beam with equivalent parts of H_2 and D_2 is used. Again, it is anti-seeded with Ar to achieve a similar kinetic energy as during D_2 sticking. The crystal is kept at 500 K, i.e. well above the recombinative desorption temperature of small surface concentrations of atomic H (D). This high temperature in combination with the limited flux of molecular H_2 (D_2) ensures a low steady state atomic H (D) coverage during exposure to the beam. Relative HD formation rates are measured using a second QMS located in the UHV system (Pfeiffer, QMA200). We open a beam shutter in the second differential pumping stage to only allow a narrow part of the surface to be bombarded by the mixed H_2-D_2-Ar beam. We wait for a few seconds to obtain a stable current at m/e = 3 as determined by the QMS prior to shutting the beam. Measurements of HD formation are taken for several non-overlapping parts on the surface by moving the crystal relative to the beam within the course of several minutes. Thereafter the crystal is cleaned and experiments are repeated using various orders and different sections along the crystal's curved surface. The QMS signal is corrected for the background current obtained at m/e = 3 at the times intermittent to beam exposure. Relative reactivities are reported as the QMS current produced only resulting from HD formation by the crystal's local surface structure during initial exposure to the beam. As we have recently demonstrated that HD formation is more sensitive to structural changes than even LEED,[47, 48] the consistent linear increase of HD formation with step density presented in figure 5.3 confirms that no step doubling or facetting is occuring.

5.3. RESULTS AND DISCUSSIONS

5.3.1. STM ANALYSIS OF INTENTIONAL AND NON-INTENTIONAL DEFECTS

We start by describing our general observations from the STM analysis. At the apex, atomically flat terraces as long as 1500 nm are observed along with areas showing heavy step bunching. On most larger terraces, single layered vacancy islands are found in between parallel steps. We attribute this to the relatively short annealing time at low temperature during the last step of our cleaning routine.[40, 49] Towards

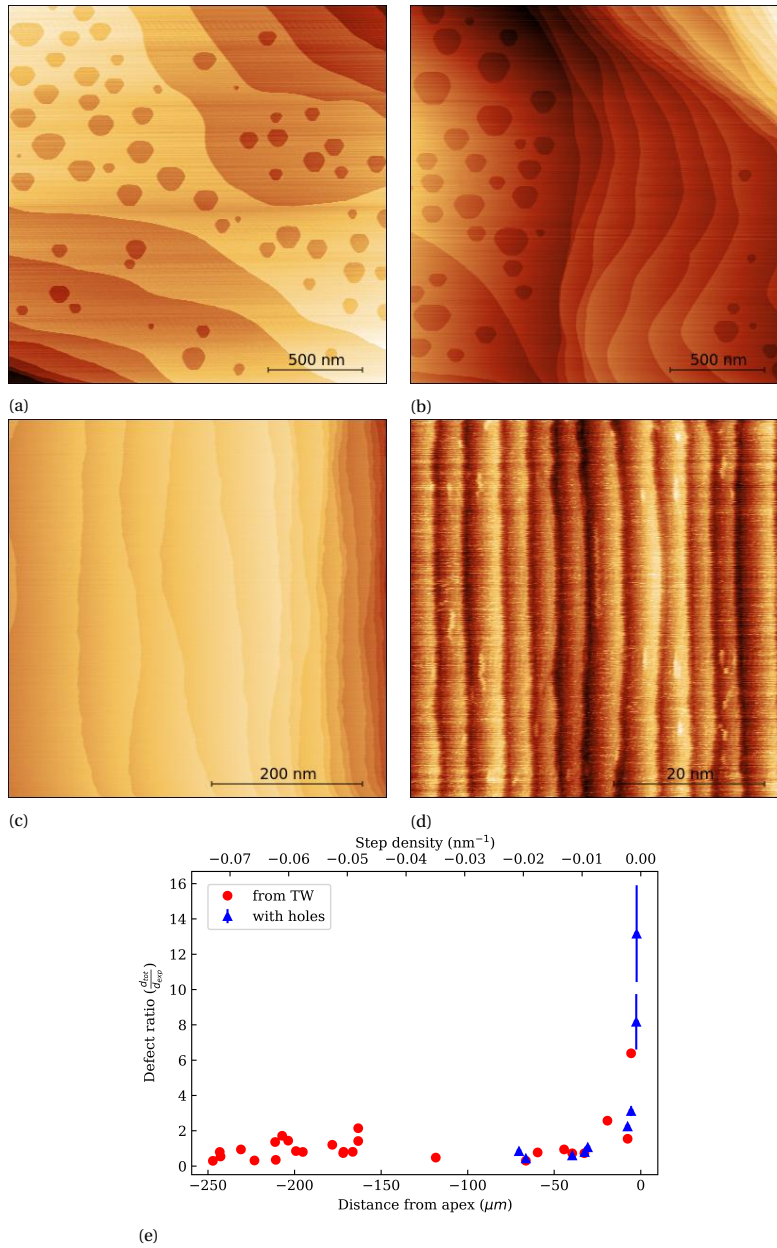

Figure 5.2: Typical STM images obtained close to the (111) apex. (a) distance to apex: 7.4 µm; mean TW: 211 nm, max TW: 1200 nm (b) distance to apex: -19 µm; mean TW: 148 nm, max TW: 357 nm (c) distance to apex: -135 µm; mean TW: 8.7 nm, max TW: 24 nm (d) mean TW: -800 µm; mean TW: 8.4 nm, max TW: 22 nm. (e) Defect ratio of line defects and vacancy islands as a function of distance from the apex (with expected step density indicated on top axis). Red circles represent surfaces with no vacancy islands. Blue triangles represent images with vacancy islands.

~100 µm from the apex, the number of vacancy islands per area decreases and less step bunching is observed, however, step edges still meander slightly. As the step density increases, gradually the lines straighten out along the inherent step direction. Terrace widths are measured by drawing lines scans from step edge to step edge, neglecting vacancy islands as the end of a terrace.

Our general observations are illustrated in the STM images of figure 5.2a)-d). In a), in close proximity (7.4 µm) to the apex, the mean terrace width is 458 nm. In this image only large terraces are present, consisting of a topological ridge with decreasing steps to either side. The step edges meander considerably and their overall alignment deviates significantly from the expected direction along $(11\bar{2})$ (vertical direction in the image). The STM image in figure 5.2b), 19 µm from the apex, shows significant step bunching in combination with large terraces containing vacancy islands. The largest terrace spans up to 1200 nm, whereas the mean TW in this image is 211 nm. While still meandering considerably, the steps are more aligned along the direction determined by the crystal curvature. Vacancy islands are only observed on wider terraces. In figure 5.2c) at 135 µm from the apex, step bunching is reduced and we observe a clear reduction in the distribution of terrace widths. Step edges now follow the expected direction but still meander slightly. This difference is likely due (at least in part) to the disappearance of vacancy islands relatively close to a step edge being "absorbed" by the edge during the final annealing cycle. Further from the apex large-scale meandering is no longer observed and vacancy islands are absent. Figure 5.2d) shows parallel and equidistant step edges in the expected direction with an average TW of 4.24 nm and a maximum terrace width of 5.23 nm.

For a perfect surface as created by the truncated bulk, we expect the only 'defect sites' to be the highly kinked step edges sketched in figure 5.1c) appearing in our STM images as lines running perpendicular to the curvature of the crystal. As shown in figure 5.2, near the apex the number of defect sites is increased due to meandering steps and vacancy islands. By quantifying the lengths of all steps, including those forming vacancy islands in our STM images, we can obtain the ratio between intentional and unintentional defect sites. We divide by the expected TW at that position to create a normalized value. The value equals 1 in case the defect density equals that of an array of steps with an average terrace width as expected at that position for the ideally truncated bulk. In case more defects remain, the value increases. The results in figure 5.2e) plot the ratio of total defect sites to expected defect sites, $\frac{d_{tot}}{d_{exp}}$ as a function of distance from the apex (lower axis) and step density (upper axis). Blue data indicates that the image(s) used to determine defect lengths contained vacancy islands. Red data reflect results for images that did not show these islands. Within the first 30 µm on either side of the apex, we find a significant surplus in defect sites. This is also where we observe the most vacancy islands. Between 30 and 100 µm, as the surface

approaches what we observe in figure 5.2d), the defect ratio approaches 1. Beyond 100 µm from the apex, the presented data is estimated based on terrace widths alone as vacancy islands do not occur. The value fluctuates around 1. These STM-based results and those shown for the LEED analysis in the supporting information, allow us to conclude that the applied cleaning procedure for this crystal yields the expected defect density along the crystal's curvature from a step density ≤ 0.005 nm^{-1}, i.e. an expected TW ≤ 200 nm). For wider terraces, significant numbers of defects, both in the form of vacancy islands and bunched steps, occur. These increase the expected surface defect concentration with a factor of ~ 10^1 very close to the apex.

5.3.2. D_2 DISSOCIATION AND HD FORMATION ON THE CURVED CRYSTAL

The detailed insights into the structure of the kinked surfaces along our curved crystal provide a background to revisit previously determined dissociation probabilities for D_2 on this this crystal in chapter 4. $S_0(D_2)$ has been shown to be nearly temperature independent between 100 - 350 K for Pt(111) and vicinal surfaces.[50–54] We therefore expect no appreciable differences between the surface structures found in the STM study at room temperature, and during the molecular beam study at 155 K. Figure 5.3 shows in the bottom half of the graph the absolute dissociation probabilities of D_2 versus step density. The grey shaded areas indicate the part of the curved crystal that has a reduced width due to tapering of the crystal's edges. The molecular beam is wider here than the crystal. Our measurements in this range, therefore, do not necessarily reflect the actual dissociation probability accurately. We omit the data in these regimes from our analysis and arguments.

The dissociation probabilities in figure 5.3 increase approximately linearly from the (111) surface towards higher step densities at the sides of the crystal. We find no significant difference between the left and right sides of the crystal. This is expected for D_2 dissociation, as there is no reason to assume enantiomeric selectivity. The STM analysis presented in figure 5.2e) shows that when terraces are narrower than 200 nm, the ratio of total defects over intended defects hovers around 1, i.e. unintended contributions to the defect density are absent. Furthermore, STM images in this range predominantly show rather well-defined arrays of terraces. We may thus safely conclude that indeed the increasing reactivity results from the linear increase in step density.

In figure 5.2e), we found that the defect density did not reflect the expected value very close to the apex. The blue shaded area in the plot marks this range of the curved crystal's surface. The observed number of defects is considerably higher than the expected step density. The size of this area is clearly very small in comparison to the range over which the apparent linear dependence of the dissociation probability

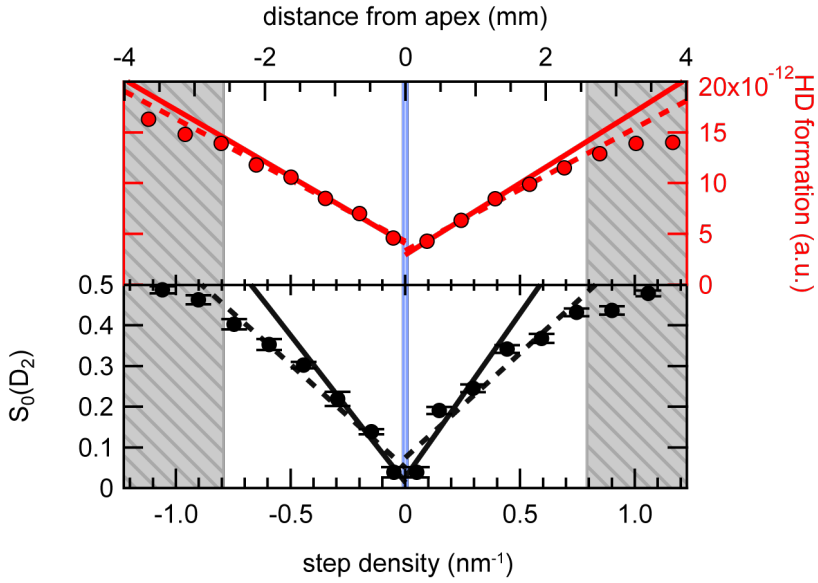

Figure 5.3: D_2 sticking probability, S_0 (black circles) and HD formation (red circles) across the curved crystal. Expected step densities (bottom axis) are calculated as a function of distance from the apex (top axis). The blue shaded region in the center highlights the region of the crystal where the defect ratio on the crystal is above 1, and thus the observed step density exceeds the expected step density. The lowest two circles, measured at the apex, are shifted to the actual step density probed by the molecular beam at the apex. Grey shaded areas indicate where the molecular beam becomes wider than the single crystal's surface; data in the grey areas are not included in any fits. Solid lines are fits to the data including points up to 1 mm from the center. Dashed lines are fits including data up to 2.6 mm from the center, i.e. all data in the white area of the plot. Fit lines are extrapolated to a step density of zero, as well as to step densities at the outermost parts of our crystal.

appears. This area may be even smaller during molecular beam experiments, when the last annealing step was carried out at a slightly higher temperature than before STM imaging. In fact, it is already twice smaller than the area covered by rectangularly-shaped molecular beam. Consequently, although the defect density may be one order of magnitude higher than the expected value in the blue shaded area, the absolute defect density that the beam probes at the center is on average still very small, and reactivity in the area close to the apex is expected to mostly be due to dissociation at the terraces. The quality of a fit that includes the data at or near the apex is not influenced much by the increased defect density.

The slope extracted from a linear fit to the data represents the reactivity of the step in a somewhat odd unit of nm. It represents the length measured normal to the edge over which the step influences to the impinging molecule such that it leads to dissociation.[32] Multiplied by the unit cell width, we obtain the absolute differential reaction cross-section in nm^2 for the kinked step at the determined collision energy.[34] To improve upon the value determined in chapter 4, we now include the

dissociation probability measured at the apex, but displace it parallel to the x-axis to the position that reflects the same defect density as determined by STM imaging. Also, we note that, although the data seem linear with defect density over the regime that we may include in our analysis, some curvature appears beyond ~ 1.5 mm from the apex. Hence, we successively apply a linear fit function to increasing data from the apex. A fit that only includes the data up to 1 mm from the apex represents those data very well with a slope of 0.764 nm (averaged over both sides). This fit overestimates reactivity at positions further away than 2 mm from the apex. Hence the fit adequately covers the reactivity dependence on step density from 'infinite' to ~6 atom wide terraces. Including additional data up to 2.6 mm from the apex, corresponding to an average of 4.5 atom wide terraces, gives a slope of 0.510 nm.

The cause for the non-linearity is not clear at this time. We consider that our measurements may miss a small amount in the measured reactivity for narrower terraces as the local surface area is quite reactive. Judging from the original data, we do not believe this to be true though. Also, some physical process may lower the chance for a molecule to dissociate when terraces are very narrow. It is well-known that the grating formed by the step arrays for several transition metals becomes better defined, i.e. shows reduced terrace width distributions, with decreasing terrace width.[55, 56] We wonder whether improved molecular diffraction from these highly ordered areas near the edge causes increased scattering at the expense of dissociation.

Reversing the direction of extrapolation, we consider our fits at the center of the plot, i.e. at a step density of absolute zero. We thus obtain the reactivity for a "perfect", i.e. defect free, (111) surface. Being able to do so is a great advantage when comparing measured reactivities to those obtained in theoretical studies. Such comparisons usually have to accept that while experimental studies will always be carried out on a surface having a residual defect density, theoretical studies are usually computed on perfectly constructed (111) surfaces and cannot easily capture the effect of statistical defects. For the initial sticking probability of D_2 we reach slightly different values for zero step density, namely 0.026 ± 0.06 and 0.014 ± 0.03 for the fits involving the data up to 1 mm from the apex. For the fits over the wider range, up to 2.6 mm from the apex, we find 0.075 ± 0.03 and 0.050 ± 0.02. While there is some disparity between those values, they indicate the range in which to expect sticking probabilities for a perfect (111) surface. The initial sticking probability S_0 experimentally obtained closest to the apex, 0.039 ± 0.013, falls within that range.

The upper half of figure 5.3 shows HD formation resulting from a mixed H_2/D_2 molecular beam. These data again show a linear increase with step density. Both sides of the apex also yield nearly identical results. Here, we carry out linear fits once more, first for the data within 1 mm of the apex, then for the range up to 2.6 mm from

the apex. We note that the data does not show the same curvature as the $S_0(D_2)$ data. The fits show a similar slope and offset, regardless of the included fitting range.

For HD to be produced, the following elementary reactions are relevant:

$$\begin{aligned} H_2 + 2* &\rightleftharpoons 2\,H_{ads} \\ D_2 + 2* &\rightleftharpoons 2\,D_{ads} \\ H_{ads} + D_{ads} &\longrightarrow HD + 2* \end{aligned}$$

The two equations expressing the dissociation of H_2 and D_2 are equilibria as the surface bound H_{ads} and D_{ads} atoms produced by dissociation of H_2 and D_2 may desorb with their original partner or another atom of the same isotope. Only if they encounter and desorb with an atom of the other isotopic type, is HD formed, as expressed in the third reaction. For the dissociation equilibria, the probability for dissociation equals S_0.

To understand the relative kinetics of HD formation, several aspects are important. First, for the kinetic energy used here, there is also no significant temperature dependence to reactivity. This is important as we will compare the dependence in dissociation measured at 300 K to the H-D exchange at 500 K. Second, none of the supersonic molecular beam studies of hydrogen dissociation on Pt(111) and stepped Pt surfaces has ever reported an isotope effect, while all surfaces show a slightly different kinetic energy dependence.[50–54, 57] As we use a single beam containing both H_2 and D_2, their velocities are (nearly) identical. Their values for S_0 at the conditions used here, therefore, differ. For a single surface type, e.g. Pt(111), we can estimate the instantaneously produced surface concentrations of H_{ads} and D_{ads} from S_0 and the flux. However, the measured reactivity along the curved surface may be considered a combination of the reactivity on (111) planes and steps. The previously reported kinetic energy dependencies for Pt(111) and highly stepped surfaces are inverted, but vary with the surface. On Pt(111), reactivity only increases with kinetic energy, while on all stepped surfaces the reactivity initially drops with kinetic energy prior to it increasing again. This makes it difficult to unravel the ratio of produced H_{ads} and D_{ads} from the impinging molecules. We make no attempt to estimate them here. However, it is unlikely that the expected statistical 1:2:1 ratio of $H_2 : HD : D_2$ product formation is achieved in our experiments as a result of unequal concentrations of H_{ads} and D_{ads}.

On the other hand, we note that the rate of HD formation increases only by a factor of 3.4 over the entire range from the apex to the edge where our molecular beam fits onto the crystal's surface, i.e. at 4-5 atom wide terraces. The dissociation probability

measured in the same range increases by at least a factor of 7.5, depending on the exact value used for S_0 at Pt(111). HD production, therefore, does not track the change in elementary dissociation. We interpret this observation as possibly suggesting that the higher binding energy of H(D) atoms at steps limits their mobility and diffusion, hence increasing the chance to desorb with their original partner. Shifting the balance in the two equilibria of the homonuclear isotopologues puts formation of the heteronuclear isotopologues at a disadvantage, reducing the rate of HD formation relative to the dissociation. The impact of diffusion on the rate of product formation was recently also implied in a study of CO oxidation on Pt(111) and stepped surfaces. [22] There also, steps break the symmetry of the (111) plane and cause diffusion to be non-isotropic.

5.4. OUTLOOK AND CONCLUSION

We have presented a structural analysis of a curved Pt single crystal with (111) at the apex and kinked surfaces towards the sides. We find that, with the applied cleaning procedure, most parts of the surface are cleaned thoroughly and form ordered stepped arrays. Using the equilibrated shape of residual vacancy islands near the apex, we can identify A- and B-type steps within the kinked step edges and determine the chirality of stepped surfaces on either side of the apex. This opens possibilities for chemical experiments probing chiral activity. The unintentional defects in close proximity to the apex are abundant, but do not significantly affect experiments that probe chemical reactivity towards achiral reactions, i.e. D_2 dissociation and HD formation. For both reactions we find a (nearly) linear increase with step density. For the dissociation, it reconfirms that steps provide much higher dissociation probabilities than terrace sites and that, over a wide range, the measured reactivity may be taken as a linear sum of individual contributions by steps and terraces. A slight deviation from linearity at the highest step densities may be indicative of improved diffractive scattering from highly ordered step arrays or another mechanism that lowers reactivity. The linearity of the entire range, but considerably lower dependence on step density for HD production, may indicate anisotropic diffusion caused by higher binding of H (D) atoms at steps sites. Lastly, we note the potential of curved crystals to extract reactivities for perfect, defect-free flat surfaces, such as (111), forging an important bridge between experimental and theoretical results.

REFERENCES

[1] R. D. Muiño and H. F. Busnengo, editors. *Dynamics of gas-surface interactions*, volume 50. Springer, 2013.

[2] I. L. Buurmans and B. M. Weckhuysen. Heterogeneities of individual catalyst particles in space and time as monitored by spectroscopy. *Nature chemistry*,

4(11):873–886, 2012.

[3] K. Honkala, A. Hellman, I. N. Remediakis, A. Logadottir, A. Carlsson, S. Dahl, C. H. Christensen, and J. K. Nørskov. Ammonia synthesis from first-principles calculations. *Science*, 307(5709):555–558, 2005.

[4] H. A. Al-Abadleh and V. H. Grassian. Oxide surfaces as environmental interfaces. *Surface Science Reports*, 52(3-4):63–161, 2003.

[5] A. T. Bell. The impact of nanoscience on heterogeneous catalysis. *Science*, 299(5613):1688–1691, 2003.

[6] D. Liang, G. Abend, J. Block, and N. Kruse. Formation of nickel subcarbonyls from nickel and carbon monoxide. *Surface Science*, 126(1-3):392–396, 1983.

[7] J. Block and N. Kruse. Chemical surface reactions of CO on the atomic scale: Investigations by field ion microscopy and mass spectrometry. *Reaction Kinetics and Catalysis Letters*, 35(1-2):11–20, 1987.

[8] C. Voss and N. Kruse. Oscillatory behavior in the catalytic reduction of NO and NO_2 with hydrogen on Pt field emitter tips. *Applied surface science*, 94:186–193, 1996.

[9] C. Voss and N. Kruse. Chemical wave propagation and rate oscillations during the NO_2/H_2 reaction over Pt. *Ultramicroscopy*, 73(1-4):211–216, 1998.

[10] T. Visart de Bocarmé and N. Kruse. Kinetic instabilities during the NO_x reduction with hydrogen on Pt crystals studied with field emission on the nanoscale. *Chaos: An Interdisciplinary Journal of Nonlinear Science*, 12(1):118–130, 2002.

[11] T. V. de Bocarmé, T.-D. Chau, and N. Kruse. Imaging and probing catalytic surface reactions on the nanoscale: Field Ion Microscopy and atom-probe studies of O_2-H_2/Rh and NO-H_2/Pt. *Topics in catalysis*, 39(1-2):111–120, 2006.

[12] C. Barroo, Y. De Decker, T. Visart de Bocarmé, and N. Kruse. Complex oscillation patterns during the catalytic hydrogenation of NO_2 over platinum nanosized crystals. *The Journal of Physical Chemistry C*, 118(13):6839–6846, 2014.

[13] C. Barroo, Y. De Decker, T. Visart de Bocarmé, and P. Gaspard. Fluctuating dynamics of nanoscale chemical oscillations: theory and experiments. *The journal of physical chemistry letters*, 6(12):2189–2193, 2015.

[14] C. Barroo, V. Voorsluijs, T. V. de Bocarmé, P. Gaspard, and Y. De Decker. Reconstructing stochastic attractors from nanoscale experiments on a non-equilibrium reaction. *Physical Chemistry Chemical Physics*, 20(33):21302–21312, 2018.

[15] J.-S. McEwen, P. Gaspard, Y. De Decker, C. Barroo, T. Visart de Bocarmé, and N. Kruse. Catalytic reduction of NO_2 with hydrogen on Pt field emitter tips: kinetic instabilities on the nanoscale. *Langmuir*, 26(21):16381–16391, 2010.

[16] A. Kleyn. Molecular beams and chemical dynamics at surfaces. *Chemical Society Reviews*, 32(2):87–95, 2003.

[17] D. A. McCormack, R. A. Olsen, and E. J. Baerends. Mechanisms of H2 dissociative adsorption on the Pt(211) stepped surface. *Journal of Chemical Physics*, 122(19):194708, 2005.

[18] A. den Dunnen, S. Wiegman, L. Jacobse, and L. B. Juurlink. Reaction dynamics of initial O_2 sticking on Pd(100). *The Journal of Chemical Physics*, 142(21):214708, 2015.

[19] A. Gutiérrez-González, F. F. Crim, and R. D. Beck. Bond selective dissociation of methane (CH_3D) on the steps and terraces of Pt (211). *The Journal of Chemical Physics*, 149(7):074701, 2018.

[20] E. W. Smeets, G. Füchsel, and G. J. Kroes. Quantum Dynamics of Dissociative Chemisorption of H_2 on the Stepped Cu(211) Surface. *Journal of Physical Chemistry C*, 123(37):23049–23063, 2019.

[21] H. Chadwick, A. Gutiérrez-González, R. D. Beck, and G. J. Kroes. CHD_3 Dissociation on the Kinked Pt(210) Surface: A Comparison of Experiment and Theory. *Journal of Physical Chemistry C*, 123(23):14530–14539, 2019.

[22] J. Neugebohren, D. Borodin, H. W. Hahn, J. Altschäffel, A. Kandratsenka, D. J. Auerbach, C. T. Campbell, D. Schwarzer, D. J. Harding, A. M. Wodtke, et al. Velocity-resolved kinetics of site-specific carbon monoxide oxidation on platinum surfaces. *Nature*, 558(7709):280–283, 2018.

[23] L. Zhou, A. Kandratsenka, C. T. Campbell, A. M. Wodtke, and H. Guo. Origin of Thermal and Hyperthermal CO_2 from CO Oxidation on Pt Surfaces: The Role of Post-Transition-State Dynamics, Active Sites, and Chemisorbed CO2. *Angewandte Chemie*, 131(21):6990–6994, 2019.

[24] K. Cao, R. van Lent, A. W. Kleyn, M. Kurahashi, and L. B. Juurlink. Steps on Pt stereodynamically filter sticking of O_2. *Proceedings of the National Academy of Sciences of the United States of America*, 116(28):13862–13866, 2019.

[25] A. Gutiérrez-González, M. Torio, H. Busnengo, and R. D. Beck. Site selective detection of methane dissociation on stepped Pt surfaces. *Topics in Catalysis*, 62(12-16):859–873, 2019.

[26] H. Chadwick, A. Gutiérrez-González, D. Migliorini, R. D. Beck, and G. J. Kroes. Incident Angle Dependence of CHD_3 Dissociation on the Stepped Pt(211) Surface. *Journal of Physical Chemistry C*, 122(34):19652–19660, 2018.

[27] H. Chadwick, A. Gutiérrez-González, R. D. Beck, and G. J. Kroes. Transferability of the SRP32-vdW specific reaction parameter functional to CHD_3 dissociation on Pt(110)-(2 × 1). *Journal of Chemical Physics*, 150(12):124702, 2019.

[28] F. Muttaqien, Y. Hamamoto, K. Inagaki, and Y. Morikawa. Dissociative adsorption of CO_2 on flat, stepped, and kinked Cu surfaces. *The Journal of chemical physics*, 141(3):034702, 2014.

[29] B. Poelsema, K. Lenz, and G. Comsa. The dissociative adsorption of hydrogen on defect-'free' Pt (111). *Journal of physics: condensed matter*, 22(30):304006, 2010.

[30] B. Poelsema, K. Lenz, and G. Comsa. The dissociative adsorption of hydrogen on Pt(111): Actuation and acceleration by atomic defects. *The Journal of chemical physics*, 134(7):074703, 2011.

[31] S. V. Auras and L. B. Juurlink. Recent advances in the use of curved single crystal surfaces. *Progress in Surface Science*, to be published.

[32] R. Van Lent, S. V. Auras, K. Cao, A. J. Walsh, M. A. Gleeson, and L. B. Juurlink. Site-specific reactivity of molecules with surface defects—the case of H_2 dissociation on Pt. *Science*, 363(6423):155–157, 2019.

[33] F. Schiller, M. Ilyn, V. Pérez-Dieste, C. Escudero, C. Huck-Iriart, N. Ruiz del Arbol, B. Hagman, L. R. Merte, F. Bertram, M. Shipilin, et al. Catalytic Oxidation of Carbon Monoxide on a Curved Pd Crystal: Spatial Variation of Active and Poisoning Phases in Stationary Conditions. *Journal of the American Chemical Society*, 140(47):16245–16252, 2018.

[34] S. V. Auras, R. van Lent, D. Bashlakov, J. M. Piñeiros Bastidas, T. Roorda, R. Spierenburg, and L. B. F. Juurlink. Scaling Platinum-Catalyzed Hydrogen Dissociation on Corrugated Surfaces. *Angewandte Chemie International Edition*, 59(47):20973–20979, 2020.

[35] E. Hahn, H. Schief, V. Marsico, A. Fricke, and K. Kern. Orientational instability of vicinal Pt surfaces close to (111). *Physical review letters*, 72(21):3378, 1994.

[36] G. Comsa, G. Mechtersheimer, and B. Poelsema. He beam scattering and LEED evidence for partial facetting of a Pt(997) surface. *Surface Science*, 97(1):L297–L303, 1980.

[37] M. Sander, R. Imbihl, and G. Ertl. Kinetic oscillations in catalytic CO oxidation on a cylindrical Pt single crystal surface. *The Journal of chemical physics*, 97(7):5193–5204, 1992.

[38] J. Schweicher, A. Bundhoo, A. Frennet, and N. Kruse. Dynamic Hydrogen–Deuterium Exchange to Determine Metallic Surface Areas of Catalysts. *Catalysis letters*, 144(2):204–210, 2014.

[39] C. F. McFadden, P. S. Cremer, and A. J. Gellman. Adsorption of chiral alcohols on "chiral" metal surfaces. *Langmuir*, 12(10):2483–2487, 1996.

[40] T. Michely, T. Land, U. Littmark, and G. Comsa. Morphological effects induced by the formation of a Pt-adatom lattice gas on Pt(111). *Surface science*, 272(1-3):204–210, 1992.

[41] D. A. King and M. G. Wells. Molecular beam investigation of adsorption kinetics on bulk metal targets: Nitrogen on tungsten. *Surface Science*, 29(2):454–482, 1972.

[42] K. Lu and R. Rye. Flash desorption and equilibration of H_2 and D_2 on single crystal surfaces of platinum. *Surface Science*, 45(2):677–695, 1974.

[43] K. Christmann and G. Ertl. Interaction of hydrogen with Pt(111): the role of atomic steps. *Surface Science*, 60(2):365–384, 1976.

[44] M. J. van der Niet, A. den Dunnen, L. B. Juurlink, and M. T. Koper. The influence of step geometry on the desorption characteristics of O_2, D_2, and H_2O from stepped Pt surfaces. *The Journal of chemical physics*, 132(17):174705, 2010.

[45] M. J. Kolb, A. L. Garden, C. Badan, J. A. G. Torres, E. Skúlason, L. B. Juurlink, H. Jónsson, and M. T. Koper. Elucidation of temperature-programmed desorption of high-coverage hydrogen on Pt(211), Pt(221), Pt(533) and Pt(553) based on density functional theory calculations. *Physical Chemistry Chemical Physics*, 21(31):17142–17151, 2019.

[46] C. Badan, M. T. Koper, and L. Juurlink. How well does Pt(211) represent Pt[n(111)×(100)] surfaces in adsorption/desorption? *The Journal of Physical Chemistry C*, 119(24):13551–13560, 2015.

[47] R. van Lent. *Steps in gas-surface reactions*. PhD thesis, Leiden University, 2019. Chapter 4.

[48] K. Cao. *Structure dependence of molecular reactions on surfaces*. PhD thesis, Leiden University, 2018. Chapter 5.

[49] T. Michely and G. Comsa. Temperature dependence of the sputtering morphology of Pt(111). Technical report, 1991.

[50] A. Luntz, J. Brown, and M. Williams. Molecular beam studies of H_2 and D_2 dissociative chemisorption on Pt (111). *The Journal of chemical physics*, 93(7):5240–5246, 1990.

[51] A. Gee, B. Hayden, C. Mormiche, and T. Nunney. The role of steps in the dynamics of hydrogen dissociation on Pt(533). *The Journal of Chemical Physics*, 112(17):7660–7668, 2000.

[52] I. M. Groot, A. W. Kleyn, and L. B. Juurlink. The energy dependence of the ratio of step and terrace reactivity for H_2 dissociation on stepped platinum. *Angewandte Chemie International Edition*, 50(22):5174–5177, 2011.

[53] I. Groot, K. Schouten, A. Kleyn, and L. Juurlink. Dynamics of hydrogen dissociation on stepped platinum. *The Journal of chemical physics*, 129(22):224707, 2008.

[54] K. Cao, R. van Lent, A. Kleyn, and L. Juurlink. A molecular beam study of D_2 dissociation on Pt(111): Testing SRP-DFT calculations. *Chemical Physics Letters*, 706:680–683, 2018.

[55] A. L. Walter, F. Schiller, M. Corso, L. R. Merte, F. Bertram, J. Lobo-Checa, M. Shipilin, J. Gustafson, E. Lundgren, A. X. Bríon-Ríos, et al. X-ray photoemission analysis of clean and carbon monoxide-chemisorbed platinum (111) stepped surfaces using a curved crystal. *Nature communications*, 6(1):1–7, 2015.

[56] J. E. Ortega, M. Corso, Z. Abd-el Fattah, E. Goiri, and F. Schiller. Interplay between structure and electronic states in step arrays explored with curved surfaces. *Physical Review B*, 83(8):085411, 2011.

[57] P. Samson, A. Nesbitt, B. Koel, and A. Hodgson. Deuterium dissociation on ordered Sn/Pt(111) surface alloys. *The Journal of chemical physics*, 109(8):3255–3264, 1998.

6

IT'S NOT JUST THE DEFECTS - A CURVED CRYSTAL STUDY OF H_2O DESORPTION FROM AG

We investigate water desorption from hydrophobic surfaces using two curved Ag single crystals centered at (111) and (001) apices. On these types of crystals the step density gradually increases along the curvature, allowing us to probe large ranges of surface structures in between the (001), (111) and (110) planes. Subtle differences in desorption of submonolayer water coverages point toward structure dependencies in water cluster nucleation. The B-type step on hydrophobic Ag binds water structures more strongly than adjacent (111) planes, leading to preferred desorption from steps. This driving force is smaller for A-type steps on (111) terraces. The A'-type step flanked by (001) terraces shows no indication of preferred desorption from steps. Extrapolation to the (311) surface, not contained within either curved surface, demonstrates that both A- and A'-type steps can be regarded chemically identical for water desorption. The different trends in desorption temperature on the two crystals can thus be attributed to stronger water adsorption at (001) planes than at (111) planes and identical to adsorption at the step. These results show that our approach to studying the structure dependence of water desorption is sensitive to variations in desorption energy smaller than 'chemical accuracy', i.e. 1 kcal/mol.

This chapter is based on the following publication:
Sabine V. Auras, Robert A. B. van Bree, Dima L. Bashlakov, Richard van Lent, and Ludo B. F. Juurlink. It's not just the defects – a curved crystal study of H_2O desorption from Ag. *Phys. Chem. Chem. Phys.*, **21** 15422–15430 (2019).

6.1. INTRODUCTION

WATER IS UBIQUITOUS on our planet and crucial to many processes both in nature and industry. As such, the study of water sparks interest in many different areas of research, from meteorology and astronomy to physics, chemistry, and engineering. Specifically, the interface of water with metal surfaces, relevant for electrochemistry, corrosion phenomena, and others, is complex and highly structure sensitive. Despite many years of research in this area, the underlying principles that determine water structures on different metals are not yet fully understood.[1, 2]

Generally, water on metal surfaces tends to form 2D clusters with distinct structures at sufficiently low temperatures, due to a low diffusion barrier even at those temperatures.[2] At sub-monolayer coverages, adsorption is influenced by the competition between water-metal bonding and the internal hydrogen bonding of water networks. As a consequence, three types of adsorption are found: wetting, non-wetting and (partially) dissociative.

The exact structure of adsorbed water is highly surface dependent and can have a strong influence on the resulting adsorption/desorption behaviour. We have previously shown this for water adsorption on Pt(111) surfaces.[3–6] There, nucleation of ice preferentially happens at step edges. The subsequent growth depends not only on the width of the adjacent terrace but differences were also observed for the two different step types found on (111) terraces, A- and B-type steps.[3] To understand the principles of water adsorption it is therefore necessary to not only consider high symmetry facets, but also the influence of lower coordinated sites, which can have deviant reactivities, adsorption or desorption properties. However, while there is substantive literature on water on close packed surfaces of various metals, less is known about surfaces with a more open symmetry.

This study focuses on differences in water adsorption on Ag surfaces with different terrace and step geometries. As Ag is a less reactive metal than Pt, the changes in adsorption on different surfaces are expected to be even more subtle. Ag surfaces are known to be non-wetting for the first layer of H_2O. Their weak metal-water interactions[7] cause the formation of 3D clusters that optimise hydrogen bonding in the water network. On Ag(100) 3D clusters are found even before the first layer is completed.[8] Subsequent multilayer water adsorption can result in the formation of amorphous solid water (ASW) or crystalline ice (CI); the transition from ASW to CI on water happens at >145 K. [9, 10]

In an early flash desorption study comparing Ag surfaces on a small spherical crystal it was found that Ag(100) and Ag(111) have the same 0^{th} order desorption feature at 170 K (in agreement with a study on Ag(311)). The resulting desorption energy matched the sublimation energy of ice.[11] The authors therefore concluded

that ASW on Ag is not substrate dependent and sublimates freely. However, it is known that water on Ag(111) exclusively forms clusters of hexamers up to nonamers at very low coverages, while with increasing coverage larger amorphous clusters start to dominate.[12] It is therefore possible that at low coverages water adsorption has surface dependencies that were not observed in the earlier study.

Here we report that despite identical behaviour of multilayers of ASW on the different Ag surfaces, substrate dependence is observable for sub-monolayer adsorption. We use our curved crystal approach to examine these effects that would likely not be observable with a traditional flat single-crystal approach. Two curved Ag single crystals allow for easy variation of surface structure in order to examine small influences of step type and density. The two crystals, one with (111) the other with (001) terraces, linearly increase their step density from 0.01 nm^{-1} at the apex to >1 nm^{-1} at the sides.

6.2. EXPERIMENTAL

Cleaning and structural investigation by electron diffraction of the curved Ag crystals described in this study were performed using a UHV instrument with a base pressure of $1.5 \cdot 10^{-10}$ mbar as measured with an uncallibrated cold cathode pressure gauge (PFEIFFER IKR 261). It is equipped with a BALZERS QME 200 quadrupole mass spectrometer (QMS) used for residual gas analysis (RGA), a Low Energy Electron Diffraction (LEED) apparatus consisting of an electron gun (LEG 24) and LEED optics (VG, RVL-900), a sputter gun (PREVAC IS 40C1), and a hot cathode pressure gauge controlled by a MULTI VARIAN controller. After trying different cleaning procedures, it was found that both crystals could be cleaned over their entire surface areas by 10 min Ar^+ sputtering at low sputtering currents (0.5 μA) from low sputtering energies (0.25 kV). We sputtered under a 45° angle from the apex so that ions approached the surface along the step edges. Subsequently, crystals were annealed for 20 minutes at 670 K.

Scanning Tunneling Microscopy (STM) images were taken in a commercial vacuum system (OMICRON) consisting of a preparation and analysis chamber, as well as a load lock for transferring samples in and out of vacuum. Preparation and analysis chamber both had a base pressure of $2 \cdot 10^{-10}$ mbar measured by two individual Bayard-Alpert type manometers and could be separated by a gate valve. The Omicron STM system has been described in detail before.[13]

Spatially resolved temperature-programmed desorption (TPD) experiments were carried out in a third UHV chamber with a base pressure of $9 \cdot 10^{-11}$ mbar as measured with a uncalibrated cold cathode pressure gauge (PFEIFFER IKR 261). This system has been described previously as well.[4, 14] Cleaning of samples followed the same procedure that had been confirmed by LEED and STM to deliver clean and well-defined surfaces. Water (MILLIPORE, 18.2 MΩ) was degassed by multiple freeze-pump-thaw cycles prior to dosing. The water flask was part of a homebuilt dosing system based

on the design of a capillary array doser and exposed to 1.1 bar He as a carrier gas at a water temperature of 323 K. The gas mixture was subsequently directly dosed onto the crystal at 90 K. The lowest coverages shown in this paper were achieved by determining the lowest dose that still resulted in an observable desorption signal. In the case of c-Ag(111) this was 4 L (He/H_2O), in the case of Ag(001) 8 L (He/H_2O). A second quadrupole mass spectrometer(BALTZERS QMA400) in a differentially pumped stage was separated from the main chamber by a plate with a 0.5 x 5 mm^2 rectangular slot. In order to optimize the spatial resolution during TPD experiments, the crystal was brought in close proximity of the slot and aligned parallel to it. TPDs were performed at a temperature rate of 1 K/s, going from 90 K to 270 K.

To mount either of the two curved Ag samples in the UHV instruments, it was held by a polycrystalline Ag cap onto a Cu baseplate. Two screws firmly attached the cap to the plate. The assembly was attached to a Cu extension of a bath cryostat using two screws at the top of the Cu base plate. Crystal temperatures as low as 88 K can be reached. The Cu base plate was heated radiatively or by electron bombardment with a commercial light bulb filament positioned behind the crystal assembly. The crystal temperature was measured with a type-K thermocouple inserted into a small opening between the crystal and the Ag cap. To obtain temperature control we used a PID controller (EUROTHERM 2416).

The curved crystals may be viewed as 31 ° sections of a cylinder with a 15 mm radius that has its rotational axis along the [1$\bar{1}$0] direction. On the c-Ag(111)31° [1$\bar{1}$0] crystal, the section is centered at the [111] vector as depicted in figure 6.1a). The macroscopic curvature is caused by decreasing (111) terraces separated by (001)-oriented steps at one side (blue section in figure 6.1a)) and (110)-oriented steps at the other side of the crystal (red section). These two different step types are referred to as A- and B-type respectively.[15] Their atomic structure in bird's eye view and side view can be found in figure 6.1 a) and b) respectively. Step densities on this crystal go up to 0.114 $Å^{-1}$ at the edges, which corresponds to stepped surfaces with 8.77 Å wide terraces. Respectively, the c-Ag(001)31° [1$\bar{1}$0] crystal is centered at [001]. To both sides of the (001) apex steps with {111}-oriented microfacets cause the curvature. In the absence of restructuring, surfaces range from (001) at the middle of the crystal to a step density of 0.132 $Å^{-1}$, or 7.58 Å wide terraces, at the outer edges. We suggest the nomenclature of c-Ag(111)31° [1$\bar{1}$0] and c-Ag(001)31° [1$\bar{1}$0] to fully describe the crystallographic properties of these crystals, however for the sake of brevity we will use the shorter notation of c-Ag(111) and c-Ag(001) to distinguish the two crystals within this paper.

As figure 6.1a) illustrates, the hollow site of steps on the (001) terraces resembles the hollow site of A-type steps on (111) terraces. We consequently note them as A'-type steps. This hollow site, known as a B_5 site,[16] consists of 5 atoms arranged in a square site adjacent to a triangular site. This site is a (311) microfacet. The crystallographic orientation of (311) relative to the (001) and (111) surfaces is indicated in figure 6.1a).

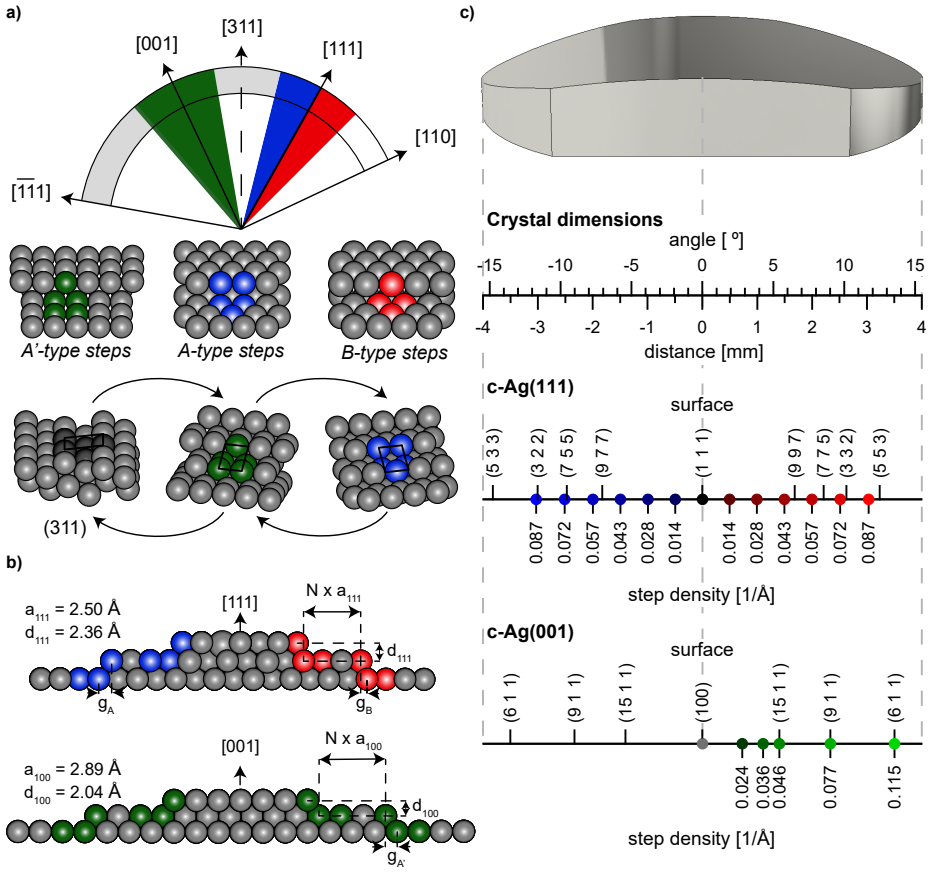

Figure 6.1: Schematic drawings of orientation and surface structures of the two curved crystals employed in this study. **a)** Orientation of the c-Ag(001)31° [1$\bar{1}$0] (green) and c-Ag(111)31° [1$\bar{1}$0] (blue and red) crystals on a cylinder with its rotational axis along [1$\bar{1}$0]. Below the step types that separate (001)/(111) terraces on the two crystals respectively. Also shown, the (311) surface and its unit cell, and how this surface can be seen as consisting of only A- or only A'-type steps. **b)** Schematic microscopic side view of the two crystals, indicating parameters used in equation 6.1. In the center, the crystals feature wide terraces. As the crystal curves to the sides, steps are introduced to accommodate the macroscopic curvature. **c)** Drawing of the macroscopic shape of the crystals linking macroscopic properties of the crystal (angle of curvature, distance from apex), to microscopic properties found on the surface, i.e. Miller indices of surface structures at specific points of the crystal. Positions of measurements in figure 6.4 are indicated in blue, red, and green with their respective step densities. Step densities for monoatomic steps do not follow the same scale on the two crystals because of different step heights on (001) and (111) terraces, as indicated in b).

While we cannot investigate this surface directly, we approach it from two sides on two separate crystals.

Both crystals used here have the same dimensions: 8 mm along the length across a curvature of 31°and a width of 7 mm at the widest part of the crystal. Figure 6.1c) indicates positions across the crystals where our measurements were carried out and the prevailing step density at that position in case of monoatomic height steps. The figure also indicates the Miller indices of some commonly used vicinal surfaces and where they can be found on our curved crystals.

6.3. RESULTS

Results for the curved Ag(111) crystal have been published before, but were newly analysed from the raw data here for consistent comparison with the curved Ag(001) crystal, leading to new insights.[14]

6.3.1. SURFACE STRUCTURE INVESTIGATION

In order to confirm that the crystal surface exhibits the structures we would predict at each position on the crystal, we first investigate the surface structure and cleanliness with LEED and STM.

LEED is a useful technique to acquire information on the overall order of a surface. While expected diffraction patterns at the low Miller index surfaces at the center of the crystals are easy to construct, at angles away from the apex, the crystal curvature causes periodic steps on the surface. The offset between successive terraces yields additional diffraction,[17] that can be described according to equation 6.1 [18]:

$$\Delta\varphi = \lambda/[(Na+g)\cos\varphi - d\sin\varphi] \tag{6.1}$$

where λ is the wavelength of the electron beam, N is the number of atom rows within one terrace (including the step edge), a is the separation of atom rows in Å, g is the horizontal shift of the top layer in Å and d is the step height in Å. Parameters are visualized in figure 6.1b). As a consequence, split spots appear in the LEED patterns. The length of spot splitting relative to the row spacing in LEED patterns of stepped surfaces is dependent on terrace length. Van Hove and Somorjai[19] calculated these ratios for a large number of different surface structures.

The low energy electron diffraction pattern was checked over the entire surface areas of the two crystals to ensure cleanliness and the absence of faceting. Additionally, the energy dependence of the (0,0) spot splitting behaviour was examined according to *Henzler*[18] to confirm the presence of mono-atomic steps across the crystals, as has also been previously described for a similar curved Ag crystal.[20]

After sufficient cleaning, the apices yielded the typical hexagonal and square patterns for the (111) and (001) surfaces respectively. As figure 6.2a) displays, diffraction spots at the apices are well-defined and symmetrically round. Moving away from the apex results in elongated, oval-shaped spots that eventually split into two spots. Spot splitting then increases linearly with angle away from the apex in both cases. Figure 6.2b) plots the measured spot splitting to row spacing ratios (*ss/rs*) at different positions on the crystal surface, which follows the predicted values closely.[19] The different slope of *ss/rs* on the c-Ag(111) and c-Ag(001) crystals is a direct result of the difference in step height on (111) and (001) terraces, as indicated in figure6.1b). Larger step heights require fewer steps, i.e. a smaller step density, on a flat terrace to achieve the same tilt in surface normal, thus a smaller spot splitting will be observed. The ratio between *ss/rs* on the stepped Ag(111) surfaces (slope_{111}=0.021/1°) and *ss/rs* on the stepped Ag(001) surfaces (slope_{100}=0.0245/1°) is 0.857. The inverse of the ratio between step heights (d_{111}=2.36 A and d_{100}=2.04 A) is 0.864.

STM images (figure 6.2c)) from the apices of the two crystals and the sides confirm cleanliness as well as the absence of faceting and show large arrays of ordered steps with the predicted orientation. Images show frizzy step edges as commonly found on Ag surfaces.[20–22]

On the c-Ag(111) crystal, white protrusions appear over <2 % of the surface area. As they cannot be removed by extensive cleaning procedures, they appear to be chemically inert and likely remnants of the polishing process. While the mean terrace width expected at each position along the curvature is not affected by these protrusions, they impact the regular ordering of the terrace arrays, by pinning the steps. Checking their occurrence at different positions on the surface gives a uniform density over the entire range of the c-Ag(111) crystal. Therefore they cannot be the cause for structure dependencies in water desorption discussed in this paper. On the c-Ag(001) crystal, while the overall step density is as expected, we find large variations between the widths of terraces as well as within individual terraces. At more highly stepped surfaces, very regular arrays of terraces are found.

6.3.2. TEMPERATURE PROGRAMMED DESORPTION

TEMPERATURE CALIBRATION

TPD is a technique demonstrating the differences between accuracy and precision in scientific measurements. The precision with which the temperature can be measured during TPD can be influenced by different factors, such as temperature gradients across the surface due to non-uniform heating or fast heating-ramps. In general, however, temperatures can be recorded very precise and reproducible within the same set of data. On the other hand accuracy, i.e. absolute values, are often difficult to compare between different samples. Amongst others, small differences in ther-

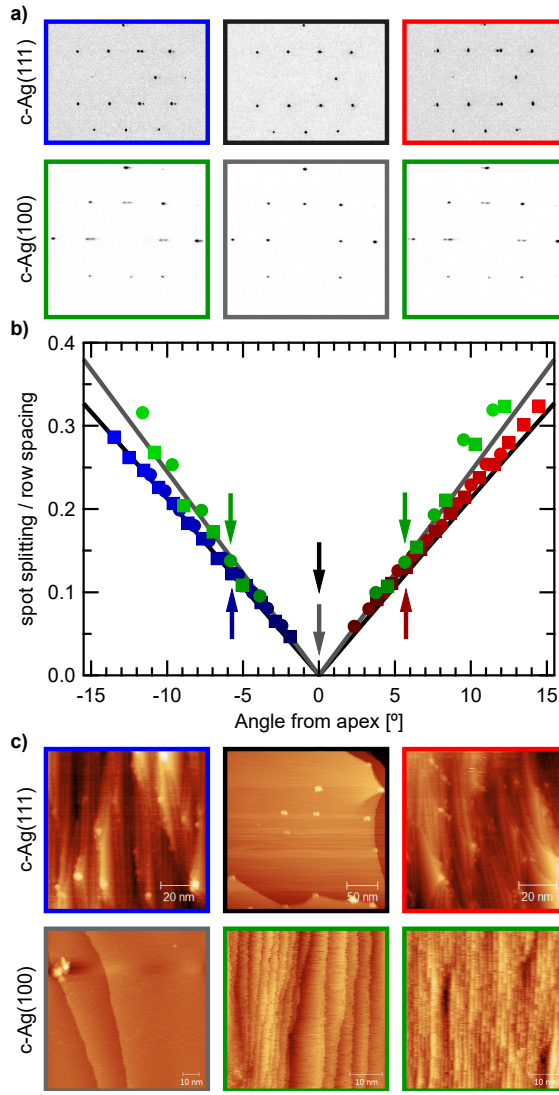

Figure 6.2: **a)** Top row: LEED images from the c-Ag(111) crystal. At the center of the crystal (black frame) the hexagonal diffraction pattern expected from (111) surfaces is observed. Left and right images: diffraction patterns showing spot splitting, obtained at 1.5 mm from the apex to the side with A-type steps (blue frame) and 1.5 mm to the side with B-type steps(red frame). Bottom row: LEED images from the c-Ag(001) crystal. At the center of the crystal (grey frame) the square diffraction pattern characteristic for (001) surfaces is observed. LEED patterns obtained at 1.5 mm from the apex on both sides (green frames) produce the same spot splitting on both sides, and the same sharpness of the spots as the center, showing that our cleaning procedure results in well-defined and clean surfaces over the entire crystal. **b)** Spot splitting over row spacing (*ss*/*rs*) ratios measured across the range of the two crystals. Arrows indicate positions of the images in a). Black/grey lines indicate the expected values on stepped (111) and (001) surfaces. **c)** Top row: STM images of the c-Ag(111) crystal at -1.6 mm from center, apex and 2.2 mm from center(left to right). At the apex, very large terraces are observed, with terrace widths comparable to that of flat (111) crystals typically used in experiments. Bottom row: STM images of the c-Ag(001) crystal at the apex, 1.8 and 2.3 mm from the apex (from left to right).

mocouple connectivity to the sample may have significant influence on the accuracy of the experiments while maintaining precision. Here, water desorption from thick layers provides us with an internal thermostat that allows us to responsibly compare subtle differences at lower coverages, even when experiments were carried out on two crystals at different times.

In the following we elucidate step for step the observations that allow us to internally calibrate temperature readings from separate sets of data: Firstly, figure 6.3a) shows TPD spectra from Ag(001) at various initial coverages. Only one desorption feature is present with the typical shape of 0^{th} order desorption: all traces follow the same onset, then rapidly drop off at a point determined by the different coverages. This 0^{th} order behaviour is observed for all Ag surfaces, i.e. not only on the c-Ag(001) crystal, but also on the c-Ag(111) crystal.

Next, comparing desorption from different surfaces on the c-Ag(001) crystal after the same dose in figure 6.3b) demonstrates a good overlap in onset, height and overall shape of the desorption feature. This confirms that there is no temperature gradient across the surface of our crystal. Again, the same is observed when comparing the same dose on various surfaces on the c-Ag(111) crystal. We conclude that high coverages of H_2O give the same 0^{th} desorption feature independent of Ag surface structure, in agreement with results obtained by Klaua and Madey.[11] However, when comparing data from the (001) and the (111) surface in figure 6.3c), the onset of desorption differs visibly. This must be due to slight experimental differences in our temperature measurements at the two different crystals. We thus need to adjust the temperature scales of the two sets of data. As we do not know which scale is closer to the actual temperature, we arbitrarily choose to shift surfaces on the c-Ag(001) crystal to match the onset of the c-Ag(111) surfaces. Analysing the onset of desorption from all measured surfaces after 120 L doses gives a difference of 2.8 K between the two crystals. Shifting data from Ag(001) by 2.8 K in figure 6.3d) results in a matching onset of desorption with Ag(111). When comparing various surfaces on the two crystals we now observe the same good overlap as observed internally on each crystal. This observation allows us to internally calibrate our temperature measurements between the two sets of experiments. In the following all data from the c-Ag(001) crystal is shifted by the same value, regardless of coverage. This temperature shift is crucial as in the following section we are investigating rather subtle surface dependencies in water adsorption, i.e. the influence of terrace and step geometries on the overall weak interactions between water and the Ag surfaces.

SUBMONOLAYER COVERAGES

In order to probe metal-water interactions directly we dose amounts of water resulting in submonolayer coverages. Experiments on the two curved crystals were carried out at the same surface temperature and with the same dosing flux, to ensure that

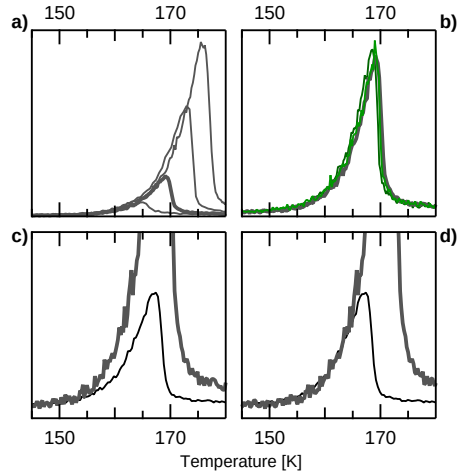

Figure 6.3: **a)** TPD spectra from Ag(001) after various doses of the He/H_2O gas mixture. Doses from 40 L, 120 L (bold), 240 L, and 480 L. The spectra follow the same onset, with the position of the peak maximum depending on the dose. This behaviour is typical for 0^{th} order desorption. The same behaviour at varying doses was observed at all measured surfaces on both the c-Ag(001) and c-Ag(111) crystal. Doses refer to the pressure of the He/H_2O mixture dosed during experiments. **b)** TPD spectra from Ag(001) (grey bold) and stepped surfaces (green) after the same (120 L) dose. The spectra overlap very well, showing consistent dosing within one set of experiments and no surface dependency of the desorption feature. Similarly, dosing the same amount at different surfaces on the c-Ag(111) crystal resulted in overlapping TPD spectra.[14] **c)** Comparing TPD spectra from Ag(001) (grey bold) and Ag(111) (black) after a dose of 120 L, reveals that the onsets don't overlap. d) Shifting the Ag(001) data in b) by 2.8 K gives a good overlap of the onset of desorption in both cases.

differences in desorption temperature are not due to these experimental parameters. Here, differences in desorption from different surfaces become apparent as demonstrated in figure 6.4a). The two left panels show TPD spectra obtained after a 4 L dose of the He/H_2O mixture using the c-Ag(111) crystal. We have previously determined this dose to correspond to a surface coverage of 0.06-0.08 ML.[14] The higher background signal after the desorption peaks (in figure 6.3 and 6.4) is due to the long vacuum time constant of water in our apparatus. While we have previously described an adequate background subtraction to correct for this,[23] we here show the raw data where only the background before the peak is set to zero. Spectra for surfaces containing the A-(B-)type steps are shown in the left (middle) panel. From bottom to top, step density increases. Firstly, the typical shape of 0^{th} order desorption is lost and instead a more symmetric peak is observed that can be fitted well with a Gaussian line shape. The center of the fitted Gaussian line shape for the (111) apex is indicated as a dashed line. As we increase step density for both A- and B-type steps, the center of the Gaussian fits shift visibly to higher temperatures.

Results from experiments performed with the c-Ag(001) crystal after a 8 L dose of the He/H_2O mixture are shown in the right panel of figure 6.4a). Results after a 4 L dose show the same trends but the water desorption signals are barely distinguishable from the baseline and difficult to fit. In both cases the same flux as in the experi-

ments on c-Ag(111) was used. Additionally, a 16 L dose also shows the same, allowing us to exclude a coverage dependence on desorption. Contrarily to c-Ag(111), the peak desorption temperature at the (001) apex, indicated with the grey dashed line, shows no clear shift as the density of A'-type steps is increased. The peak desorption temperature of (001) even seems marginally higher than at the stepped surfaces.

We analyze our data quantitatively by considering the Gaussian fit parameters. Each fit yields three parameters, i.e. a peak desorption temperature, an amplitude and a width. The peak desorption temperatures as obtained from our fits are plotted against step density in figure 6.4b). Note that both step density axes (c-Ag(111) at the bottom and c-Ag(001) at the top) are extended considerably beyond the densities present on the curved crystals. The range on the crystals is indicated by vertical dashed lines.

For the c-Ag(111) crystal, the desorption temperature monotonically increases with step density over the entire crystal curvature. A linear fit to the data for the A-type steps (blue), indicates that the desorption temperature increases with 22 K·Å. Error bars to the linear fit are represented by the shaded area. On the B side the increase is significantly steeper, 44 K·Å. Error bars are of similar size, but not shown for clarity. We have also analyzed the amplitude and width parameters - they show no trend with step density and vary only marginally over the entire step density range that was investigated. This indicates that the area under the curves, i.e. the H_2O coverage, does not vary significantly between experiments and thus confirms consistency in the very small doses of water required for these measurements.

In line with our qualitative observation from figure 6.4a), the desorption temperature for c-Ag(001) crystal in figure 6.4b) is mostly independent of step density. A linear fit to the data yields a small negative slope of –2.6 K·Å. When extrapolating this linear fit, a change in desorption temperature of <0.7 K is implied over the range of (001) to (311), i.e. the smallest possible (001) terrace separated by A'-type steps. The shaded area reflects that this slope is smaller than the uncertainty in the fit.

6.4. DISCUSSION

Submonolayer desorption from Pt, a metal that more strongly interacts with water, but also shows no thermal dissociation, is reflected in two separate desorption peaks for terraces and steps.[6, 24] Similarly, for the stepped Ni (11 11 9) surface, a separate desorption peak of molecular water from steps could be identified.[25, 26] For various stepped Pt(111) surfaces with A-type steps, we have found that the desorption peak attributed to the step occurs at the same temperature regardless of step density.[27]

Considering the similarity of Pt and Ag in not dissociating water, we have previously explained the linear shift in peak desorption temperature for c-Ag(111) as also re-

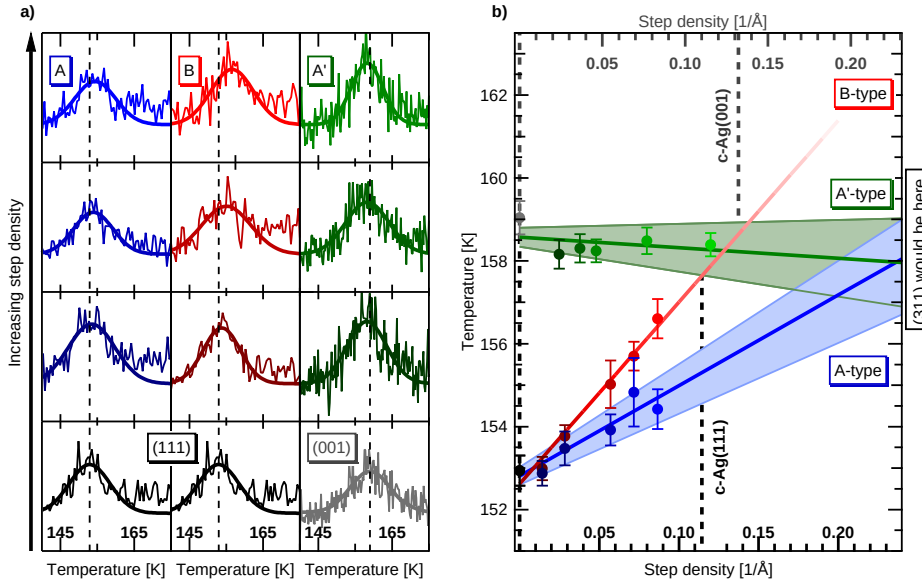

Figure 6.4: **a)**) Desorption of submonolayer coverages of water from various Ag surfaces after doses of 4 L (c-Ag(111) crystal) and 8 L (c-Ag(001) crystal) of a He/H_2O mixture.(111) and (001) terrace width are varied from bottom to top, showing 100 nm, 15, 10, and 8 atom wide terraces, with A-type (blue), B-type (red) and A'-type (green) steps respectively. Gaussian fits for each spectrum are also shown. Dashed lines indicate the center of Gaussian fits at the (111) or (001) surfaces. **b)** Desorption temperatures at different step densities, as extracted from the Gaussian fits. Top axis shows step densities on the c-Ag(001) crystal, bottom axis shows step densities on the c-Ag(111) crystal. Both axes are scaled to range from the apex of the crystal to the step density of the (311) surfaces would be found, 0.2308 $Å^{-1}$ on the top axis and 0.2398 $Å^{-1}$ on the bottom axis. Dashed lines indicate the edges of our crystal, 4 mm and 15.5 ° from the apex. Straight lines were fitted to the data and extrapolated to (311) in the case of A-type and A'-type steps. The B-type steps do not run toward this surfaces.

sulting from two independent contributions from terraces and steps.[14] However, the peak temperatures of the individual contributions apparently differ so little that desorption is not deconvoluted in our experiments on Ag and only a single peak is observed. A simple modelling exercise using two individual Gaussian contributions representing step and terrace desorption for a fixed total coverage at different surfaces confirms an apparent linear shift in desorption temperature for the convoluted peaks. Assuming the shift is due to an increasing contribution of desorption from steps indicates stronger binding at the steps than at terraces. This pragmatic, but somewhat risky interpretation of desorption temperature with binding energy, is supported by STM studies on Ag(111) which have also shown that H_2O preferentially binds to step edges on Ag(111).[28, 29]

At the apex of our c-Ag(111) surface, the step density is far too low to accommodate the submonolayer coverage of water, and water desorbs predominantly from (111) planes. As steps become more closely spaced moving toward the sides of our c-Ag(111) crystal, a growing fraction of the fixed total coverage desorb from step sites. The steeper slope in figure 6.4b) indicates a larger difference in peak desorption tem-

perature for the B-type step than the A-type step in comparison to the Ag(111) plane. It is noteworthy that the same step-type effect was observed for Pt.[23]

In the absence of a general and specific understanding of diffusion rates of monomers and water clusters on low-Miller index surfaces of metals,[30] we will here assume similar diffusion rates of water on the (001) terraces as on the (111) terraces and consequently the formation of ice clusters on both terraces and steps. In the following we extend the interpretation of the shift in peak desorption temperature to our results for c-Ag(001). The absence of a detectable shift within our uncertainty implies that if there are two separate contributions, the peak desorption temperatures must be so close that varying step-to-terrace ratios does not yield a clear shift. We conclude that A'-type steps do not bind water molecules more strongly than the (001) terraces. Since there appears to be no preference for desorption from steps or terraces, it may be suggested that water cluster nucleation should happen evenly over the entire surface, regardless of the presence of steps. Similarly, in a previous study using electron energy loss spectroscopy, no separate step and terrace contributions could be observed for water adsorbed on Ag(115), a stepped surface with (001) terraces and A'-type steps.[8]

Due to the range of surface structures contained on our c-Ag(111) crystal, we can only measure desorption temperatures that are a combination of desorption from (111) terraces and steps. In figure 6.4b), the data from A-type steps shows a clear linear trend, indicating that the observed desorption peak is indeed a linear combination of the two contributions (of water desorbing from terraces and molecules desorbing from steps). In order to separate the terrace and step contributions we extrapolate the fit to (311), a surface that can be seen as only consisting of A-type steps with no terraces (figure 6.1a)). Thus, the contribution from terraces in a linear combination would be zero. The temperature we obtain from this extrapolation to (311) corresponds to the step contribution of desorption temperatures we measure on our crystal. At this point we must stress that this extrapolation cannot predict which desorption temperature would actually occur for H_2O on Ag(311), as highly corrugated surfaces like this often feature different surface structures than those observed at stepped surfaces with wider terraces.[4, 31–34] We can not say how far the linear dependence of desorption temperature on step density extends beyond the surface range of our crystals. We therefore solely use this extrapolation to extract the step contribution on the surfaces contained on the curved crystals.

As (311) only consists of square {100} microfacets adjacent to hexagonal {111} microfacets, the steps could also be seen as A'-type steps when approaching the step edge from the other direction, see figure 6.1a). Strikingly, extrapolating the linear fit of data from the c-Ag(001) crystal towards (311) gives the same value with the same error bars. This indicates that the A- and A'-type steps at surfaces present on our crystals have the same binding energy for water. They can therefore be considered the same

step type in regards to both their atomic arrangement and chemical behaviour. As the A- and A'-type steps would give the same desorption temperature, the different trends in desorption temperature between stepped Ag(111) and stepped Ag(001) surfaces must indicate the difference in binding energy of the two terrace types flanking the steps.

The linear dependence of desorption temperature on step density can reasonably be expected to hold true until the terraces become so short that the structures nucleating at the step edges must change in order to accomodate the water clusters on the surface. On Ag(111) terraces, hexamers as the smallest nucleation cluster at very low coverages have previously been observed by STM.[12] These hexamers would not fit flat on short terraces even before (311) is reached. Further studies of H_2O adsorbed on steps of Ag surfaces with short terrace lengths would be very helpful in order to evaluate for which structures the linear trends in desorption temperature can still hold true.

Applying a Redhead analysis using the extremes of the desorption temperatures from the linear fits in figure 6.4b) suggests that the binding energy difference for Ag(111) and the A-type step is 1.04 kJ/mol. The difference in binding energy for Ag(001) and the A'-type step is at most on the order of 0.17 kJ/mol. Here, we have used the desorption temperatures as extrapolated to Ag(311) for both A- and A'-type steps. These small differences were likely not observable to Klaua and Madey[11] in their flash desorption experiments with limited spatial resolution. In contrast, here it proves that in our spatially resolved experiments we can achieve an accuracy well within chemical accuracy.[35]

6.5. CONCLUSIONS

Due to the design of our experiments, the interactions between water molecules and Ag surfaces can be probed consistently and in great detail. We have shown the influence of both terrace and step type on the adsorption of water on stepped surfaces of a weakly reactive hydrophobic metal.

Within the interpretation that desorption reflects binding, on the c-Ag(111) crystal, the steps bind water molecules measurably stronger than the (111) terraces, resulting in a desorption temperature shift as the step density increases. We detect changes in binding energy that vary less than < 1 kcal/mol, which is considered 'chemical accuracy'. The binding energy at the two step types can also be shown to not be the same - the difference between B-type steps and the (111) terrace is twice as large as the difference between the A-type step and the same terrace. On the c-Ag(001) crystal, the A'-type steps bind water approximately equally strong as the (001) terrace. As a result the desorption temperature at very low coverages does not change significantly with step density. We predict that on (001) terraces water cluster nucleation is not

dominated by steps.

As the trendlines for water desorption from surfaces with A-type steps and A'-type steps runs towards the same value at the maximally stepped (311) surface, we conclude that the steps themselves have the same binding energy for water and can in fact be seen as the same type of step. However, here we can clearly see the influence of the different terrace types. When extending the (111) facets from (311), we see a decrease in desorption temperature, indicating a weaker binding at the (111) terraces. On the other hand, extending the (001) facets from (311) doesn't result in a change in desorption temperature, indicating that the (001) terraces have a very similar binding energy. The difference indicates the fundamental difference between (111) and (001) terraces and illustrates the influence of terrace type on adsorption at steps. Controlling the combination of terraces and steps in terms of terrace type, step type and step density thus provides an extremely sensitive tuning mechanism for the location of water nucleation.

REFERENCES

[1] A. Hodgson and S. Haq. Surface Science Reports Water adsorption and the wetting of metal surfaces. *Surface Science Reports*, 64(9):381–451, 2009.

[2] J. Carrasco, A. Hodgson, and A. Michaelides. A molecular perspective of water at metal interfaces. *Nature Materials*, 11(8):667–674, 2012.

[3] M. J. Kolb, F. Calle-Vallejo, L. B. Juurlink, and M. T. Koper. Density functional theory study of adsorption of H_2O, H, O, and OH on stepped platinum surfaces. *Journal of Chemical Physics*, 140:134708, 2014.

[4] C. Badan, M. T. Koper, and L. B. Juurlink. How well does Pt(211) represent Pt[n(111) × (100)] surfaces in adsorption/desorption? *Journal of Physical Chemistry C*, 119(24):13551–13560, 2015.

[5] M. J. Kolb, R. G. Farber, J. Derouin, C. Badan, F. Calle-Vallejo, L. B. Juurlink, D. R. Killelea, and M. T. Koper. Double-Stranded Water on Stepped Platinum Surfaces. *Physical Review Letters*, 116(13):1–5, 2016.

[6] C. Badan, Y. Heyrich, M. T. M. Koper, and L. B. F. Juurlink. Surface Structure Dependence in Desorption and Crystallization of Thin Interfacial Water Films on Platinum. *Journal of Physical Chemistry Letters*, 7(9):1682–1685, 2016.

[7] V. A. Ranea, A. Michaelides, R. Ramírez, J. A. Vergés, P. L. De Andres, and D. A. King. Density functional theory study of the interaction of monomeric water with the Ag{111} surface. *Physical Review B - Condensed Matter and Materials Physics*, 69(20):1–9, 2004.

[8] H. Ibach. Electron energy loss spectroscopy of the vibration modes of water on Ag(100) and Ag(115) surfaces and comparison to Au(100), Au(111) and Au(115). *Surface Science*, 606(19-20):1534–1541, 2012.

[9] M. G. Sceats and S. A. Rice. Amorphous Solid Water and Its Relationship to Liquid Water: A Random Network Model for Water. In F. Franks, editor, *Water and Aqueous Solutions at Subzero Temperatures*, pages 83–214. Springer, 1982.

[10] R. S. Smith, C. Huang, E. K. Wong, and B. D. Kay. Desorption and crystallization kinetics in nanoscale thin films of amorphous water ice. *Surface Science*, 367(1):L13–L18, 1996.

[11] M. Klaua and T. E. Madey. The adsorption of H_2O on clean and oxygen-dosed silver single crystal surfaces. *Surface Science*, 136(1):L42–L50, 1984.

[12] A. Michaelides and K. Morgenstern. Ice nanoclusters at hydrophobic metal surfaces. *Nature Materials*, 6(8):597–601, 2007.

[13] D. L. Bashlakov, L. B. Juurlink, M. T. Koper, and A. I. Yanson. Subsurface oxygen on Pt(111) and its reactivity for CO oxidation. *Catalysis Letters*, 142(1):1–6, 2012.

[14] J. Janlamool, D. Bashlakov, O. Berg, P. Praserthdam, B. Jongsomjit, and L. B. Juurlink. Desorption of water from distinct step types on a curved silver crystal. *Molecules*, 19(8):10845–10862, 2014.

[15] H. Ibach. *Physics of Surfaces and Interfaces*, volume 2006. Springer, 2006.

[16] R. van Hardeveld and A. van Montfoort. The influence of crystallite size on the adsorption of molecular nitrogen on nickel, palladium and platinum: An infrared and electron-microscopic study. *Surface Science*, 4(4):396–430, 1966.

[17] W. Ellis and R. Schwoebel. LEED from surface steps on UO_2 single crystals. *Surface Science*, 11(1):82–98, 1968.

[18] M. Henzler. LEED-investigation of step arrays on cleaved germanium (111) surfaces. *Surface Science*, 19(1):159–171, 1970.

[19] M. A. Van Hove and G. A. Somorjai. A new microfacet notation for high-Miller-index surfaces of cubic materials with terrace, step and kink structures. *Surface Science*, 92(2-3):489–518, 1980.

[20] J. E. Ortega, M. Corso, Z. M. Abd-El-Fattah, E. A. Goiri, and F. Schiller. Interplay between structure and electronic states in step arrays explored with curved surfaces. *Physical Review B - Condensed Matter and Materials Physics*, 83(8):1–7, 2011.

[21] K. Morgenstern, K. F. Braun, and K. H. Rieder. Surface-State Depopulation on Small Ag(111) Terraces. *Physical Review Letters*, 89(22):20–23, 2002.

[22] J. E. Ortega, G. Vasseur, I. Piquero-Zulaica, S. Matencio, M. A. Valbuena, J. E. Rault, F. Schiller, M. Corso, A. Mugarza, and J. Lobo-Checa. Structure and electronic states of vicinal Ag(111) surfaces with densely kinked steps. *New Journal of Physics*, 20(7):073010, 2018.

[23] M. J. Van Der Niet, A. Den Dunnen, L. B. Juurlink, and M. T. Koper. The influence of step geometry on the desorption characteristics of O_2, D_2, and H_2O from stepped Pt surfaces. *Journal of Chemical Physics*, 132(17):174705, 2010.

[24] A. Picolin, C. Busse, A. Redinger, M. Morgenstern, and T. Michely. Desorption of H_2O from flat and stepped Pt(111). *Journal of Physical Chemistry C*, 113(2):691–697, 2009.

[25] C. Nöbl and C. Benndorf. Adsorption behavior of H_2O on clean and oxygen precovered Ni(s)(111). *Surface Science*, 182(3):499–520, 1987.

[26] C. Mundt and C. Benndorf. Influence of steps on the H_2O adsorption on Ni(s)(111). *Surface Science*, 287-288:119–124, 5 1993.

[27] A. Den Dunnen, M. J. Van Der Niet, C. Badan, M. T. Koper, and L. B. Juurlink. Long-range influence of steps on water adsorption on clean and D-covered Pt surfaces. *Physical Chemistry Chemical Physics*, 17(13):8530–8537, 2015.

[28] K. Morgenstern. Scanning tunnelling microscopy investigation of water in submonolayer coverage on Ag(111). *Surface Science*, 504:293–300, 2002.

[29] K. Morgenstern and J. Nieminen. Intermolecular bond length of ice on Ag(111). *Physical Review Letters*, 88(6):1–66102, 2002.

[30] C. Bertram, W. Fang, P. Pedevilla, A. Michaelides, and K. Morgenstern. Anomalously Low Barrier for Water Dimer Diffusion on Cu(111). *Nano Letters*, 19(5):3049–3056, 2019.

[31] T. Yamada, S. Tamamori, H. Okuyama, and T. Aruga. Anisotropic water chain growth on Cu(110) observed with scanning tunneling microscopy. *Physical Review Letters*, 96(3):2–5, 2006.

[32] J. Carrasco, A. Michaelides, M. Forster, S. Haq, R. Raval, and A. Hodgson. A one-dimensional ice structure built from pentagons. *Nature Materials*, 8(5):427–431, 2009.

[33] C. Lin, G. Corem, O. Godsi, G. Alexandrowicz, G. R. Darling, and A. Hodgson. Ice Nucleation on a Corrugated Surface. *Journal of the American Chemical Society*, 140(46):15804–15811, 2018.

[34] C. Lin, N. Avidor, G. Corem, O. Godsi, G. Alexandrowicz, G. R. Darling, and A. Hodgson. Two-Dimensional Wetting of a Stepped Copper Surface. *Physical Review Letters*, 120(7):76101, 2018.

[35] C. Díaz, E. Pijper, R. A. Olsen, H. F. Busnengo, D. J. Auerbach, and G. J. Kroes. Chemically accurate simulation of a prototypical surface reaction: H_2 dissociation on Cu(111). *Science*, 326(5954):832–834, 2009.

7

OUTLOOK

In chapter 2, we have shown recent advances in the applications of curved crystals exploring magnetic, electronic and chemical properties of vicinal surfaces. Our group has made significant advances in gas-surface reaction dynamics by revealing site-specific reactivity and surface structure effects - initially by using flat single crystals with stepped surfaces, and progressively by incorporating curved crystals with tunable surface structures.[1–4]

This thesis exclusively covers work on curved single crystal surfaces. We have illustrated their benefits when studying gas-surface reactions. Specifically, cylindrical slices of Ag and Pt single crystals were employed to study the effect of surface structure on elementary reaction steps, e.g. dissociative adsorption or molecular desorption. This chapter provides an outlook on on-going experiments employing curved single crystals that were initiated during the course of this PhD project. These include research on CO_2 adsorption on stepped and kinked Pt surfaces, with the goal of studying structure-dependent CO_2 dissociation. We are also investigating a novel curved crystal surface comprised of an ordered bimetallic alloy, i.e. *c*-NiAl(110)[001]-31°.

7.1. EXPLORING REACTIVE SITES TOWARDS CO_2 DISSOCIATION

RISING CO_2 LEVELS in the atmosphere and depleting fossil fuel reserves are two faces of the same global challenge we are currently confronted with. The first model linking atmospheric CO_2 levels to global climate was developed by Arrhenius in the 19th century.[5, 6] In this context, capturing and converting CO_2 to higher-value chemicals presents an attractive alternative. However, CO_2 is the final product of all oxidation processes involving carbon species, being inherently thermodynamically stable. On a molecular level, two C=O double bonds require substantial energy to break, before any other molecular species can be formed. A catalyst, by definition, cannot change the thermodynamics of a chemical reaction; CO_2 conversion remains an endothermic reaction, even at a catalytic surface. However, the activation energy of the process can be lowered by a catalyst, improving the energetic cost of possible applications. A commonly proposed pathway is the reduction of CO_2 to CO. CO could then subsequently be converted into larger hydrocarbon chains by the Fischer-Tropsch reaction.

For CO formation from CO_2, the probability of bond breaking is expected to increase if the asymmetric C=O stretch vibration is excited when the molecule hits the catalyst's surface. Our group is currently initiating experiments to measure state-resolved CO_2 dissociation using the supersonic molecular beam. The asymmetric stretch vibration of CO_2 is stimulated using a laser at the vibrational eigenfrequency (2350 cm^{-1}), with the goal of measuring the vibrational efficacy:

$$CO_2^{\nu_3} + 2* \rightleftharpoons CO_{ads} + O_{ads} \tag{7.1}$$

It is therefore prudent to first study CO_2 sticking without vibrational excitation. As a first step, we have explored structure dependencies of molecular CO_2 adsorption on Pt surfaces vicinal to (111). Pt is a commonly used catalyst for the CO oxidation reaction, which can be considered the reverse of equation 7.1.

We combine the two curved Pt crystals also used in chapter 4, *c*-Pt(111)[1$\bar{1}$0]-31° and *c*-Pt(111)[11$\bar{2}$]-31°, to study CO_2 sticking on stepped and kinked Pt surfaces. They each expose the (111) plane at the apex and curve 15.5° to each side, thereby introducing close-packed or highly kinked steps respectively. We impinge a molecular beam of pure CO_2 onto the surfaces. From time-of-flight measurements, a beam energy of 77.5 meV is determined. The beam impinges on the crystal surface with a rectangular imprint to improve spatial resolution along the curvature, as discussed in chapter 4. For the experiment, both crystals are cooled with super-cooled liquid nitrogen, resulting in a measured surface temperature of 81 K for the crystal with A- and B-type steps and 87 K for the crystal with {210} steps. At these temperatures, CO_2 is expected to physisorb on Pt.[7, 8] We attribute the temperature difference to

different thermal conductance of the sample holder after exchanging the crystals, in addition to small changes in the thermocouple connections. Initial sticking probabilities (S_0) are obtained by the King-and-Wells method.[9] Measurements are carried out sequentially at different positions of the curved crystal. As surface chirality is not expected to influence reactivity for this system, results obtained on the two side of the *c*-Pt(111)[11$\bar{2}$]-31° crystal are averaged.

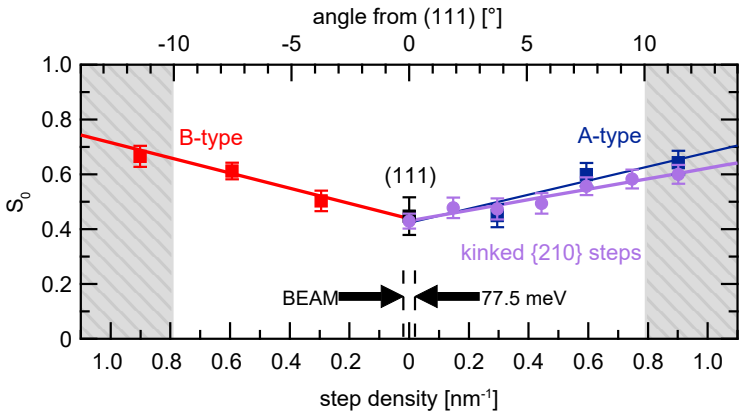

Figure 7.1: Initial sticking probabilities of a supersonic molecular beam of CO_2 (77.5 meV) obtained on the surfaces of two curved Pt crystals. For the *c*-Pt(111)[1$\bar{1}$0]-31° crystal (blue, red, black), sticking probabilities are measured at T_{surf} = 81 K. Sticking probabilities on the *c*-Pt(111)[11$\bar{2}$]-31° crystal (purple) are measured at T_{surf} = 87 K. Grey areas of the plot indicate where the surface width becomes more narrow than the beam width. Only data in the white area of the plot are included in the linear fits for each step-type (solid lines). Black arrows and dashed lines indicate the size of the beam along the curvature of the crystal.

Figure 7.1 plots initial sticking probabilities (S_0) of CO_2 on the Pt surfaces as a function of step density. At the apex of the two different crystals, $S_0^{(111)}$ is measured as 0.447 and 0.429, confirming that results from the two crystals are comparable despite slightly different surface temperatures. This sticking probability is in good agreement with $S_0^{(111)}$ values determined by Kulginov *et al.* at comparable kinetic energies.[10] For all three step types, S_0 increases with step density. This mirrors results on other metallic surfaces where low-Miller index planes are found to be particularly inert towards physisorption of CO_2, while lower coordinated sites or surfaces with co-adsorbed alkali metals are more reactive.[8, 11, 12]

The physisorption well for CO_2 on Pt(111) is about 0.2 eV.[10] Sticking can be seen as a two-step process, where a molecule approaching the surface may first get trapped and must subsequently equilibrate its energy with the surface. Trapping in this well can occur by transferring incident translational energy into rotational or vibrational motion, or lattice vibrations. Molecules getting trapped must quickly dissipate their (normal) translational energy, or they desorb again without sticking. However, for CO_2 on Pt(111), energy transfer to lattice vibrations is limited to ~0.55 eV, and vibra-

tional excitation was negligibly small for E_i <1 eV.[10] In an earlier study, sticking was found to be reasonably high ($S_0 = 0.6$) at low incident kinetic energies of ~60 meV.[10] With increasing kinetic energy, initial sticking probabilities decrease quickly, due to limited energy dissipation in the relatively shallow well. However, a high-energy tail remains and S_0 never reduces to zero, even at energies >1 eV. This phenomenon was attributed to improved translational to rotational coupling at high energy.

We see two possible mechanisms for improved sticking of CO_2 at vicinal surfaces for the low kinetic energy that was probed here (77.5 meV). Firstly, edges may improve the conversion from normal to lateral motion during the initial trapping. However, this may still result in desorption, as the translational energy is preserved in the collision. Secondly, steps may improve translational to rotational coupling already at lower kinetic energies than for the flat surface, and thus improve the sticking probability. Coupling to vibrational modes is unlikely here, as even the lowest molecular vibrational mode, the bend mode, has a frequency of 83 meV on the Pt(111) surface.[13] Only a small portion of molecules, at the higher end of the kinetic energy distribution in our beam, could thus be vibrationally excited.

We fit the data of S_0 in figure 7.1 for each step type with a linear function:

$$S_0(SD) = S_0^{(111)} + \Sigma_0 \cdot SD \tag{7.2}$$

Data in the grey area of the plot, where the rectangular beam is wider than the available crystal surface, is excluded from the fits. Fits yield S_0 values of 0.423, 0.439, and 0.430 for the ideal, defect-free (111), in good agreement with the results on the as-prepared (111) surface of the two crystals. The slopes of the fits (Σ_0) are 0.256 nm, 0.277 nm, and 0.192 nm for A-type, B-type and {210} steps respectively. Table 7.1 summarises these results.

In chapter 4, we converted Σ_0 to reaction cross-sections (σ_0^{step}) for dissociation of D_2 at steps, corresponding to the reactive area in the potential energy surface (A) near the step. This interpretation works well at low kinetic energy, where sticking at terraces is low and the sticking probability when impinging on the area A is approximately unity. At higher kinetic energies, the indirect mechanism to dissociation at steps is reduced. The experimentally determined reaction cross-section (σ_0^{step}) may then be smaller than A, due to the reduced efficacy of dissociation.[14] The experimentally determined reaction cross-section (σ_0^{step}) is then the product of the reactive area (A) of the potential energy surface and the probability of dissociation when a molecule impinges on this area (S_0^A):

$$\sigma_0^{step} = S_0^A \cdot A \tag{7.3}$$

A similar model may be applicable to link the cross-sections σ_0 for CO_2 sticking at step edges, as determined from the slopes Σ_0, to the potential energy surface for CO_2 adsorption on vicinal Pt surfaces.

crystal	$S_0^{(111)}$ experimentally	step-type	$S_0^{(111)}$ from fit	Σ_0 from fit
c-Pt(111)[1$\bar{1}$0]-31°	0.447	A / {001}	0.423	0.256 nm
		B / {110}	0.439	0.277 nm
c-Pt(111)[11$\bar{2}$]-31°	0.429	{210}	0.430	0.192 nm

Table 7.1: Results for CO_2 sticking from a 77.5 meV beam on Pt surfaces on two curved crystals.

Differences in sticking efficiency of the three step-types cannot be conclusively discussed here due to the limited number of probed surfaces. Future studies varying kinetic energies, and probing more points across the curved surface is expected to yield more detailed insights into the mechanism of CO_2 sticking on Pt and the role of specific surface sites.

In addition to CO_2 adsorption we have also studied the molecular desorption of CO_2 from vicinal Pt surfaces. Figure 7.2 shows preliminary results of temperature-programmed desorption of CO_2 from the *c*-Pt(111)[11$\bar{2}$]-31° crystal with {210} steps. CO_2 was dosed with the molecular beam for 180 s at different positions along the curved surface at 91 K. During a subsequent temperature ramp of ~1 K/s, CO_2 desorption was detected with a quadrupole mass spectrometer. The rate of desorption from a surface is given as:[2]

$$r(\theta) = -\frac{\mathrm{d}\theta}{\mathrm{d}t} = \nu_{des} \cdot \theta^n \cdot e^{-\frac{E_{des}}{RT}} \tag{7.4}$$

Here, r is the reaction rate, θ is the surface coverage, t is time, ν_{des} is the attempt frequency, n is the order of desorption, E_{des} is the desorption energy, R is the universal gas constant, and T is temperature.

For multilayer desorption of CO_2 from graphene-covered Pt(111), 0^{th} order kinetics were recently determined.[15] While we cannot confirm the desorption order definitively without varying coverage, the desorption traces in figure 7.2b) indicate similar kinetics here. In the assumption of 0^{th} order kinetics, plotting the natural logarithm of the desorption signal against the inverse of the desorption temperature in figure 7.2 allows us to determine the desorption energies, according to equation 7.4. Values for E_{des} obtained at different parts of the surface range from 24.7 kJ/mol to 38.8 kJ/mol.

Due to the large doses in the experiment, the desorption signal must stem largely from CO_2 molecules desorbing from layers of CO_2 ice. The desorption energies in figure 7.2c) reflect this: they resemble the enthalpy of sublimation (ΔH_s) for CO_2 under standard conditions, 28.8 kJ/mol.[16] Accordingly, no clear variation with step density can be observed.

Supplementary TPD experiments for smaller doses are expected to further elucidate

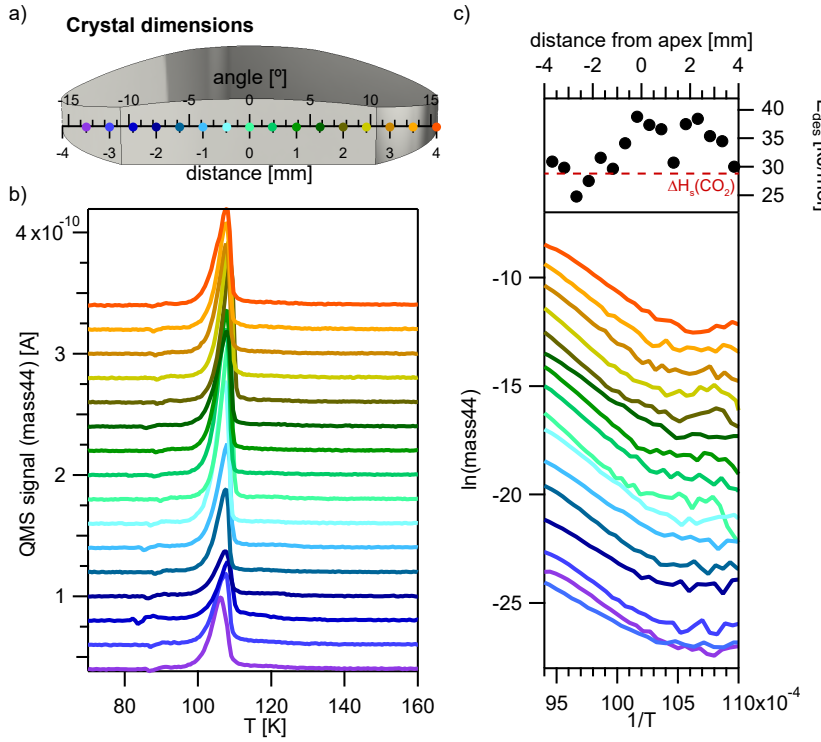

Figure 7.2: a) Schematic drawing of the *c*-Pt(111)[11$\bar{2}$]-31° crystal and its dimension. Circles mark the position on the surface where TPDs were recorded. b) QMS signal of mass 44 during temperature-programmed desorption of CO_2 from different parts of the crystal. c) Arrhenius plot of desorption data in b) and desorption energies obtained from fits to the linear parts of the traces. ΔH_s indicates the standard enthalpy of sublimation of solid CO_2.

7

adsorption energies at steps and terraces. However, detecting low coverages of CO_2 desorbing from the small surface area covered by the rectangular molecular beam is expected to be challenging. Instead, the apparatus described in chapter 6 is better suited for spatially-resolved TPD experiments involving small doses of CO_2.

7.2. DETERMINING ADSORPTION SITES AND STRUCTURES BY LOW-TEMPERATURE STM

Combining low-temperature STM with curved crystals opens new possibilities to resolve adsorption sites and adsorption structures of molecules and to observe the effects of increasingly narrow terraces on adsorption.

We have investigated adsorption of CO_2 on stepped Pt surfaces in a low-temperature STM study of the *c*-Pt(111)[1$\bar{1}$0]-31° crystal at Loyola University in Chicago, USA. The experimental set-up has previously been described in detail by the Loyola group.[17, 18] In short, the apparatus consists of a preparation and an STM chamber. Surface preparation of the curved Pt crystal is performed according to the procedure described in chapter 4 and the progress of surface preparation is monitored by LEED. In the preparation chamber, the sample can only be cooled to 110 K using a liquid nitrogen cryostat. As we have shown in figure 7.2, this temperature is above onset of desorption for CO_2. Therefore, the freshly prepared sample is transferred first to the STM, which is cooled by a close-cycle He cryostat. First, the clean surface is imaged at 30 K at different points across the surface. In figure 7.3, we find regular step arrays. Only close to the apex steps deviate from the expected step direction due to meandering. After cleaning the surface again, transferring, and cooling the sample to 30 K in the STM cryostat, CO_2 is background dosed onto the crystal. The surface is then imaged again after exposures of 1 L and 3 L.

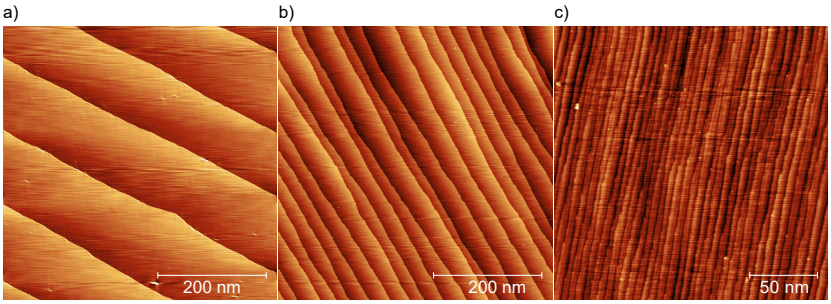

Figure 7.3: STM images after surface preparation of surfaces featuring wide and narrow step arrays, before dosing of CO_2.

CO_2 molecules cannot be atomically resolved but the entire molecule appears as a round bright protrusion instead, as shown in figure 7.4. After the 1 L dose, STM images show molecules evenly dispersed on the Pt(111) terraces. On wide terraces, no clustering or formation of adsorbate structures is observed. CO_2 diffusion is reported to be slow in the few instances where it has been studied.[8] Here, we observe no ordering or clustering of molecules on the terraces appears on wider terraces even days after dosing. The (3 × 3) structure previously reported for CO_2 on Pt(111) could not be observed.[7] On stepped images, however, CO_2 molecules are observed dec-

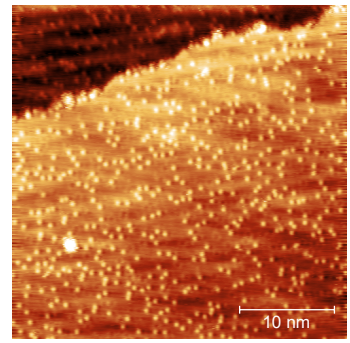

Figure 7.4: 35 nm×35 nm STM image near the apex of the curved crystal after dosing 1 L of CO_s.

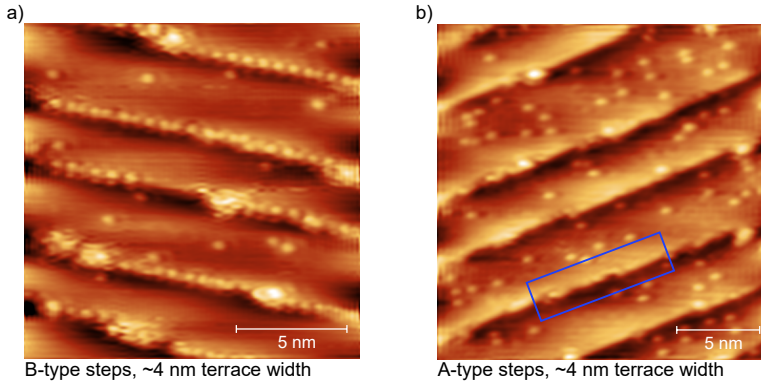

Figure 7.5: STM images of surfaces on the *c*-Pt(111)[1$\bar{1}$0]-31° crystal, after dosing 1 L CO_2 at 30 K. a) 15 nm×15 nm image with B-type steps, on ~4 nm wide (111) terraces. Individual molecules are observed on the terraces, and resolved decorating the step edges. b) 15 nm×15 nm image with A-type steps, on ~4 nm wide (111) terraces. Molecules are resolved on the terraces but not along the steps. Instead, bright lines appear along the step edges. The blue rectangle highlights part of a step edge where adsorbates at the step edge are just barely resolved.

7

orating the step edges and in some instances forming larger clusters. They appear either molecularly resolved or as bright stripes along the step edge, as illustrated in figure 7.5. However, height profiles across the steps reveal that the bright step edges are also covered. Terraces on highly stepped surfaces appear depleted of molecules, indicating that diffusion on the Pt(111) terraces indeed occurs, but does not lead to ordered structures on the terraces.

In figures 7.6 and 7.7, we extract line profiles along step edges for two images where molecules are resolved at the steps. We obtain the distance between the molecules, which appear as rounded peaks in the line profiles, to determine their intermolecular spacing. From figure 7.6, after the 1 L dose, an average value of 6.46 Å is found. In figure 7.7, molecules are spaced on average 6.63 Å apart. The additional dosing of CO_2 thus does not change the coverage at steps. This spacing does not match well with Pt atomic spacings along the step edge (n×2.77 Å).

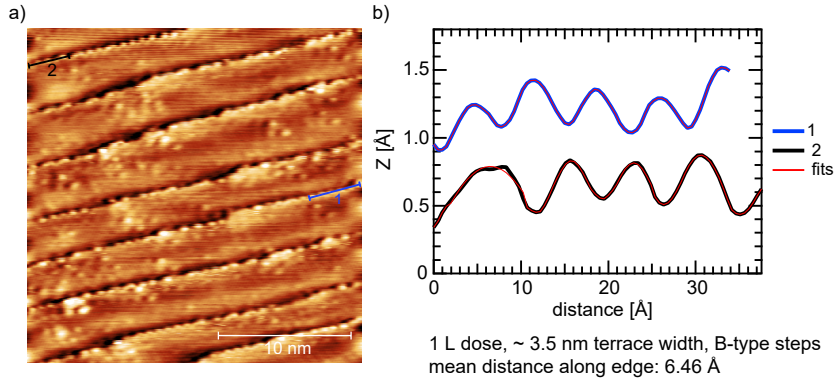

Figure 7.6: a) 25 nm×25 nm STM image of a surface with B-type steps on ~3.5 nm wide terraces, after a 1 L dose of CO_2 at 30 K. Blue and black lines indicate where line profiles were taken to determine spacing of molecules along the step edge. b) Line profiles (blue, black) extracted from the image. Multiple gaussian fits (red) are used to determine centers of peaks and consecutively distances between molecules.

While it would be interesting to determine structure dependent coverages and changes relating to different doses, we encounter the challenge that molecules at step edges are not always resolved. We therefore have to quantify coverage on the terraces and changes with step density, in order to deduce the relative coverages at steps. We have initiated a collaboration with the theory group in Leiden, to develop an algorithm to identify molecules on terraces and train it by machine learning. The goal is to quantify coverages for a high number of STM images and obtain statistically relevant results regarding effects of step density, step type, and CO_2 dose. Figure 7.8 shows current results of the training process. The aim is to train the algorithm so that it can detect molecules on terraces with the same accuracy as a human would by eye.

On some of the stepped surfaces we observe the bright features as 'dimers' (after the 1 L dose) or 'trimers' (after the 3 L dose), instead of monomers. In specific instances they appear to form larger ordered structures. Figure 7.9a) shows an STM image where "dimers" are covering all three terraces. In figure 7.9b) the contrast of the middle terrace is adjusted to make more details visible. The dimers appear approximately in parallel to each other and follow the same internal structure with one protrusion brighter than the other one. From line profiles we obtain average "C-C distances" of 6.57 Å within these clusters. Figures 7.9c) and d) show surfaces where "trimers" were observed. Again, they cover all terraces in the image. They form triangles that are aligned in the same direction relative to the step edges, and scale with the image size. Line profiles give an average of 4.28 Å. Figure 7.9e) shows the distributions of these distances, separated by the directions in the cluster, for trimers in d). Notably, one direction, approximately parallel to the steps, is larger than the other two in all clusters.

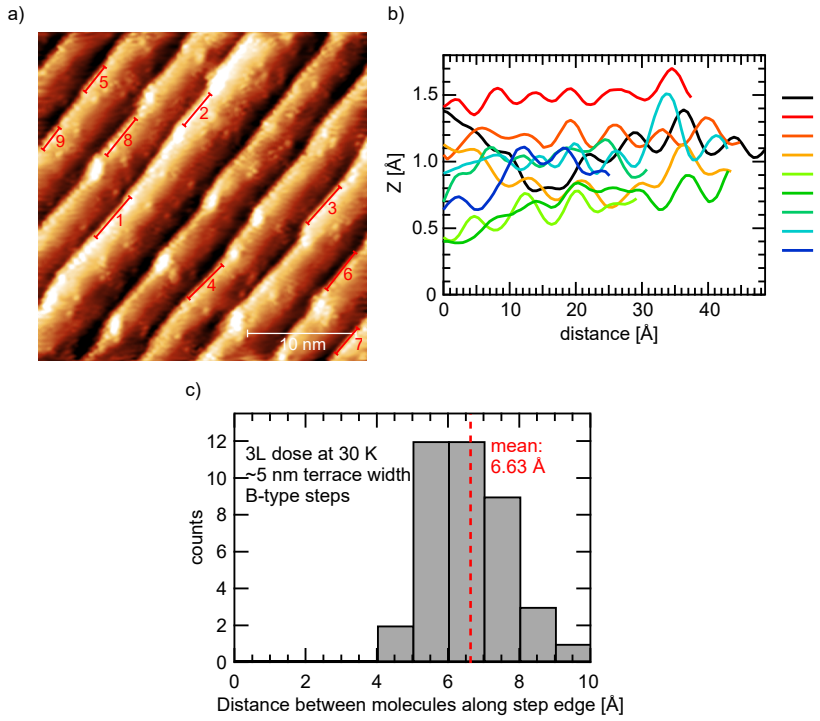

Figure 7.7: a) 25 nm×25 nm STM image of a surface with B-type steps on ~3.5 nm wide terraces, after a 3 L dose of CO_2 at 30 K. Red lines indicate where line profiles were taken to determine spacing of molecules along the step edge. b) Line profiles extracted from the image. c) Distribution of molecule spacings along step edges.

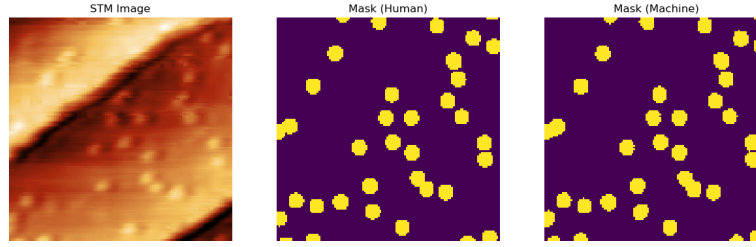

Figure 7.8: STM image used to train the machine learning algorithm to recognize and count molecules on terraces. Left: the original image. Middle: Mask created from molecules detected by human eye. Right: Mask found by algorithm. Figure by Paul Spiering.

Trimers of adsorbed CO_2 have previously been observed in STM studies on Ru(0001) and Ni(110).[19, 20] They also occur in gas-phase CO_2.[21] In the gas-phase, C-C distances of 3.60 Å and 4.03 Å are reported for dimers and trimers respectively. For the CO_2 trimers on Ru(0001) and Ni(110), effects of the underlying terrace on the orientation of clusters have been observed. On Ru(0001), CO_2 was adsorbed at (three-fold

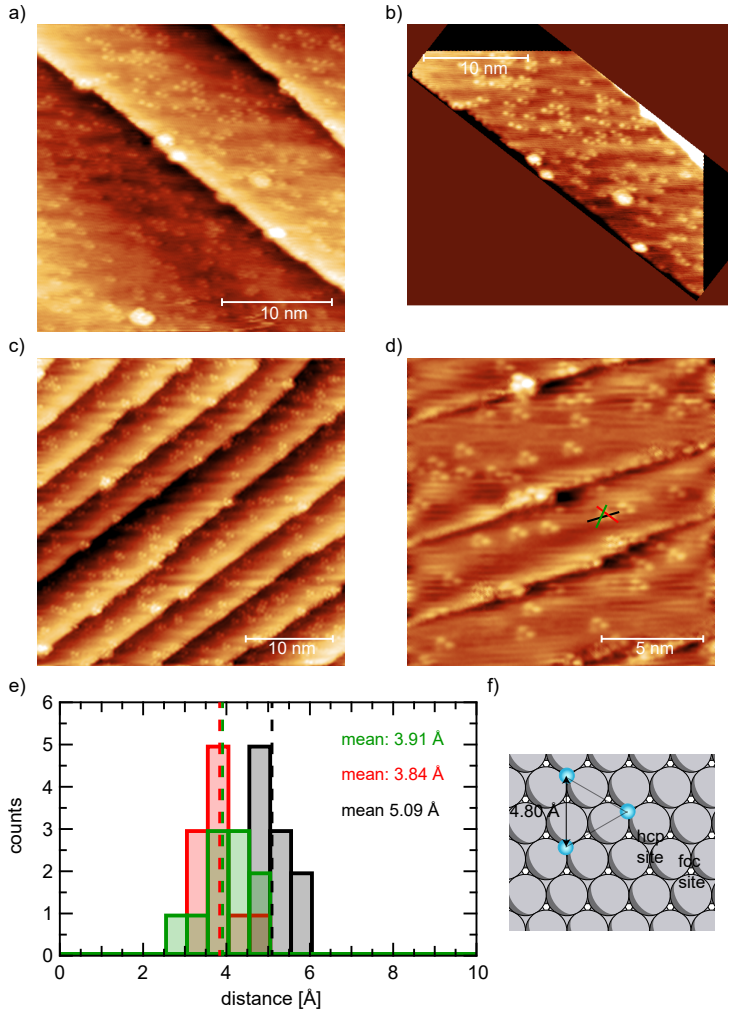

Figure 7.9: a) 30 nm×30 nm STM image where protrusions appear as "dimers" on terraces (B-type steps) after a 1 L dose of CO_2. b) Middle terrace of image a), contrast adjusted. c) 35 nm×35 nm STM image where "trimers" cover ~4.5 nm wide terraces (A-type steps) across a larger surface area, after a 3 L dose. d) 15 nm×15 nm STM image taken in the same position, showing well resolved trimer clusters. Red, green, and black lines indicate axes along which C-C distances were determined. e) Distributions of C-C distances in clusters in image d), separated by directionality. Colours of the bars correlate lines in d). f) Suggested sites of adsorption of CO_2 on Pt(111).

hollow) *hcp* sites.[19] The trimer orientation therefore switched on adjacent terraces due to the stacking order of the hcp lattice. Similarly, CO_2 was adsorbed at hollow sites of the Ni(110) surface.[20] The distance for protrusions within trimers we observe on the Pt(111) terraces, 4.28 Å, potentially indicates adsorption on next-nearest *hcp* sites, as illustrated in figure 7.9f).

We must note, however, that in the STM images where we observe dimeric or trimeric

protrusions on narrow terraces, these clusters appear very uniform in size and shape. Furthermore, only few monomers can be found in these images. The "dimers" and "trimers" could therefore also be artifacts of imaging with a double or triple tip. On the other hand, step edges appear crisp and absent of doubling effects, and CO_2 adsorbed at steps can still be observed as single protrusions. Future experiments are recommended to confirm the formation of dimer and trimer clusters on these stepped surfaces.

7.3. INTRODUCING CURVED CRYSTALS OF BIMETALLIC ALLOYS

So far, curved crystals cut from single-crystalline metals are by far the most commonly employed type. However, their use does not have to be limited to this material type. Recently, curved crystals of metal oxides, which are common materials for industrial heterogeneous catalysts, have been studied.[22, 23] In another instance, curved Ag crystals were used to grow a stepped bimetallic alloy.[24] Here, we examine the curved surface of a bulk bimetallic alloy, NiAl.

NiAl crystallizes in the CsCl crystal structure, i.e. a body-centered cubic lattice of two distinct types of atoms. The (110) plane, as displayed in figure 7.10a), consists of alternating rows of the two elements. For NiAl(110), the surface is not a perfect bulk termination. Instead, Ni atoms are slightly relaxed towards the bulk and Al atoms are elevated out of plane, causing a rippled structure with a 0.22 Å height displacement between rows of Ni and Al.[25] Surface oxidation of NiAl(110) results in the formation of Al_2O_3. Alumina is often used as an oxide support for catalytic nanoparticles in industrial catalysts. The surface science approach to heterogeneous catalysis frequently makes use of NiAl to grow well-ordered films of Al_2O_3. In this way, the behavior of the surface oxide can be studied, while maintaining a conducting metallic bulk, which is essential to many electron-based surface-science techniques. While on NiAl(110) different rotational domains of Al_2O_3 are formed, the introduction of step edges on vicinal surfaces can aid in aligning these domains.[26, 27]

Vicinal surfaces of bare NiAl also present an interesting fundamental problem regarding to their surface properties. First, we introduce the sample and its surface structure. The crystal we study can be considered a 31° slice of a cylinder curved around the [001] axis, exposing NiAl(110) at its apex, as figure 7.10b) illustrates. Following the nomenclature introduced in chapter 2, we refer to it as *c*-NiAl(110)[001]-31°. Steps introduced towards the side of the crystal therefore form {100} microfacets, consisting of rows of the same atom type at the upper and lower step edges, as shown in figure 7.10a). The problem referred to above is then as follows: As essentially a microfacet of only one element type is formed at the steps, it may be assumed that steps of either Ni or Al are preferred. NiAl(001) surfaces have been reported to terminate

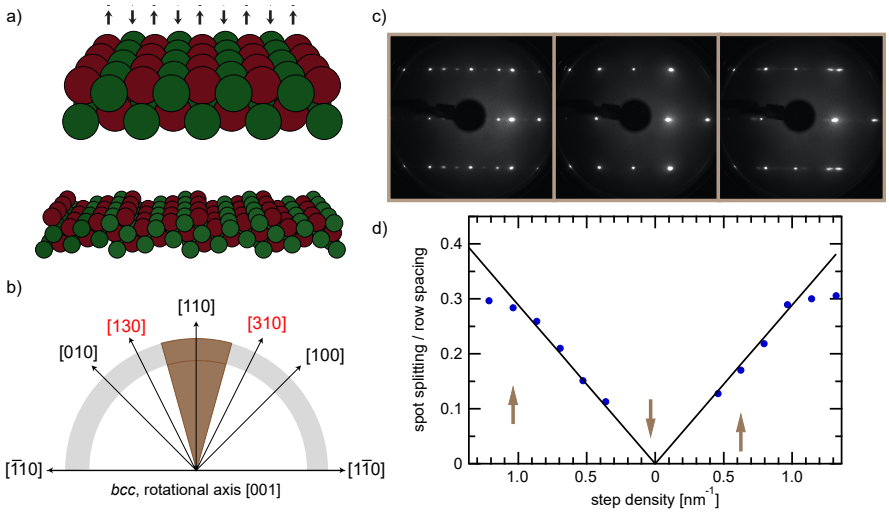

Figure 7.10: a) Schematic structure of NiAl(110). Instead of a perfect bulk termination, Al rows (red) are displaced slightly above the Ni atoms (green). Below, example of the stepped surfaces with {100} steps found on the *c*-NiAl(110)[001]-31° crystal. b) schematic drawing of the cylinder that the crystal slice is cut from. c) LEED images from different parts of the curved crystal, showing a (110) diffraction pattern (center), and spot splitting caused by regularly stepped surfaces (left, right) d) Spot splitting over row spacing ratios determined at different parts of the surface (blue circles), and expected ratios (black lines). Arrows indicate positions of LEED patterns in c).

preferentially on Ni planes.[28] If indeed one type of element is preferred at the step edges, on our crystal the Ni:Al ratio of surface atoms should gradually shift away from the 50:50 ratio at the (110) surface. Surface sensitive techniques, e.g. XPS and AES, are expected to detect this shift. A preferred registry of terrace widths may also be observable in terrace width distributions from STM images.

Surface preparation of this crystal has proven to be extremely sensitive to background pressures of O_2 and H_2O, as well as temperature. However, we can now prepare clean surfaces across the entire range of the curved crystal. Figure 7.10c) depicts LEED patterns from the (110) apex, as well as the sides. LEED spots are well-defined and distinct split spots appear at the stepped surfaces. In figure 7.10d) we confirm that spot splitting to row spacing ratios follow the expected trend. Expected spot splitting to row spacing ratios were determined according to table 2.1 in chapter 2.

An STM study of the *c*-NiAl(110)[001]-31° crystal was carried out at the Materials Physics Center in San Sebastián, Spain. The apparatus is a variable temperature setup similar to the one described in chapter 6. While meandering step edges are observed at the apex, steps start aligning at very small miscut angles, where they separate wide (110) terraces, as figure 7.11a) shows. As step density increases, we find regularly stepped surfaces. In figure 7.11b), step edges follow predominantly the direction that is expected as a result of the crystal's curvature. Kinks occur occasionally

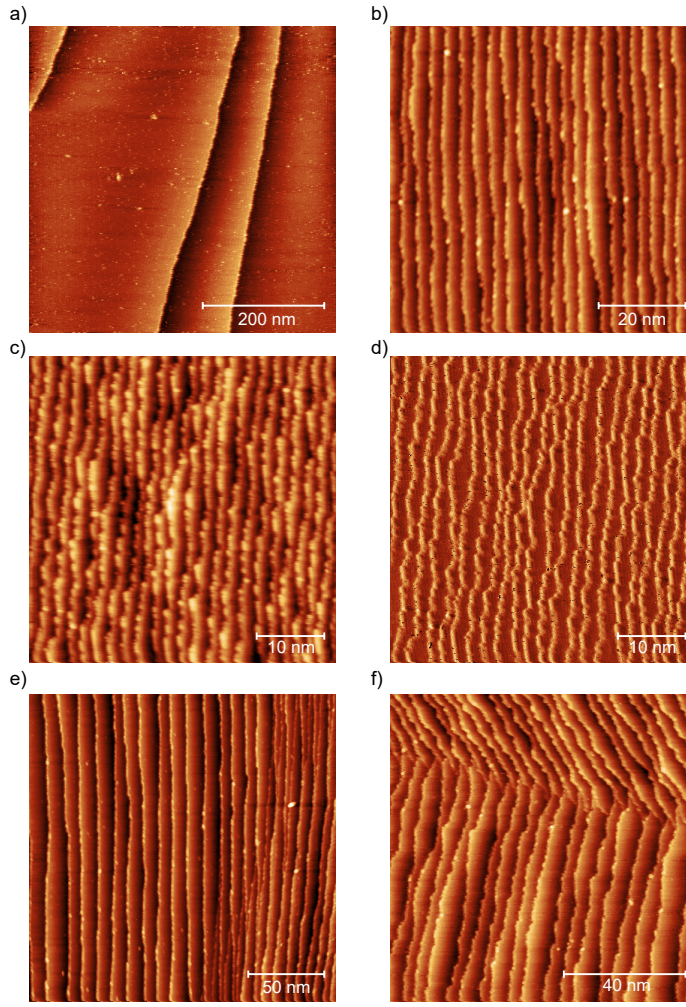

Figure 7.11: STM image take across the *c*-NiAl(110)[001]-31° crystal. a) Wide terraces are found close to the apex. b) Towards the sides of the crystal, narrow terraces form regularly stepped arrays. c) Step edges on the vicinal surfaces can be difficult to trace in the Z-channel of the image. d) In the I-channel of the same image, step outlines are more clearly detectable. e) On some surfaces step bunching occurs. f) Step edges deviating from the expected orientation and changing directions.

but the majority portion of each step runs parallel to the [001] vector.[1] We observe that step edges often appear brighter than terraces. The bright protrusions hinder determination of outlines of step edges at narrower terraces, as illustrated in figure 7.11c). For statistical analysis of terrace widths and kinks in steps, as done in chapter 3, it is thus more useful to use the I-channel of these images. In figure 7.11d) the outlines of step edges reveal that kinks here occasionally cause larger deviations from the ex-

[1] Surface vectors and step types on the NiAl(110) surface are consistent with those illustrated for *bcc*(110) surfaces in figure 2.3.

pected step direction, along the direction of close-packed steps. The group has currently started a through analysis of STM images with the goal of determining whether one element is preferred at the step edge by identifying preferred terrace widths.

While regularly stepped arrays are found predominantly, we occasionally find surfaces that diverge from the expected structures. In figure 7.11e), step bunching occurs on the right side of the image, but regularly stepped, wider terrace recur in the left part of the image. A more curious phenomenon is displayed in figure 7.11f). There, steps in the top part of the image have a different orientation than steps at the bottom part. Both directions deviate from the ideal step direction given by the curvature, i.e. vertically in the image. However, in both parts steps run in parallel to other steps and appear to form ordered arrays. Where they meet, a small overlap of steps in both directions is observed. The relative orientation of the two types of step array suggest the formation of close-packed {211} microfacets, rather than the more open {100} steps here. The cause of the structural transformation is not clear.

Further exploration of structural phenomena on vicinal NiAl surfaces may give insight into the role of terrace width and lateral confinement by steps on the resulting surface structure of this interesting phenomenon. Supplementary AES/XPS studies may elucidate whether minute surface contaminations induce structural changes. A thorough understanding of this surface is required before initiating experiments regarding chemical reactivity.

7.4. POSSIBLE FUTURE APPLICATIONS OF CURVED CRYSTALS

Beyond on-going research presented in this chapter, curved crystals have extensive potential in studying structural effects in surface chemistry. Their variable surface structure could be a useful tool, e.g. when studying reactions in which diffusion between reactive sites plays an important role, or reactions involving multiple reactants with different affinity to surface sites. Curved crystals exposing chiral surfaces, like the *c*-Pt(111)[11$\bar{2}$]-31° crystal we have extensively studied, may prove valuable on the path towards efficient chiral catalysis. Orientations in between close-packed and fully-kinked step directions, may be preferable for larger chiral reactants, e.g. amino acids.

Lastly, we would like to emphasize the value of combining multiple curved crystals, as demonstrated in chapters 4 and 6. This approach allows exploration of a large range of surfaces, when dome-shaped samples or full cylinders are not feasible. Combination of cylindrical slices make it possible to target particularly interesting ranges, and avoid multiples of the same surface structure.

REFERENCES

[1] A. den Dunnen. *Surface-structure dependencies in catalytic reactions.* PhD thesis, Leiden University, 2015.

[2] C. Badan. *Surface-Structure Dependence of Water-Related Adsorbates on Platinum.* PhD thesis, Leiden University, 2016.

[3] K. Cao. *Structure dependence of molecular reactions on surfaces.* PhD thesis, Leiden University, 2018.

[4] R. van Lent. *Steps in gas-surface reactions.* PhD thesis, Leiden University, 2019.

[5] S. Arrhenius. On the Influence of Carbonic Acid in the Air upon the Temperature of the Ground. *The Philosophical Magazine*, 41:237–276, 1896.

[6] S. Arrhenius. Über den Einfluss des atmosphärischen Kohlensäurengehalts auf die Temperatur der Erdoberfläche. *Bihang till Kungl. Svenska Vetenskapsakademiens handlinga*, 22:1–102, 1896.

[7] C.-L. Kao, A. Carlsson, and R. J. Madix. The adsorption dynamics of molecular carbon dioxide on Pt(111) and Pd(111). *Surface science*, 497(1-3):356–372, 2002.

[8] U. Burghaus. Surface chemistry of CO_2–Adsorption of carbon dioxide on clean surfaces at ultrahigh vacuum. *Progress in surface science*, 89(2):161–217, 2014.

[9] D. A. King and M. G. Wells. Molecular beam investigation of adsorption kinetics on bulk metal targets: Nitrogen on tungsten. *Surface Science*, 29(2):454 – 482, 1972.

[10] D. Kulginov, M. Persson, C. Åkerlund, I. Zorić, and B. Kasemo. CO_2 sticking on Pt(111): The role of kinetic energy and internal degrees of freedom. *Journal of Vacuum Science & Technology A*, 13(3):1511–1516, 1995.

[11] G.-C. Wang, L. Jiang, Y. Morikawa, J. Nakamura, Z.-S. Cai, Y.-M. Pan, and X.-Z. Zhao. Cluster and periodic DFT calculations of adsorption and activation of CO_2 on the Cu(hkl) surfaces. *Surface science*, 570(3):205–217, 2004.

[12] S.-G. Wang, D.-B. Cao, Y.-W. Li, J. Wang, and H. Jiao. Chemisorption of CO_2 on nickel surfaces. *The Journal of Physical Chemistry B*, 109(40):18956–18963, 2005.

[13] W. D. Mieher and W. Ho. Bimolecular surface photochemistry: Mechanisms of CO oxidation on Pt(111) at 85 K. *The Journal of Chemical Physics*, 99(11):9279–9295, 1993.

[14] C. Jansen and L. B. F. Juurlink. Absolute dissociation cross sections for D_2 dissociation on Pt steps. submitted.

[15] R. S. Smith and B. D. Kay. Desorption Kinetics of Carbon Dioxide from a Graphene-Covered Pt(111) Surface. *The Journal of Physical Chemistry A*, 123(15):3248–3254, 2019.

[16] H. Shakeel, H. Wei, and J. Pomeroy. Measurements of enthalpy of sublimation of Ne, N_2, O_2, Ar, CO_2, Kr, Xe, and H_2O using a double paddle oscillator. *The Journal of Chemical Thermodynamics*, 118:127 – 138, 2018.

[17] J. Derouin, R. G. Farber, and D. R. Killelea. Combined STM and TPD study of Rh(111) under conditions of high oxygen coverage. *The Journal of Physical Chemistry C*, 119(26):14748–14755, 2015.

[18] R. G. Farber, M. E. Turano, E. C. Oskorep, N. T. Wands, E. V. Iski, and D. R. Killelea. The Quest for Stability: Structural dependence of Rh(111) on oxygen coverage at elevated temperature. *The Journal of Physical Chemistry C*, 121(19):10470–10475, 2017.

[19] X. Feng, J. I. Cerdá, and M. Salmeron. Orientation-Dependent Interaction between CO_2 Molecules Adsorbed on Ru(0001). *The journal of physical chemistry letters*, 6(9):1780–1784, 2015.

[20] C. Dri, A. Peronio, E. Vesselli, C. Africh, M. Rizzi, A. Baldereschi, M. Peressi, and G. Comelli. Imaging and characterization of activated CO_2 species on Ni(110). *Physical Review B*, 82(16):165403, 2010.

[21] N. Moazzen-Ahmadi and A. McKellar. Spectroscopy of dimers, trimers and larger clusters of linear molecules. *International Reviews in Physical Chemistry*, 32(4):611–650, 2013.

[22] L. A. Miccio, M. Setvin, M. Müller, M. Abadía, I. Piquero, J. Lobo-Checa, F. Schiller, C. Rogero, M. Schmid, D. Sánchez-Portal, U. Diebold, and J. E. Ortega. Interplay between Steps and Oxygen Vacancies on Curved TiO2(110). *Nano Letters*, 16(3):2017–2022, 2016.

[23] E. Grånäs, B. Arndt, C. Seitz, M. Wagstaffe, and A. Stierle. Atomic scale step structure and orientation of a curved surface ZnO single crystal. *The Journal of Chemical Physics*, 152(7):074705, 2020.

[24] J. E. Ortega, G. Vasseur, I. Piquero-Zulaica, J. Raoult, M. A. Valbuena, S. Schirone, S. Matencio, A. Mugarza, and J. Lobo-Checa. Atomically precise step grids for the engineering of helical states. *arXiv preprint arXiv:1902.05777*, 2019.

[25] H. Davis and J. Noonan. Rippled relaxation in the (110) surface of the ordered metallic alloy NiAl. *Physical review letters*, 54(6):566, 1985.

[26] M. Kulawik, N. Nilius, H.-P. Rust, and H.-J. Freund. Atomic Structure of Antiphase Domain Boundaries of a Thin Al_2O_3 Film on NiAl (110). *Physical review letters*, 91(25):256101, 2003.

[27] C. Ellinger, V. Vonk, N. Khorshidi, A. Vlad, A. Stierle, and H. Dosch. In situ x-ray study of the oxidation of a vicinal NiAl(6,7,1) surface. *New Journal of Physics*, 11(11):113004, 2009.

[28] D. Mullins and S. Overbury. The structure and composition of the NiAl(110) and NiAl(100) surfaces. *Surface Science*, 199(1-2):141–153, 1988.

8

SUMMARY

CURVED CRYSTALS with their variable, but well-defined surfaces have enormous potential for applications in surface chemistry, to unravel the role of specific sites in the reaction mechanism. Measurements can be repeated on the same crystal with incremental changes of the surface structure. Because effects of sample heterogeneity are avoided, curved crystals make it possible to detect even subtle differences in surface reactivities and assign them to specific surface sites. They were used throughout this thesis to study effects of surface structure on elemental chemical reaction steps.

In chapter 2 we introduce the different types of curved crystals that have been used in literature. We expand on their advantages and challenges in different types of applications. Most standard surface science techniques require adaptations to improve spatial resolution to benefit from the variable surface structure. Improving the spatial resolution by limiting the exposed area, in turn can lead to reduced signal-to-noise ratios; a noteworthy exception is STM, where inherently only a small surface area is probed.

We introduce a nomenclature for crystals in the shape of domes (*d*-M(*hkl*)-x°), cylinders (*cyl*-M[*abc*]), and cylindrical slices (*c*-M(*hkl*)[*abc*]-x°). These are the three shapes that have been used in recent studies involving curved crystals. Depending on the crystal shape, lattice type and crystallographic orientation, curved crystals expose a range of surface structures, with different types of high-symmetry planes, separated by steps and kinks. In this context, LEED provides a useful means to examine overall surface structures across curved surfaces and detect large-scale reconstructions or faceting, by analyzing spot splitting observed in diffraction patterns of vicinal surfaces. Complementary STM studies can give insight into local fluctuations to the average structure.

In regards to surface chemistry, curved crystals have in recent years been used to study the relation between surface structure and chemical reactivity. Prominent examples include the use of cylindrical sections in the study of CO adsorption and oxidation at near-ambient pressures and the use of dome-shaped crystals to investigate the enantioselective adsorption and decomposition of chiral organic molecules on Cu surfaces. In our own group, a fully cylindrical crystal has been employed to study hydrogen dissociation on Ni. More recently, a cylindrical slice of single-crystalline Pt has been used to investigate the surface dynamics of dissociative hydrogen chemisorption, and molecular oxygen adsorption on Pt surfaces, as well as the sites of adsorption of CO. New studies involving curved crystals to examine structure dependencies of elemental chemical reactions, are presented in this thesis.

In chapter 3, we thoroughly study the surface structure of a *c*-Pt(111)[11$\bar{2}$]-31° crystal. Its apex is oriented to expose the (111) surface. With increasing curvature towards the sides of the crystal, kinked step edges forming {210} microfacets are introduced, resulting in chiral surface structure. The kinked steps consist of short segments in the direction of A- and B-type steps.

The overall surface structure is confirmed by LEED spot splitting analysis. A subsequent STM study then examines in detail local variations in surface structure. At the apex, (111) planes that are >100 nm wide and freely meandering step edges are found. To a small extent, vacancy islands remain after sputtering and mild annealing. The equilibrium shape of these vacancy islands reveals the direction of A- and B-type steps on the (111) terrace, and consequently lets us assign short segments of these step types within the kinked {210} steps. This in turn determines the handedness of the chiral stepped surfaces on the two sides of the crystal.

With increasing angle from the apex, steps align along the direction dictated by the crystal's curvature. Terrace width distributions are narrow and symmetric, with a single peak maximum at high step densities. At lower step densities distributions are asymmetric and exhibit, besides the main peak, secondary local maxima at lager terrace widths. Fitting the distributions with a Gaussian function therefore results in better fits at narrowly stepped arrays than wider arrays. Plotting the Gaussian width of these fits against mean terrace width has displayed a non-linear trend in a previous STM study by Walter *et al.* of a similar curved Pt crystal with close-packed steps, which was attributed to a transition in step-step interactions. For the crystal with kinked {210} steps this transition cannot be observed, but also not excluded with certainty.

The highly kinked {210} steps can assume a large range of configurations with varying corrugation, while maintaining their overall orientation as given by the surface curvature of the crystal. The two extremes of this are firstly, the perfect bulk

termination, featuring fully kinked steps consisting of only inner and outer kinks, and secondly the full reconstruction into long segments of A- and B-type steps, separated by only few kinks. To which degree this reconstruction happens is highly relevant if gas-surface reactions are investigated. Chapter 3 therefore includes a thorough analysis of the varying segment lengths along the step. No significant variation of kink densities, nor consistent changes in the distribution of segments, are found for surface arrays with mean terrace widths ranging from <1 nm to >100 nm, showing that the step morphology does not change with step density across the curved crystal. Additionally, the majority of segments along the kinked step edges are 1-3 atoms wide. Long segments, which may behave as {001} or {110} microfacets, rather than {210} microfacets occur only rarely.

The detailed surface characterization of the *c*-Pt(111)[11$\bar{2}$]-31° crystal is an important prerequisite for the chemical reactivity measurements described in chapters 4 and 5.

A molecular beam study of the dissociative chemisorption of D_2 at low kinetic energy is described in chapter 4. It involves both the crystal described above, as well as a *c*-Pt(111)[1$\bar{1}$0]-31° crystal, exhibiting A- and B-type steps on the two sides respectively. Initial sticking probabilities (S_0) are increased on vicinal surfaces compared to (111). Fitting the increase of S_0 with step density reveals small differences between the three different step types on the two curved crystals.

The thorough STM analysis of the kinked steps, in combination with the site-specific reactivities of A- and B-type steps, allows us to conclude that kinks aid dissociation more than atoms in straight steps. However, the measured reactivity difference for the three step types is not adequately captured by models that rely on the (generalized) coordination number of various types of surface atoms. We believe that the origin of the discrepancy is the dynamical nature of the interaction. For a light-weight molecule interacting at low collision energy with a surface that is characterized by (at most) modest barriers to dissociation, molecular wells close to the dissociation site increase the dissociation probability. We therefore describe the interaction in terms of a cross section, σ_0. It reflects the physical area near the step where impingement leads to trapping and dissociation as found in earlier theoretical dynamics studies. The average length of this area, Σ_0, measured normal to the step, is derived directly from the experimentally determined dependence of reactivity on step density. We believe that the reactivities determined here provide a useful tool for modeling dissociation on vicinal surfaces with potentially large unit cells. Furthermore, they allow careful prediction of reactivities on industrially relevant catalyst sites by bridging the whole range of stepped Pt surfaces.

In chapter 5, surfaces close to the apex of the *c*-Pt(111)[11$\bar{2}$]-31° crystal are re-

examined. Meandering step edges, as well as vacancy islands that remain after the gentle last cleaning cycle of surface preparation, are found instead of a perfect (111) surface. We manually extract defect densities at, and close to, the apex and compare them to the step densities expected from the angle of curvature. Only in a range of ±100 µm from the apex are the defect densities increased.

We can thus revisit sticking probabilities of D_2 on the kinked vicinal surfaces. We also probe HD formation from a mixed beam of H_2 and D_2. Data close to (111) is corrected according to the actually probed defect density, but the difference does not affect our previous finding in chapter 4 significantly. However, by fitting the increase of S_0 with step density, we can now extrapolate towards zero and extract the sticking probability for a perfect 'defect-free' (111) surface. This closes a common gap between theoretical studies that compute a perfect (111) unit cell, and experimental results where, even in case of perfect surface preparation, entropy creates a residual defect density.

Both D_2 dissociation probabilites and HD formation probabilities increase nearly linearly with step density. Measured reactivity can thus be approximated as a linear sum of individual contributions by steps and terraces. However, a slight curvature of the data may indicate diffractive scattering of the small molecules at highly ordered step arrays. The lower dependence on step density for HD production than D_2 dissociation may indicate anisotropic diffusion caused by higher binding of H (D) atoms at steps sites.

Further expanding on the advantage of curved crystals, we investigate water desorption from hydrophobic surfaces using two curved Ag single crystals in chapter 6. The crystals are two slices of the same cylinder, centered at (111) and (001) respectively: *c*-Ag(111)[1$\bar{1}$0]-31° and *c*-Ag(001)[1$\bar{1}$0]-31°. Besides the two high-symmetry planes, surfaces with three types of steps are probed, A-type, B-type, and A'-type ({111} microfacets on (001) terraces).

8

Subtle differences in desorption of submonolayer water coverages point toward structure dependencies in water cluster nucleation. Within the interpretation that desorption reflects binding, on the *c*-Ag(111) crystal water molecules are bound measurably stronger by steps than (111) terraces, resulting in a desorption temperature shift as the step density increases. We detect changes in binding energy that vary less than 1 kcal/mol, which is considered 'chemical accuracy'. The binding energy at the two step types can also be shown to not be the same. The A'-type steps bind water approximately equally strong as the (001) terrace. As a result the desorption temperature at very low coverages does not change significantly with step density. We predict that on (001) terraces water cluster nucleation is not dominated by steps.

Water desorption both from surfaces with A-type steps and surface with A'-type steps is extrapolated towards the maximally stepped (311) surface. We conclude that the

A- and A'-steps themselves have the same binding energy for water and can in fact be seen as the same type of step, where facets forming the step edge and terrace are inverted. However, here we can clearly see the influence of the different terrace types. When extending the (111) facets from (311), we see a decrease in desorption temperature, indicating a weaker binding at the (111) terraces. On the other hand, extending the (001) facets from (311) doesn't result in a change in desorption temperature, indicating that the (001) terraces have a very similar binding energy. The difference indicates the fundamental difference between (111) and (001) terraces and illustrates the influence of terrace type on adsorption at steps. Controlling the combination of terraces and steps in terms of terrace type, step type and step density thus provides an extremely sensitive tuning mechanism for the location of water nucleation.

Beyond the work in chapters 3-6, we emphasize the potential of curved crystals in surface science in chapter 7. When studying adsorbates on vicinal surfaces by STM, curved crystals provide a wide range of surface structures, which are exposed to the adsorbing molecule at the same time. Samples do not need to be exchanged to study different surfaces, and different experimental conditions can be avoided. Therefore, gradual changes, e.g. in terrace coverage or adsorbate structure, can be tracked. With regards to gas-surface dynamics, surface-dependent changes in reaction probabilities can be determined, even when these effects are subtle.

Different materials, shape, and orientation may be chosen for curved crystals, allowing to study surface-sensitive reactions, e.g. on alloys or oxides, and opening the door towards efficient chiral heterogeneous catalysis.

9

SAMENVATTING

GEKROMDE KRISTALLEN met goed gedefinieerde variabele oppervlaktestructuren hebben veel potentie om de rol van specifieke oppervlaktesites in het reactiemechanisme te ontrafelen. Door experimenten uit te voeren op verschillende plekken aan het gekromde kristal kan de structuurafhankelijkheid bestudeerd worden met een enkel éénkristal. Omdat effecten, zoals heterogeniteit van monsters worden vermeden, maken gekromde kristallen het mogelijk om subtiele verschillen in oppervlaktereactiviteiten te detecteren en toe te wijzen aan specifieke oppervlakten. Gekromde kristallen worden in dit proefschrift gebruikt om effecten van oppervlaktestructuur op elementaire chemische reactiestappen te bestuderen.

In hoofdstuk 2 introduceren we de verschillende soorten gekromde kristallen die in de literatuur zijn gebruikt. We beschrijven hun voordelen en uitdagingen in verschillende soorten toepassingen. De meeste standaard oppervlaktetechnieken vereisen aanpassingen om de ruimtelijke resolutie te verbeteren om zo te profiteren van de variabele oppervlaktestructuur. Het verbeteren van de ruimtelijke resolutie door het belichte gebied te beperken, kan leiden tot verminderde signaal-ruisverhoudingen; een opmerkelijke uitzondering is de rastertunnelmicroscopie, waarbij inherent slechts een klein gebied op het oppervlak wordt onderzocht.

We introduceren een nomenclatuur voor kristallen in de vorm van koepels, cilinders en cilindrische snedes. Dit zijn de drie vormen die zijn gebruikt in recent onderzoek met gekromde kristallen. Afhankelijk van de kristalvorm, het roostertype en de kristallografische oriëntatie leggen gekromde kristallen een reeks oppervlaktestructuren bloot met verschillende soorten hoogsymmetrische terrassen, welke door treden en knikken gescheiden worden. In deze context is LEED een nuttig middel om algemene oppervlaktestructuren van gekromde oppervlakken te onderzoeken.

Diffractiepatronen splitsen in aanwezigheid van regelmatig gestapte oppervlakken, waarmee grootschalige reconstructies en/of facetten worden gedetecteerd. Complementair STM-onderzoek kan inzicht geven over lokale fluctuaties van de gemiddelde structuur.

Met betrekking tot de oppervlaktechemie zijn gekromde kristallen de afgelopen jaren gebruikt om de relatie tussen oppervlaktestructuur en chemische reactiviteit te bestuderen. Prominente voorbeelden zijn het gebruik van cilindrische snedes bij de studie van CO-adsorptie en oxidatie bij drukken nabij de atmosferische druk, evenals het gebruik van koepelvormige kristallen om enantioselectieve adsorptie en ontleding van chirale organische moleculen aan koperoppervlakken te onderzoeken. Binnen onze eigen groep is een volledig cilindrisch kristal gebruikt om waterstof dissociatie aan nikkeloppervlakken te bestuderen. Onlangs is een cilindrische snede van éénkristallijn platina gebruikt om de oppervlaktedynamica van dissociatieve waterstofchemisorptie en moleculaire zuurstofadsorptie aan platinaoppervlakken te onderzoeken. Hetzelfde platina kristal is ook gebruikt voor onderzoek naar de adsorptieplaatsen van CO. In dit proefschrift worden nieuwe studies gepresenteerd, waarin gekromde kristallen worden gebruikt om de oppervlaktestructuurafhankelijkheid van elementaire chemische reacties te bestuderen.

In hoofdstuk 3 bestuderen we de oppervlaktestructuur van een gekromd Pt-kristal (*c*-Pt(111)[11$\bar{2}$]-31°). De apex is uitgelijnd om het (111) oppervlak bloot te leggen. Met toenemende kromming naar de zijkanten van het kristal worden geknikte stapranden die {210} microfacetten vormen geïntroduceerd, waardoor een chirale oppervlaktestructuur ontstaat. De geknikte stappen bestaan uit korte segmenten in de richting van A- en B-type stappen.

De algehele oppervlaktestructuur wordt bevestigd door analyse van *spot splitting* in het LEED patroon. Een daaropvolgende STM-studie onderzoekt vervolgens in detail lokale variaties van de oppervlaktestructuur. Bij de apex worden (111) vlakken gevonden die >100 nm breed zijn, gescheiden door vrij meanderende stapranden. Na sputteren en mild annealen blijven er in kleine mate *vacancy islands*. De evenwichtsvorm van deze putten onthult de richting van de A- en B-type stappen op het (111) terras. Deze identificatie brengt ons in staat korte segmenten van deze soorten treden toe te wijzen binnen de geknikte {210} stapranden. Dit bepaalt op zijn beurt de handigheid van de chirale getrapte oppervlakken aan de twee zijden van het kristal.

Met toenemende hoek vanaf de apex worden de treden uitgelijnd in de richting die wordt voorgeschreven door de kromming van het kristal. De terasbreedteverdelingen zijn smal en symmetrisch, met een enkel piekmaximum bij hoge stapdichtheden. Bij lagere stapdichtheden zijn verdelingen asymmetrisch en vertonen naast de hoofdpiek secundaire lokale maxima bij grotere terrasbreedten. Het fitten van de verdelin-

gen met een Gauss-functie resulteert daarom in betere fits bij nauw getrapte arrays dan bij bredere reeksen. In een eerdere STM-studie door Walter *et al.* van een soortgelijk gekromd Pt-kristal met ongeknikte (A- of B-type) stappen, vertoonde de Gauss breedte van deze fits een niet-lineaire trend tegenover de gemiddelde terrasbreedte. Dit gedrag werd toegeschreven aan een overgang in de stap-stap-interacties. Voor het kristal met geknikte {210} stappen is deze overgang niet waargenomen in dit proefschrift, maar kan ook niet met zekerheid worden uitgesloten.

De sterk geknikte {210}-stappen kunnen een groot aantal configuraties met variërende corrugatie aannemen terwijl de algehele oriëntatie behouden blijft zoals gegeven door de oppervlaktekromming van het kristal. De twee uitersten hiervan zijn in de eerste plaats de perfecte bulkafsluiting, met volledig geknikte treden die alleen uit binnen- en buitenknikken bestaan, en ten tweede de volledige reconstructie tot lange segmenten van A- en B-type treden, gescheiden door slechts enkele knikken. In hoeverre deze reconstructie plaatsvindt is essentiël voor onderzoek naar gas-oppervlakreacties. Hoofdstuk 3 bevat daarom een grondige analyse van de variërende segmentlengte langs de stap. De knikdichtheid en de segmentdistributies vertonen geen significante verschillen als functie van terrasbreedten voor oppervlakte-arrays met gemiddelde terrasbreedtes van <1 nm tot >100 nm. Dit toont aan dat op het gekromde kristal de stapmorfologie niet verandert met de stapdichtheid. Bovendien zijn de meeste segmenten langs de geknikte stapranden 1-3 atomen breed. Lange segmenten, die zich gedragen als {001} of {110} microfacetten in plaats van als {210} microfacetten, komen slechts zelden voor.

De gedetailleerde oppervlaktekarakterisering van het *c*-Pt(111)[11$\bar{2}$]-31° kristal is een belangrijk voorwaarde voor de chemische reactiviteitsmetingen beschreven in hoofdstukken 4 en 5.

Een moleculaire bundelstudie van de dissociatieve chemisorptie van D_2 bij lage kinetische energie wordt beschreven in hoofdstuk 4. Het omvat zowel het hierboven beschreven kristal als een *c*-Pt(111)[1$\bar{1}$0]-31° kristal, met gescheiden A- en B-type stappen aan de zijkanten. Initiële plakkansen (S_0) zijn hoger aan aangrenzende oppervlakken dan aan (111). Door de toename van S_0 met stapdichtheid te fitten, worden kleine verschillen tussen de drie verschillende staptypen van de twee gekromde kristallen zichtbaar.

Door grondige STM-analyse van de geknikte stappen, in combinatie met de specifieke reactiviteiten van A- en B-type stappen, kunnen we concluderen dat knikken dissociatie meer bevorderen dan atomen in rechte stappen. Het gemeten reactiviteitsverschil tussen de drie staptypen wordt echter niet voldoende beschreven door modellen gebaseerd op het (gegeneraliseerde) coördinatiegetal van verschillende soorten oppervlakte-atomen. Wij zijn van mening dat de oorsprong van de

discrepantie de dynamische aard van de interactie tussen waterstof en het platinaoppervlak is. Voor een lichtgewicht molecuul dat bij lage botsingsenergie een interactie aangaat met een oppervlak dat wordt gekenmerkt door (hoogstens) matige barrières voor dissociatie, verhogen moleculaire putten nabij de dissociatieplaats de dissociatiekans. We beschrijven de interactie daarom in termen van een doorsnede, σ_0. Het weerspiegelt het fysieke gebied nabij de trede waar botsing leidt tot *trapping* en dissociatie, zoals gevonden in eerdere theoretische dynamica-onderzoeken. De gemiddelde lengte van dit gebied, Σ_0, gemeten loodrecht op de stap, wordt rechtstreeks afgeleid uit de experimenteel bepaalde stapdichtheidsafhankelijke reactiviteit. Wij zijn van mening dat de hier bepaalde reactiviteiten een nuttig hulpmiddel zijn voor het modelleren van dissociatie aan gestapte oppervlakken met potentieel grote eenheidscellen. Bovendien maken ze een zorgvuldige voorspelling van reactiviteiten op industrieel relevante katalysatoroppervlakken mogelijk door de hele reikwijdte van gestapte platinaoppervlakken te omvatten.

In hoofdstuk 5 worden oppervlakken dichtbij de apex van het kristal opnieuw onderzocht. In plaats van een perfect (111) oppervlak worden kronkelende stapranden en *vacancy islands* gevonden die overblijven na de milde laatste schoonmakcyclus tijdens het bereiden van het oppervlak. We extraheren handmatig defectdichtheden bij (en nabij) de apex en vergelijken deze met de stapdichtheden die worden verwacht op basis van de kromminghoek. Alleen in een bereik van <100 nm vanaf de apex zijn de defectdichtheden verhoogd.

We kunnen dus de plakkansen van D_2 op de geknikte vicinale oppervlakken opnieuw bekijken. We onderzoeken ook HD-formatie uit een gemengde bundel van H_2 en D_2. Metingen dicht bij (111) worden gecorrigeerd volgens de feitelijk onderzochte defectdichtheid, maar het verschil heeft geen significante invloed op onze eerdere bevinding in hoofdstuk 4. Door de toename van S_0 echter aan te passen aan stapdichtheid, kunnen we nu naar nul extrapoleren en de plakkans bepalen voor een perfect 'defectvrij' (111) oppervlak. Dit dicht een vaak voorkomende kloof tussen theoretische studies, die een perfecte (111) eenheidscel simuleren, en experimentele resultaten waarbij, zelfs in het geval van perfecte oppervlaktevoorbereiding, entropie een resterende defectdichtheid creëert.

Zowel de kans op D_2-dissociatie als de kans op HD-vorming nemen bijna lineair toe met stapdichtheid. Gemeten reactiviteit kan dus worden benaderd als een lineaire som van individuele bijdragen door stapranden en terrassen. Een lichte kromming van de gegevens kan echter duiden op diffractieve verstrooiing van de kleine moleculen bij sterk geordende staparrays. De lagere afhankelijkheid van stapdichtheid voor HD-productie dan D_2-dissociatie kan duiden op anisotrope diffusie veroorzaakt door hogere binding van H(D)-atomen aan stappen.

Het voordeel van gekromde kristallen wordt verder duidelijk bij onderzoek naar waterdesorptie van hydrofobe oppervlakken met behulp van twee gekromd Ag-éénkristallen in hoofdstuk 6. De kristallen zijn twee snedes van dezelfde cilinder, respectievelijk gecentreerd op (111) en (001): *c*-Ag(111)[1$\bar{1}$0]-31° en *c*-Ag(001)[1$\bar{1}$0]-31°. Naast de twee hoogsymmetrische vlakken, worden oppervlakken met drie soorten stapranden bestudeerd: A-type, B-type en A'-type ({111} microfacetten op (001) terrassen).

Subtiele verschillen in desorptie van sub-monolaag waterbedekkingen wijzen op structuurafhankelijkheden in de nucleatie van waterclusters. Binnen de interpretatie dat desorptie binding weerspiegelt, binden de stappen op het *c*-Ag(111) kristal watermoleculen meetbaar sterker dan de (111) terrassen, wat resulteert in een verhooging van de desorptietemperatuur met stapdichtheid. We detecteren veranderingen van minder dan 1 kcal/mol in bindingsenergie, wat wordt beschouwd als 'chemische nauwkeurigheid'. Er kan ook worden aangetoond dat de bindingsenergie bij de twee staptypen niet hetzelfde is. De A'-type stapranden binden water ongeveer even sterk als het (001) terras. Als resultaat verandert de desorptietemperatuur bij zeer lage bedekkingen niet significant met de stapdichtheid. We voorspellen dat op (001) terrassen de nucleatie van waterclusters niet wordt gedomineerd door stappen.

Waterdesorptie van zowel oppervlakken met A-type stappen als oppervlakken met A'-type treden wordt geëxtrapoleerd naar het maximaal gestapte (311) oppervlak. We concluderen dat de A- en A'-stappen dezelfde bindingsenergie voor water hebben en in feite gezien kunnen worden als dezelfde type staprand, waarbij de facetten welke de straprand en het terras vormen zijn omgekeerd. Hier zien we echter duidelijk de invloed van verschillende terrastypes. Bij het verlengen van de (111) facetten van (311) zien we een afname van de desorptietemperatuur, wat duidt op een zwakkere binding op de (111) terrassen. In tegenstelling resulteert het verlengen van de (001)-facetten van (311) niet in een verandering in de desorptietemperatuur, wat aangeeft dat de (001)-terrassen een zeer vergelijkbare bindingsenergie hebben. Het verschil geeft het fundamentele verschil aan tussen (111) en (001) terrassen en illustreert de invloed van terrastype op adsorptie aan stapranden. Controle over de samenstelling van terrassen en stappen op het oppervlak (terrastype, staptype en stapdichtheid) verschaft dus een uiterst gevoelig inzicht op de locatie van waternucleatie.

Naast het werk in de hoofdstukken 3-6, benadrukken we in hoofdstuk 7 het potentieel van gekromde kristallen in de oppervlaktewetenschap. Bij het bestuderen van adsorbaten op gestapte oppervlakken met STM, bieden gekromde kristallen een breed scala aan oppervlaktestructuren, welke tegelijkertijd worden blootgesteld aan het adsorberende molecuul. Het kristal hoeft niet te worden uitgewisseld om verschillende oppervlakken te bestuderen en wisselende experimentele omstandigheden kunnen worden vermeden. Daarom kunnen geleidelijke veranderingen worden gevolgd, bijvoorbeeld van de bedekkingsgraad of de adsorbaatstructuur. Met betrekking tot

gas-oppervlaktedynamica kunnen oppervlakteafhankelijke veranderingen in reactiekansen worden bepaald, zelfs wanneer deze effecten subtiel zijn.

Verschillende materialen, vormen en oriëntaties kunnen worden gekozen voor gekromde kristallen, waardoor oppervlaktegevoelige reacties kunnen worden bestudeerd, bijvoorbeeld op legeringen of oxiden. Gekromde kristallen kunnen ook gebruikt worden voor toekomstig onderzoek naar efficiënte chirale heterogene katalyse.

A

Supplementary Information for Chapter 3: Surface structure characterization of a curved Pt crystal with highly kinked steps

A.1. Histograms of facet distributions in kinked steps

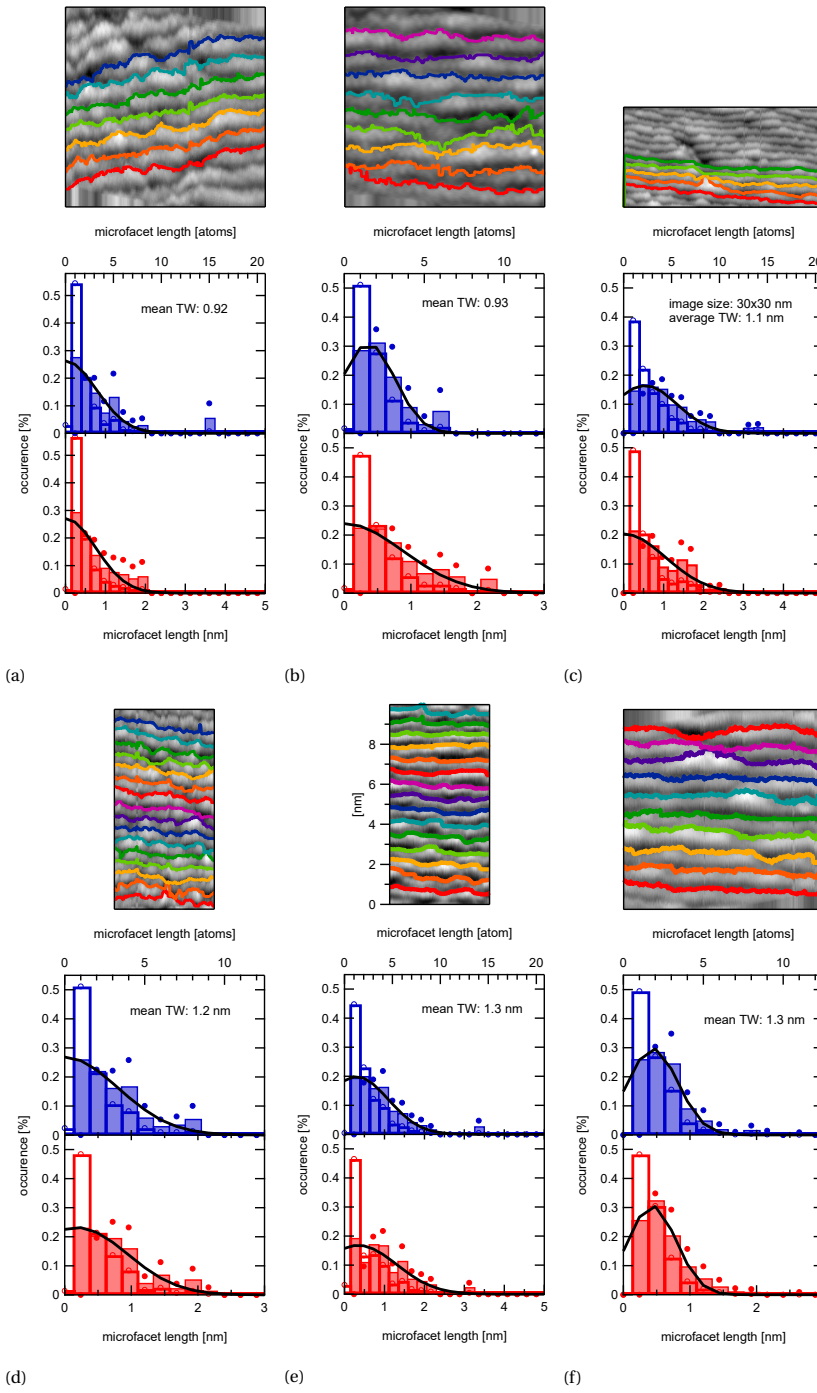

Figure A.1: a)–m) STM images and distributions of segment lengths along the kinked step edges. Kink densities and Gaussian fits are used in figure 3.9.

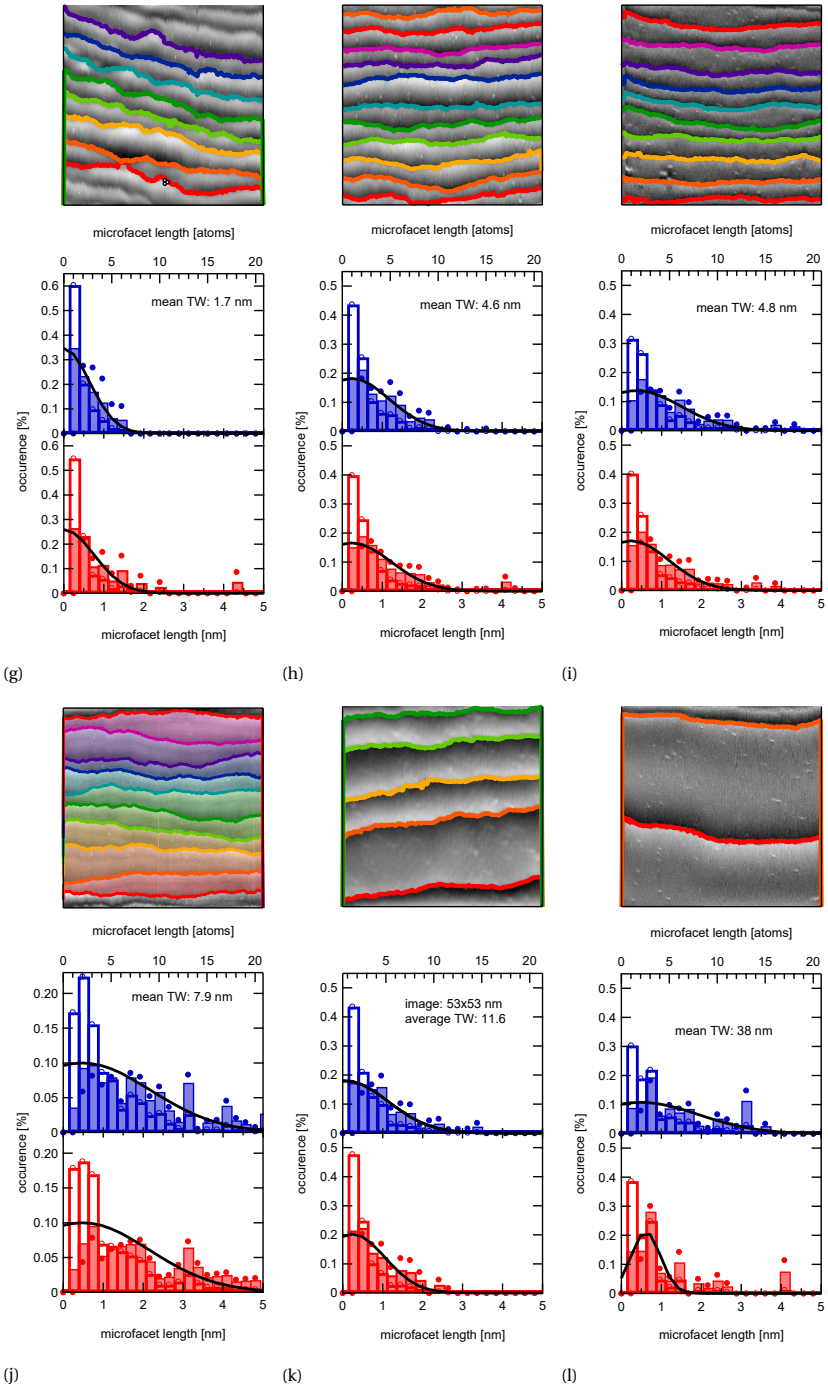

Figure A.1: a)–m) STM images and distributions of segment lengths along the kinked step edges. Kink densities and Gaussian fits are used in figure 3.9.

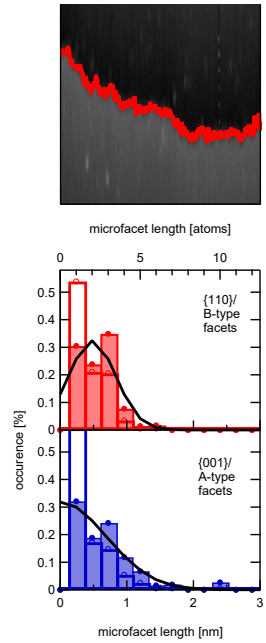

(m)

Figure A.1: a)–m) STM images and distributions of segment lengths along the kinked step edges. Kink densities and Gaussian fits are used in figure 3.9.

B

SUPPLEMENTARY INFORMATION FOR CHAPTER 4: SCALING PT-CATALYZED HYDROGEN DISSOCIATION ON CORRUGATED SURFACES

B.1. INITIAL STICKING PROBABILITIES AT STEP SITES

The slope Σ_0, as obtained from the linear fits of S_0 at different positions of the curved crystal, has a unit of nm due to the x-axis (step density) being in units of nm^{-1}.

$$S_0(SD) = S_0^{(111)} + \Sigma_0[\text{nm}] \cdot SD[\text{nm}^{-1}] \tag{B.1}$$

An alternative way to quantify the additional reactivity caused by steps is to consider the fraction of the surface area occupied by steps (f^{step}), instead of mere step density:

$$S_0 = S_0^{(111)} \cdot (1 - f^{step}) + S_0^{step} \cdot f^{step} \tag{B.2}$$

Obtaining a unitless S_0^{step} may feel more intuitive when comparing reactivities of the step edge with reactivities of the (111) terrace. However, determining a value f^{step} requires an assumption on the size of a step within the unit cell. Defining it as one atom row at the upper step edge will give a different step size for kinked steps (0.277 nm) than A- and B-type steps (0.240 nm), due to their orientation on the (111) terrace. Considering the upper edge and lower cusp of each step type will yield different step sizes for each type. The same step density may thus correspond to three different values for f^{step}, resulting in a weighing of S_0^{step} purely based on atom arrangement.
We therefore consider the weighing of reactivity by step density in equation B.1 a more appropriate approach when comparing different step types. The unit, nm, in

turn can be interpreted as length over which the step is reactive, i.e. a 'chemical step size'. The implications of Σ_0 as a physical length are further discussed in the main text.
The decreasing fraction of (111) terraces on the stepped surfaces, $(1 - f^{step})$ is neglected there, due to the inherently small value of $S_0^{(111)}$.

B

B.2. COORDINATION AT THE LOWER STEP EDGE

For atoms at the lower edges, CN and $\overline{CN}$ values for the three step types vary slightly, as listed in table B.1. The coordination number in the lower plane of the A-type step is lower than both the B-type step and any combined contribution of inner and outer kinks. The A-type should thus be most reactive. If only outer kinks contribute to reactivity, the {210} steps should react similarly to the A-type. The B-type should be least reactive.

	upper edge				lower edge			
	A	B	K_{in}	K_{out}	A	B	K_{in}	K_{out}
CN	7	7	8	6	10	11	11	10
$\overline{CN}$	5.50	5.50	6.17	4.83	8.75	9.50	9.58	8.58

Table B.1: Coordination numbers (CN) and gerneralized coordination numbers ($\overline{CN}$) [**?**] of atoms at the upper and lower edge of the three step types in this study.

B.3. STRUCTURAL ANALYSIS OF THE KINKED {210} STEPS

Table B.2 lists kink atoms (K) and step atoms (A or B) in fully-kinked (a) and longer segments (b,c,d...). In the ultimate case of step faceting, a single {210} step would break into very large segments of the A- and B-type. This reconstruction of the {210} step has a combined total length of 1.16 times that of a straight line connecting the first and last atom of the edge. These ideas form the basis for a model that extracts the average chemical reactivity of inner and outer kinks. We take into account the length and composition of possible step sections, the measured reactivity for A- and B-type steps, and the distribution of A- and B-sections in {210} steps as obtained by STM.

The STM images in figure 4.3b)–e) gives us distributions of segment lengths in averages stretches of step edges. We use those distributions and the atomic compositions of segments laid out in table B.2 and displayed in figure 4.3a) to calculate the number of kink atoms (N_K), as well as intermittent atoms in longer segments of A- or B-type orientation (N_A and N_B):

$$N_A = 0 \cdot a_A + 1 \cdot b_A + 2 \cdot c_A + \cdots \tag{B.3}$$

segment	atoms in segment	{001}-oriented		{110}-oriented	
		K	A	K	B
a	2	1	0	1	0
b	4	1	1	1	1
c	6	1	2	1	2
d	8	1	3	1	3
⋮	⋮	⋮	⋮	⋮	⋮

Table B.2: Composition of atoms found in kinked steps with various segment lengths, as displayed in figure 4.3a) of the main text. Atoms at the top of the step edge can be considered either a direct kink atom (K), or a step atom. Depending on the orientation of the segment, step atoms are either A-type (A) or B-type (B).

$$N_B = 0 \cdot a_B + 1 \cdot b_B + 2 \cdot c_B + \cdots \tag{B.4}$$

$$N_K = a_A + a_B + b_A + b_B + c_A + c_B + \cdots \tag{B.5}$$

Here a_A is the fractional occurrence of bin a of the {001} histogram, b_A is the fractional occurrence of segments in bin b of the {001} histogram, a_B is the fractional occurrence of segments in bin a of the {110} histogram, etc...

Table B.3 lists the results, as well as kink densities and Σ_0, as described in the main text.

image in fig.4.3	N_A	N_B	N_K	N	N_K/N	${\Sigma_0}^K$
b)	152.201	122.222	200	474.423	0.422	0.747
c)	139.734	161.9	200	501.634	0.399	0.734
d)	73.6264	106.522	200	380.1484	0.526	0.667
e)	163.158	127.016	200	490.174	0.408	0.758

Table B.3: Numbers of atoms found in kinked steps with various segment lengths, as displayed in figure 4.3a), averaged to 100 segments in {001} orientation and 100 segments in {110} orientation. Atoms are considered either a kink atom (K), or an atom resembling those in type A steps (A) and type B steps (B).

C

SUPPLEMENTARY INFORMATION FOR CHAPTER 5: CHIRAL SURFACE CHARACTERISATION AND REACTIVITY TOWARD H-D EXCHANGE OF A CURVED PLATINUM CRYSTAL

C.1. TERRACE WIDTH ANALYSIS

Figure C.1a) shows the averaged terrace widths for each image, 300 µm on either side of the apex. Blue data with error bars represent each image's average terrace width and standard deviation. The red dots are, for each image, the local maximum terrace width which, together with the standard deviation, provide an idea of the terrace width distribution across the crystal. The black traced lines are the expected terrace widths as described by equation 5.1. We observe a close match with the expected terrace width except for in the ~40 µm around the apex. This is more clearly visible in the zoomed-in section of the figure.

By taking the inverse of the terrace widths, we expect to see a linearly increasing step density where the slope is determined by the radius of curvature and interatomic distance. Beyond 400 µm on the (-Y) side of the crystal, terrace width distribution was low enough to simply divide the number of steps in an image by the distance between the first and last step. This data, along with the inverse of the terrace widths previously shown, is plotted in figure C.1b). We can see that all along the imaged regions of the crystal, the step density increases linearly with distance from the apex respecting the expected defect density.

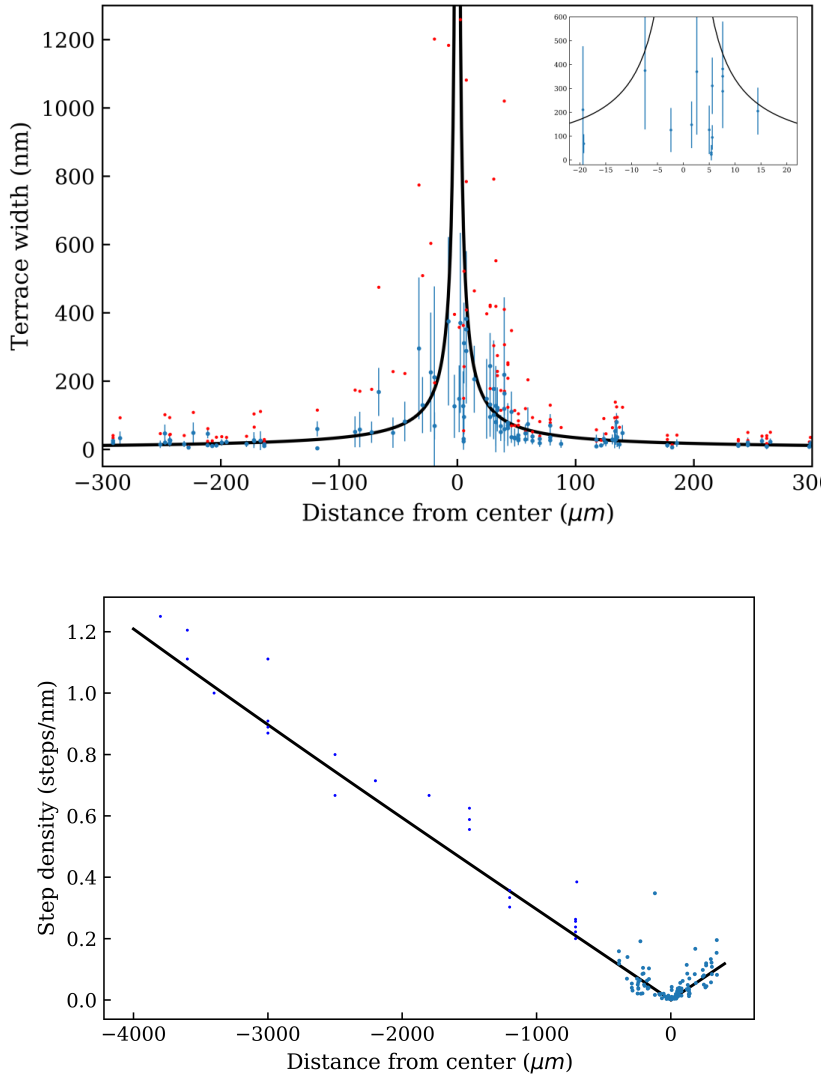

Figure C.1: a) Terrace widths as a function of distance from the apex for 330 nm on either side of the apex. Blue data points indicate the average terrace widths including the standard deviation per STM image and red data points are the maximum terrace widths per image. A subfigure in the rop right shows a zoom around the center of the graph where the averages start to deviate from the expected TW curve (in black). b) Step densities as a function of position on the crystal. Black line represents the expected step density taken from the inverse of equation 5.1.

D

STM ANALYSIS PROCEDURE TO DETERMINE OUTLINES OF STEPS IN STM IMAGES WITH IGOR PRO

D.1. PROCEDURE 1

One pixel wide line profiles in vertical direction are created across the entire STM image.

```
Function alllineprofiles(i,j,name,x)

variable i//first lineprofile
variable j//last line profile
variable x//number of pixels in image
wave name
make/n=2 xxx,yyy
wave xxx ; wave yyy
string srcwave ; string xwave ; string ywave
Display

For (i=i; i<j+1;i +=1)
xxx=i,i ; yyy=0,(x-1)
string num=num2str(i) ; string profile="Prof"+num
ImageLineProfile srcwave=name, xwave=xxx, ywave=yyy, width=3
duplicate W_; ImageLineProfile $profile
```

```
wave pro=$profile
Appendtograph pro vs W_LineProfileY
string profiledif="Prof"+num+"_dif"
differentiate pro/X=W_LineProfileY/D=$profiledif
wave dif=$profiledif
EndFor
End
```

D.2. PROCEDURE 2

Step edges are found along the horizontal direction, across all line profiles.

```
Function limitprofiles(i,j,k,x,name,A,B,n)

variable i //first x
variable j //last x that you take a lineprofile of
variable A //first point of y values in which to find the step
variable B //last point of y values in which to find the step
variable n //how manyth step in image
wave name //name of image wave
variable k //imagesize (nm)
variable x//number of pixels in image

string st="step"+num2str(n)
make/n=(j+1) $st
wave step=$st

For (i=i; i<j+1;i +=1)
string num=num2str(i) ; string profile="Prof"+num
wave pro=$profile
string profiledif="Prof"+num+"_dif"
wave dif=$profiledif
wavestats/Q/R=(A,B) dif
step[i]=V_maxRowLoc
```

```
EndFor

step[0]=step[1] ; step[j]=step[j-1]
string stnm="step"+num2str(n)+"_nm"
duplicate/O step $stnm
wave step_nm=$stnm
step_nm=step/x*k

string stx="stepX_nm"
duplicate/O step $stx
wave stepX=$stx
stepX=p/(j+1)*k

AppendtoGraph step vs W_LineProfileY
ModifyGraph mode=4,marker=19

If(n==2)
ModifyGraph rgb(step2)=(65280,21760,0)
elseif(n==3)
ModifyGraph rgb(step3)=(65280,43520,0)
elseif(n==4)
ModifyGraph rgb(step4)=(26112,52224,0)
elseif(n==5)
ModifyGraph rgb(step5)=(0,39168,0)
elseif(n==6)
ModifyGraph rgb(step6)=(0,39168,39168)
elseif(n==7)
ModifyGraph rgb(step7)=(0,9472,39168)
elseif(n==8)
ModifyGraph rgb(step8)=(19712,0,39168)
elseif(n==9)
ModifyGraph rgb(step9)=(52224,0,41728)
elseif(n==11)
ModifyGraph rgb(step11)=(65280,21760,0)
```

```
elseif(n==12)
ModifyGraph rgb(step12)=(65280,43520,0)
elseif(n==13)
ModifyGraph rgb(step13)=(26112,52224,0)
elseif(n==14)
ModifyGraph rgb(step14)=(0,39168,0)
elseif(n==15)
ModifyGraph rgb(step15)=(0,39168,39168)
elseif(n==16)
ModifyGraph rgb(step16)=(0,9472,39168)
elseif(n==17)
ModifyGraph rgb(step17)=(19712,0,39168)
elseif(n==18)
ModifyGraph rgb(step18)=(52224,0,41728)
endif

string one=nameofwave(step)+"#1"
removefromgraph/Z $one
End
```

D.3. PROCEDURE 3

The terrace widths in between step edges are determined.

```
Function maketerraces(j,k,x)

variable j //number of steps
variable k //imagesize (nm)
variable x//number of pixels in image
variable i ; variable a=0

For (i=1; i<j;i +=1)
string st="step"+num2str(i)
wave step=$st
string st2="step"+num2str(i+1)
```

```
wave step2=$st2
string ter="terrace"+num2str(i)
duplicate/O step $ter
wave terrace = $ter
terrace = step2-step
string ternm="terrace"+num2str(i)+"_nm"
duplicate/O terrace $ternm
wave terrace_nm = $ternm
terrace_nm=terrace/x*k
wavestats/Q terrace_nm
a += V_avg
EndFor

print "avg terrace width [nm]" ; print a/(j-1)
End
```

D.4. PROCEDURE 4

Terrace width distribution histograms are created from the available terrace widths.

```
Function terracehist(j,k,x)

variable j //number of terraces
variable k //image size (nm)
variable x//number of pixels in image
variable l=k*2/0.277
variable i

display

For (i=1; i<j+1;i +=1)
string ternm="terrace"+num2str(i)+"_nm"
wave terrace_nm = $ternm
string hist="terrace"+num2str(i)+"_Hist"
string number=num2str(l)
```

```
Make/N=(l)/O $hist;
wave histo=$hist
Histogram/C/R=[1,(x-2)]/B=0,0.1385,l terrace_nm,histo
AppendToGraph histo

If (i==1)
string hall="terrace_all_hist"
duplicate histo $hall
wave h_all=$hall
appendtograph h_all
ReorderTraces terrace1_Hist,terrace_all_hist
Else
h_all+=histo
endif
Endfor

ModifyGraph mode=5,hbFill=3 ; ModifyGraph tick=2,mirror=1,standoff=0
Label bottom "terrace width (nm) (1 bin = 0.1385 nm = 1/2 atom row)" ; Label left "counts"
End
```

D.5. PROCEDURE 5

Segments along a step edge (in between kink sites) are determined and their length is determined.

```
Function makeblock(step,stepX)

wave step ; wave stepX
variable x//image size
string st=nameofwave(step) //name of step wave
string stx=nameofwave(stepX) // name of x wave of step wave
duplicate/O step $st+"_dif"
wave step_dif = $st+"_dif"
Differentiate/METH=1 step/X=stepX/D=step_dif;
duplicate/O step_dif $st+"block"
```

```
wave block = $st+"block"

variable i ; variable j = numpnts(step) //number of points in wave

For (i=0; i<j;i +=1)
If(step_dif[i]>0.1)
block[i]=1
Elseif(step_dif[i]<-0.1)
block[i]=-1
Else
block[i]=0
EndIf
EndFor

duplicate/O stepX $st+"blockpos"
wave position=$st+"blockpos"
duplicate/O block $st+"blockvalue"
wave value=$st+"blockvalue"
duplicate/O position $st+"blockpos_fw"
wave posfw=$st+"blockpos_fw"
duplicate/O block $st+"blockvalue_fw"
wave valuefw=$st+"blockvalue_fw"
duplicate/O position $st+"blockpos_bw"
wave posbw=$st+"blockpos_bw"
duplicate/O block $st+"blockvalue_bw"
wave valuebw=$st+"blockvalue_bw"

For (i=0; i<j; i +=1)
if(valuefw(i)==0)
deletepoints i,1,posfw ; deletepoints i,1, valuefw
i=i-1
EndIf
EndFor
```

```
For (i=numpnts(step); i>0;i -=1)
If(valuebw[i]==0)
deletepoints i,1,posbw ; deletepoints i,1,valuebw
EndIf
EndFor

For (i=1; i<numpnts(valuefw);i +=1)
if(valuefw(i)==valuefw[i-1])
deletepoints i,1,posfw ; deletepoints i,1, valuefw
i=i-1
EndIf
EndFor

For (i=1; i<numpnts(valuefw);i +=1)
if(posfw(i)-posfw(i-1)<0.12)
deletepoints i,1,posfw ; deletepoints i,1, valuefw
i=i-1
EndIf
EndFor

For (i=1; i<numpnts(valuefw);i +=1)
if(valuefw(i)==valuefw[i-1])
deletepoints i,1,posfw ; deletepoints i,1, valuefw
i=i-1
EndIf
EndFor

For (i=0; i<numpnts(valuebw) ;i +=1)
If(valuebw(i)==valuebw(i+1))
deletepoints i,1,posbw ; deletepoints i,1,valuebw
i=i-1
EndIf
EndFor
```

```
For (i=0; i<numpnts(valuebw) ;i +=1)
If(posbw(i+1)-posbw(i)<0.12)
deletepoints i,1,posbw ; deletepoints i,1,valuebw
i=i-1
EndIf
EndFor

For (i=0; i<numpnts(valuebw) ;i +=1)
If(valuebw(i)==valuebw(i+1))
deletepoints i,1,posbw ; deletepoints i,1,valuebw
i=i-1
EndIf
EndFor

duplicate/O posfw $st+"_facet_fw"
wave facetfw=$st+"_facet_fw"
For (i=1; i<j;i +=1)
facetfw[i]=posfw[i]-posfw[i-1]
Endfor

duplicate/O posbw $st+"_facet_bw"
wave facetbw=$st+"_facet_bw"
For (i=0; i<j;i +=1)
facetbw[i]=posbw[i+1]-posbw[i]
Endfor

duplicate/O facetfw $st+"plusfacet_fw"
wave plusfw = $st+"plusfacet_fw"
duplicate/O valuefw $st+"plusvalue_fw"
wave plusvalfw = $st+"plusvalue_fw"
duplicate/O facetfw $st+"minusfacet_fw"
wave minusfw = $st+"minusfacet_fw"
duplicate/O valuefw $st+"minusvalue_fw"
wave minusvalfw = $st+"minusvalue_fw"
```

```
For (i=0; i<j;i +=1)
If(plusvalfw[i]!=1)
deletepoints i,1,plusfw ; deletepoints i,1,plusvalfw
i=i-1
Endif
Endfor

For (i=0; i<j;i +=1)
If(plusfw[i]==0)
deletepoints i,1,plusfw ; deletepoints i,1,plusvalfw
i=i-1
Endif
Endfor

For (i=0; i<j;i +=1)
If(minusvalfw[i]!=-1)
deletepoints i,1,minusfw ; deletepoints i,1,minusvalfw
i=i-1
Endif
Endfor

For (i=0; i<j;i +=1)
If(minusfw[i]==0)
deletepoints i,1,minusfw ; deletepoints i,1,minusvalfw
i=i-1
Endif
Endfor

duplicate/O facetbw $st+"plusfacet_bw"
wave plusbw = $st+"plusfacet_bw"
duplicate/O valuebw $st+"plusvalue_bw"
wave plusvalbw = $st+"plusvalue_bw"
duplicate/O facetbw $st+"minusfacet_bw"
```

```
wave minusbw = $st+"minusfacet_bw"
duplicate/O valuebw $st+"minusvalue_bw"
wave minusvalbw = $st+"minusvalue_bw"

For (i=0; i<j;i +=1)
If(plusvalbw[i]!=1)
deletepoints i,1,plusbw ; deletepoints i,1, plusvalbw
i=i-1
Endif
Endfor

For (i=0; i<j;i +=1)
If(plusbw[i]==0)
deletepoints i,1,plusbw ; deletepoints i,1,plusvalbw
i=i-1
Endif
Endfor

For (i=0; i<j;i +=1)
If(minusvalbw[i]!=-1)
deletepoints i,1,minusbw ; deletepoints i,1,minusvalbw
i=i-1
Endif
Endfor

For (i=0; i<j;i +=1)
If(minusbw[i]==0)
deletepoints i,1,minusbw ; deletepoints i,1,minusvalbw
i=i-1
Endif
Endfor

Make/O/N=200/O $st+"_plus_hist_fw"
wave plh_fw=$st+"_plus_hist_fw"
```

```
Make/O/N=200/O $st+"_minus_hist_fw"
wave mnh_fw = $st+"_minus_hist_fw"
Histogram/C/B=-0.12,0.24,200 plusfw,plh_fw
Histogram/C/B=-0.12,0.24,200 minusfw,mnh_fw
Make/O/N=200/O $st+"_plus_hist_bw"
wave plh_bw=$st+"_plus_hist_bw"
Make/O/N=200/O $st+"_minus_hist_bw"
wave mnh_bw = $st+"_minus_hist_bw"
Histogram/C/B=-0.12,0.24,200 plusbw,plh_bw
Histogram/C/B=-0.12,0.24,200 minusbw,mnh_bw
duplicate/O plh_fw $st+"_plus_hist_avg"
wave plh_avg = $st+"_plus_hist_avg"
duplicate/O mnh_fw $st+"_minus_hist_avg"
wave mnh_avg = $st+"_minus_hist_avg"
plh_avg = (plh_fw+plh_bw)/2
mnh_avg = (mnh_fw+mnh_bw)/2

killwaves block ; killwaves position ; killwaves value ; killwaves facetfw ; killwaves facetbw
killwaves plusvalfw ; killwaves plusvalbw ; killwaves minusvalfw ; killwaves minusvalbw
End
```

D.6. PROCEDURE 6

From this part of the code, distributions of segment lengths are determined separately for {001}- and {110}-oriented segments.

```
Function plotstephistograms(j)

variable j ; variable i
Display
For (i=1; i<j+1;i +=1)
string plus = "step"+num2str(i)+"_nm_plus_hist_avg"
string minus = "step"+num2str(i)+"_nm_minus_hist_avg"
wave plh_avg = $plus
wave mnh_avg=$minus
```

```
string l="L"+num2str(i) ; string b="B"+num2str(i) ; string m="L"+num2str(i+j) ; string t=
"T"+num2str(i)

Appendtograph/L=$l/B=$b plh_avg

AppendToGraph/L=$m/T=$t mnh_avg

variable a = (i-1)/j ; variable c= (i/j)

ModifyGraph axisEnab($b)=a,c ; ModifyGraph axisEnab($t)=a,c

ModifyGraph axisEnab($l)=0,0.5 ; ModifyGraph axisEnab($m)=0.5,1

ModifyGraph freePos($l)=a,kwFraction ; ModifyGraph freePos($m)=a,kwFraction

ModifyGraph freePos($b)=0,$l ; ModifyGraph freePos($t)=0,kwFraction

ModifyGraph mode=5,hbFill=4 ; ModifyGraph standoff=0 ; ModifyGraph axisOnTop=1

string mna = "step_all_nm_min_hist"

string pla = "step_all_nm_plus_hist"

If(i==1)

duplicate/O mnh_avg $mna

wave mnall =$mna

duplicate/O plh_avg $pla

wave plall =$pla

Else

mnall += mnh_avg ; plall += plh_avg

Endif

Endfor

string plat="step_all_plus_hist_atoms"

string mnat="step_all_minus_hist_atoms"

duplicate/O mnall $mnat

wave mn_at=$mnat

duplicate/O plall $plat

wave pl_at=$plat

mn_at = mnall*p ; pl_at = plall*p

End
```

List of Publications

Chapter 2

Recent advances in the use of curved single crystal surfaces

Sabine V. Auras and Ludo B.F. Juurlink *Progress in Surface Science*, submitted.

Chapter 4

Scaling Platinum-Catalyzed Hydrogen Dissociation on Corrugated Surfaces

Sabine V. Auras, Richard van Lent, Dima Bashlakov, Jessika M. Piñeiros Bastidas, Tycho Roorda, Rick Spierenburg and Ludo B.F. Juurlink *Angewandte Chemie International Edition*, **59** 20973-20979 (2020).

Chapter 5

Chiral Surface Characterisation and Reactivity Toward H–D Exchange of a Curved Platinum Crystal

Tycho Roorda*, **Sabine V. Auras*** and Ludo B.F. Juurlink *Topics in Catalysis*, **63**, 1558-1568 (2020).

Chapter 6

It's not just the defects - a curved crystal study of H_2O desorption from Ag

Sabine V. Auras, Robert A. B. van Bree, Dima L. Bashlakov, Richard van Lent, and Ludo B. F. Juurlink *Physical Chemistry Chemical Physics*, **21** 15422–15430 (2019).

*These authors contributed equally to the manuscript

OTHER PUBLICATIONS

On the correlation of structure and catalytic performance of VPO catalysts

Sebastian Böcklein, Gerhard Mestl, **Sabine V. Auras**, and Joost Wintterlin *Topics in Catalysis*, **60**,(19-20) 1682–1697 (2017).

Step-type and step-density influences on CO adsorption probed by reflection absorption infrared spectroscopy using a curved Pt(111) surface

Anton J. Walsh, Richard van Lent, **Sabine V. Auras**, Michael A. Gleeson, Otto T. Berg, Ludo B.F. Juurlink *J. Vac. Sci. Tech. A* **35**,(3) 03E102 (2017)

Site-specific reactivity of molecules with surface defects – the case of H_2 dissociation on Pt

Richard van Lent, **Sabine V. Auras**, Kun Cao, Anton J. Walsh, Michael A. Gleeson, Ludo B. F. Juurlink *Science* **363**(6423) 155-157 (2019)

CURRICULUM VITAE

Sabine Auras is a trained chemist, who received most of her education at the Ludwig-Maximilans University in Munich, Germany. After a broad undergraduate education (B.Sc. in Chemistry and Biochemistry, 2013), she developed an interest in physical chemistry during her Master studies (M.Sc. in Chemistry in 2015).

During an Erasmus stay at Leiden University in the Netherlands, Sabine had the opportunity to join the group of Dr. Ludo Juurlink for six months and studied the structure of a curved Ag(001) crystal. Subsequently, she returned to Germany to complete her M.Sc. degree. During her master thesis project, she investigated the correlations between structure and catalytic performance of VPO catalysts, under supervision of Dr. S. Böcklein and Dr. G. Mestl at Clariant AG. VPO is the industrial catalyst for the selective oxidation of maleic anhydride from *n*-butane, a reaction similar to ethylene oxidation.

Sabine started her Phd at Leiden University in December 2015, under supervision of Dr. Ludo Juurlink, where she studied the structure and reactivity of curved crystal surfaces with a variety of different techniques. Sabine explored the fundamental aspects of gas-surface dynamics, using multiple curved metal crystals (Ag, Pt, NiAl). A combination of surface structure techniques (LEED, AES, STM), spectroscopy (RAIRS) and mass spectrometry based techniques (TPD, TOF, King-and-Wells) have been the key to unraveling underlying structure dependencies in such reactions. A main focus of the PhD project has been the introduction of STM to the Juurlink group, by reviving an old VT-STM and initiating collaborations with STM-focused groups in Spain and the USA. Namely, Sabine had short-term stays abroad with the groups of Prof. Ortega (CFM, San Sebastian, Spain) and Prof. Killelea (Loyola University, Chicago, USA).

The results of her PhD work are presented in this thesis and resulted in several publications. Sabine also presented her work at various Dutch and international conferences, e.g. the Gordon Research Seminar and Conference on Chemical Reactions at Surfaces in 2017, the Gordon Research Seminar and Conference on Dynamics at Surfaces (2017 and 2019), several Dutch Scanning Probe Microscopy Days and HRSMC Symposia, the Reedijk Symposium (2017), and the AVS Prairie Chapter meeting (2017). In particular, she gave talks at the Gordon Research Seminar on Dynamics at Surfaces in 2019 and the HRSMC Symposium in 2019.

Sabine attended the NIOK course *Catalysis, An Integrated Approach* in 2017 and the HRSMC *Tulip School on Modern Advances in Spectroscopy* in 2018. She was also a

member of the HRSMC PhD platform. Throughout her time in Leiden, Sabine supervised and coached several Bachelor and Master students, and assisted teaching in the *algemene en anorganische chemie* and *practicum basisvaardigheden* courses of the *Molecular Science and Technology* B.Sc. programme of Leiden University and TU Delft.

Sabine will start her PostDoc at the Centro de Física de Materiales in Donostia, Spain in spring 2021.